Mémoire

Auteur : Vinesse, Julie
Promoteur(s) : Benmahi, Bilal
Faculté : Faculté des Sciences
Diplôme : Master en sciences spatiales, à finalité approfondie
Année académique : 2023-2024
URI/URL : http://hdl.handle.net/2268.2/21092

Université de Liège

Master's Thesis

Characterization of auroral electrons precipitating in Jupiter's polar regions with Juno/UVS data

Master in Space Sciences

Author:
Julie Vinesse

Supervisor:
Bilal Benmahi

Research Focus

June, 2024

UNIVERSITÉ DE LIÈGE

Abstract

Master in Space Sciences

Characterization of auroral electrons precipitating in Jupiter's polar regions with Juno/UVS data

by Julie VINESSE

The aurora on Jupiter is a remarkable phenomenon in our solar system. After having been observed for the first time by the Voyager 1 spacecraft in 1979, many spectral observations of these polar lights have been conducted on a continuous basis. Since 2016, the Juno spacecraft, in polar orbit around Jupiter, is gathering images and spectroscopic data that allow us to unravel the complex interplay between Jupiter's magnetosphere and atmosphere.
In this work, we use data from the UVS spectrograph onboard Juno to construct northern and southern spectral cubes for perijoves 1 to 48. From these spectral cubes, we derive H_2 brightness maps, emission angle maps and color ratio maps. We then use use a relation between color ratio, emission angle of the photons and energy of the precipitating electrons to compute energy maps for each of Juno's orbits, considering both monoenergetic and kappa energy flux distribution of electrons. These maps give an interesting overview of the evolution of several characteristics of the auroral regions over time.
We then perform a statistical analysis of the energy of the precipitating electrons as a function of time. We divide each auroral region into three sub regions: the polar, main and outer emission regions. We compare the energy of the electrons falling into these three sub regions and the energy of the electrons falling into their counterpart in the other hemisphere.
We also study the correlation between the H_2 auroral brightness and the energy of the precipitating electrons for the whole auroral emission region and for each sub region. We find that the H_2 auroral brightness is not correlated with the energy of the impinging photons by studying correlation plots as well as correlation coefficients for each perijove.
In the last part, we identify zones of the auroral emission where the color ratio seems to call into question the validity of the atmospheric model that we used. We then use TransPlanet to model synthetic spectra produced by populations of electrons falling into the atmospheric model that we use. We attempt to fit the modeled spectra to the observed ones by adjusting the energy of the impinging electrons that we computed as well as the amount of hydrocarbons in the model atmosphere. We find that the observed spectra for some of the selected zones can be fit by tuning the energy of the electrons while for others, changing the atmospheric composition is necessary. This raises the question of the consistency of the atmospheric composition across the entire auroral emission region.

Acknowledgements

When writing this master's thesis, I received help, guidance and support from many people that I would like to thank.

Firstly, I want to sincerely thank my supervisor, Bilal Benmahi, for his valuable support and constant availability. Throughout the year, he's been there to help me tackle every issue, even when we were in different countries. His guidance has motivated me to keep improving and give my best. I have truly learned so much through our collaboration.

I would also like to thank Denis Grodent and Bertrand Bonfond for their help, insightful advice, and expert guidance which guided my work in uncovering new mysteries of the jovian aurora.

My parents and my sisters have been an unwavering support through all of my academic journey and I would never have been able to produce this work without the joy and love they bring me every day.

My friends Celia, Élise, Lucy, Madeline, Jonathan, Justin and Hélène have carried me through my bachelor and master and I am grateful for each moment spent together gathering our brains, love and energy to overcome the difficulties.

Last but not least, I want to thank the astrobees for the joy, adventures, study sessions, meals and parties all throughout these two years of master's degree. The positive and uplifting environment that we created was a key element of our shared success and I could not have wished for better classmates.

Contents

1

Introduction

1.1 Jupiter

Jupiter is located 5.2 AU from the Sun and is the largest planet of the solar system (Encrenaz, 1999). It has been known since the antiquity and is still a major subject of research, with numerous spatial exploration missions targeting the planet itself as well as some of its 67 known moons. Observation of non thermal radio emissions from Jupiter in 1955 led to the discovery of its magnetic field (Burke & Franklin, 1955). It has since then been characterized in depth by several spacecrafts such as Pionneer 11, Voyager and Galileo. Its magnetic dipole moment makes an angle of 10° with respect to its rotational axis and its magnetic moment is 20 000 times stronger than Earth's (Encrenaz, 1999). Jupiter's atmosphere and magnetosphere are the subject of many studies and allow us to unravel the interactions between magnetic fields and atmospheres for all planets.

1.2 Jupiter's atmosphere

The first characterization of the jovian atmosphere was performed by Rutherfurd (1863) using an infrared spectrometer and it has since been studied in depth thanks to the data from many in situ spacecrafts, ground-based and space-based telescopes. Its main constituents are atomic hydrogen (H), molecular hydrogen (H_2) with a volume mixing ratio of 0.86, followed by helium (He) whose volume mixing ratio is 0.136 (Bagenal et al., 2006). A non exhaustive list of known atmospheric constituents of Jupiter is displayed in table 1.1 along with their mixing ratio relative to H_2 (Atreya et al., 2003).

In the framework of this master's thesis, we use a model for the jovian atmosphere in the auroral region that was presented by Grodent et al. (2001). This 1D model[1] gives us the densities as a function of altitude of the main neutral atmospheric constituents, i.e. atomic hydrogen (H), molecular hydrogen (H_2), Helium (He), methane (CH_4) and acetylene (C_2H_2) as illustrated in figure 1.1 from the tropopause to the upper thermosphere. In this model, H, H_2 and He are present at every altitude. CH_4 and C_2H_2, on the other hand, are mainly present below the homopause. The homopause is defined as the altitude where eddy and molecular diffusion rates become equivalent, but is also considered by some authors as the altitude where the optical depth (τ) of the constituent is equal to 1 (Parkinson et al., 2019).

The equation of Beer-Lambert (Liou, 2002) states that a beam of electromagnetic radiation of intensity I_λ passing through a non scattering medium between 0 and s_1

[1]The model only varies in the vertical direction and has no horizontal variations.

will undergo extinction as follows :

$$I_\lambda(s_1) = I_\lambda(0)e^{-\tau_\lambda(s_1,0)} + \int_0^{s_1} B_\lambda[T(s)]e^{-\tau_\lambda(s_1,s)}k_\lambda\rho ds. \tag{1.1}$$

Where I_λ is the intensity of the electromagnetic beam, τ is the optical depth, $B_\lambda[T(s)] = \frac{2hc^2}{\lambda^5(e^{hc/K\lambda T}-1)}$ is the Planck function with $h = 6.626 \times 10^{-34}$ J sec and $K = 1.3806 \times 10^{-23}$ J deg^{-1}. In this case, $B_\lambda[T(s)] = 0$ because we consider a single beam entering the atmosphere. Therefore, when $\tau = 1$, approximately 63% (e^{-1}) of the beam is absorbed and we consider that the light will be significantly absorbed and name this the limit the homopause. It is important to note that we use a one dimensional vertical atmospheric model, thus ignoring horizontal variations, even though it has been shown that the CH_4 homopause varies spatially in the auroral regions of Jupiter (Sinclair et al., 2020). This is a limitation of our model which will be crucial when we interpret our results.

Table 1.1: Composition of Jupiter's atmosphere.

Species	Mixing ratio relative to H_2
H_2	1.0
H	variable
He	0.157 ± 0.0036
H_2O	(2-20)× 10^{-9} (upper stratosphere) ≤ 10^{-6} (≤ 4 bar, hotspot) (5.6 ± 2.5)× 10^{-5} (12 bar, hotspot) 6.0(+3.9, -2.8)× 10^{-4} (19 bar, hotspot)
CH_4	(2.1 ± 0.4)× 10^{-3}
CH_3	Detection (polar region)
C_2H_6	(1-5) × 10^{-6} (stratosphere)
C_2H_2	(3-10) × 10^{-8} (stratosphere)
C_2H_2	<2.5 × 10^{-6} (1-10 μbar)

1.3 Jupiter's magnetosphere

The jovian magnetosphere is the largest of the solar system, a schematic representation of its structure is shown in figure 1.2. Its boundary, the magnetopause, extends up to 63-92 jovian radii (1 jovian radius = 1 R_J = 71492 km) at the subsolar point. In the direction opposite to the Sun, it forms a longer tail (Bolton et al., 2015). The magnetic field originates from a dynamo regime caused by the rapid rotation of a metallic hydrogen layer inside of Jupiter. The magnetosphere is populated by a plasma, i.e. a globally neutral gas of electrons and ions and can be divided up in three main regions: the inner, middle and outer magnetospheres that have frontiers around 10-15 R_J and 40-60 R_J (Khurana et al., 2004).

The inner magnetosphere is the region where particles are trapped along dipole-like magnetic field lines. This area includes radiation belts that are supplied by cosmic rays and the outer magnetosphere. Io, one of Jupiter's moons, orbits within this inner magnetosphere. This moon is particularly significant because the neutral gas escaping from its atmosphere is released into the magnetosphere, becomes ionized, and forms a plasma torus within the inner magnetosphere. In this region of the magnetosphere,

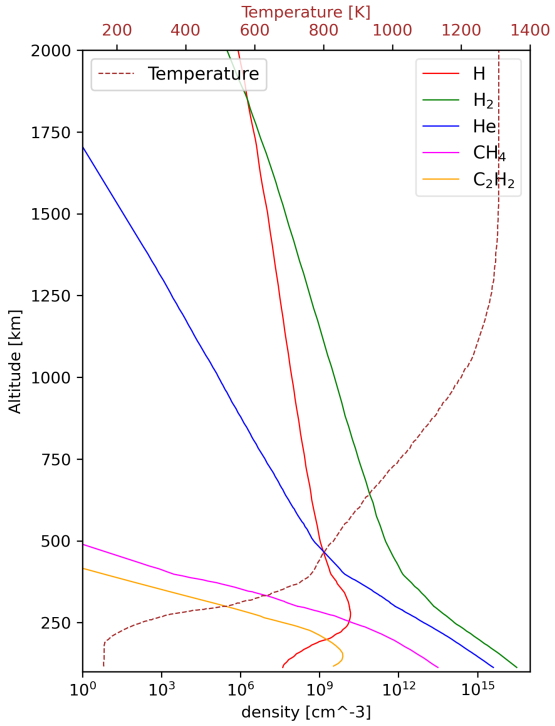

FIGURE 1.1: Densities of the main neutral elements of the atmosphere of Jupiter (H, H_2, He, CH_4 and C_2H_2) as a function of altitude as presented by Grodent et al. (2001). The altitudes are given with respect to a reference pressure level of 1 bar (0 km). Figure from Benmahi et al. (2024).

the plasma rigidly corotates with the planet due to very efficient momentum transfer from the neutral atmosphere to the magnetosphere.

The middle magnetosphere is where the field lines start to deviate from a dipole significantly. The distance from the planet is higher and the momentum transfer becomes less efficient. As a consequence, the coupling is weaker and the plasma subcorotates.

In the outer magnetosphere, the azimuthal plasma velocity lags corotation by a factor of two or more. On the dayside, the outer magnetosphere is highly variable, with the dayside magnetopause ranging from 45 R_J to 100 R_J depending on solar wind pressure. On the nightside, an additional current system, called the magnetotail current system, connects the magnetodisc currents to the magnetopause currents, creating a long magnetotail that can extend to Saturn's orbit .

The particles trapped inside of Jupiter's magnetosphere have several origins (Lopes & Williams, 2015). Io's torus is caused by atmospheric escape due to its strong volcanic activity, which is driven by tidal heating rather than by tectonic plate movements. Orbital resonance with Jupiter's other moons, Europa and Ganymede, forces Io into an eccentric orbit, causing significant tidal flexing in Io's crust and mantle. This flexing generates internal friction that produces intense heat, resulting in volcanic activity. Io's volcanic outgassing and the evaporation of SO_2 frost deposits continuously replenish its atmosphere. Io's low gravity then allows some of this material to escape into space, forming a corona, neutral clouds, and the Io torus. The ionized particles are held within the torus by Jupiter's magnetic field.

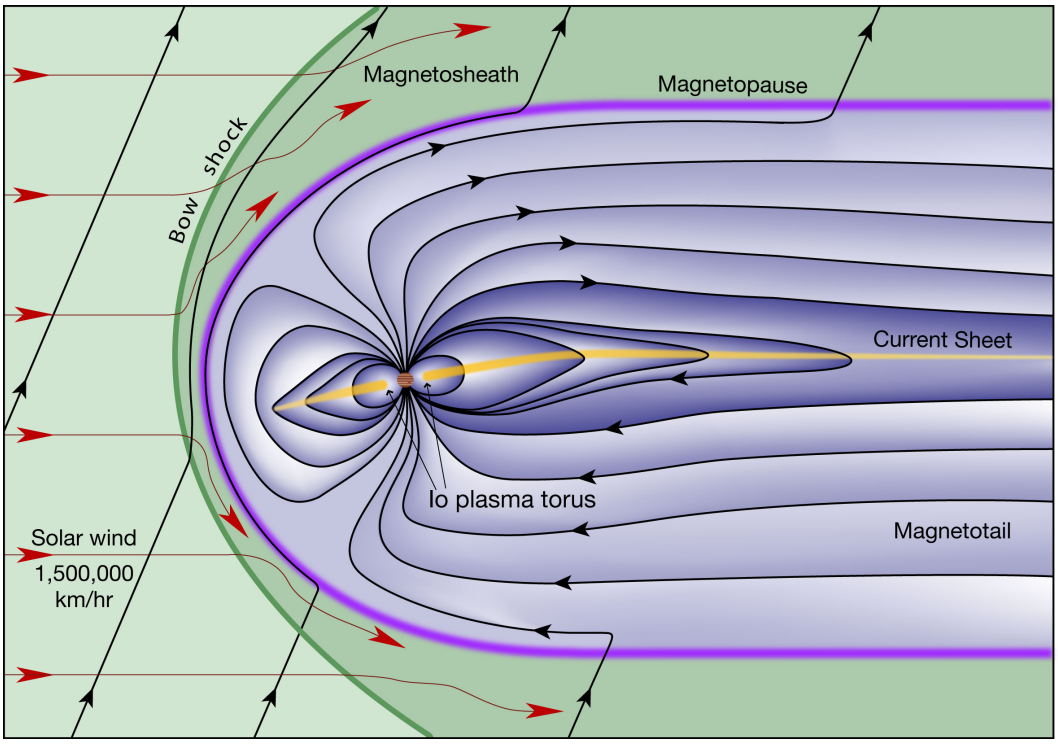

FIGURE 1.2: Representation of Jupiter's magnetosphere by Fran Bagenal and Steve Bartlett.

The magnetospheric plasma can also be fed by the other satellites of Jupiter. It has been shown by Schreier et al. (1993) that, because Europa is not protected by a magnetic field, sputtering on its surface by particles from the radiation belt can add new particles to the magnetosphere. Ganymede and Callisto could also contribute to the plasma in the magnetosphere, as was proposed by Gurnett et al. (2000) and Eviatar et al. (2000). Other mechanisms have been put forward, involving the interaction of the magnetosphere with solar wind (Delamere & Bagenal, 2010) and would mean that the plasma of the solar wind can in some way be incorporated to the magnetospheric plasma. It is however clear that volcanism on the galilean moons is the principal source of the jovian magnetospheric plasma.

1.4 Jupiter's aurorae

Jupiter's aurorae have been studied since their discovery in 1979 during the flyby of the planet by the Voyager 1 spacecraft (Broadfoot et al., 1979). This phenomenon is caused by the precipitation of energetic charged particles in the jovian atmosphere following magnetic field lines. These particles will then collide with the neutral elements of the atmosphere and transfer them a fraction of their energy. We consider that the impinging particles are mostly electrons and that the amount of precipitating ions is negligible (Mauk et al., 2002). The atmospheric constituents release their energy partly in the form of electromagnetic radiation, ranging from the ultraviolet (UV) to the infrared (IR) domain, due to excitation and subsequent de-excitation processes that produce aurorae. However, a portion of this energy is also used for ionization, leading to ion production, for dissociation and for heating.

The IR part of this emission was studied by Uno et al. (2014) while Vasavada et al.

(1999) observed the visible auroral emission of Jupiter. In this work, we study the UV emission from Jupiter's aurorae. The jovian auroral regions can be divided into three principal regions : the main, polar and outer emission regions which include the footprint emissions of some galilean moons (e.g, Io footprint emission) (Grodent, 2015). Quasi simultaneous observations of the northern and southern auroral regions using the Hubble Space Telescope (HST) (Gérard et al., 2013) showed that most auroral structures in the northern auroral region have a counterpart in the southern auroral region and that these counterparts are connected through magnetic field lines. Going forward, we will consider these three regions : the main, the polar and the outer emission regions for both the northern and southern hemispheres.

1.4.1 The main emission

The main emission region is a thin region of high brightness around the magnetic pole (1 in figure 1.3). The main auroral emissions on Jupiter have long been thought to be associated with the breakdown of rigid corotation in the Jovian magnetospheric plasma (Cowley & Bunce, 2001). However, this theory has since then been put into question by observational evidence (Bonfond et al., 2020).

In an alternative model, Alfvén waves are generated by turbulent plasma fluctuations within the equatorial current sheet in the middle magnetosphere, then travel along magnetic field lines toward the ionosphere (Saur et al., 2003, 2018). When these small-scale disturbances encounter gradients in plasma density, such as those found at the boundary of the ionosphere or within the magnetodisc, partial reflections can occur. The interactions between these reflected waves are non-linear, driving a cascade of turbulence that shifts toward shorter wavelengths. As these Alfvén waves shorten and reach scales comparable to the kinetic properties of magnetospheric particles, they can engage in wave-particle interactions through Landau damping, resulting in energy transfer to the magnetospheric plasma. This energy transfer process leads to the stochastic acceleration of particles toward the ionosphere, which corresponds with the bidirectional electron distributions detected by Juno above the auroral zones (Mauk et al., 2017). The model effectively explains the stochastic acceleration of electrons along magnetic field lines within an L-shell close to 30 R_J, generating an auroral oval that approximately corresponds to this radial distance.

1.4.2 The outer emission

In this work, we will consider the outer emissions as every emission comprised between the main emission region and the Io footprint. This encompasses what is called the secondary emission (4), the signatures of injections (5) and the footprints of Europa and Ganymede (7 and 8). The outer auroral emissions on Jupiter are primarily driven by the hot plasma injection process (Dumont et al., 2018). This involves the interchange of magnetic flux tubes containing cold, dense plasma from Io with flux tubes containing sparse, hot plasma moving towards Jupiter. This injection of hot electrons creates anisotropy, generating whistler mode waves that scatter energetic electrons into the loss cone through pitch angle diffusion, leading to the outer "diffuse" auroral emissions. The signatures of injection, on the other hand, may be associated with other mechanisms such as field aligned currents flowing along the boundary of a hot plasma cloud (Mauk et al., 2002). The footprints of each satellite are linked to the magnetic field lines that connect Jupiter to each of its satellites. The satellites constitute an obstacle to the corotating plasma and cause magnetic disturbances

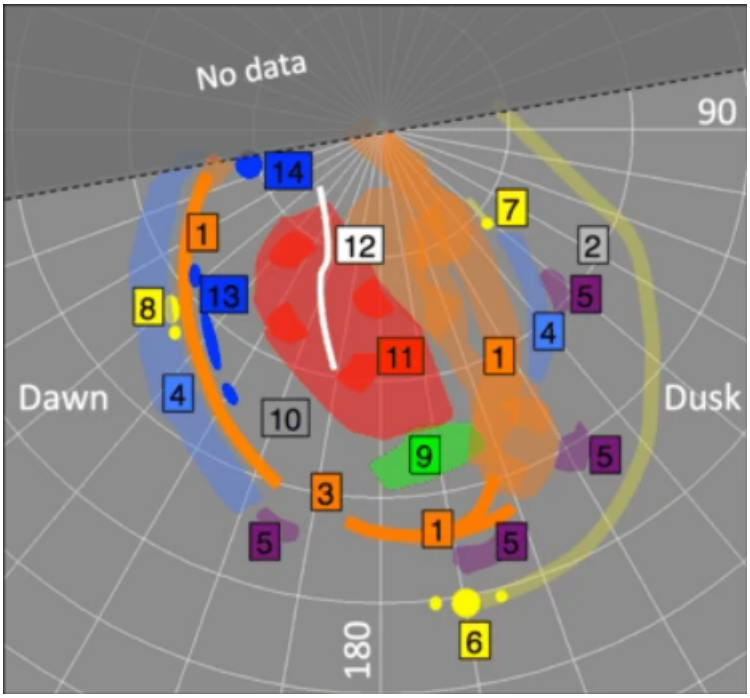

FIGURE 1.3: Representation of the jovian northern auroral region with 1. the main emission, 2. the kink region, 3. the discontinuity, 4. the secondary emission, 5. the signatures of injections, 6. the footprint of Io (multiple) and tail, 7. the footprint of Europa and tail, 8. the footprint of Ganymede (multiple), 9. the polar active region, 10. the polar dark region, 11. the polar swirl region, 12. the polar auroral filament (PAF), 13. the dawn spots and arcs; 14. the midnight spot. The upper gray shaded region is not accessible to Earth orbit instruments. Figure from Grodent (2015).

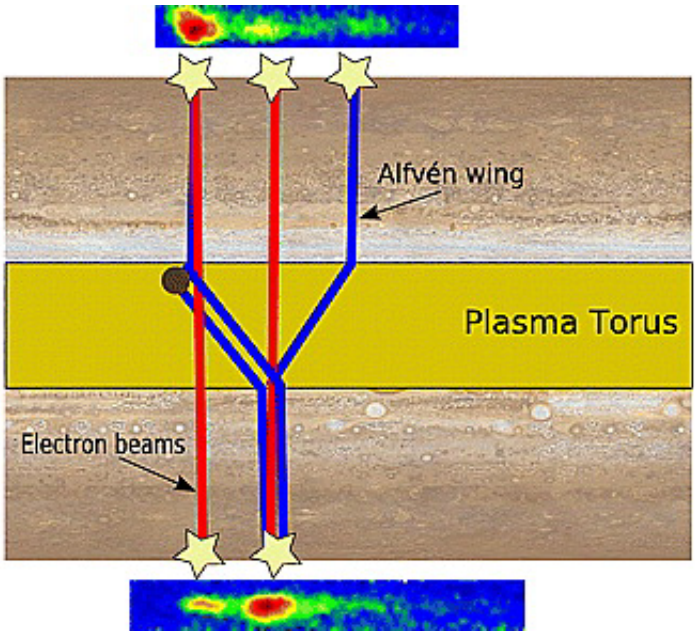

FIGURE 1.4: Schematic view of the mechanism explaining the presence of spots and tails linked to the Io footprint (Bonfond et al., 2008).

that propagate along Jupiter's magnetic field lines in the form of Alfvèn waves. The reflection of these waves on the density gradients of plasma when exiting the torus and entering the atmosphere explain the presence of spots and multiple footprints (Bonfond et al., 2008). Figure 1.4 illustrates this phenomenon.

1.4.3 The polar emission

The polar emission region is defined as the auroral emissions that are located poleward of the main emission region. There is no clear consensus on the origin of these emissions. They are linked to the outer magnetosphere and Greathouse et al. (2021) showed that they depend on magnetic local time. They do not appear to be linked with the main emission or with emission from any satellites, it is however suspected that they may be linked with the solar winds through interactions on the boundary of the outer magnetosphere with the solar winds plasma (Delamere & Bagenal, 2010). Modelings conducted by Zhang et al. (2021) indicate that the magnetic field over the polar region has a complex structure with the presence of open and closed magnetic field lines. Bunce et al. (2005) suggested the polar emissions could be linked to pulsed reconnection at the magnetopause while Masters et al. (2021) put forward the idea that magnetic reconnection can also happen closer to Jupiter, a few jovian radii above the surface due to Jupiter's strong magnetic field.

In figure 1.3, they are separated into the active (9), dark (10) and swirl (11) regions. Other structures appear on top of these regions, like the polar filaments (12) or the polar auroral bright spot (Haewsantati et al., 2021). However, in the framework of this master's thesis, we will consider them as a single region.

1.5 Juno

The Juno mission is a part of NASA's new frontiers program whose primary goal is to study in depth the composition of Jupiter, map its magnetic and gravitational field,

as well as its atmospheric composition (Grammier, 2009). It was selected by NASA in 2005 and was launched in 2011. After a fly-by of the Earth in 2013, it reached its orbit around Jupiter 33 months later, on the 4th of July 2016.

The main objectives of the mission are stated by Bolton et al. (2017) and the goals specifically linked to the magnetosphere were detailed by Bagenal et al. (2017). The main scientific objectives of the Juno mission are as follows:

- Gaining a better understanding of the formation of the solar system, discriminating between different scenarios and constraining the composition and role of planetesimals.
- Determining whether Jupiter has a core composed of heavy elements by mapping its gravitational and magnetic field.
- Determining the structure of the atmosphere below the top of the clouds thanks to an in-depth study of the atmospheric dynamics.
- Studying Jupiter's strong auroral emissions thanks to a very close approach.
- Better understanding the magnetosphere of Jupiter and its relation with the aurora.

Juno was put on a highly elliptical polar orbit in such a way as to make close-in measurements at each perijove (PJ) [2] while avoiding the regions of high radiation. The trajectories of the 35 first perijoves are shown in figure 1.5. The duration of each of these orbits was 52.867 days on average. With its highly eccentric polar orbit, Juno allows us to investigate the aurorae of Jupiter like never before. Indeed, before Juno, the only available data about Jupiter's aurorae came from remote imaging with spacecrafts on a terrestrial orbit. Only the dayside of both auroral regions can be observed with such a method. With Juno, the spacecraft gets to a minimal distance of 4200 km from Jupiter's surface and reaches its apoapsis at 113 R_J. This allows for observations of the whole aurora, at every local time.

Figure 1.6 shows how the perijoves were arranged in such a way that each pole can be mapped uniformly. This configuration allows for measurements of the gravitational and magnetic field as well as the aurorae.

Juno is equipped with nine scientific instruments that take measurements and images of Jupiter as the spacecraft flies by Jupiter. These instruments are listed as follows: Gravity science (GRAV), Magnetometer (MAG), MicroWave Radiometer (MWR), JunoEnergetic paricle Detector Instrument (JEDI), Jovian Auroral Distributions Experiment (JADE), Waves, Jovian InfraRed Auroral Mapper (JIRAM), Juno Camera (JunoCam) and the UltraViolet Spectrograph (UVS), which we are interested in for this study.

1.6 UVS

In the present work, we use data from the UVS spectrograph onboard Juno (Gladstone et al., 2017) for perijoves 1 to 48. This ultraviolet spectrograph works in a wavelength

[2] The perijove is the point of closest approach of the spacecraft to Jupiter, by extension this term is used to refer to an orbit of Juno.

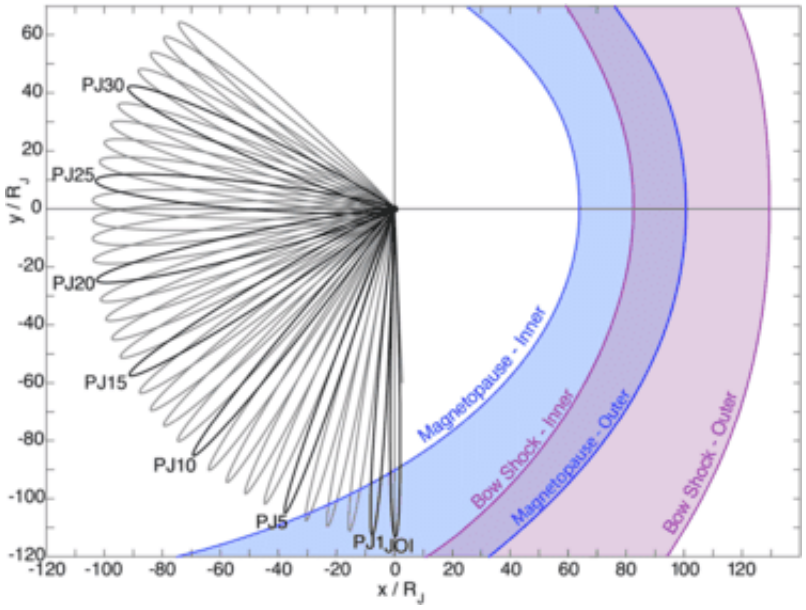

FIGURE 1.5: Representation of the first 35 orbits of Juno in the xy-plane, with the x-axis pointing in the direction of the Sun and the z-axis aligned with the spin axis of Jupiter (Bolton et al., 2017)

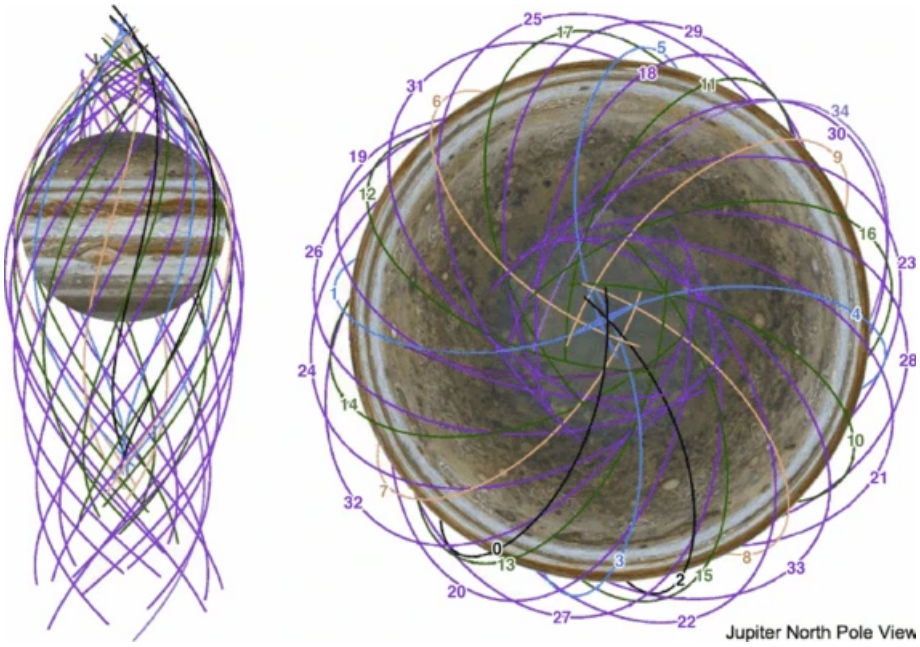

FIGURE 1.6: Representation of the first 35 orbits of Juno separated in such a way that they map the poles uniformly. The blue lines are separated by 90°, adding the orange lines reduces the separation to 45°, the green lines provide 22.5° sections and 11.25° sections with the purple lines. Left : side view with the spin axis of Jupiter towards the top. Right : View from above the North pole of Jupiter.) (Bolton et al., 2017)

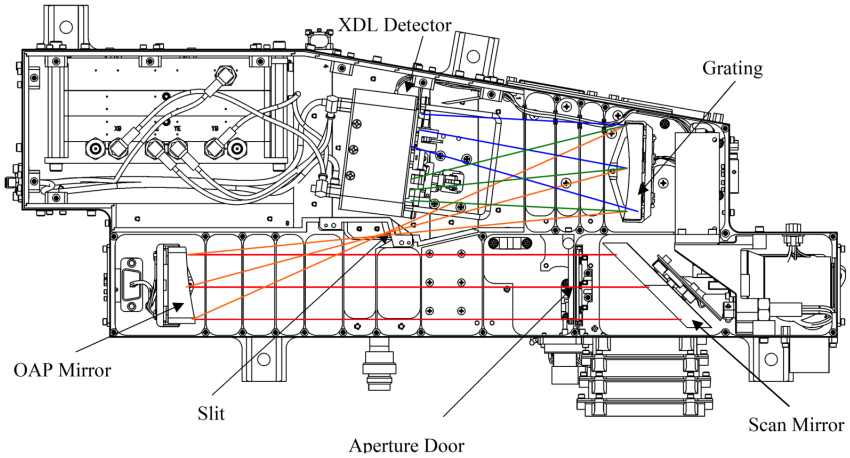

FIGURE 1.7: Schematic of the UVS spectrograph. The light is reflected on a scan mirror and then focused on the slit by the primary mirror. The grating disperses the light on the detector Hue et al. (2019).

range between 68 and 210 nm, covering extreme- and far-ultraviolet regions. When the light enters the instrument, it hits a flat scanning mirror that directs it to the primary mirror. The focused light passes through a slit that has a "dogbone" shape, i.e. consecutive segments with different field of views (0.2°×2.5°, 0.025°×2°, and 0.2°×2.5°). The two larger slits on both extremities are called the wide slits while the central one is called the narrow slit. The electromagnetic radiation is then dispersed by a diffraction grating before falling onto a 2D detector. The spectrograph is represented in figure 1.7.

The spacecraft is spin-stabilized and makes a full rotation on itself every 30 seconds, swiping the planet and retrieving data. For each of these rotations, the UVS data consists of count rates of UV photons as well as their wavelengths and emission angles. The kernels of the spacecraft inform us about its spatial location in the Jupiter SIII coordinate system [3] and the pointing direction of the spacecraft as a function of time. On this basis, it is possible to reconstruct a UV spectral cube of the auroral emissions integrated over a period of time of several tens of minutes before and after perijove, providing views of the northern and southern auroral regions, respectively. We also use the kernels of the spacecraft to know its precise position projected on the planet Jupiter, as well as its position with respect to the magnetic field of Jupiter.

In the UV domain [80,180 nm], the observed jovian auroral emissions are due to H (with the strong Lyman-α emission) and H_2 de-excitation by electronic transition through the Lyman and Werner bands (Benmahi et al., 2024).

1.7 Color ratio

The concept of color ratio (CR) was first introduced by Yung et al. (1982). It relies on the presence of absorption bands of hydrocarbons in the electromagnetic spectrum. In this study, we focus on the spectrum between 125 and 170 nm. In this region of the spectrum, the emission is due to the de-excitation of H_2 through optically allowed

[3] In this system, the Z-axis coincides with the rotation axis of Jupiter, the X-axis is defined as 0° latitude and the Y-axis is orthogonal to both the X and Z-axis.

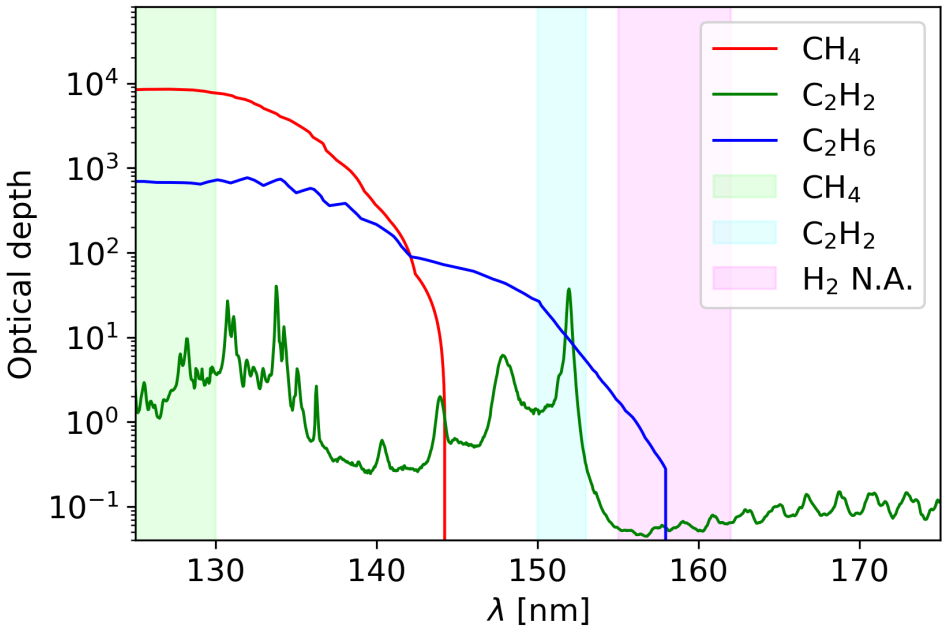

FIGURE 1.8: Optical depths as a function of wavelength of CH_4 (red line), C_2H_2 (green line), C_2H_6 (blue line) and selected bands that are characterized by a strong CH_4 absorption (green), large C_2H_2 absorption (blue) and almost no absorption (pink). One may consider that the emission is fully absorbed when the optical depth is >= 1. Figure from Benmahi et al. (2024).

electronic transitions. However, some atmospheric constituents also absorb this emission and lower the intensity of the spectrum for certain bands. CH_4 mainly absorbs below 140 nm. We define the band between 123 and 130 nm as the absorption band of CH_4 as the H_2 emission is strongly absorbed by CH_4 and much less by C_2H_2. This latter hydrocarbon absorbs significantly up to 153 nm and we select the band between 150 and 153 nm to characterize its absorption as CH_4 does not absorb in that wavelength range. We also define the range between 155 and 162 nm as the unabsorbed part of the spectrum where the H_2 emission is almost not affected by these hydrocarbons. Figure 1.8 shows the optical depths of CH_4, C_2H_2 and C_2H_6 (ethane) as a function of wavelength in the FUV domain superimposed over the regions defined here above, confirming that the corresponding constituents absorb significantly in the selected zones. C_2H_6 absorbs below 157 nm, however it is not taken into account in the atmospheric model that we use, which will be discussed in section 5. These bands are used to evaluate the auroral emission depth thanks to the color ratio from which we will infer the energy of the impinging electrons.

Based on these regions, we define the CH_4 and C_2H_2 color ratios (CR_{CH_4} and $CR_{C_2H_2}$) as the ratios between the integrated intensity over the unabsorbed region and the integrated intensity over the absorption band of the hydrocarbon:

$$CR_{CH_4} = \frac{I(155nm - 162nm)}{I(125nm - 130nm)} \quad \text{and} \quad CR_{C_2H_2} = \frac{I(155nm - 162nm)}{I(150nm - 153nm)}. \tag{1.2}$$

$I(\lambda_{\min} - \lambda_{\max})$ is the measured intensity (in photon units) integrated between $\lambda_{\min}$ and $\lambda_{\max}$. These color ratios will be high when the spectrum is highly absorbed by the compound in question and low in the opposite case. This informs us about the penetration power of the precipitating electrons in these regions and, consequently,

about the energy of the electrons precipitating in the region since we know that in our atmospheric model, CH_4 is present at altitudes higher than C_2H_2. For example, in regions where the CH_4 color ratio is high and the C_2H_2 color ratio is low one may expect that electrons were energetic enough to reach below the homopause of CH_4 but not energetic enough to reach the homopause of C_2H_2.

From these considerations, and using the electron transport model TransPlanet, Benmahi et al. (2024) developed the following relation between the CH_4 color ratio, the characteristic energy of the precipitating electrons (E_0) and the emission angle of the emitted photons with respect to the vertical (θ) :

$$\mathrm{CR}\left(E_0, \theta\right) = A \cdot C \cdot \left(\tanh\left(\frac{E_0 - E_c}{B} + 1\right)\right) \cdot \ln\left(\left(\frac{E_0}{D}\right)^{\alpha} + e\right)^{\beta} \cdot \left(1 + \delta \cdot \sin(\theta)^{\gamma}\right). \tag{1.3}$$

A is the minimum value of the modeled color ratio (i.e. the unabsorbed value), E_c is a treshold energy and B, C, D, α, β, δ and γ are fit parameters. E_0 is the characteristic energy of the electron population. These parameters have been computed by Benmahi et al. (2024) for a kappa and a monoenergetic distribution of electrons and are displayed in table 1.2. This relation links the energy of precipitating electrons, the emission angle of the photons and the CH_4 color ratio for one single point. For an extended region, we can use averages of two of these parameters to estimate the third one but we will lose in accuracy.

The electrons precipitating in Jupiter's auroral regions exhibit energetic distributions that have not been captured by the various spacecraft that have flown by Jupiter. Although spacecraft such as Voyager (Russell, 1993), Ulysses (Zarka, 1998), Galileo, Cassini-Huygens (Hansen et al., 2004), and New Horizons (Krupp, 2007) have studied Jupiter's magnetosphere at their respective altitudes, they have not characterized the energy distributions of electrons precipitating immediately above the polar auroral altitudes. Once electrons pass the average flying altitude of spacecraft, they continue to undergo complex processes before precipitating into the ionosphere. These processes include acceleration by inertial Alfvén waves and whistler waves, as well as alterations due to ion and electron inverted-V structures.

Previous studies, such as those by Salveter et al. (2022) and Mauk et al. (2018), have measured broadband electron distributions in Jupiter's auroral regions using Juno/JEDI data and found that these distributions typically follow a kappa distribution. For this study, we will adopt this approach and use kappa distributions to characterize the electron populations. Additionally, to provide a comparison with the realistic kappa distribution, we will also consider monoenergetic electron populations.

To determine the characteristic energies of these electron populations, we will use the method developed by Benmahi et al. (2024), which establishes a relationship between the CH_4 color ratio and the characteristic energy of precipitating electrons. By measuring the color ratio, we can thus infer the energy of the electrons without direct measurement.

In the case of monoenergetic electron populations, the characteristic energy is the same as the mean energy $\langle E \rangle = E_0$. For kappa distributions of electrons, each energy

level is populated according to the following distribution:

$$f_k(E, \langle E \rangle) = Q_0 \frac{4}{\pi} \frac{\kappa(\kappa-1)}{(\kappa-2)^2} \frac{E}{\langle E \rangle} \frac{\langle E \rangle^{\kappa-1}}{\left(\frac{2E}{\kappa-2} + \langle E \rangle\right)^{\kappa+1}}. \tag{1.4}$$

Here, Q_0 is the total energy flux, κ is the parameter of the distribution, and $\langle E \rangle$ is the mean energy computed from the characteristic energy of the distribution ($\langle E \rangle = 2E_0 \frac{\kappa}{\kappa-2}$).

According to Salveter et al. (2022), Juno/JEDI data from the first 20 perijoves indicate that electrons precipitating in Jupiter's auroral regions follow a kappa distribution with a κ parameter of 2.5.

TABLE 1.2: Parameters of fit for the CR (E_0, θ) relation for kappa and monoenergetic distribution of electrons for the northern and southern auroral regions as computed by Benmahi et al. (2024).

Fit parameters	Kappa distribution (north pole)	Kappa distribution (south pole)	Mono-energetic distribution (north pole)	Mono-energetic distribution (south pole)
E_c[eV]	2559	1417	2972	1511
A	1.59	1.69	1.88	1.8
B[eV]	10588	20569	800000	96641.40
C	1.48	1.15	0.59	0.51
D[eV]	17879	7642	56967	60847
α	1.69	1.2	3.16	3.15
β	1.93	2.28	2.15	2.07
δ	0.62	0.63	0.91	0.89
γ	6.63	6.74	7.9	7.9

1.8 Models

1.8.1 Electron transport model : TransPlanet

In the final section of this study, we will simulate electron precipitation in the Jovian auroral atmosphere as modeled by Grodent et al. (2001). To achieve this, we will utilize the electron transport model TransPlanet. The initial version of this code was developed by Lilensten (1989) and has since undergone multiple improvements and adaptations for various planetary scenarios. Benmahi (2022) introduced the most recent iteration of the TransPlanet code, which consists of three components: a kinetic part that simulates electron precipitation in an atmosphere, an emission part that models H2 UV emission, and a fluid part, which will not be used in this study. TransPlanet simulates a population of electrons precipitating in the jovian atmosphere and interacting with the atmospheric particles, depositing part of their energy. This interaction between suprathermal electrons and neutral atmospheric constituents is described by the dissipative Boltzmann equation which models binary interactions between particles as solid spheres. Accounting for the discrete energy loss for each of these collisions as well as the creation of secondary electrons, the Boltzmann equation can ultimately model the precipitation of electrons in an atmosphere.

If the electrons follow a distribution function $f(\vec{r}, \vec{v}, t)$ where r is the position, v

the velocity of the electrons and t the time, the distribution function follows the non conservative Boltzmann equation :

$$\frac{\partial f}{\partial t} + \boldsymbol{v} \cdot \frac{\partial f}{\partial \boldsymbol{r}} + \frac{\partial}{\partial \boldsymbol{v}} \left(\frac{f \boldsymbol{X}}{m_e} \right) = Q. \tag{1.5}$$

Q is a source function of the electrons produced at $(\vec{r}, \vec{v}, t)$, m_e is the mass of the electron and X is an external force acting on the electrons.

The atmosphere that the electrons will precipitate in is the one presented in Grodent et al. (2001) that is described in section 1.2. The collision between the electrons and the atmospheric particles can be either elastic or inelastic. Therefore, it is essential to consider both the elastic collisions of all particles in the model with electrons and the inelastic collisions detailed in table 1.3.

After solving the Boltzmann equation for a given electron population precipitating in the jovian atmopshere, we obtain an electron flux as a function of altitude and energy that is used as an initial condition in the UV emission part of the code.

1.8.2 H_2 UV emission model

In the study by Benmahi et al. (2024), an H_2 UV emission model was developed to simulate the UV emissions in Jupiter's auroral regions. This emission primarily arises from the Lyman and Werner bands of H_2, producing spectral lines between 80 and 190 nm. The model simulates electron transport and the excitation of H_2 molecules through photon absorption and electron collisions.

The model calculates the excitation rates of H_2 molecules, considering processes such as electron collisions that result in the transition of H_2 to excited states. These excited states can then de-excite, emitting UV light. The volume excitation rate of a rovibrational state is determined by the sum of direct and cascade excitation rates. Self-absorbed photons are redistributed to lower-energy transitions.

For validation, the model's simulations were compared with experimental results from Liu et al. (1995), using a 100 eV mono-energetic electron beam to bombard H_2 molecules. The model showed good agreement with experimental spectra, despite some discrepancies in spectral line amplitudes due to electron energy spectrum inhomogeneity.

Ultimately we obtain a total 1D vertical flux of electrons (neglecting horizontal variations) in the atmosphere as well as a synthetic spectrum of H_2 emission taking into account the absorption by hydrocarbons. These modeled spectra will be used in section 5.

TABLE 1.3: Inelastic collisions between the jovian atmospheric particles and electrons. Table from Benmahi et al. (2024)

Reactions	Products
$e^- + \mathrm{H} \longrightarrow$	$\mathrm{H}^* + e^-$ $\mathrm{H}^+ + 2e^-$
$e^- + \mathrm{H_2} \longrightarrow$	$\mathrm{H_2^*} + e^-$ $\mathrm{H_2^+} + 2e^-$ $\mathrm{H} + \mathrm{H} + e^-$ $\mathrm{H}^+ + \mathrm{H} + 2e^-$
$e^- + \mathrm{He} \longrightarrow$	$\mathrm{He}^* + e^-$ $\mathrm{He}^+ + 2e^-$ $\mathrm{He}^{2+} + 3e^-$
$e^- + \mathrm{CH_4} \rightarrow$	$\mathrm{CH_4^*} + e^-$ $\mathrm{CH_4^+} + 2e^-$ $\mathrm{CH_3^+} + \mathrm{H} + 2e^-$ $\mathrm{CH_2^+} + 2\mathrm{H} + 2e^-$

2

Data reduction as spectral cubes

In this work, we used data from the UVS spectrograph to study several characteristics of Jupiter's auroral emissions. The first task consisted in turning the UVS data from each perijove into a spectral cube for the northern and southern auroral regions.

A spectral cube is a three dimensional dataset, that can be described as a stack of maps, each representing the auroral (northern or southern) emission, i.e. the amount of photons emitted by the atmosphere, for a given wavelength. Therefore, each element of the spectral cube represents a unique point on the map, identified by three coordinates: x, y, and the wavelength. Slicing the cube at a given wavelength gives a map of the emissions at that specific wavelength while extracting a given point on the map in every slice of the cube gives the spectrum of this point. The spectral cube was sampled every 1° in latitude and longitude and every 0.1 nm in wavelengths. Additionally, to enhance the signal-to-noise ratio (S/N) of the UV emission spectra, we only mapped photons measured by the two UVS wide slits, which have a spectral resolution of around 2.1 nm (Greathouse et al., 2013), and discarded the photons coming from the narrow slit.

We constructed these spectral cubes for all perijoves as mentioned in table 2.1. The ones marked with an asterisk did not have sufficient data for the northern auroral region and we could thus only construct a spectral cube for the southern emission regions. In table 2.1 we printed the dates and times of start and finish of data acquisition for each perijove as well as the equatorial time; i.e. the time at which the spacecraft crosses the equatorial plane of Jupiter. The photons that are detected before the equatorial time belong to the northern aurora while the ones that hit the detector after that time are added to the southern cube. This table shows that the time spent over the northern hemisphere becomes shorter with time which explains the fact that some perijoves near the end of the table do not have enough photons for the construction of a northern spectral cube. This procedure provided us with 36 spectral cubes corresponding to northern auroral emissions and 44 spectral cubes corresponding to southern auroral emissions

2.1 Brightness maps

Using these spectral cubes, we mapped the H_2 brightness of the auroral emissions for the northern and southern emission regions. We define the H_2 brightness as the emission over the wavelength range of the unabsorbed part of the spectrum as defined in section 1.7 (155 - 162 nm). To distinguish photons between the ones that are scattered from solar emissions and the true auroral photons, we also fixed a treshold for

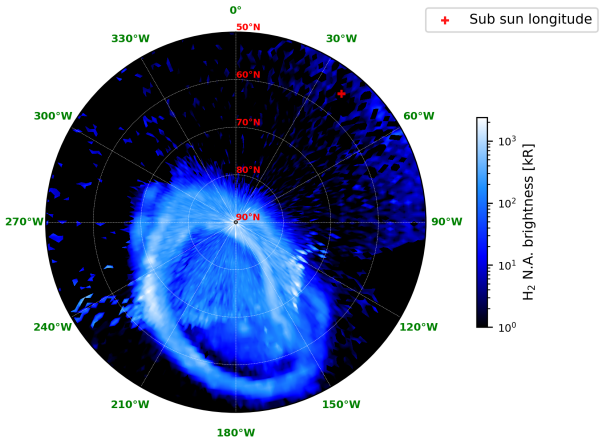

FIGURE 2.1: H_2 brightness map for Jupiter's northern auroral region during PJ1. The sub sun longitude in marked by the red cross.

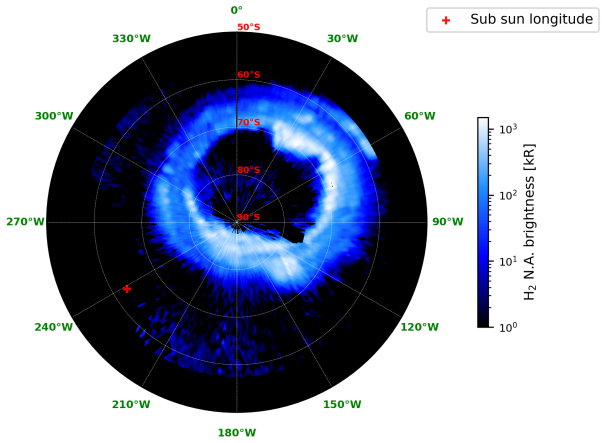

FIGURE 2.2: H_2 brightness map for Jupiter's southern auroral region during PJ1. The sub sun longitude in marked by the red cross.

the signal to noise ratio (S/N)≥2 related to the unabsorbed part of the spectrum as defined by Benmahi et al. (2024).

We used a polar projection to map the H_2 brightness in kiloRayleighs (kR) [1] using the planetocentric latitude and Jupiter's SIII longitude as coordinates [2].

The polar maps of H_2 brightness for the northern and southern auroral regions for PJ1 are shown in figures 2.1 and 2.2. The brightness maps constructed in the same way for all perijoves are displayed in annex A. On these maps as well as the other maps, the sub sun longitude corresponds to the mean over the duration of the perijove of the longitude of the point of Jupiter's reference ellipsoid facing the Sun.

Several observations can be made about those maps. The shape of the H_2 emission is not constant in time. The maximum H_2 brightness ranges from 8 $\times 10^2$ kR to 6 $\times 10^3$ kR for the northern auroral emission and from 6 $\times 10^2$ kR to 7 $\times 10^3$ kR for the southern auroral emission. For both the southern and northern hemisphere, certain perijoves show regions with especially high H_2 brightness in the aurora. However, a high brightness in the northern auroral emissions does not necessarily mean there will be high brightness in the southern auroral emissions during the same perijove, and vice versa.

2.2 Angle emission maps

The ancillary data provided by the Juno mission allow us to infer the emission angle for each photon detected by UVS. This parameter corresponds to the angle between the direction of the photon reaching the spacecraft and the radial direction with respect

[1] 1 Rayleigh represents a photon source flux of 106 cm^{-2} s^{-1} radiating into 4π steradians.

[2] The SIII longitude comes from the Jupiter System III coordinates system which corotates with the planet. In this system, the Z-axis coincides with the rotation axis of Jupiter, the X-axis is defined as 0° latitude and the Y-axis is orthogonal to both the X and Z-axis.

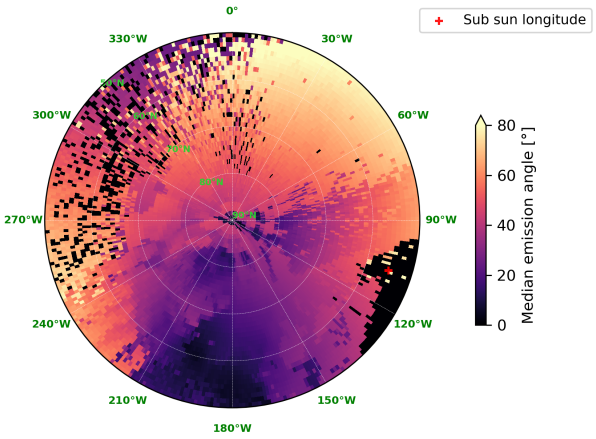

FIGURE 2.3: Mean emission angle map for Jupiter's northern auroral region during PJ1. The sub sun longitude in marked by the red cross.

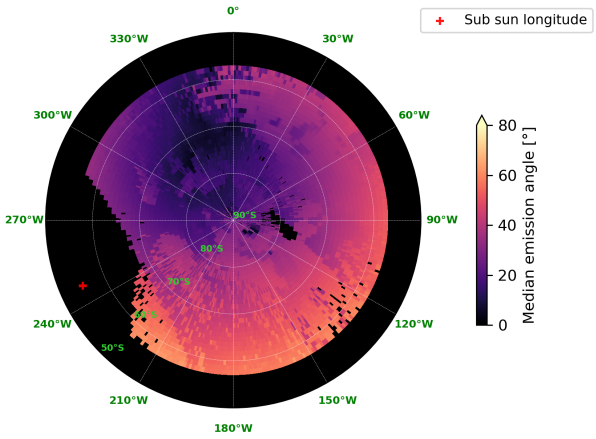

FIGURE 2.4: Mean emission angle map for Jupiter's southern auroral region during PJ1. The sub sun longitude in marked by the red cross.

to Jupiter. The polar regions are mapped progressively as the Juno probe flies by. This means that each point in these regions is observed multiple times (given the rotation of the probe itself) and with different emission angles that can vary between 0° and approximately 80°. We can thus plot the median emission angle for each polar region and for each perijove. This emission angle is necessary for the computation of the mean energy of the precipitating electrons using the CR (E_0, θ) relation. Emission angle maps for the northern and southern hemisphere for PJ1 are displayed in figures 2.3 and 2.4.

2.3 Color ratio maps

After extracting the spectrum for each map and computing the value of the CH_4 and C_2H_2 color ratio, we can map the values of both these color ratios for each perijove and each polar region. These maps were created for each analyzed perijove and can be found in annex A. The ones corresponding to PJ1 are shown in figures 2.5 and 2.6 for the CH_4 color ratio and in figures 2.7 and 2.8 for the C_2H_2 color ratio.

The maximum CH_4 color ratio ranges from 10 to 60 for the northern auroral region and from 5 to 50 for the southern auroral region. The minimum CH_4 color ratio, corresponding to auroral regions where CH_4 did not absorb the auroral emission, is 1.7 according to the H_2 emission model. Still according to this model, the minimum C_2H_2 color ratio is 5 while the maximum ranges from 10 to 22 for the northern auroral region and from 8.5 to 13 for the southern auroral region.

In these figures, the red zones have the highest color ratio, meaning the highest absorption by the molecule. This means that the electrons reached a lower altitude in the atmosphere, lower than the homopause and the resulting photons are strongly absorbed by the atmosphere.

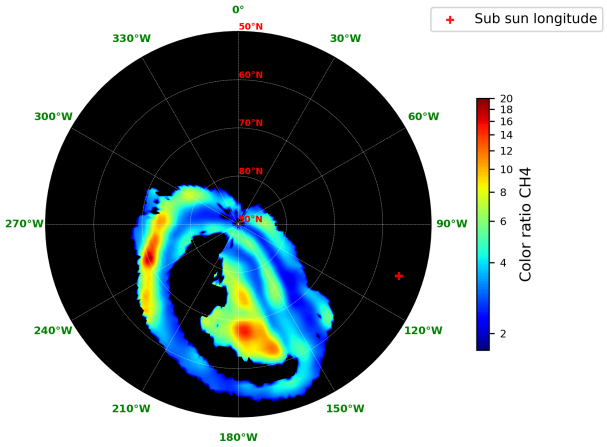

FIGURE 2.5: Color ratio of Jupiter's northern auroral emission with CR $= \frac{I(155nm-162nm)}{I(125nm-130nm)}$, characterizing the absorption of the H_2 UV emission spectrum by CH_4. The sub sun longitude in marked by the red cross.

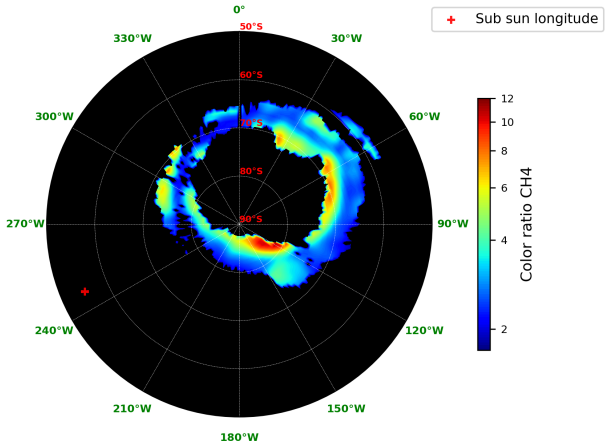

FIGURE 2.6: Color ratio of Jupiter's southern auroral emission with CR $= \frac{I(155nm-162nm)}{I(125nm-130nm)}$, characterizing the absorption of the H_2 UV emission spectrum by CH_4. The sub sun longitude in marked by the red cross.

The density profile of C_2H_2 is lower than the density profile of CH_4, as explained in section 1.2 and illustrated in fig 1.1. We should thus observe zones where none of the two molecules absorb, which means the electrons only reached altitudes above the homopause of CH_4, other zones where only CH_4 absorbs and others where both C_2H_2 and CH_4 absorb. Most of the maps displayed in annex A confirm this first idea. However, upon closer examination of the maps, we identify some regions in some perijoves that challenge this assumption (perijoves 6, 10, 12, 15, 20, 27, 32, 33, 35, 36 and 48). This problem will be further discussed in section 5.

2.4 Energy maps

Using the CH_4 color ratio maps across the entire auroral region and the median emission angle maps of the observed photons, we apply relation 1.3 with the parameters listed in table 1.2 to map the energies of the precipitating electron populations for all points in the auroral regions. We map the mean energies for the northern and southern auroral regions for electrons following monoenergetic or kappa energy flux distributions by selecting the corresponding parameters for each scenario in table 1.2. The results of these calculations for PJ1 are shown in figures 2.9 and 2.10 for the kappa distribution case, and in figures 2.11 and 2.12 for the monoenergetic distribution case. Energy maps for all perijoves are provided in annex A.

The maps for kappa distributions indicate mean energies generally ranging from 1 to 10^3 keV, while monoenergetic distributions exhibit mean energies between 1 and 200 keV. Although the energy distributions vary over time, they tend to remain within a comparable range for both the northern and southern auroral emission regions.

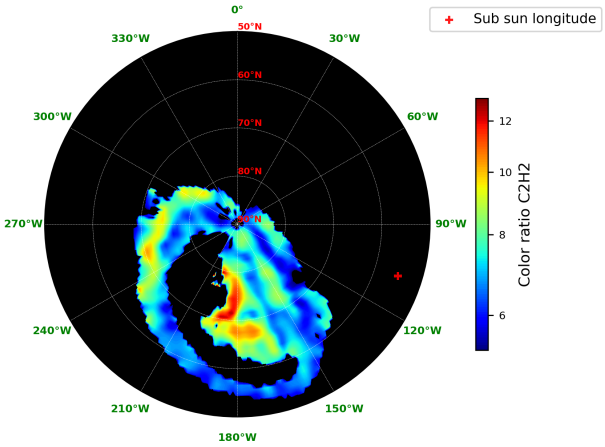

FIGURE 2.7: Color ratio of Jupiter's northern auroral emission with CR $= \frac{I(155nm-162nm)}{I(150nm-153nm)}$, characterizing the absorption of the UV emission spectrum by C_2H_2. The sub sun longitude in marked by the red cross.

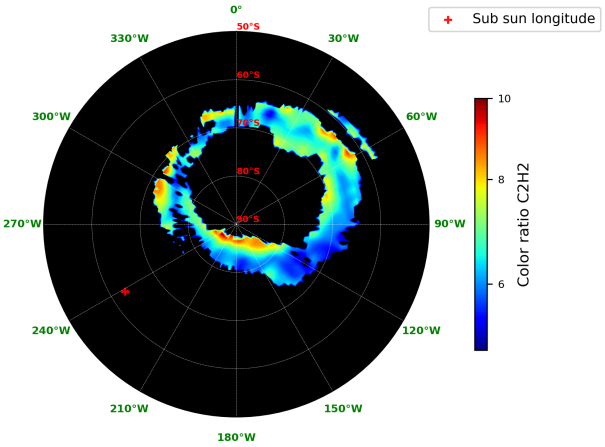

FIGURE 2.8: Color ratio of Jupiter's southern auroral emission with CR $= \frac{I(155nm-162nm)}{I(150nm-153nm)}$, characterizing the absorption of the UV emission spectrum by C_2H_2. The sub sun longitude in marked by the red cross.

All of these maps give a useful picture of many aspects of the evolution of the jovian aurora. In the following sections, we will take advantage of the fact that the data was gathered over an extended period of time and study the variability of the mean energy of the precipitated electrons in time. We will then study the correlation between the H_2 brightness of the auroral emissions and the energy of the precipitating electrons and study the evolution of that correlation over time. Lastly, we will attempt to investigate the anomalies that arise in some color ratio maps using spectral modeling.

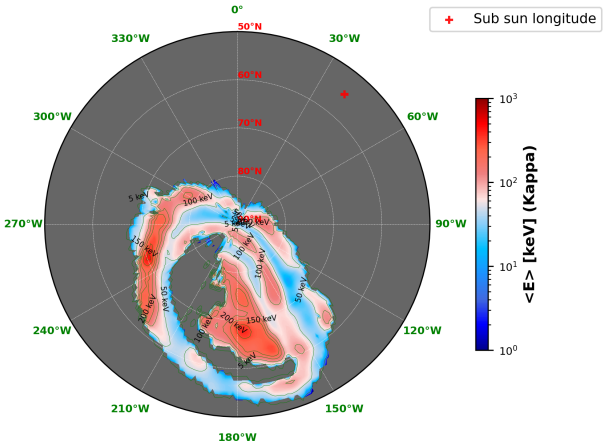

FIGURE 2.9: Mean energy map obtained from the CR (E_0, θ) relation for an electron population with a kappa distribution of energies for the northern auroral region during PJ1. The sub sun longitude in marked by the red cross.

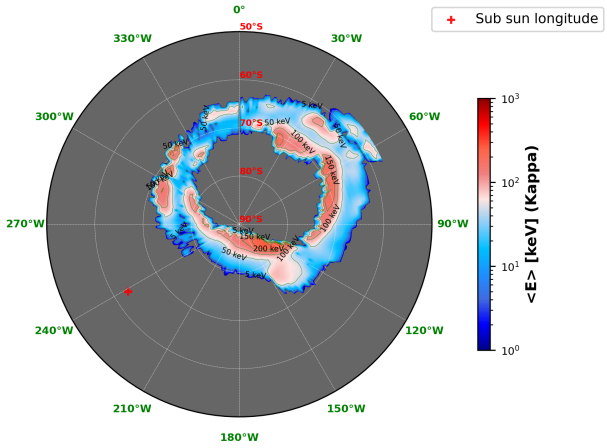

FIGURE 2.10: Mean energy map obtained from the CR (E_0, θ) relation for an electron population with a kappa distribution of energies for the southern auroral region during PJ1. The sub sun longitude in marked by the red cross.

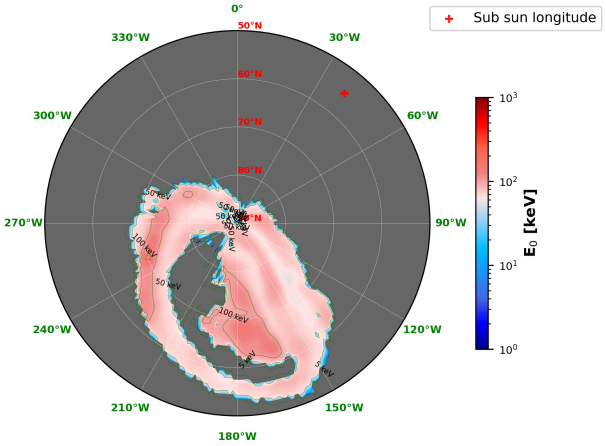

FIGURE 2.11: Mean energy map obtained from the CR (E_0, θ) relation for an monoenergetic electrons population for the northern auroral region during PJ1. The sub sun longitude in marked by the red cross.

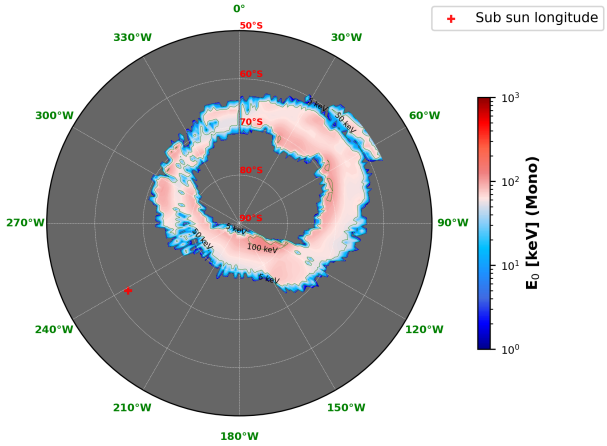

FIGURE 2.12: Mean energy map obtained from the CR (E_0, θ) relation for an monoenergetic electrons population for the southern auroral region during PJ1. The sub sun longitude in marked by the red cross.

TABLE 2.1: Dates and times of start of data acquisition, equatorial time (i.e. when the spacecraft crosses the equatorial plane) and end of data acquisition for each studied perijove. For the perijoves marked by an asterisk only the southern spectral cube was constructed.

	Start of acquisition	Equatorial time	End of acquisition
PJ1	2016-08-27 04:51:15	2016-08-27 12:52:21	2016-08-27 15:49:28
PJ3	2016-12-11 12:04:05	2016-12-11 17:06:12	2016-12-11 22:01:50
PJ4	2017-02-02 08:01:09	2017-02-02 13:00:02	2017-02-02 17:56:01
PJ5	2017-03-27 03:53:47	2017-03-27 08:54:50	2017-03-27 13:49:56
PJ6	2017-05-19 01:01:05	2017-05-19 06:04:11	2017-05-19 10:39:48
PJ7	2017-07-10 20:55:20	2017-07-11 01:58:37	2017-07-11 06:53:07
PJ8	2017-09-01 19:49:26	2017-09-01 21:52:53	2017-09-02 02:47:02
PJ9	2017-10-24 12:19:22	2017-10-24 17:47:16	2017-10-24 22:41:00
PJ10	2017-12-16 13:45:18	2017-12-16 18:02:11	2017-12-16 22:57:00
PJ11	2018-02-07 10:14:14	2018-02-07 13:56:40	2018-02-07 18:49:52
PJ12	2018-04-01 06:28:11	2018-04-01 09:51:05	2018-04-01 14:43:41
PJ13	2018-05-24 03:37:30	2018-05-24 05:45:47	2018-05-24 10:38:04
PJ14	2018-07-16 02:53:56	2018-07-16 05:23:38	2018-07-16 10:15:43
PJ15	2018-09-06 23:43:48	2018-09-07 01:18:20	2018-09-07 06:09:55
PJ16	2018-10-29 20:08:41	2018-10-29 21:12:48	2018-10-30 02:04:37
PJ17	2018-12-21 12:10:27	2018-12-21 17:07:02	2018-12-21 21:58:28
PJ18	2019-02-12 12:40:01	2019-02-12 17:42:06	2019-02-12 21:26:45
PJ19	2019-04-06 11:08:11	2019-04-06 12:22:38	2019-04-06 17:12:06
PJ20	2019-05-29 06:35:04	2019-05-29 08:17:05	2019-05-29 13:06:28
PJ21	2019-07-21 03:04:28	2019-07-21 04:12:03	2019-07-21 09:00:53
PJ22	2019-09-12 02:30:57	2019-09-12 03:50:00	2019-09-12 08:39:02
PJ23	2019-11-03 21:18:43	2019-11-03 22:27:31	2019-11-04 03:16:48
PJ24	2019-12-26 16:41:21	2019-12-26 17:45:45	2019-12-26 22:18:42
PJ25*	2020-02-17 17:35:45	2020-02-17 17:35:45	2020-02-17 22:50:04
PJ26	2020-04-10 12:32:30	2020-04-10 13:57:38	2020-04-10 18:44:56
PJ27	2020-06-02 09:09:32	2020-06-02 10:29:57	2020-06-02 15:17:48
PJ28	2020-07-25 05:30:26	2020-07-25 06:25:33	2020-07-25 11:13:18
PJ29*	2020-09-16 01:46:33	2020-09-16 01:46:33	2020-09-16 07:08:36
PJ30	2020-11-08 01:14:46	2020-11-08 02:00:31	2020-11-08 06:48:17
PJ31*	2020-12-30 21:30:29	2020-12-30 21:30:29	2020-12-31 02:43:32
PJ32	2021-02-21 16:23:18	2021-02-21 17:52:12	2021-02-21 22:38:33
PJ33	2021-04-15 22:40:27	2021-04-15 23:44:14	2021-04-16 04:29:52
PJ34	2021-06-08 06:56:42	2021-06-08 07:57:30	2021-06-08 12:44:01
PJ35	2021-07-21 07:23:38	2021-07-21 08:26:49	2021-07-21 13:12:57
PJ36	2021-09-02 22:01:43	2021-09-02 22:55:04	2021-09-03 03:41:16
PJ38	2021-11-29 13:24:52	2021-11-29 14:25:51	2021-11-29 19:11:30
PJ39	2022-01-12 09:48:03	2022-01-12 10:45:50	2022-01-12 15:30:57
PJ41	2022-04-09 11:27:14	2022-04-09 16:02:58	2022-04-09 20:47:06
PJ42	2022-05-23 01:25:56	2022-05-23 02:29:41	2022-05-23 07:13:52
PJ43*	2022-07-05 08:30:14	2022-07-05 09:31:51	2022-07-05 14:15:32
PJ44*	2022-08-17 14:18:49	2022-08-17 15:00:22	2022-08-17 19:43:51
PJ45*	2022-09-29 16:41:39	2022-09-29 17:27:07	2022-09-29 22:07:03
PJ46*	2022-11-06 20:43:10	2022-11-06 21:54:02	2022-11-07 02:36:30
PJ48*	2023-01-22 05:17:45	2023-01-22 06:00:45	2023-01-22 10:41:31

3

Statistical analysis of the energy of the electrons precipitating in the auroral regions

In the previous section, we showed how we constructed spectral cubes for the northern and southern auroral regions for each perijove. We were then able to map the H_2 brightness, the emission angle and the CH_4 and C_2H_2 color ratios for all the studied perijoves. Using the CR(E,θ) relation as well as the CR and emission angle maps, we derived the mean energy maps by considering a population of precipitating electrons with a kappa or a monoenergetic energy flux distribution.

In this section, we will conduct a statistical analysis of the mean energies of the electrons precipitating in the auroral regions. For this purpose, we will divide the auroral regions in several sub-regions and compute the median of the mean energy in these sub-regions. The aim of this study is to identify trends in the way these energies evolve with time and in the difference between the energy of electrons precipitating in each sub-region.

3.1 Method

We started by characterizing sub-regions of the aurorae. As presented in section 1.4, the auroral emissions can be divided in several sub-regions. The principal ones which we will be using in this work are the main, outer and polar emission regions. The distinction between these sub-regions is not straightforward and there exists a variety of subregions as has been discussed in section 1.4.

Moreover, the sub-regions are not fixed in time in SIII coordinates (Head et al., 2024), they must thus be defined for each perijove one by one. Luckily, this work has already been conducted by Groulard et al. (2024), and we will reuse the masks that he has defined to discriminate these three sub-regions. His results contain masks for perijoves 1 to 39, meaning that we are lacking masks for perijoves 41, 42, 43, 44, 45, 46 and 48. We made the decision to use averages of the other masks to apply to the latter perijoves, it must be considered that the delimitation of the sub-regions for these perijoves is thus less accurate and less reliable.

The study of Groulard et al. (2024) provides the boundary of the main emission region. The polar emission region was defined as the sub-region inside (poleward) of the main emission while the outer emission region is the sub-region located between

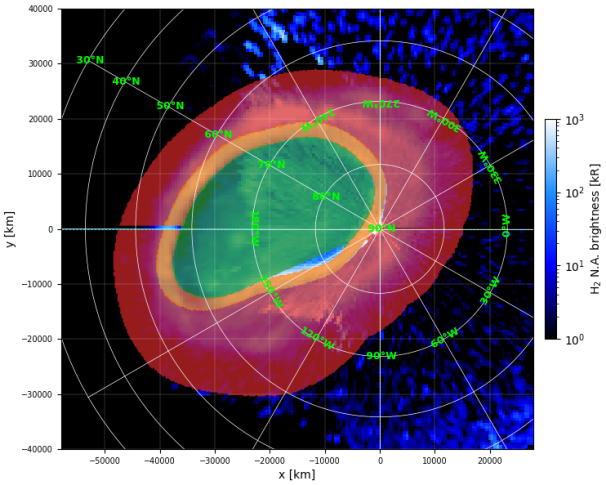

FIGURE 3.1: Masks for the three sub-regions (outer emission region in red, main emission region in orange and polar emission region in green) for the northern auroral region during PJ1, based on the main emission region boundary derived by Groulard et al. (2024).

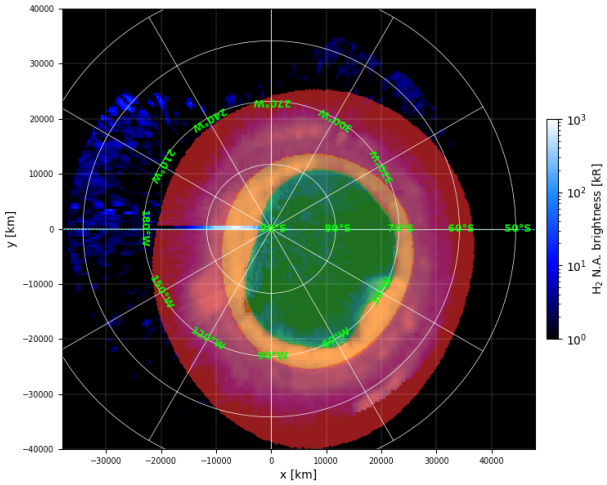

FIGURE 3.2: Masks for the three sub-regions (outer emission region in red, main emission region in orange and polar emission region in green) for the southern auroral region during PJ1, based on the main emission region boundary derived by Groulard et al. (2024).

the equatorward most boundary of the main emission region and Io's footpath corresponding to the magnetic trace of Io's orbit. Plots showing the selected sub-regions are displayed for PJ1 in figures 3.1 and 3.2 and for all perijoves in annex B.

The masks allowed to select the pixels corresponding to each sub-region of the aurora. These pixels were then further selected to eliminate those for which the auroral emission is too dim to accurately infer the energy. Ultimately, after applying the masks to the energy maps, we computed the mean, median, standard deviation, 16^{th} percentile and 84^{th} percentile of the energy inside each sub-region for each perijove for the remaining pixels. A different number of pixels was thus selected for each sub-region and each perijove, and it can happen that for a perijove, no pixels at all are selected for one of the sub-regions.

This procedure was undertaken for the maps corresponding to a monoenergetic electron population and the ones corresponding to a population of electrons following a kappa energy flux distribution. The results from these computations are displayed in tables in annex C, for the northern and southern auroral regions, with the last two lines showing the mean and standard deviation of the mean, median and standard deviation of energy over time for one sub-region.

As explained in section 1.7, choosing a kappa distribution of energy for the population of precipitating electrons is much more consistent with the current literature about Jupiter's aurorae (Salveter et al., 2022) and we will thus be conducting the following study considering that the energy flux of electrons precipitating in Jupiter's atmosphere follows a kappa distribution.

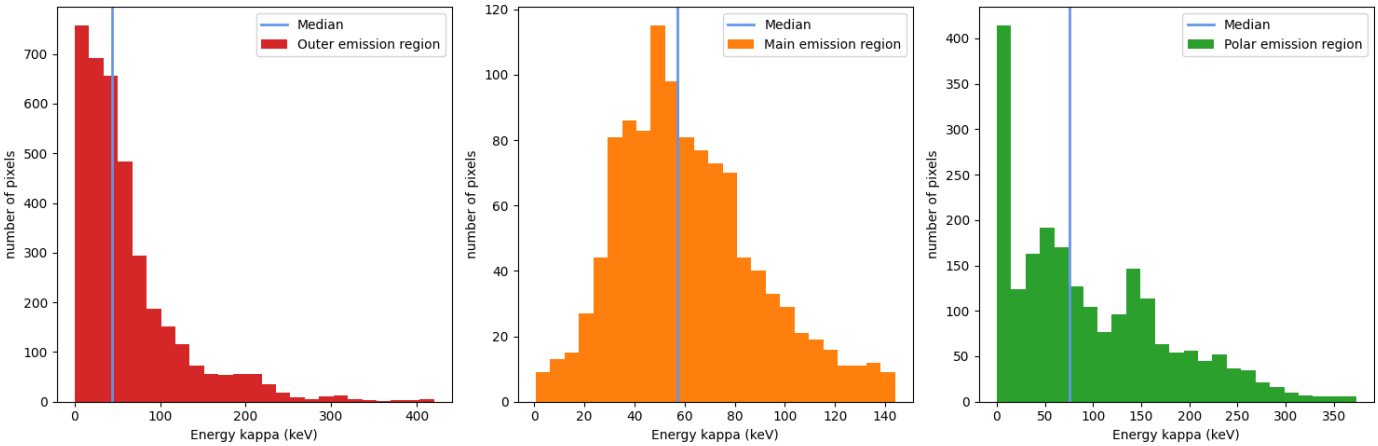

FIGURE 3.3: Histograms of the mean energies of the populations of electrons precipitating in all sub-regions of the northern auroral region during PJ1. We use the same color code as in figure 3.1 (and 3.2) to distinguish the three auroral sub-regions. The blue line represents the median.

3.2 Results

Figures 3.3, 3.4, 3.5 and 3.6 show histograms of the mean energy for each sub-region for perijoves 1, 3, 4 and 5. The median values are marked with a blue line. We observe that they share the general characteristics of a Poissonian distribution with a majority of occurrences near the low values and a tail elongated towards the larger values. This concurs with the 16^{th} and 84^{th} percentiles from the tables in annex C, in which we can observe that the 16^{th} percentile is generally smaller than the 84^{th}.

We then plotted the evolution of the median mean energy of the electrons over time for the northern and southern auroral regions. The dates of the perijoves correspond to their equatorial times and are taken from table 2.1. These plots are shown in figure 3.7 where each curve corresponds to one sub-region of the auroral regions and the data are taken from the tables in annex C. The lower boudary of the shaded area corresponds to the 16^{th} percentile, while the upper one corresponds to the 84^{th}, and both correspond to a 1 sigma interval.

For the northern auroral region, we observe that, with the exception of PJ8, the median mean energy of the electrons precipitating in the outer emission region is always smaller than the for the two other sub-regions. The median energy of the electrons precipitating in the polar emission region is consistently the greatest compared to the other sub-regions except for perijoves 19, 20, 27, 35 and 38.

For the southern auroral region, the median mean energy of the electrons precipitating in the outer emission region is also generally lower than the ones corresponding to the two other sub-regions. However this trend is less pronounced than for the northern auroral region. For perijoves 3, 8, 13, 17, 22, 24, 30, 36, 38 and 39, the median energy for the outer emission region becomes greater than the one for the polar emission region, and even overtakes the energy in the main emission region during PJ8. Contrary to what we observe for the northern auroral region, in this case, the median mean energy of the main emission region is almost systematically higher than for the polar emission region except for perijoves 7, 16, 28, 39, 42, 43 and 44 that go

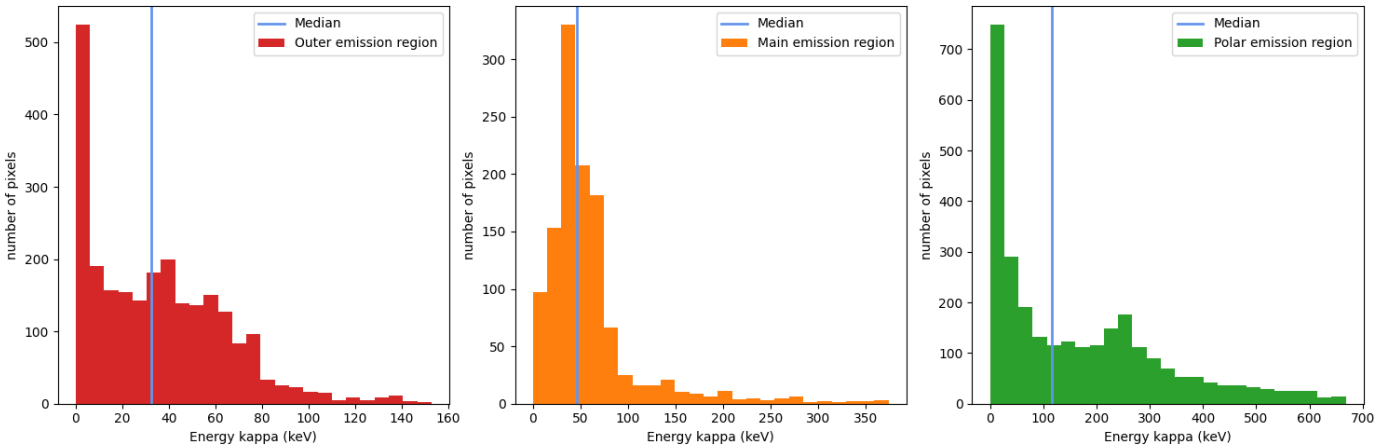

FIGURE 3.4: Histograms of the mean energies of the populations of electrons precipitating in all sub-regions of the northern auroral region during PJ3. We use the same color code as in figure 3.1 (and 3.2) to distinguish the three auroral sub-regions. The blue line represents the median.

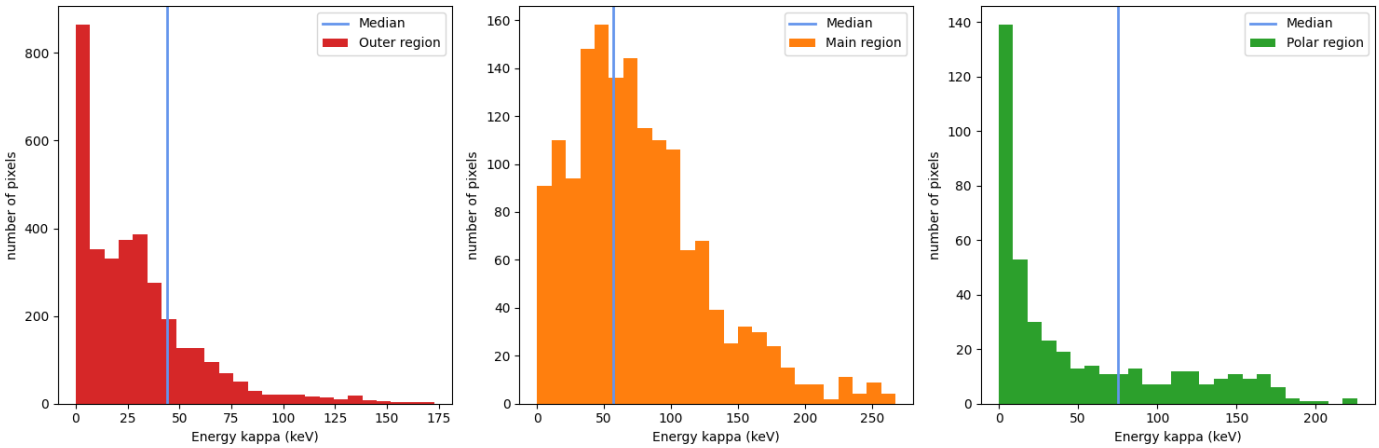

FIGURE 3.5: Histograms of the mean energies of the populations of electrons precipitating in all sub-regions of the southern auroral region during PJ1. We use the same color code as in figure 3.1 (and 3.2) to distinguish the three auroral sub-regions. The blue line represents the median.

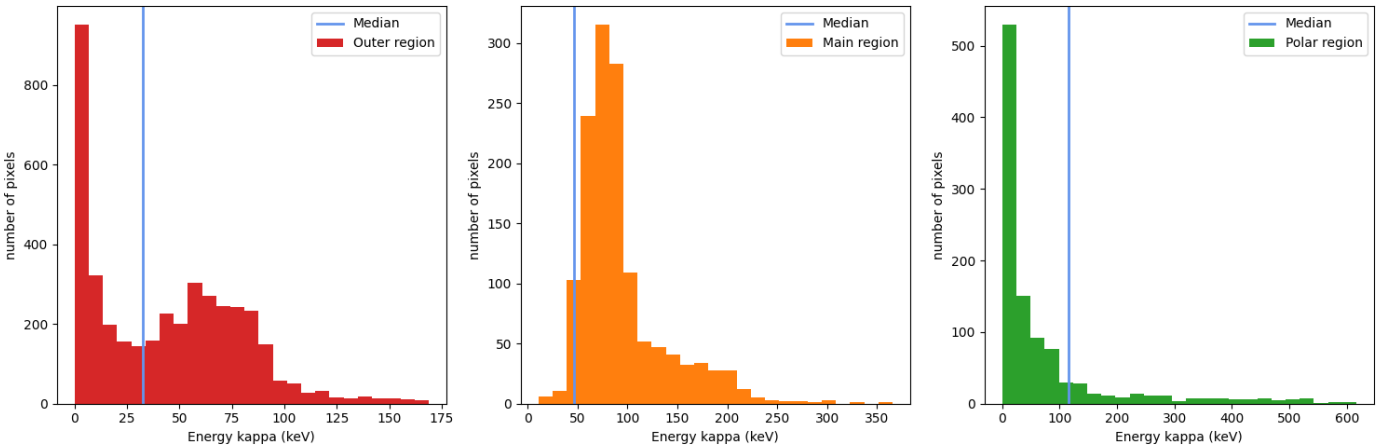

FIGURE 3.6: Histograms of the mean energies of the populations of electrons precipitating in all sub-regions of the southern auroral region during PJ3. We use the same color code as in figure 3.1 (and 3.2) to distinguish the three auroral sub-regions. The blue line represents the median.

against that trend. However, we must remember that for perijoves beyond PJ39, the masks used were less accurate and there is a probability that some of the pixels were assigned to the wrong sub-region, compromising the confidence that can be placed in this comparison.

In the top panels of figures 3.8, 3.9 and 3.10, we plotted the temporal evolution of the median mean energy of the precipitating electrons for the northern and southern auroral region, for the outer, main and polar emission regions respectively. The level of accuracy is represented by the 16^{th} and 84^{th} percentiles of the distributions. The bottom panel represents the median mean energy of electrons for the northern auroral region divided by the one for the southern. This ratio allows us to quantify which hemisphere has the largest median mean energy for each analyzed perijove.

For the outer emission region, the electrons precipitating in the northern region have a lower median mean energy than the ones precipitating in the southern region except during PJ1. The same trend can be observed for the main emission region, apart from perijoves 5 and 16. For the polar emission region it is more difficult to identify a trend. We have a larger median energy in the southern polar emission reigon for 11 out of the 36 studied comparable perijoves and the opposite situation for the others 25.

Figures 3.11, 3.12 and 3.13 show the correlation diagrams of the median mean energy, computed for all perijoves, between the northern and southern auroral regions for the outer, main and polar emission regions respectively.

3.3 Discussion

In this section, we study the evolution of the mean energy of the electron populations precipitating in the auroral regions of Jupiter. We separated the auroral region in three sub-regions as described in section 1.4 in an effort to study the energy of precipitating electrons that have different origins in the magnetosphere.

The origin of the main auroral emission is presumably principally associated with

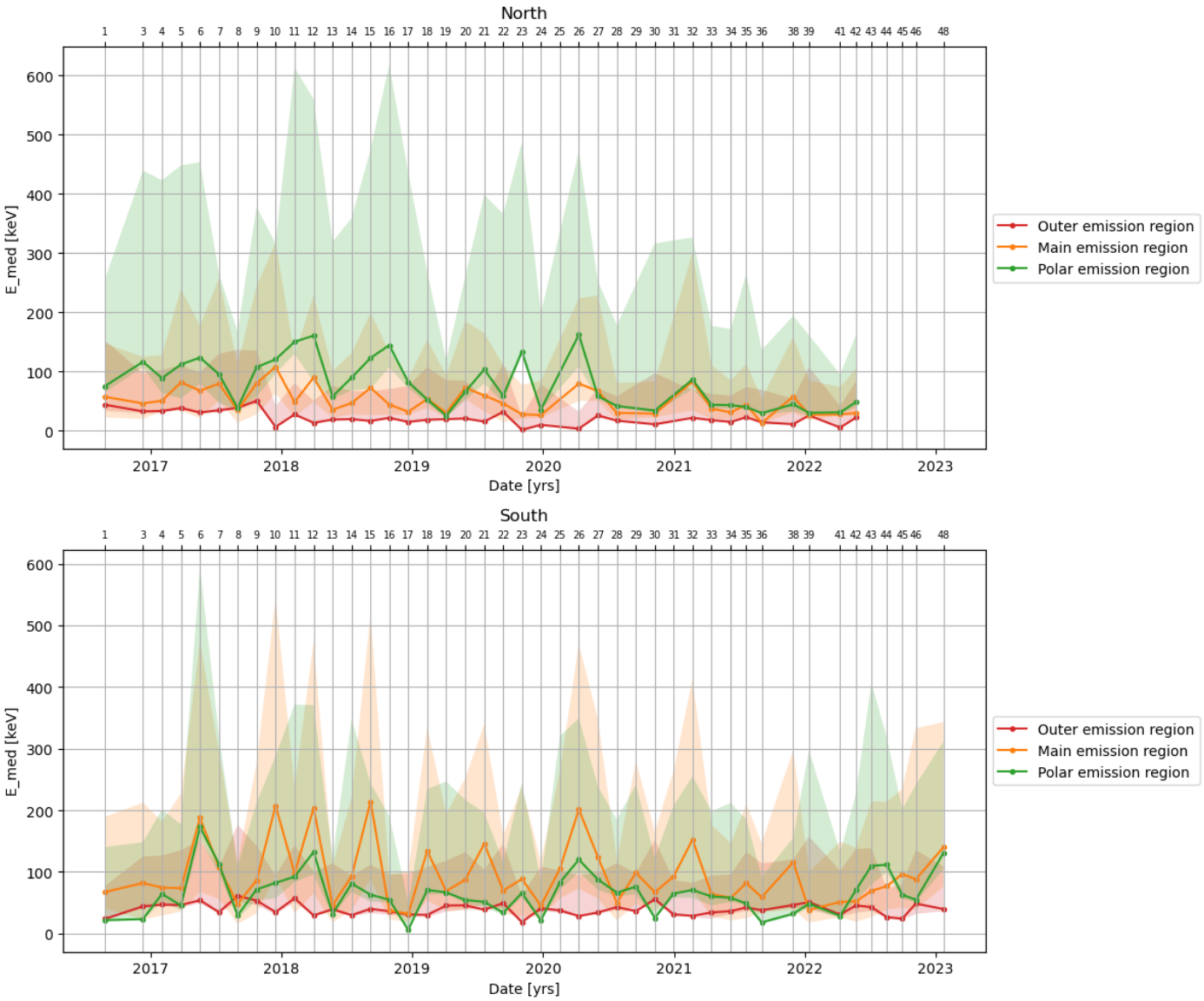

FIGURE 3.7: Evolution of the median mean energy of the population of electrons following a kappa distribution precipitating in the northern (top) and southern (bottom) auroral regions as a function of time for the three sub-regions (outer, main and polar). The shaded areas are constructed from the percentiles 16 and 84 of the distribution of energies sub-region by sub-region, for each perijove and give an idea of the accuracy of the derived energy. In both hemispheres, the red curve (outer emission region) is almost always the lowest. The green curve (polar emission region) is higher than the orange one (main emission region) for most perijoves for the northern auroral region and lower for most perijoves for the southern auroral region.

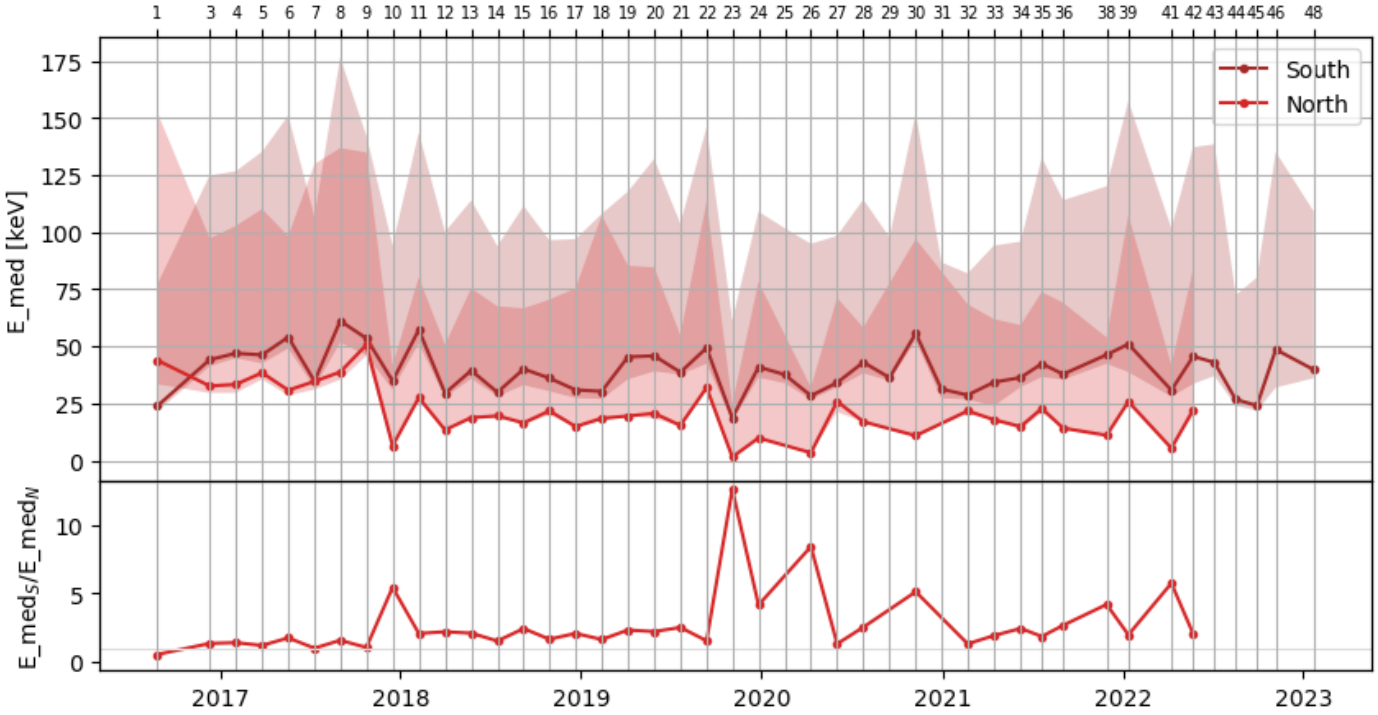

FIGURE 3.8: Evolution of the median mean energy of the population of electrons following a kappa distribution precipitating in the northern and southern outer emission region as a function of time. The error bars correspond to the 16^{th} and 84^{th} percentiles of the distribution of energies for the outer emission region for each perijove. The median mean energy of electrons in the outer emission region is generally higher in the southern hemisphere than in the northern hemisphere.

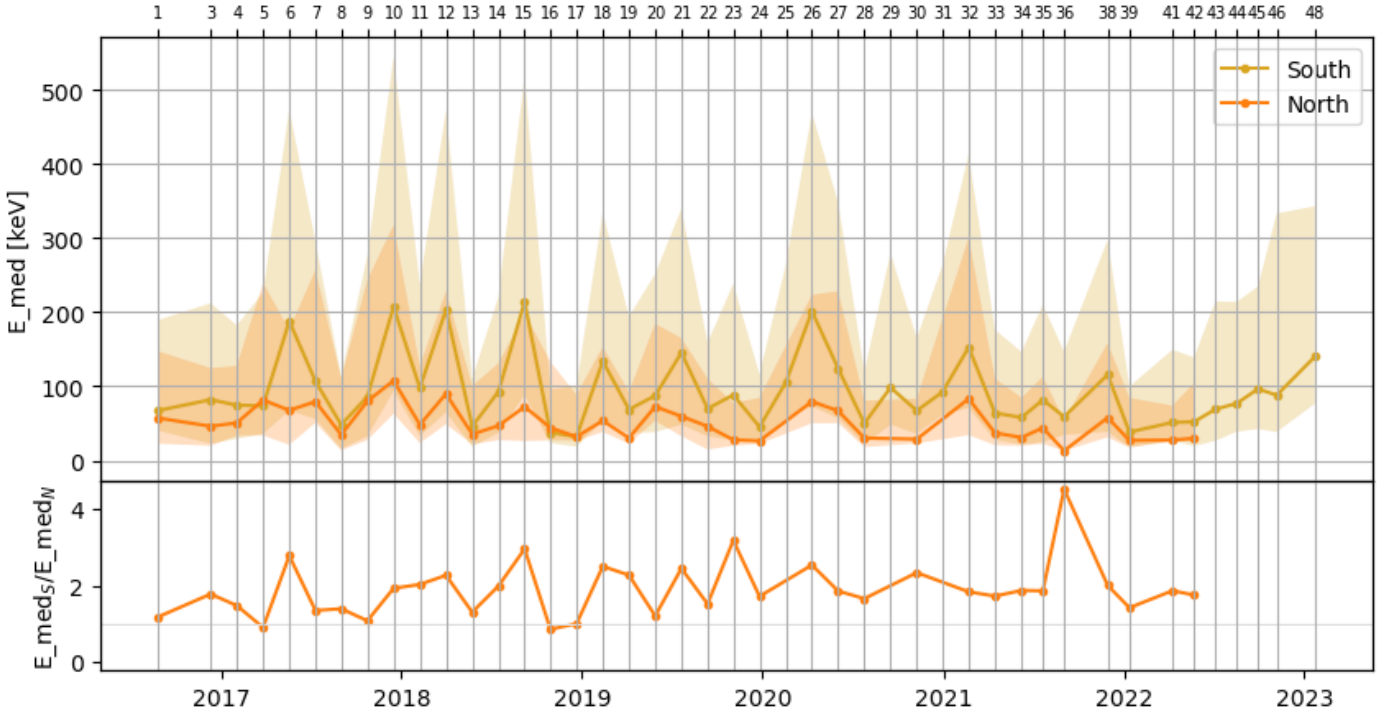

FIGURE 3.9: Evolution of the median mean energy of the population of electrons following a kappa distribution precipitating in the northern and southern main emission region as a function of time. The error bars correspond to the 16^{th} and 84^{th} percentiles of the distribution of energies for the main emission region for each perijove. The median mean energy of electrons in the main emission region is generally higher in the southern hemisphere than in the northern hemisphere.

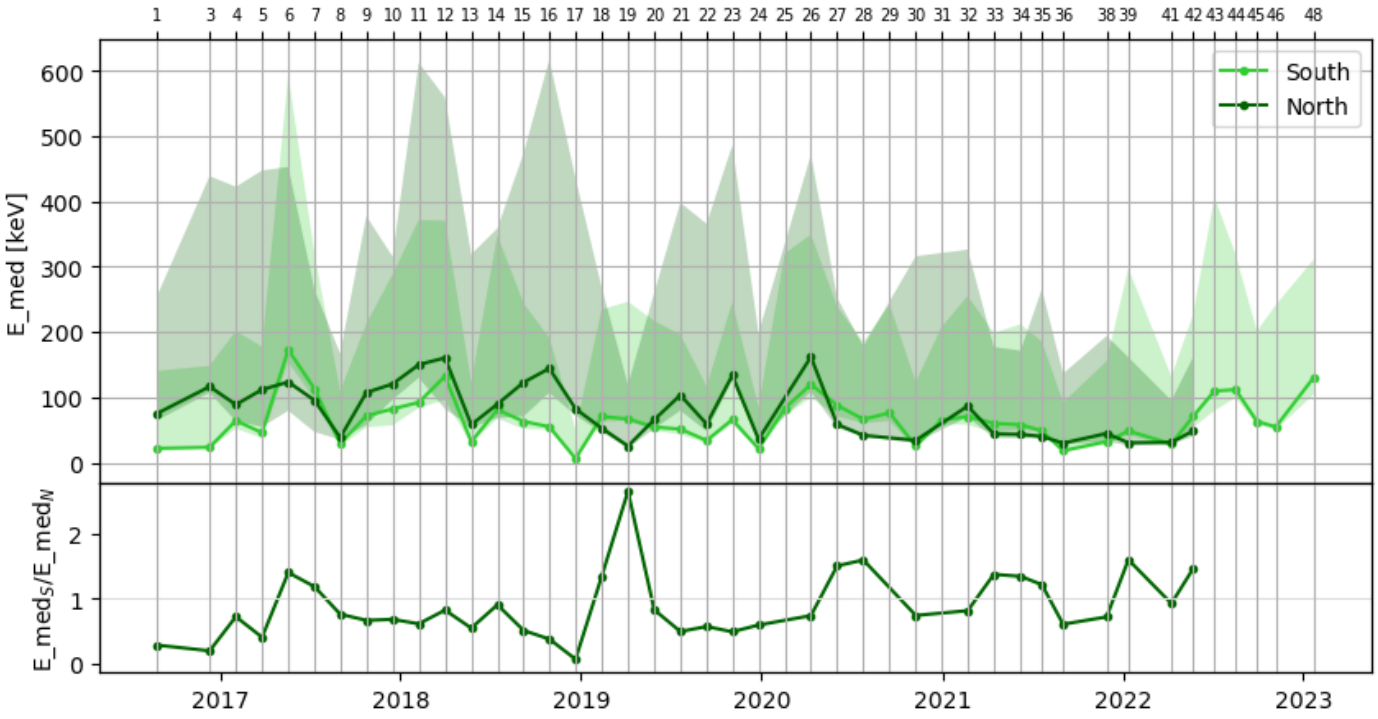

FIGURE 3.10: Evolution of the median mean energy of the population of electrons following a kappa distribution precipitating in the northern and southern polar emission region as a function of time. The error bars correspond to the 16^{th} and 84^{th} percentiles of the distribution of energies for the polar emission region for each perijove. The median mean energy of electrons in the polar emission region is generally higher in the northern hemisphere than in the southern hemisphere.

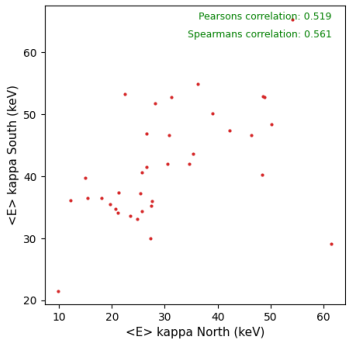

FIGURE 3.11: Relationship between the computed mean energy of the electron population precipitating in the jovian atmosphere in the northern and southern outer emission regions.

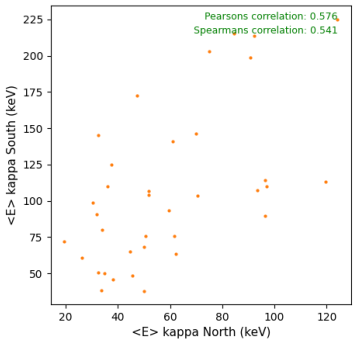

FIGURE 3.12: Relationship between the computed mean energy of the electron population precipitating in the jovian atmosphere in the northern and southern main emission regions.

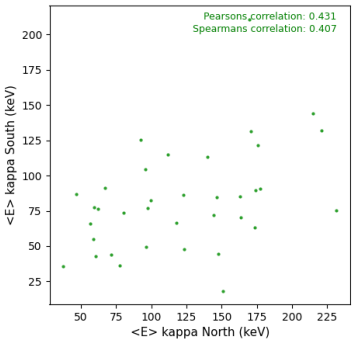

FIGURE 3.13: Relationship between the computed mean energy of the electron population precipitating in the jovian atmosphere in the northern and southern polar emission regions.

turbulent fluctuations in the equatorial current sheet in the middle magnetosphere that give rise to Alfvénic waves propagating along magnetic field lines towards the ionosphere (Saur et al., 2018). On their way, these waves eventually dissipate their energy through wave-particle interaction with electrons (Landau damping), stochastically accelerating them towards and away from the auroral regions. This process appears to be more efficient along field lines within an L-shell near 30 R_J thus creating an auroral "oval" roughly mapping to 30 R_J.

The outer emissions are thought to result from the hot plasma injection process associated with the interchange of magnetic flux tubes containing cold dense iogenic plasma, moving away from Jupiter, and replaced with flux tubes containing sparse hot plasma, moving towards Jupiter (Dumont et al., 2018). The anisotropy brought by the hot electron injection is suggested to generate whistler mode waves able to scatter energetic electrons into the loss cone, the pitch angle diffusion process, giving rise to the outer "diffuse" auroral emissions. The outer emission region also notably encompasses the footprints of the satellites.

The polar emission region receives electrons and to some extent ions from the outer magnetosphere, meaning they have a different origin than the particles creating the main and outer emissions. They are difficult to explain due to the complex structure of the magnetic field above this emission region (Zhang et al., 2021).

The outer emissions for both the northern and southern auroral regions are the ones caused by the least energetic electrons according to our computations. This is consistent with the fact that, contrary to the Alfvénic energization of the main auroral electrons, the pitch-angle scattering process mainly redistributes the energy of the electrons with respect to the magnetic field direction rather than increasing that energy.

The energy of electrons in the polar emission region is almost systematically higher than the energy of the ones precipitating in the main emission region in the northern auroral region. For the southern auroral region, on the contrary, the energy of the electrons precipitating in the main emission region is generally higher that the energy of the ones precipitating in the polar emission region. The reason for this difference remains a mystery since the acceleration processes in the polar emission region are not well known. The results obtained for the northern auroral region are however consistent with the ones presented by Gérard et al. (2014) who found the highest color ratios and mean energy of electrons in the polar emission region. Further research is needed to reach an explanation as to why the energy of the electrons precipitating in the southern polar emission region are less energetic than the ones precipitating in the southern main emission region. These results should however be taken with caution because the polar emission region is subdivided into several sub-regions (swirl, active, dark), each associated with different processes. Additionally, the selection masks we used are not perfect and do not completely isolate the polar, main, and outer emission regions, especially for the last few perijoves, which might blur the effects of different phenomena. Conducting the same analysis as the one that was presented in this section with subdivisions between the active, dark and swirl regions would allow to better differentiate the energies of electrons accelerated by different processes. Gérard et al. (2014) also mentions that the polar emission region is the sub-region where the color ratio shows the strongest spatial variations, which means that the computed values of energy also vary strongly in this sub-region. This significant variability suggests

that the electrons precipitating in each sub-polar region are accelerated by distinct processes.

Figures 3.11, 3.12 and 3.13 show the comparison between the median mean energy of electrons falling into each northern sub-region and their southern counterpart. In the main and outer emission regions, the mean energy of precipitating electrons is higher in the southern auroral region than in the northern. The polar emission region follows the opposite trend with the southern polar emission region being hit by less energetic electrons. This analysis would likely be improved by dividing up the polar emission region into subregions to better distinguish the electrons accelerated by different phenomena.

We also notice that the mean energy of the electrons precipitating in the northern and southern auroral regions appear to be decorrelated even though they should be coming from the same magnetospheric region and account for the same energetic phenomena. This lack of correlation may result from the fact that the northern and southern regions were not observed simultaneously and that within several tens of minutes or hours one can expect significant variations between the poles. However, it could also be linked with some asymmetric properties of the magnetosphere.

3.4 Conclusion

The main results from this analysis of the mean energy of the electrons precipitating in the auroral regions are as follows: the electrons precipitating in the outer emission regions almost always have the lowest median mean energy compared to the other two sub-regions. In the northern auroral region, the electrons precipitating in the polar emission region have a higher median mean energy than those precipitating in the main emission region; however, this trend is reversed in the southern auroral emission region. The impinging electrons in the southern outer emission region have higher energy than those in the northern outer emission region. This observation also holds true for the main emission region, but the trend is less clear and mostly inverted for the polar emission region. Lastly, the mean median energy of the precipitating electrons over time is not strongly correlated between each sub-region and its magnetic counterpart.

4

Correlation between H_2 emission brightness and energy of the precipitating electrons

In this section, we determined whether there is a correlation between the brightness of the auroral emissions observed by the Juno spacecraft and the mean energy of the electrons precipitating in the auroral regions following a kappa energy flux distribution. This energy was determined using the CR(E_0, θ) relation from Benmahi et al. (2024).

Previous studies (Cowley & Bunce, 2001; Gérard et al., 2016) have anticipated a correlation between brightness of the auroral emission and the energy of the precipitating electrons based on the work by Knight (1973). Indeed, the H_2 brightness in auroral emissions is linked to the energy of the precipitating electrons because the brightness depends on the energy flux of these electrons, which in turn depends on how much they are accelerated by the electric potentials along magnetic field lines.

Looking at some of our energy and brightness maps from annex A, we got the sense that, contrary to what could be assumed, a region where we observe very bright auroral emissions is not necessarily a region where very energetic electrons precipitate. PJ4 provides an example for which the brightness and mean energy maps are displayed in figures 4.1 and 4.2, respectively. The brightness is the greatest in the region between 50°N and 60°N and between 150°W and 180°W. However, the energy takes the greatest values around 70°N and 180°W. On the other hand, for some other cases, the correlation seems more plausible. The brightness and mean energy maps of the southern auroral region during PJ15 are displayed in figures 4.3 and 4.4. For those maps, the zones where the most energetic electrons precipitate seem to coincide with the ones with the brightest emissions. In this section, we will study correlation plots and coefficients to determine to which extent a correlation between H_2 auroral brightness and energy of the precipitating electrons exists.

4.1 Method

To better quantify the relation between brightness and energy, we derived correlation plots for the dataset that we considered. The method consisted in creating lists of dimension [N,1], where N is the number of pixels for which we can compare the brightness to the energy. For each perijove, we selected in the brightness map only the

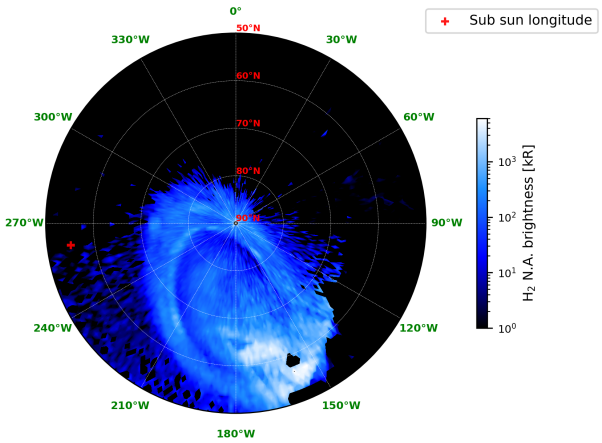

FIGURE 4.1: Map of the total brightness of the northern auroral emissions during PJ4. The sub longitude of the sun is indicated by the red cross. The brightness is the greatest in the region between 50 and 60°N and between 150 and 180°W.

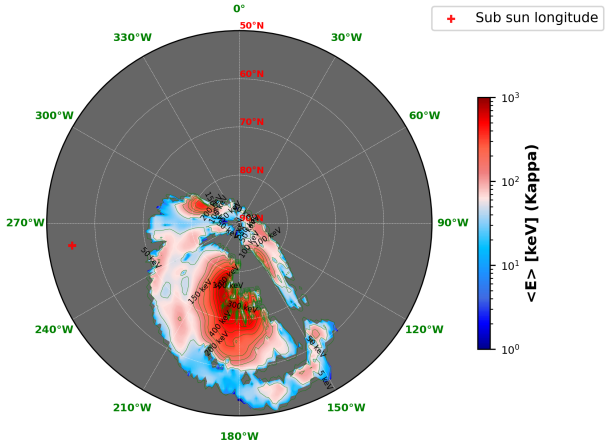

FIGURE 4.2: Map of the mean energy of the electrons precipitating in the northern auroral region during PJ4 and following a kappa distribution. The energy takes the greatest values around 70°N and 180°W

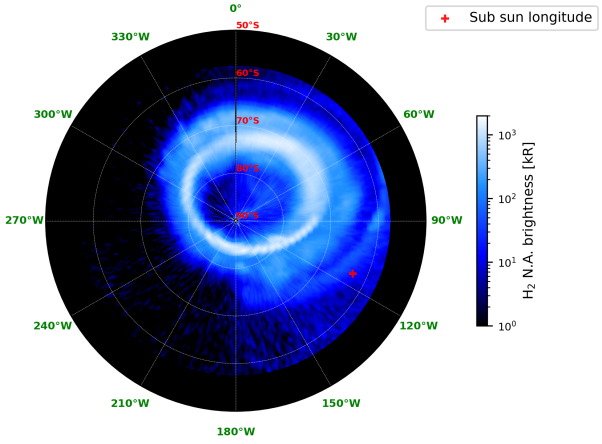

FIGURE 4.3: Map of the total brightness of the northern auroral emissions during PJ15. The sub longitude of the sun is indicated by the red cross.

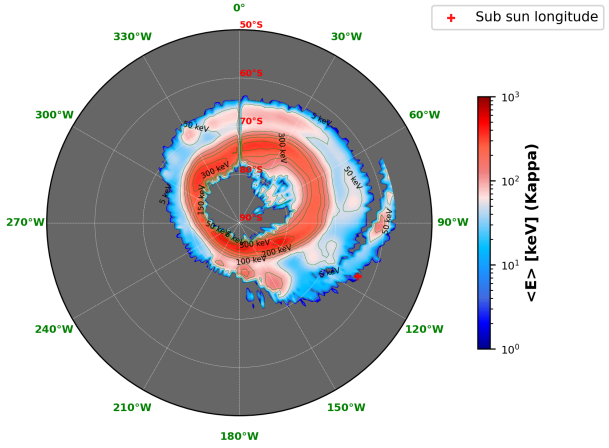

FIGURE 4.4: Map of the mean energy of the electrons precipitating in the northern auroral region during PJ15 and following a kappa distribution.

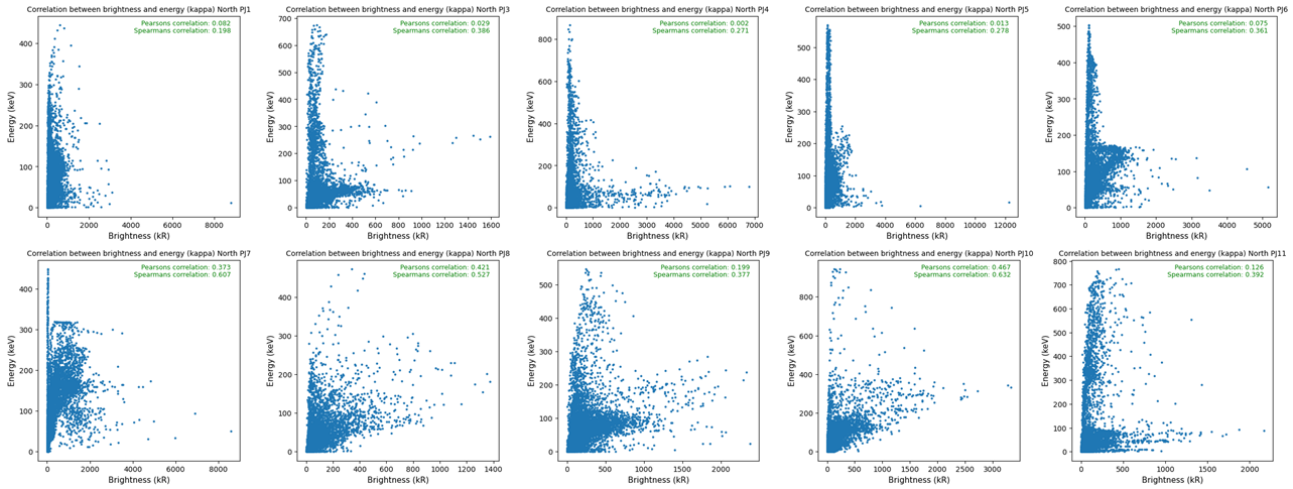

FIGURE 4.5: Relation between the brightness of the northern auroral emissions and the mean energy of the population of electrons precipitating in the jovian atmosphere during perijoves 1, 3, 4, 5, 6, 7, 8, 9, 10 and 11.

pixels for which it was possible to compute an energy, i.e. the pixels corresponding to the points of the auroral regions that were observed. We obtained two lists, one for the brightness and one for the energy, for each hemisphere for each perijove. Because we wanted to expand this comparison to a detailed analysis for each sub-region of the auroral region (polar, outer and main emission regions), we also reproduced the same procedure with the auroral region masks from Groulard et al. (2024), selecting one vector for energy and one for brightness, both having the same dimension, for each auroral sub-region. These lists were then plotted against each other in a correlation scatter plot and the Pearson correlation coefficients between the brightness and the mean energy of the electrons were computed for the auroral region and for each sub-region. This coefficient quantifies the linear correlation, allowing to identify relations between datasets, with values varying from -1 (corresponding to a perfect negative linear relationship) to 1 (perfect positive linear relationship), with 0 meaning an absence of linear relationship.

4.2 Results

4.2.1 Entire auroral emission region

We start by studying the correlation between brightness and mean energy of the electrons for the whole auroral region. For each perijove, we obtain relation plots as well as the Pearson correlation coefficient of the two datasets. The relations plots for perijoves 1, 3, 4, 5, 6, 7, 8, 9, 10 and 11 for the northern auroral region are displayed in figure 4.5 and for the southern auroral region in figure 4.6. The Pearson coefficients are computed for all perijoves.

Many correlation plots for the northern auroral region present structures that show that for low values of the brightness, we have a wide range of values of the mean energy of the electrons. Similarly, in most plots, for low values of the energy, the variability of the values of the brightness is large. This translates as a low Pearson coefficient since this coefficient is meant to quantify linear correlation and in this case the two datasets are visibly not linearly correlated.

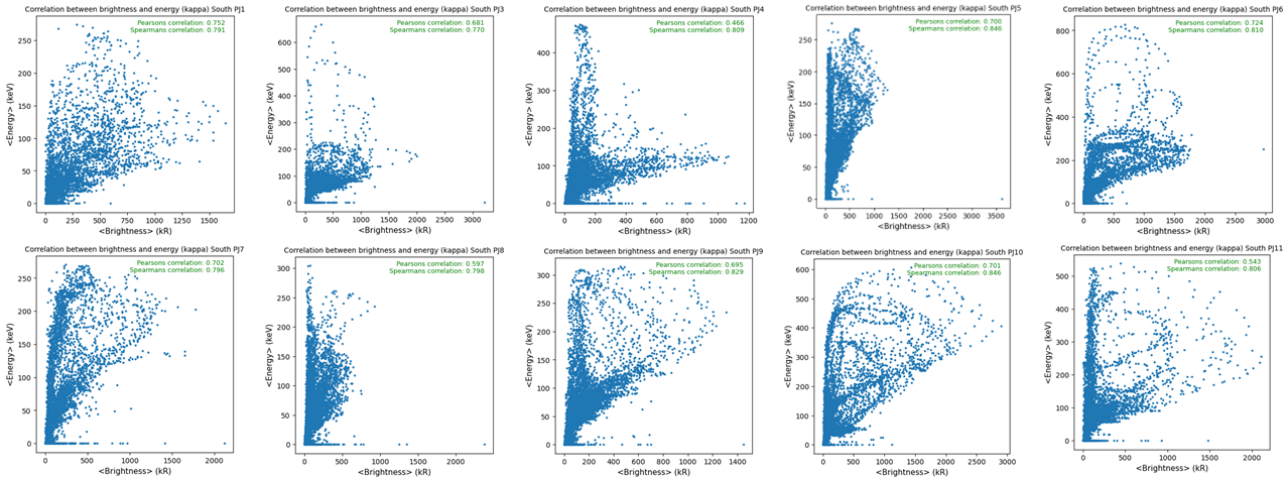

FIGURE 4.6: Relation between the brightness of the southern auroral emissions and the mean energy of the population of electrons precipitating in the jovian atmosphere during perijoves 1, 3, 4, 5, 6, 7, 8, 9, 10 and 11.

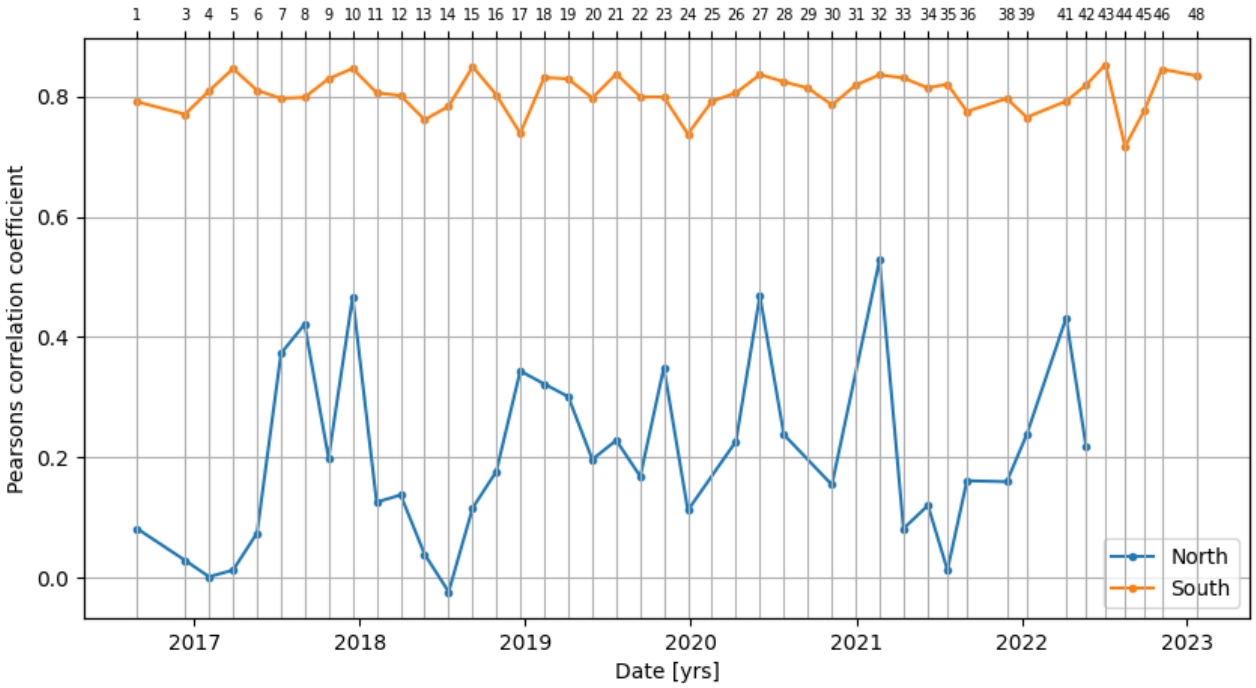

FIGURE 4.7: Evolution of the Pearson correlation coefficient between brightness and mean energy of the electrons with time for the northern (in blue) and southern (in orange) auroral regions.

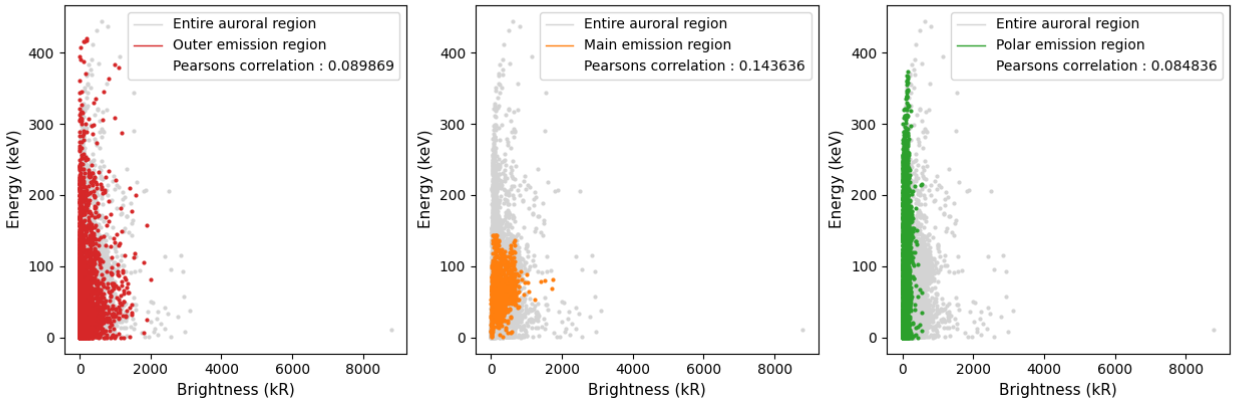

FIGURE 4.8: Relation between the brightness of the northern auroral emissions (x-axis) and the mean energy of the population of electrons following a kappa distribution precipitating in the jovian atmosphere (y-axis) during PJ1. The grey dots represent the relation for the whole northern auroral region, on top of which we have plotted in red the relation for the outer emission region, in orange for the main emission region and in green for the polar emission region.

Figure 4.7 shows the evolution of this coefficient with time for the northern and southern auroral regions. The correlation plots for the northern auroral region generally present lower and more variable Pearson coefficients. The Pearson correlation coefficient for the southern auroral region are generally higher and do not deviate much from 0.8. This is linked to the fact that the data points are generally more spread toward the middle of the plot for the southern auroral region compared to the northern auroral region. The linear correlation becomes stronger as the points more closely align to form a straight line.

However, there is a risk in overinterpreting this coefficient since correlation is not necessarily linear (Armstrong, 2019). This analysis must thus be taken with caution and the correlation coefficient is used only in conjunction with correlation graphs. Moreover, these correlation plots account for the whole emission region of each aurora, and may thus be mixing various populations of electrons without distinguishing them by their magnetospheric origin. In the next section, we will attribute colors to the dots according to the auroral region they correspond to in order to better distinguish between electrons populations.

4.2.2 Auroral emission sub-regions

The electron populations that fall into the atmosphere have different mean energies in each of the auroral sub-regions as has been discussed in section 3. Therefore, it is more relevant to distinguish the sub-regions as they have been defined in section 3.1 with the masks of Groulard et al. (2024).

The correlation plots differentiating these sub-regions for PJ1 are displayed in figures 4.8 and 4.9 for the northern and southern auroral region respectively. The Pearson coefficients are computed by sub-region for each perijove and their evolution in time for the northern and southern auroral regions are plotted in figures 4.10 and 4.11.

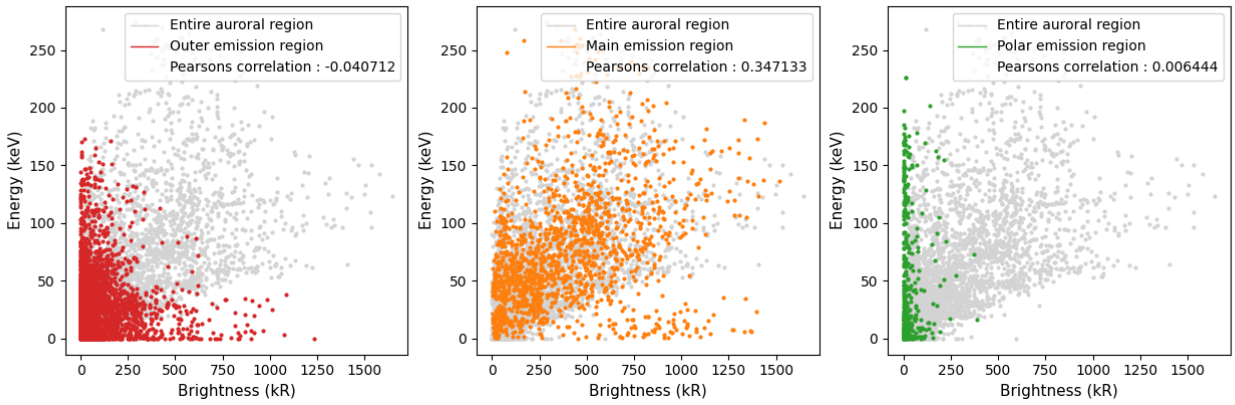

FIGURE 4.9: Relation between the brightness of the southern auroral emissions (x-axis) and the mean energy of the population of electrons following a kappa distribution precipitating in the jovian atmosphere (y-axis) during PJ1. The grey dots represent the relation for the whole southern auroral region, on top of which we have plotted in red the relation for the outer emission region, in orange for the main emission region and in green for the polar emission region.

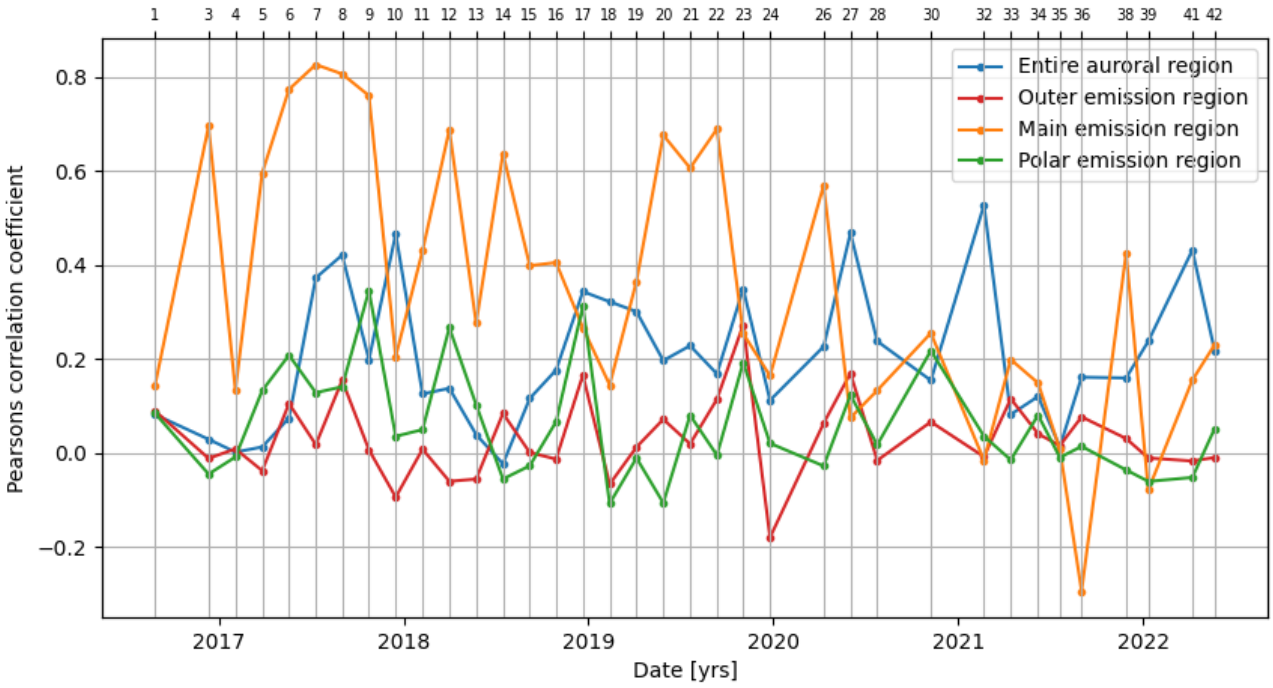

FIGURE 4.10: Evolution of the Pearson correlation coefficient between brightness and mean energy of the electrons following a kappa distribution with time for the northern auroral region. The blue line represents the Pearson coefficient for the whole aurora, the red is the outer emission region, the orange is the main emission region and the green is the polar emission region.

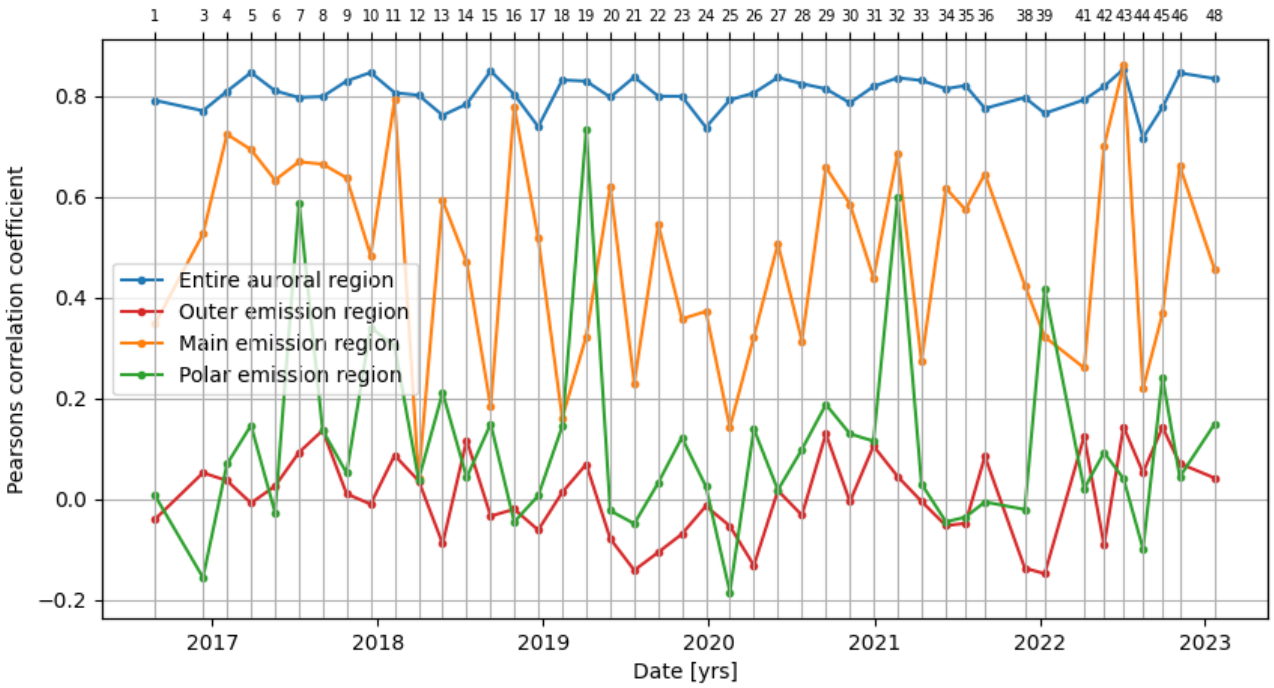

FIGURE 4.11: Evolution of the Pearson correlation coefficient between brightness and mean energy of the electrons following a kappa distribution with time for the southern auroral region. The blue line represents the Pearson coefficient for the whole aurora, the red is the outer emission region, the orange is the main emission region and the green is the polar emission region.

The correlation coefficients for each region in the northern auroral region do not follow specific trends, similarly to the correlation coefficient for the whole auroral region, with some strong peaks for the correlation coefficient for the main emission region.

On the other hand, the Pearson coefficient for the sub-regions of the southern auroral region are contradicting the impression of stronger correlation that was given by the correlation coefficients of the whole aurora. Indeed, the coefficients for each sub-region are lower than the ones for the whole region and considerably lower than 1, except for some peaks in the main emission region that reach values comparable to those of the whole aurora. This reinforces the idea that the correlation coefficients give a distorted view of the real correlation between mean energy of the electrons and the brightness of the auroral emissions.

4.3 Discussion

In this section, we studied the correlation between the brightness of the auroral emissions and the mean energy of the precipitating electrons. On first inspection and without distinguishing the different regions of the aurora, the H_2 brightness is decorrelated from the mean energy of electrons for the northern auroral region but a slight correlation emerges between those datasets for the southern auroral region. The Pearson coefficients that were computed for each of the perijoves confirm that idea.

After classifying the data by auroral sub-regions, it becomes clear that the slight correlation that was suggested by the higher Pearson coefficient for the southern auroral region is misleading. The correlation coefficient for the entire southern auroral region is higher than the correlation coefficients of each sub-region of the southern auroral region taken separately. The relatively high Pearson coefficients obtained when taking the whole auroral region into account give a good example of the fact that this coefficient can detect false correlations.

The absence of correlation between brightness and mean energy of the electrons for the jovian aurora was already suggested by Gérard et al. (2014). The zones where the most energetic electrons precipitate do not necessarily coincide with the zones where the largest number of electrons precipitate.

These results are also consistent with Gérard et al. (2016) who studied the correlation between H_2 emission brightness and CH_4 color ratio with data from the Hubble Space Telescope (HST). We compare our results to theirs because we computed the values of the energies on the basis of the CH_4 color ratio. We thus know that CH_4 color ratio and energy are directly correlated. They chose smaller regions to study the correlation, and the comparison between our results is not straightforward. However, for the regions that are assimilated with the main emission region, they find higher correlation coefficients than for the other regions which we also observe in our results with some exceptions. For the regions corresponding to the outer emission region they find correlation coefficients that are generally smaller than those for their other sub-regions, but still larger than the coefficients we observed for the outer emission region. For the polar emission region, the values of the correlation coefficients are generally smaller than the ones of the main emission region and larger than the ones of the outer emission region, with some exceptions. These results are similar to what is displayed in figures 4.10 and 4.11. The comparison between our results and theirs

is nevertheless limited by the fact that they compare the H_2 brightness with the CH_4 color ratio, while we compare it to the energy and by the fact that we are not defining the zones exactly in the same way.

4.4 Conclusion

The main conclusion from this part of the master's thesis is the absence of correlation between the H_2 brightness of the auroral emission and the energy of the electrons precipitating in the auroral region.

Our initial analysis, without distinguishing between different auroral sub-regions, reveals a lack of correlation for the northern auroral region and a slight correlation for the southern auroral region. The Pearson coefficients computed for each perijove support this observation.

However, when we classify the data by auroral sub-regions, it becomes evident that the apparent correlation for the southern auroral regions is misleading. The overall higher Pearson coefficient for the southern auroral regions does not hold when analyzing the sub-regions separately, highlighting the potential for false correlations when considering the entire auroral region.

These findings align with previous research by Gérard et al. (2014), which suggested that the zones of highest electron energy do not necessarily coincide with the zones of greatest electron precipitation. Additionally, our results are consistent with Gérard et al. (2016), who studied the correlation between H_2 emission brightness and CH_4 color ratio using Hubble Space Telescope (HST) data. Although their approach differed slightly, their observation of higher correlation coefficients in the main emission region compared to other regions is reflected in our findings.

Overall, our study confirms the complex relationship between auroral brightness and electron energy, emphasizing the need for careful regional analysis to avoid misleading conclusions about their correlation.

5

Spectral modeling for intriguing zones of the color ratio maps

In this section, we study more in depth the spectrum of several small regions of the aurorae, specifically ones that are deemed interesting as they seem to put in question our assumptions about the atmospheric composition of Jupiter.

As seen in section 1.2, the atmosphere of Jupiter is composed predominantly of H, H_2 and He, with the presence of minor species such as CH_4, C_2H_2, C_2H_6 and other hydrocarbons (Atreya et al., 2003).

We have defined the concept of color ratio in section 1.7. In the case of H_2 FUV auroral emissions, it is a ratio between the intensity of the spectrum in one region where a constituent, like methane, has a negligible absorption cross section and another part of the spectrum where the constituent supposedly has an important absorption cross section. The color ratio can thus be used as a proxy for the amount of the absorbing species present in the atmosphere of Jupiter, taking into account the energy of the electrons precipitating in the auroral region. Indeed, a low color ratio can either mean that the absorbing species is not abundant in that region, or that the electrons are not energetic enough to reach an altitude where the density of this constituent is significant.

By mapping the CH_4 and C_2H_2 color ratios for the northern and southern auroral regions, we can identify, for each point of the auroral region, the level of absorption by each of these molecules.

In some cases, the color ratios on these maps appear to contradict our atmospheric model (Grodent et al., 2001). Indeed, we can identify zones where the C_2H_2 color ratio is unexpectedly high compared to the rest of the map, but in the same zone, the CH_4 color ratio is small relative to the rest of the map. Such zones can be observed in the southern auroral region for perijoves 6, 10, 12, 15, 20, 27, 32, 33, 35, 36 and 48.

This leads us to suspect that the photons that were produced in this region by a precipitation of energetic electrons were significantly absorbed by C_2H_2, and thus that the electrons were energetic enough to reach the C_2H_2 layer. However, this should also imply that the electrons penetrated the CH_4 layer before reaching the C_2H_2 layer, since the CH_4 homopause is at a higher altitude than the C_2H_2 one (see fig 1.1). In such a case, one would expect a strong absorption by CH_4.

This counter intuitive low level of CH_4 absorption might be explained in a few ways. Firstly, the homopauses for CH_4 and C_2H_2 might differ from our model's predictions,

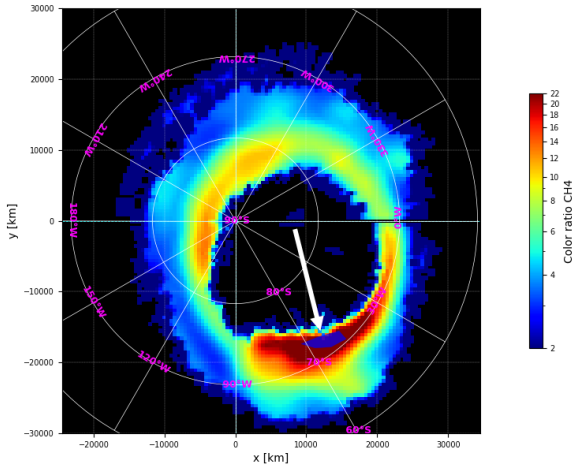

FIGURE 5.1: CH_4 color ratio map for the southern auroral region during PJ6, the polygon chosen in a region of strong relative absorption by CH_4 and low absorption by C_2H_2 is represented in dark blue (around 60°W and 70°S).

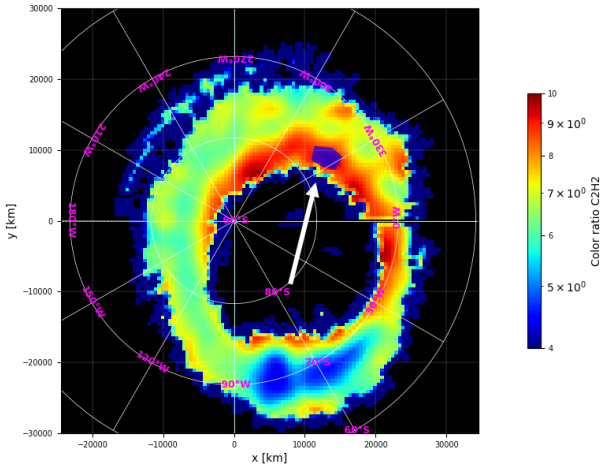

FIGURE 5.2: C_2H_2 color ratio map for the southern auroral region during PJ6, the polygon chosen in a region of strong relative absorption by C_2H_2 and low absorption by CH_4 is represented in dark blue (around 330°W and 80°S).

with CH_4's homopause being lower or C_2H_2's being higher. Secondly, this observation might result from exceptionally high CH_4 absorption in the rest of the aurora, making the absorption in this specific zone appear relatively low. To invalidate or confirm these ideas, we conducted modelings of the average spectra in some zones of interest.

The H_2 emission spectrum between 125 and 170 nm is characterized by isolated spectral regions that are known to be strongly absorbed by almost exclusively CH_4 or C_2H_2 as will be discussed in section 5.1.2. This property of the spectrum will allow us to determine whether the suspected anomalies that we observe come from an unusual distribution of the relative hydrocarbon abundances. We compare the observed spectra with a modeled spectra that take as input parameters the mean energy of the precipitating electrons population and the amount of each hydrocarbon in order to infer their abundance.

5.1 Method

In the framework of this master's thesis, we focus on two of these intriguing cases; perijoves 6 and 10. For each of them we defined two polygonal regions in the auroral maps, one presenting a strong C_2H_2 color ratio and a low CH_4 color ratio (compared to the rest of the map) and one with a low C_2H_2 color ratio and a high CH_4 color ratio (compared to the rest of the map). The goal is to use our models to better understand if the first category of polygons really present an anomaly as we suspect, and to use our modeling methods on a zone that we do not find suspicious to check that the models work as expected. The chosen polygons are displayed in dark blue in figures 5.1, 5.2, 5.3 and 5.4.

For each case, we used the spectral cube that was computed as described in section 2, and extracted the spectrum for each pixel of the surface of the polygon. We then computed the mean of all those spectra to obtain an average spectrum for each

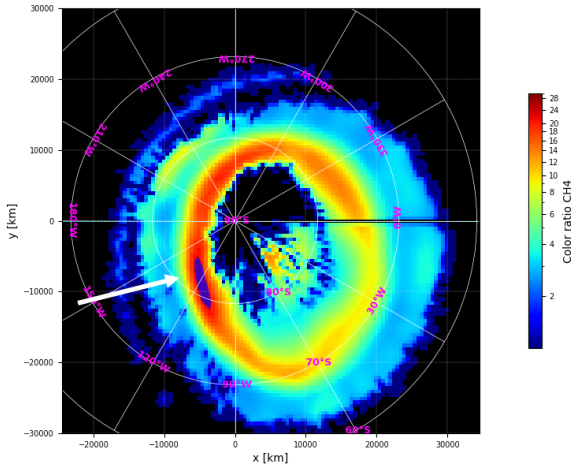

FIGURE 5.3: CH_4 color ratio map for the southern auroral region during PJ10, the polygon chosen in a region of strong relative absorption by CH_4 and low absorption by C_2H_2 is represented in dark blue (around 120°W and 80°S).

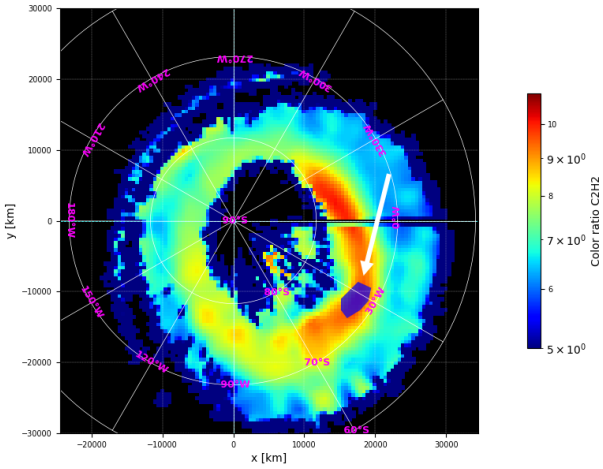

FIGURE 5.4: C_2H_2 color ratio map for the southern auroral region during PJ10, the polygon chosen in a region of strong relative absorption by C_2H_2 and low absorption by CH_4 is represented in dark blue (around 30°W and 70°S).

polygon. We also computed the median emission angle of photons and the median CH_4 color ratio for this polygon. These values are displayed in table 5.1.

TABLE 5.1: Values of median emission angle and CH_4 color ratio for the chosen polygons.

	Median emission angle	Median CH_4 color ratio
PJ6 polygon high CH_4 absorption	18.3°	29.6
PJ6 polygon high C_2H_2 absorption	38.3°	7.6
PJ10 polygon high CH_4 absorption	29.3°	21.7
PJ10 polygon high C_2H_2 absorption	38.3°	8.3

Using these values, it is possible to infer the expected value of the mean energy of the electrons that precipitated in this zone, assuming these electrons follow a kappa distribution. We used the CR(E_0, θ) relation from Benmahi et al. (2024) presented in section 1.7. The energies that were obtained from this method are displayed in table 5.2.

TABLE 5.2: Values of mean energy of the kappa distribution of electrons evaluated with the CR(E_0, θ) relation for the chosen polygons.

	Mean energy (keV)
PJ6 polygon high CH_4 absorption	732.7 keV
PJ6 polygon high C_2H_2 absorption	184.1 keV
PJ10 polygon high CH_4 absorption	542.3 keV
PJ10 polygon high C_2H_2 absorption	203.0 keV

We used these values to produce modeled spectra for all these regions and fit them to the average observed spectra that we had obtained.

We used the electron transport model TransPlanet that we presented in section 1.8.1 to model an electron flux going through the atmosphere of Jupiter. The code computes the flux of electrons at each altitude as well as the expected H_2 emission spectrum in the FUV domain for a given point. It requires an energy distribution, a mean energy, an emission angle, and an atmospheric model. In our case, we use a kappa distribution with the mean energies presented in table 5.2, the emission angles from table 5.1, and the atmospheric model presented in Grodent et al. (2001).

5.1.1 Energy fitting

We conducted this modeling using several strategies. Firstly, we adjusted the model spectrum to the observed one with the value of the mean energy. It is expected that the greater the energy, the deeper the electrons will reach inside the atmosphere and thus the larger the absorption by CH_4 and then C_2H_2, making the intensity of the spectrum drop. We tried values of the energy lower and higher than the one predicted by the CR(E_0, θ) relation, trying to find a value of the energy for which the model offered a good fit over the whole spectrum. If this strategy produced a satisfactory fit, the difference between the modelled and observed spectrum could be explained by a wrong prediction of the mean energy of the electron population by the CR(E_0, θ) relation.

5.1.2 Determination of the adjustment factors

Afterwards, we tried adjusting the density profile of some of the atmospheric constituents of Jupiter. The densities of these constituents are artificially modified by multiplying them by an ad hoc adjustment factor, or fudge factor, (F_{CH_4}, $F_{C_2H_2}$ and $F_{C_2H_6}$). An adjustment factor of 1.0 means that we use the quantity predicted by the model, while an adjustment factor of 2.0 doubles the entire density profile.

When Jupiter is observed, the FUV bandwidth of 125-170 nm is dominated by the auroral emission from H_2. In the auroral regions, this emission itself may be mainly absorbed by CH_4 and C_2H_2. This absorption depends on wavelength, and each hydrocarbon gives rise to a drop in intensity for certain parts of the emission spectrum as illustrated in figure 1.8. In addition to CH_4 and C_2H_2, C_2H_6 is alsoexpected to contribute to the absorption of the FUV auroral emission at specific wavelengths. Consequently, we also considered a C_2H_6 abundance profile modeled by Moses et al. (2005) in Jupiter's model atmosphere.

In figure 1.8 we can see which parts of the spectrum are absorbed by CH_4, C_2H_2 and C_2H_6. Figures 5.5, 5.6 and 5.7, represent spectra with several values of the adjustment factor for CH_4, C_2H_2 and C_2H_6 respectively. These spectra were modeled using TransPlanet, assuming a kappa distribution of precipitating electrons with a mean energy of 45 keV, an emission angle of 0°, and a total emission from 157 to 162 nm arbitrarily normalized to unity. For each hydrocarbon, we tried various values for its adjustment factor while setting the adjustment factors of the two others. This allows us to evaluate which of the adjustment factors we can modify to fit each part of the H_2 emission spectrum. As expected, CH_4 absorbs in the region between 125 and 130 nm. However C_2H_6 also has a non negligible absorption cross section for these wavelengths. The interval between 150 and 153 nm may be considered the absorption range of C_2H_2 for the computation of the C_2H_2 color ratio. Nonetheless, results from

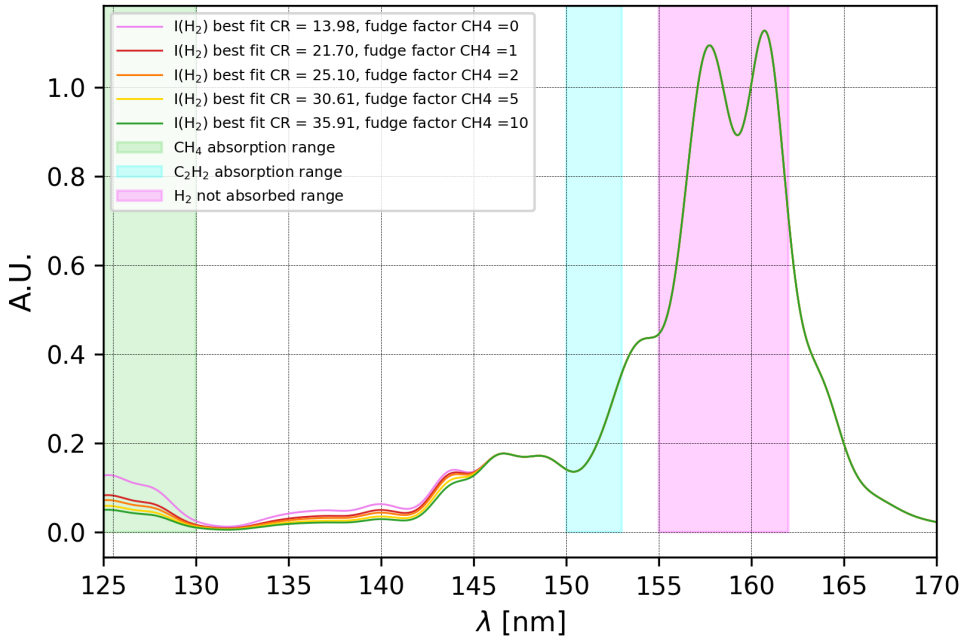

FIGURE 5.5: Spectra modelled with TransPlanet for a kappa distribution with $\langle E \rangle = 450$ keV, θ=0° and $F_{C_2H_2}$=1, $F_{C_2H_6}$=1 for various values of F_{CH_4}.

figures 5.7 and 1.8 imply that C_2H_6 also significantly absorbs the electromagnetic radiation in that region. From 142 to 150 nm, we note that absorption can be caused by C_2H_2 but also by C_2H_6.

This shows that a spectrum can be adjusted either by adjusting all three fudge factors, or by adjusting only the CH_4 and C_2H_6 fudge factors, or by adjusting only the C_2H_2 and C_2H_6 fudge factors. In all cases, the absorption by C_2H_6 must be considered, otherwise it is impossible to flatten the emission bump near 146 nm (see figure 5.6). These are thus the three strategies that have been tried for each spectrum. The method used here is a trial and error strategy where we modified the adjustment factors focusing on one region of the spectrum at a time and using figures 5.5, 5.6 and 5.7 as a reference to know which constituents affect the intensity in each zone of the spectrum.

5.2 Results

All the spectra presented in this section have been normalized by dividing the intensity of the entire spectrum by its mean intensity between 157 and 162 nm. This wavelength range is minimally affected by hydrocarbons, making it consistent across all spectra and thereby facilitating comparison.

5.2.1 Regions with high C_2H_2 color ratio ($CR_{C_2H_2}$) and low CH_4 color ratio (CR_{CH_4})

Perijove 6

We start by synthesizing an auroral H_2 emission spectrum assuming a kappa distribution of electrons with mean energy 184.1 keV precipitating in the atmosphere of Jupiter as presented in Grodent et al. (2001) (thus without C_2H_6), causing an emission of photons with an angle of 38.3°. We thus set the adjustment factors to 1 for

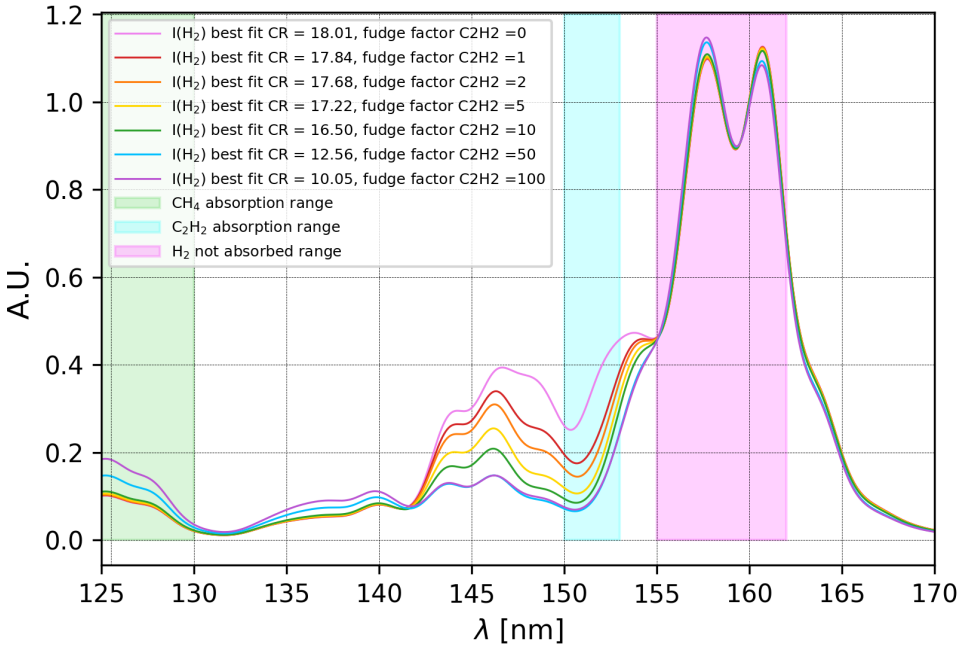

FIGURE 5.6: Spectra modelled with TransPlanet for a kappa distribution with $\langle$ E $\rangle$ = 450 keV, θ=0° and F_{CH_4}=1, $F_{C_2H_6}$=0 for various values of $F_{C_2H_2}$.

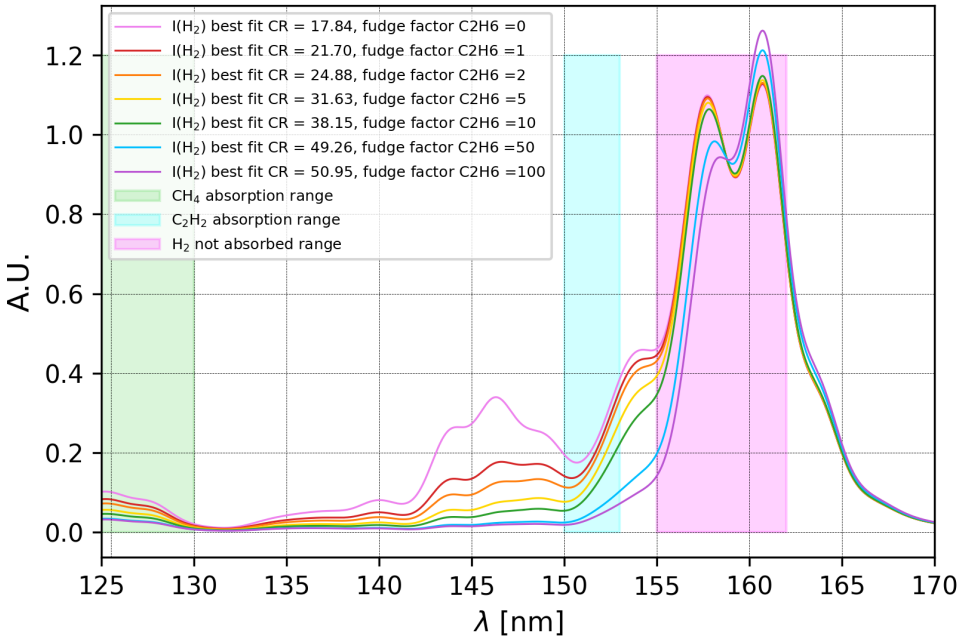

FIGURE 5.7: Spectra modelled with TransPlanet for a kappa distribution with $\langle$ E $\rangle$ = 450 keV, θ=0° and F_{CH_4}=1, $F_{C_2H_2}$=1 for various values of $F_{C_2H_6}$.

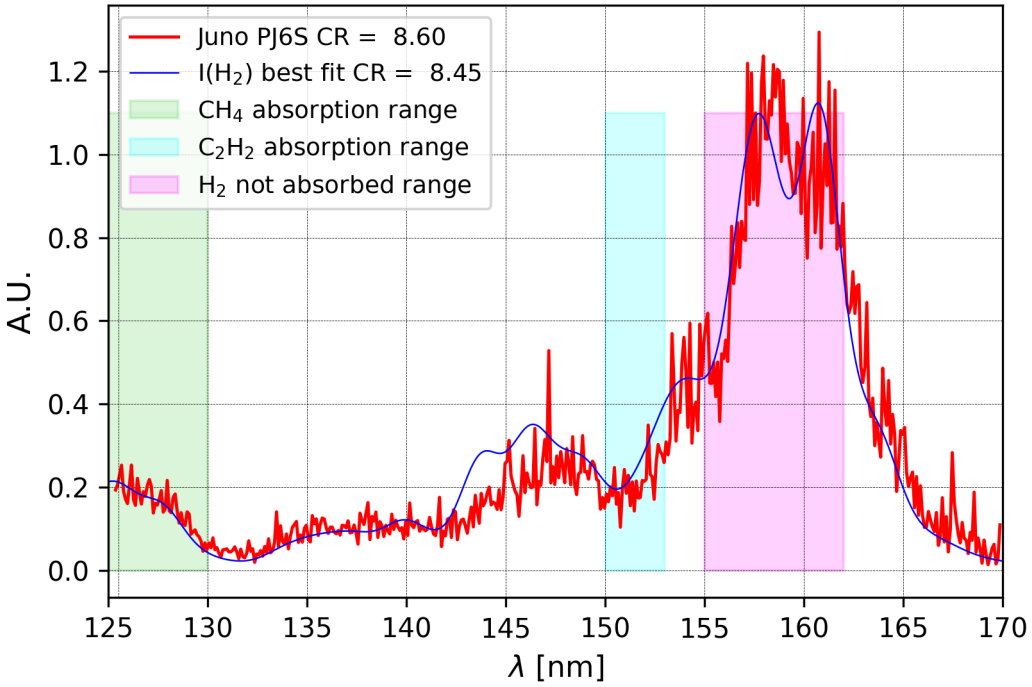

FIGURE 5.8: Comparison of the spectrum modeled with TransPlanet (blue solid line) and the observed spectrum (noisy red line) for a region with high $CR_{C_2H_2}$ and low CR_{CH_4} in PJ6 (see region selected in fig 5.2).

CH_4 and C_2H_2, and to 0 for C_2H_6. The spectrum produced by TransPlanet with these parameters as well as the observed spectrum for the selected polygon (see fig 5.2) are displayed in figure 5.8. We note that the region where the two spectra differ significantly is between 142 and 150 nm, which is where we expect absorption by C_2H_6, specifically flattening the emission bump around 146 nm. Accordingly, we decide to use our added vertical density profile of C_2H_6 in the atmospheric model for the rest of the modeling.

Energy fitting

To fit the observed spectrum by modifying the mean energy of the electrons population, we try values around the initial value of 184.1 keV. The values tested are 250 keV, 200 keV, 150 keV and 100 keV, all while keeping the atmospheric model from Grodent et al. (2001) with an added C_2H_6 vertical density profile. In figure 5.9, all these spectra are plotted over the observed spectrum. The one that seems to offer the best fit is the one with a mean energy of 150 keV.

TABLE 5.3: Values of the adjustment factors for the region with high $CR_{C_2H_2}$ and low CR_{CH_4} in PJ6.

PJ6	F_{CH_4}	$F_{C_2H_2}$	$F_{C_2H_6}$
All adjustment factors free	0.5	3.0	1.0
F_{CH_4} fixed	1.0	5.0	0.6
$F_{C_2H_2}$ fixed	0.2	1.0	1.2

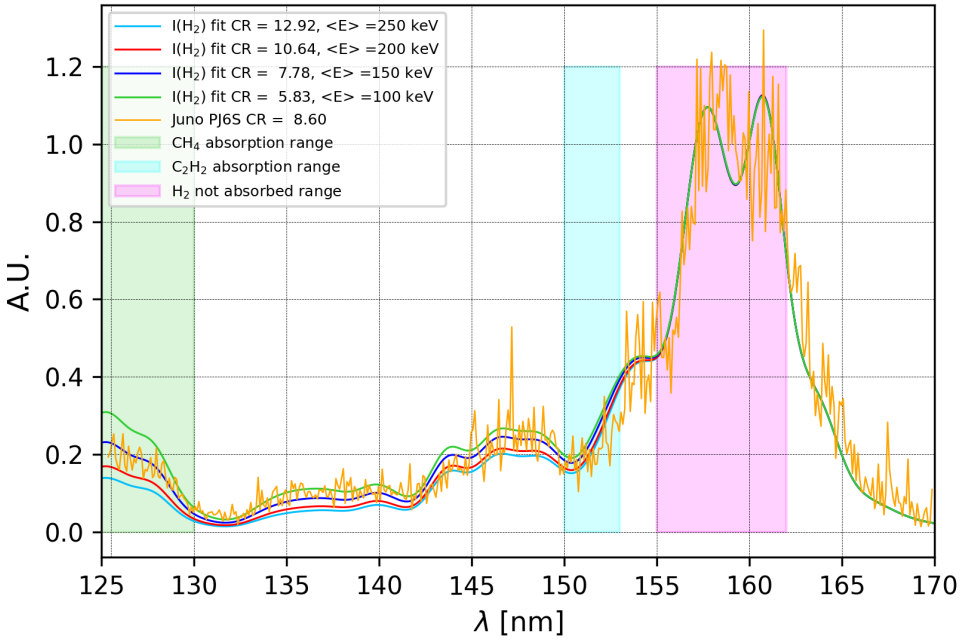

FIGURE 5.9: Comparison of the spectra modeled with TransPlanet (solid lines) with various mean energies and the observed spectrum (noisy yellow line) for a region with high $CR_{C_2H_2}$ and low CR_{CH_4} in PJ6 (see region selected in fig 5.2).

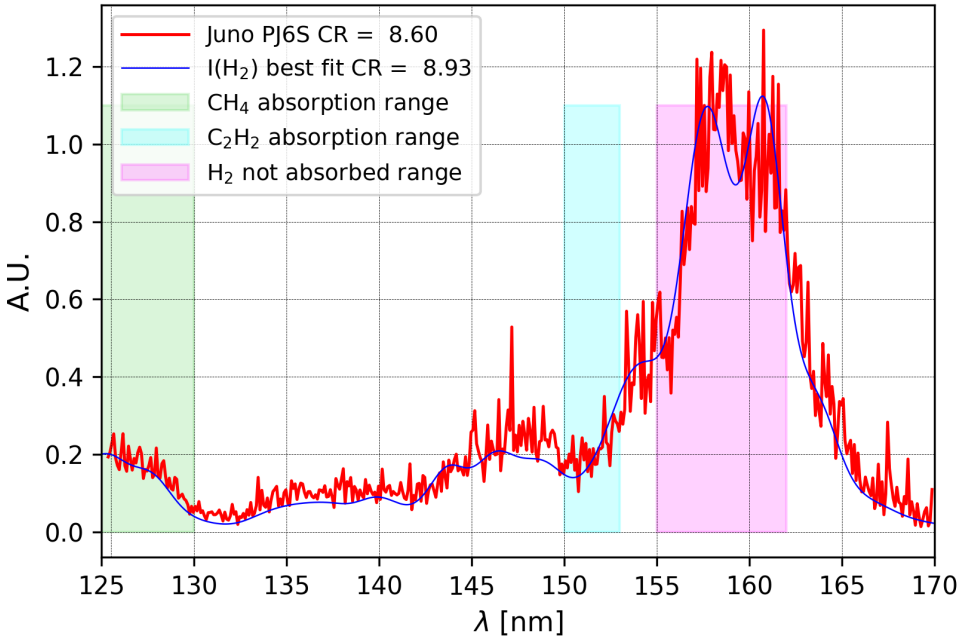

FIGURE 5.10: Comparison of the spectrum modeled with TransPlanet (blue solid line) with $\langle E \rangle = 184.1$ keV, $F_{CH_4} = 0.5$, $F_{C_2H_2} = 3.0$, $F_{C_2H_6} = 1.0$ and the observed spectrum (noisy red line) for a region with high $CR_{C_2H_2}$ and low CR_{CH_4} in PJ6 (see region selected in fig 5.2).

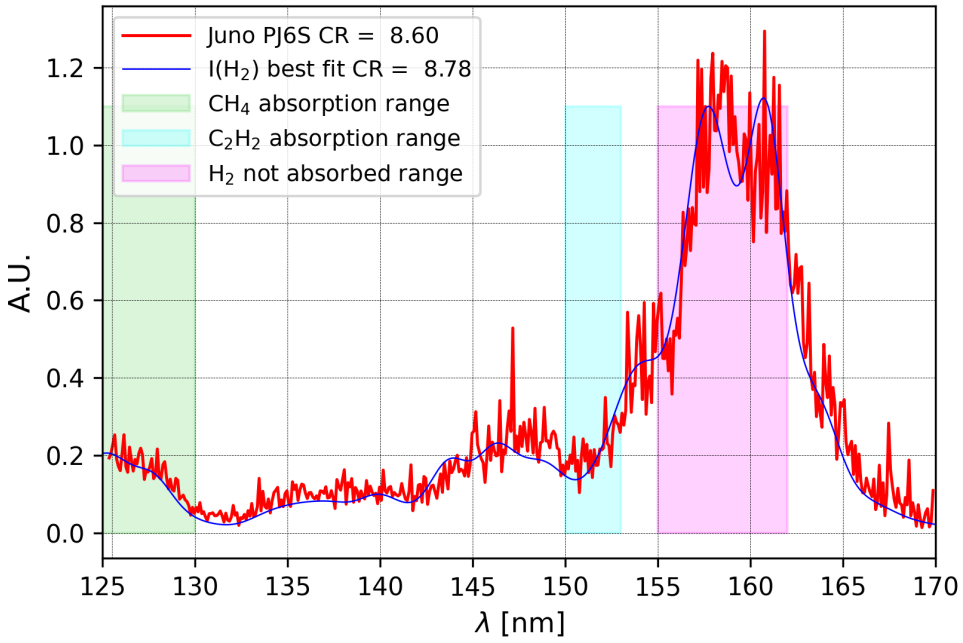

FIGURE 5.11: Comparison of the spectrum modeled with TransPlanet (blue solid line) with $\langle$ E $\rangle$ = 184.1 keV, $F_{CH_4} = 1.0$, $F_{C_2H_2} = 5.0$, $F_{C_2H_6} = 0.6$ and the observed spectrum (noisy red line) for a region with high $CR_{C_2H_2}$ and low CR_{CH_4} in PJ6 (see region selected in fig 5.2).

Determination of the adjustment factors

When attempting to fit the spectrum by modifying the adjustment factors of the atmospheric hydrocarbons, we keep the original mean energy predicted by the CR(E_0, θ) relation, which is 184.1 keV in our case.

The best fit that is obtained by tuning the adjustment factors for each hydrocarbon is presented in figure 5.10. It corresponds to a composition of Jupiter's atmosphere modified by the following adjustment factors: $F_{CH_4} = 0.5$, $F_{C_2H_2} = 3.0$ and $F_{C_2H_6} = 1.0$ as stated in the first line of table 5.3. This suggests that the atmospheric model currently employed does not accurately represent conditions in this region. Indeed, we need half the amount of CH_4 predicted by the model and three times the amount of C_2H_2 to get a satisfactory fit.

As explained in section 5.1.2, we then adjust the spectrum by modifying only the adjustment factors for two of the three hydrocarbons. Initially, we keep the the adjustment factor of CH_4 fixed at 1 (assuming the atmospheric model correctly predicts the CH_4 density profile). This yields the adjustment factors displayed in the second line of table 5.3. The spectrum produced by TransPlanet with these parameters is displayed in figure 5.11. Using the same method but setting the adjustment factor of C_2H_2 to 1, we find the adjustment factors that are displayed in the third line of table 5.3. The result of this modeling is shown in figure 5.12.

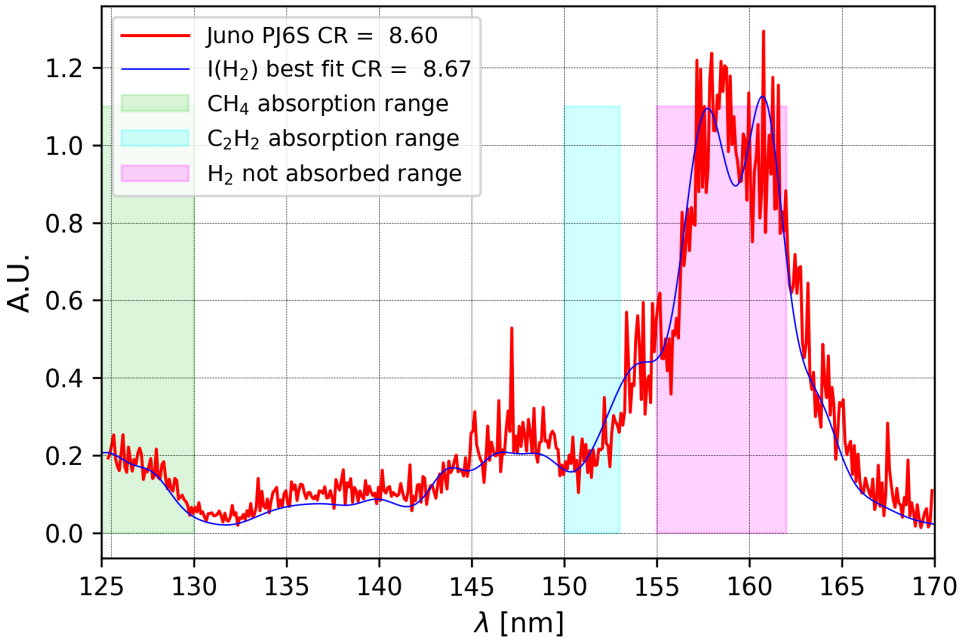

FIGURE 5.12: Comparison of the spectrum modeled with TransPlanet (blue solid line) with $\langle$ E $\rangle$ = 184.1 keV, F_{CH_4} = 0.2, $F_{C_2H_2}$ = 1.0, $F_{C_2H_6}$ = 1.2 and the observed spectrum (noisy red line) for a region with high $CR_{C_2H_2}$ and low CR_{CH_4} in PJ6 (see region selected in fig 5.2).

Perijove 10

As for PJ6, we select a polygon covering a zone of the southern auroral region where the C_2H_2 color ratio is higher than for the rest of the map while the CH_4 color ratio is low relative to the rest of the map. This polygon is the one represented in figure 5.4. We use TransPlanet to model a spectrum with the following input parameters: $\langle$ E $\rangle$ = 203.0 keV, F_{CH_4} = 1.0, $F_{C_2H_2}$ = 1.0 and $F_{C_2H_6}$ = 0.0. The result of this modeling is displayed in figure 5.13. As for the previous case, we decide to also consider the C_2H_6 vertical density profile to determine the energy of electrons as its absorption effect flattens the emission bump between 142 and 150 nm.

Energy fitting

The mean energy predicted by the CR(E_0, θ) relation is 203.0 keV. For this perijove, we consider mean energies of 400, 200, 150 and 100 keV, while setting the three adjustment factors to 1.0. The synthetic spectrum that best fits the observed spectrum corresponds to a precipitating electrons population following a kappa distribution with a mean energy of 150 keV.

TABLE 5.4: Values of the adjustment factors for the region with high $CR_{C_2H_2}$ and low CR_{CH_4} in PJ10.

PJ10	F_{CH_4}	$F_{C_2H_2}$	$F_{C_2H_6}$
All adjustment factors free	0.2	1.6	0.8
F_{CH_4} fixed	1.0	2.5	0.5
$F_{C_2H_2}$ fixed	0.2	1.0	0.8

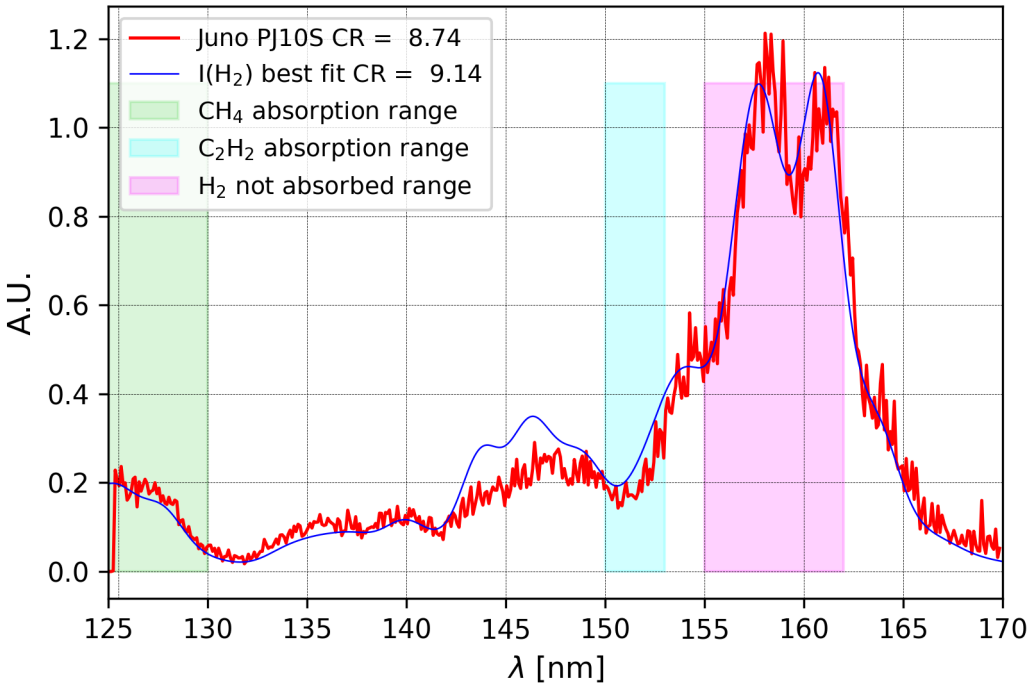

FIGURE 5.13: Comparison of the spectrum modeled with TransPlanet (blue solid line) and the observed spectrum (noisy red line) for a region with high $CR_{C_2H_2}$ and low CR_{CH_4} in PJ10 (see region selected in fig 5.4).

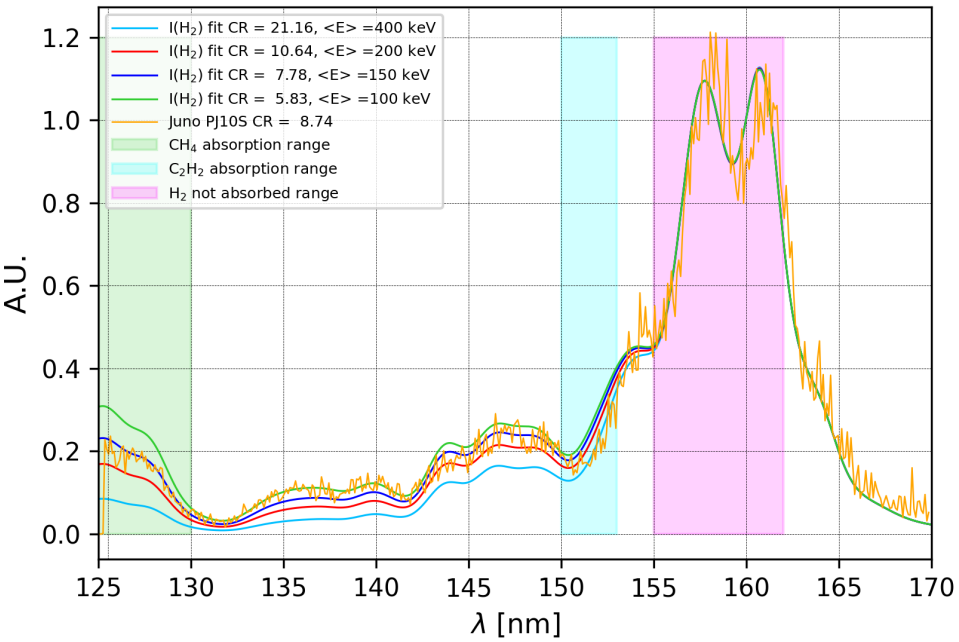

FIGURE 5.14: Comparison of the spectra modeled with TransPlanet (solid lines) with various mean energies and the observed spectrum (noisy yellow line) for a region with high $CR_{C_2H_2}$ and low CR_{CH_4} in PJ10 (see region selected in fig 5.4).

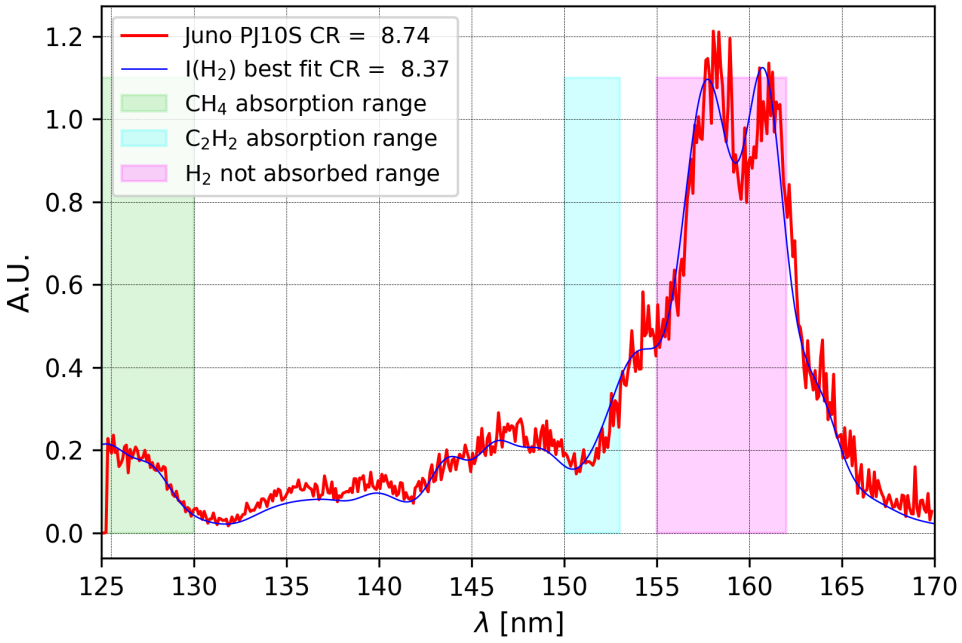

FIGURE 5.15: Comparison of the spectrum modeled with TransPlanet (blue solid line) with $\langle$ E $\rangle$ = 203.0 keV, $F_{CH_4} = 0.2$, $F_{C_2H_2} = 1.6$, $F_{C_2H_6} = 0.8$ and the observed spectrum (noisy red line) for a region with high $CR_{C_2H_2}$ and low CR_{CH_4} in PJ10 (see region selected in fig 5.4).

Determination of the adjustment factors

The best fit that was obtained by tuning the adjustment factors, while keeping an energy of 203.0 keV corresponds to: $F_{CH_4} = 0.2$, $F_{C_2H_2} = 1.6$ and $F_{C_2H_6} = 0.8$ as stated in table 5.4. The modeled spectrum obtained with these input parameters is displayed in figure 5.15. As for PJ6, we find that we need to drop significantly the amount of CH_4 while adding more C_2H_2 in order to reach a satisfactory fit. **These are major modifications to the atmospheric model we used initially.**

Figure 5.16 shows the best fit that was obtained by adjusting only the quantities C_2H_2 and C_2H_6. The adjustment factor of CH_4 was set to 1.0 an the energy was still fixed at 203.0 keV. With these initial conditions, the best fit was found by setting the adjustment factors to the values of the second line of table 5.4. Repeating the same procedure but fixing the adjustment factor of C_2H_2 instead of CH_4 to 1.0, we obtain the fit in figure 5.17, with the adjustment factors from the third line of table 5.4. **These two cases imply a singnificant change in Jupiter's atmospheric composition compared with our model.**

5.2.2 Regions with high CH_4 color ratio (CR_{CH_4}) and low C_2H_2 color ratio ($CR_{C_2H_2}$)

In this section, we reproduce the steps undertaken for regions with a high $CR_{C_2H_2}$ and low CR_{CH_4} compared with the rest of the map but for the opposite case, i.e. regions with a low $CR_{C_2H_2}$ and high CR_{CH_4} compared with the rest of the map.

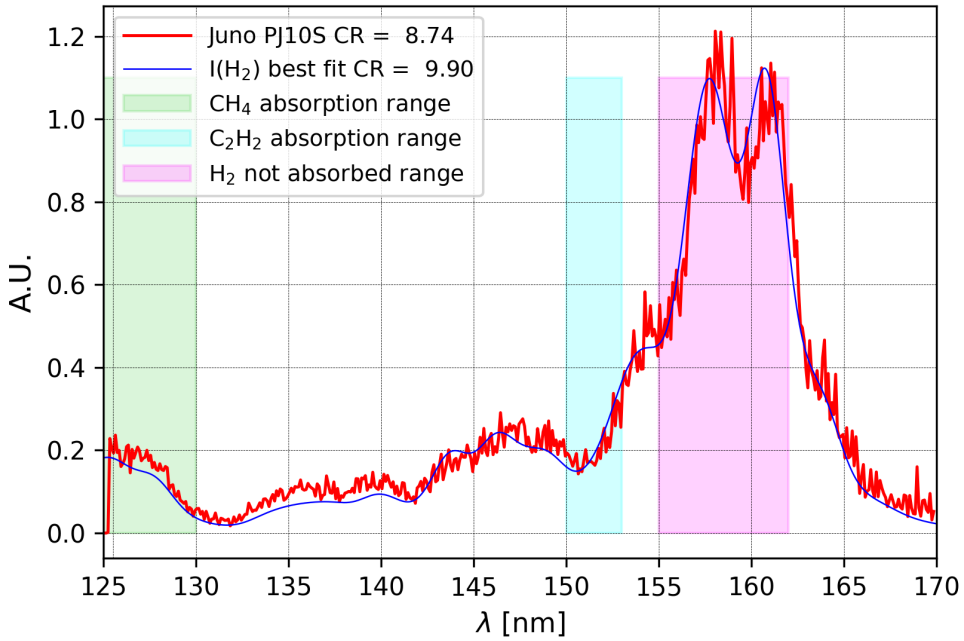

FIGURE 5.16: Comparison of the spectrum modeled with TransPlanet (blue solid line) with $\langle E \rangle = 203.0$ keV, $F_{CH_4} = 1.0$, $F_{C_2H_2} = 2.5$, $F_{C_2H_6} = 0.5$ and the observed spectrum (noisy red line) for a region with high $CR_{C_2H_2}$ and low CR_{CH_4} in PJ10 (see region selected in fig 5.4).

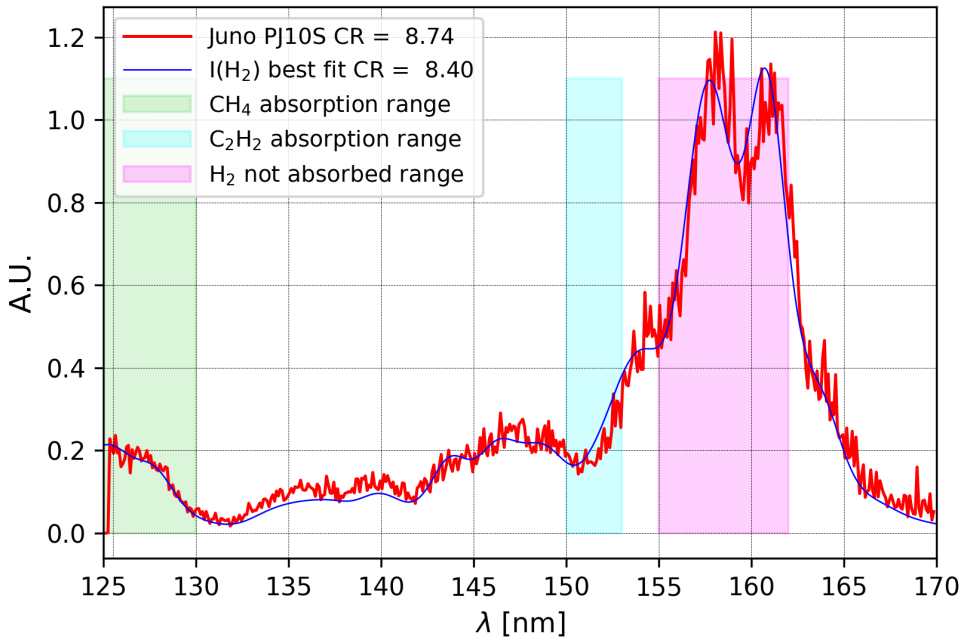

FIGURE 5.17: Comparison of the spectrum modeled with TransPlanet (blue solid line) with $\langle E \rangle = 203.0$ keV, $F_{CH_4} = 0.2$, $F_{C_2H_2} = 1.0$, $F_{C_2H_6} = 0.8$ and the observed spectrum (noisy red line) for a region with high $CR_{C_2H_2}$ and low CR_{CH_4} in PJ10 (see region selected in fig 5.4).

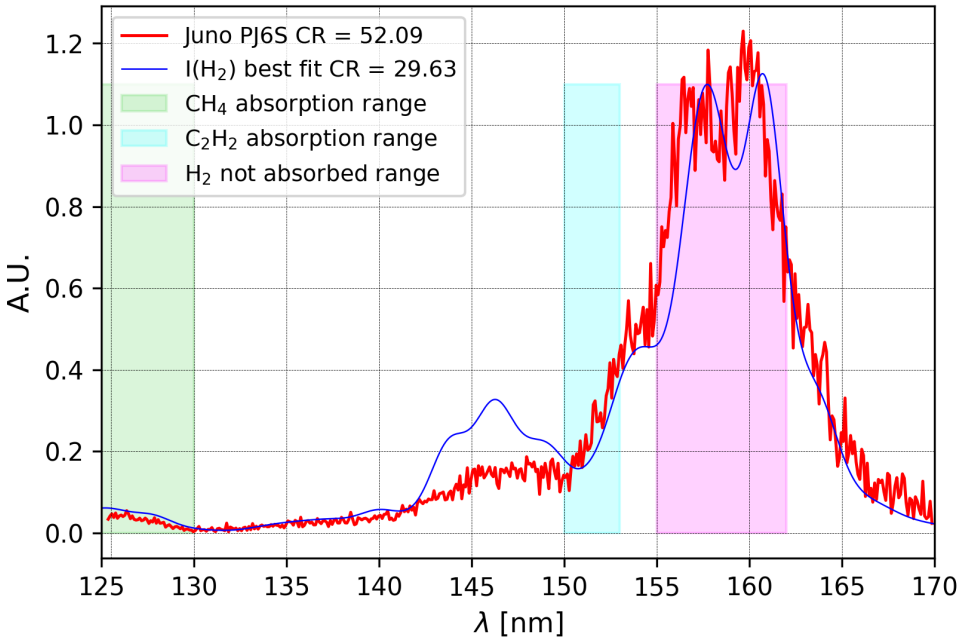

FIGURE 5.18: Comparison of the spectrum modeled with TransPlanet (blue solid line) and the observed spectrum (noisy red line) for a region with low $CR_{C_2H_2}$ and high CR_{CH_4} in PJ6 (see region selected in fig 5.1).

Perijove 6

The polygon that we consider in this section is displayed in figure 5.1. As before, we start by plotting the observed spectrum on the same plot as the result of the TransPlanet modeling (see figure 5.18). Here, we use an energy of 732.7 keV for the mean energy for the population of electrons with a kappa distribution that precipitates in Jupiter's atmosphere. We keep the same atmospheric composition as the one presented by Grodent et al. (2001), i.e. $F_{CH_4} = 1.0$, $F_{C_2H_2} = 1.0$ and $F_{C_2H_6} = 0.0$. For the following adjustments, as explained before, we add C_2H_6 to our atmospheric model before we start changing the energy, as it gets rid of the emission bump between 142 and 150 nm.

Energy fitting

In figure 5.19, we illustrate the values of the mean energy that have been tried to fit the observed spectrum. The values are chosen around the one computed with the CR(E_0, θ) relation : 732.7 keV. We have thus plotted the spectra for mean energies of 950, 750, 550 and 150 keV. This latter energy is arguably quite remote from the initial value, but as can be observed by looking at the corresponding green model spectrum in figure 5.19, it is necessary to consider such a low energy to fit the part of the spectrum located between 150 and 153 nm. However, none of these mean energies provide an acceptable fit while keeping the composition of the atmosphere from Grodent et al. (2001) with or without the added C_2H_6 vertical density profile.

Determination of the adjustment factors

The result of the fit produced by adjusting all adjustment factors while setting the

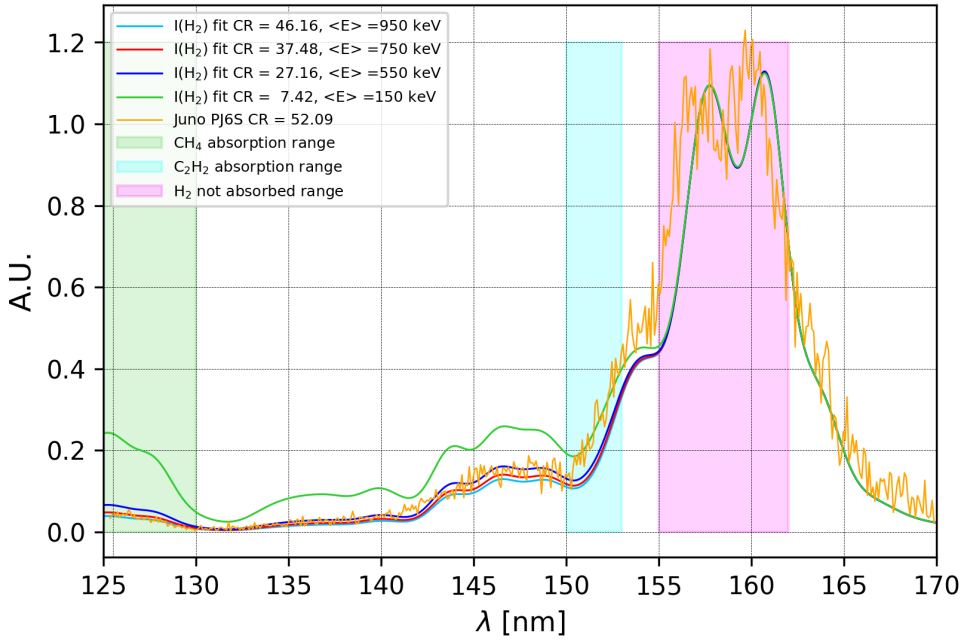

FIGURE 5.19: Comparison of the spectra modeled with TransPlanet (solid lines) with various mean energies and the observed spectrum (noisy yellow line) for a region with low $CR_{C_2H_2}$ and high CR_{CH_4} in PJ6 (see region selected in fig 5.1).

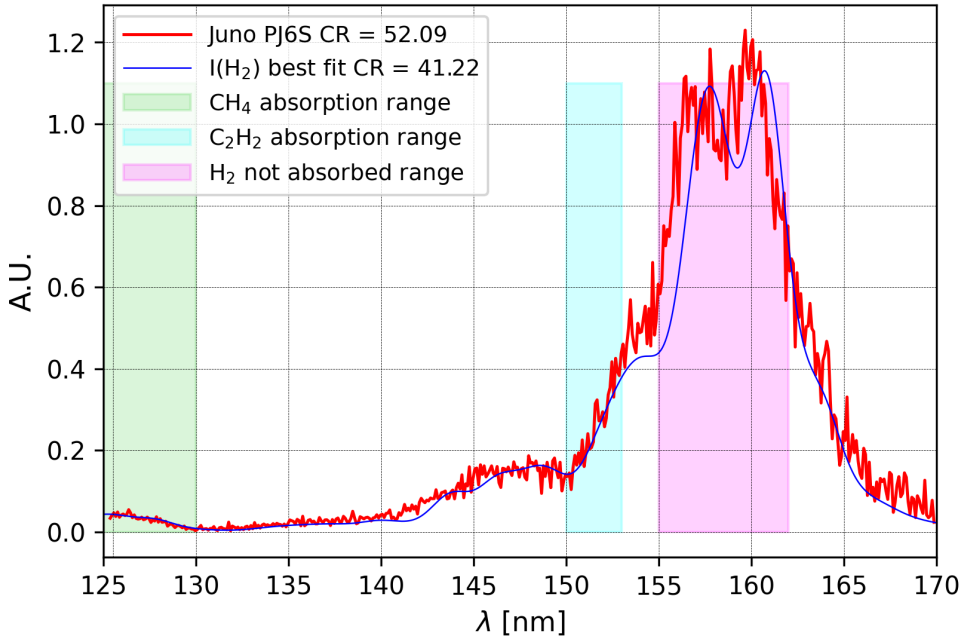

FIGURE 5.20: Comparison of the spectrum modeled with TransPlanet (blue solid line) with $\langle E \rangle = 732.7$ keV, $F_{CH_4} = 1.5$, $F_{C_2H_2} = 0.1$, $F_{C_2H_6} = 1.1$ and the observed spectrum (noisy red line) for a region with low $CR_{C_2H_2}$ and high CR_{CH_4} in PJ6 (see region selected in fig 5.1).

TABLE 5.5: Values of the adjustment factors for the region with low $CR_{C_2H_2}$ and high CR_{CH_4} in PJ6.

PJ6	F_{CH_4}	$F_{C_2H_2}$	$F_{C_2H_6}$
All adjustment factors free	1.5	0.1	1.1
F_{CH_4} fixed	1.0	0.2	1.0
$F_{C_2H_2}$ fixed	1.5	1.0	0.6

energy at 732.7 keV is displayed in figure 5.20. To obtain a satisfactory fit, we tune the values of the adjustment factors to the ones from the first line of table 5.5 : F_{CH_4} = 1.5, $F_{C_2H_2}$ = 0.1, $F_{C_2H_6}$ = 1.1. In this case, a greater quantity of CH_4 and one tenth of the initial amount of C_2H_2 are needed to correctly fit the observed spectrum. **This once again is a serious modification of our initial atmospheric model.**

When fitting the spectra with one of the adjustment factors fixed at 1.0, the values we find for the other two adjustment factors do not differ significantly from the fit where all three adjustment factors are free parameters as can be seen in table 5.5. Indeed, for F_{CH_4} fixed at 1.0, we find $F_{C_2H_2}$ = 0.2 and $F_{C_2H_6}$ = 1.0, very close to the values found in the previous fit. Moreover, when modeling a spectrum with $F_{C_2H_2}$ = 1.0, we find the best fit by setting F_{CH_4} = 1.5 and $F_{C_2H_6}$ = 0.6. The results from these two strategies offer approximately the same adjustment factors as when all three factors are allowed to vary freely. However, the fit is less accurate in the primary absorption region of the hydrocarbon whose adjustment factor was fixed at 1.0. In figure 5.21, we fix F_{CH_4} to 1.0, the fit in the absorption band of CH_4 (125-130 nm) is thus slightly less accurate than in figure 5.20. Similarly, in figure 5.22 where we set $F_{C_2H_2}$ = 1, the synthesized spectrum deviates from the observed spectrum particularly in the range between 150 and 153 nm, corresponding to the absorption range of C_2H_2.

Perijove 10

The polygon selected for PJ10 for a region of relatively high CR_{CH_4} and low $CR_{C_2H_2}$ is the one displayed in figure 5.3. We model a spectrum for a population of electrons following a kappa distribution with mean energy 542.3 keV, precipitating in an atmosphere corresponding to the model from Grodent et al. (2001). The result of this modeling as well as the observed spectrum for this polygon are plotted in figure 5.23.

Energy fitting

As in the other cases, to adjust the energy, we start by adding a C_2H_6 vertical density profile to the atmospheric model, as this appears to systematically improve the fit in our tests. We try mean energies of 750, 550, 450 and 250 keV, for which all curves are displayed in figure 5.24. In the same way as for the previous polygon that we chose in PJ6, obtaining a good fit by only tuning the energy is unmanageable. In fact, the only curvature that adapts reasonably well to the region of the spectrum between 142 and 150 nm is the one with a characteristic energy of 250 keV. However, this same curve differs from the observed spectrum by more than the size of the noise in the region between 125 and 130 nm. All three other curves, on the other hand, fit this region with a better accuracy. It is therefore necessary to adjust the quantity of all hydrocarbons in the atmosphere in order to best fit the observed spectrum.

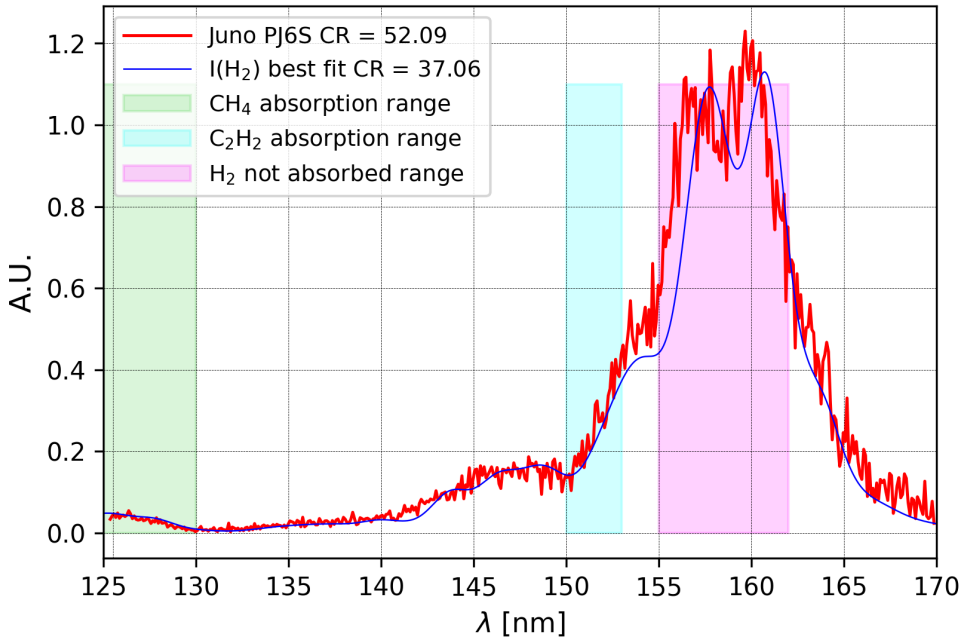

FIGURE 5.21: Comparison of the spectrum modeled with TransPlanet (blue solid line) with $\langle E \rangle = 732.7$ keV, $F_{CH_4} = 1.0$, $F_{C_2H_2} = 0.2$, $F_{C_2H_6} = 1.0$ and the observed spectrum (noisy red line) for a region with low $CR_{C_2H_2}$ and high CR_{CH_4} in PJ6 (see region selected in fig 5.1).

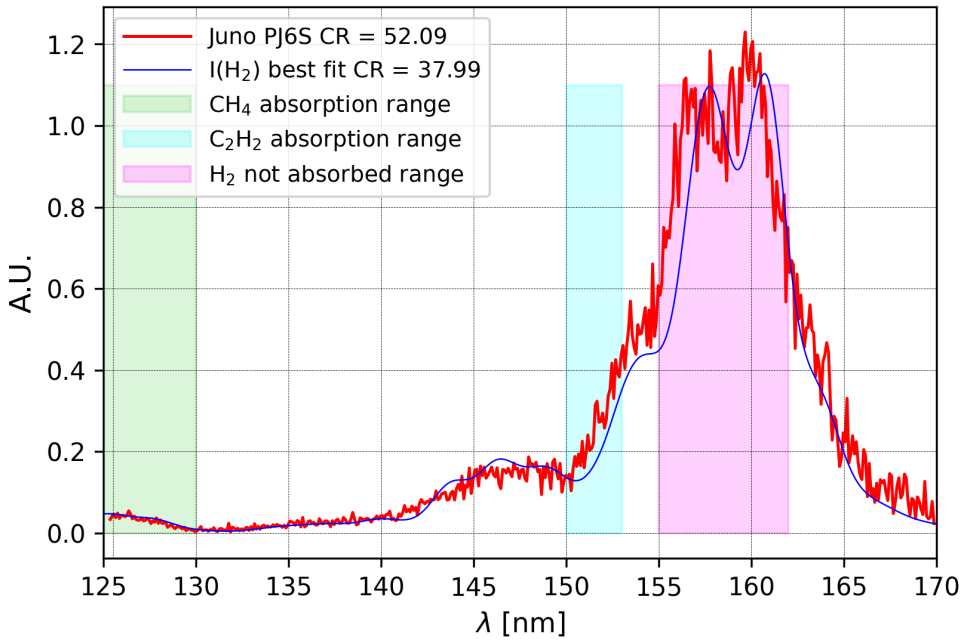

FIGURE 5.22: Comparison of the spectrum modeled with TransPlanet (blue solid line) with $\langle E \rangle = 732.7$ keV, $F_{CH_4} = 1.5$, $F_{C_2H_2} = 1.0$, $F_{C_2H_6} = 0.6$ and the observed spectrum (noisy red line) for a region with low $CR_{C_2H_2}$ and high CR_{CH_4} in PJ6 (see region selected in fig 5.1).

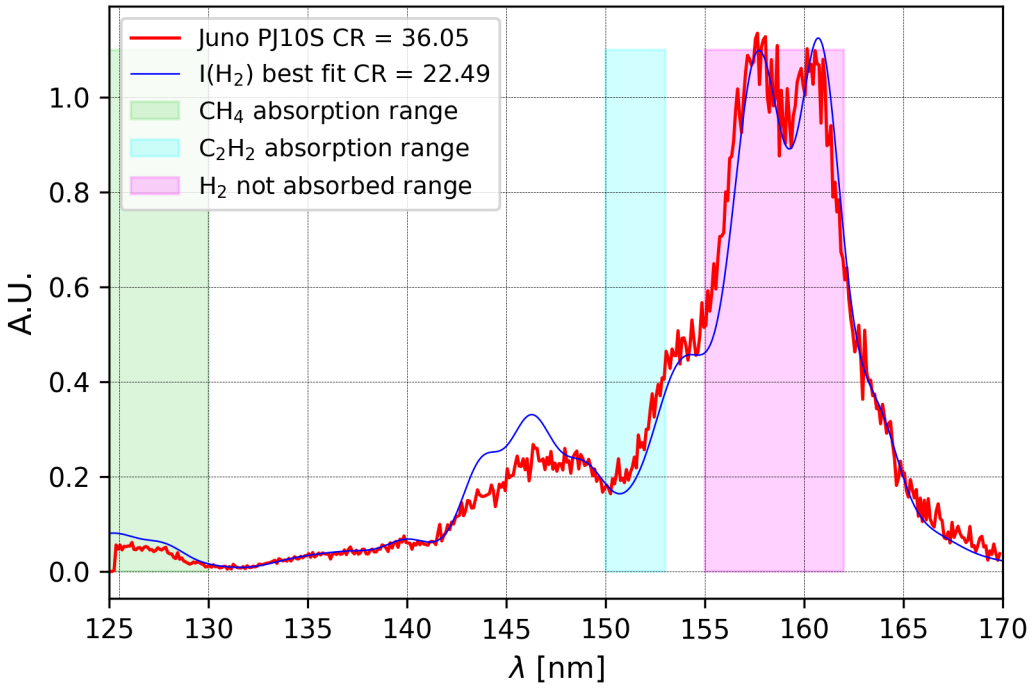

FIGURE 5.23: Comparison of the spectrum modeled with TransPlanet (blue solid line) and the observed spectrum (noisy red line) for a region with low $CR_{C_2H_2}$ and high CR_{CH_4} in PJ10 (see region selected in fig 5.3).

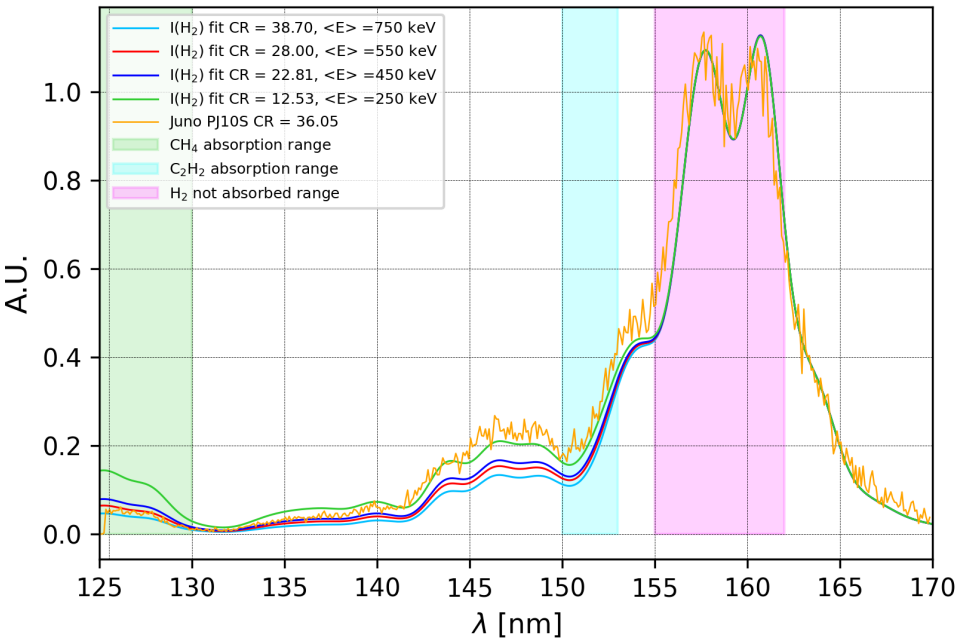

FIGURE 5.24: Comparison of the spectra modeled with TransPlanet (solid lines) with various mean energies and the observed spectrum (noisy yellow line) for a region with low $CR_{C_2H_2}$ and high CR_{CH_4} in PJ10 (see region selected in fig 5.3).

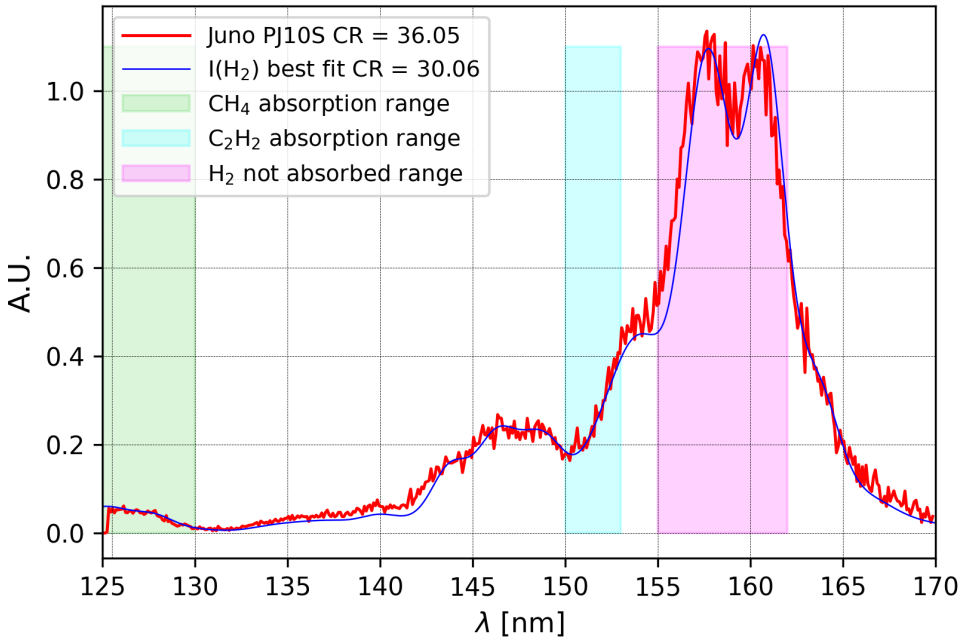

FIGURE 5.25: Comparison of the spectrum modeled with TransPlanet (blue solid line) with $\langle E \rangle = 542.3$ keV, $F_{CH_4} = 2.0$, $F_{C_2H_2} = 0.3$, $F_{C_2H_6} = 0.4$ and the observed spectrum (noisy red line) for a region with low $CR_{C_2H_2}$ and high CR_{CH_4} in PJ10 (see region selected in fig 5.3).

TABLE 5.6: Values of the adjustment factors for the region with low $CR_{C_2H_2}$ and high CR_{CH_4} in PJ10.

PJ10	F_{CH_4}	$F_{C_2H_2}$	$F_{C_2H_6}$
All adjustment factors free	2.0	0.3	0.4
F_{CH_4} fixed	1.0	0.3	0.4
$F_{C_2H_2}$ fixed	1.8	1.0	0.3

Determination of the adjustment factors

Figure 5.25 shows the spectrum modeled for a distribution of electrons with a mean energy of 542.3 keV and the following adjustment factors: $F_{CH_4} = 2.0$, $F_{C_2H_2} = 0.3$ and $F_{C_2H_6} = 0.4$. These offer the best fit when all three adjustment factors are left as free parameters. The results have similar trends as the polygon chosen with high CR_{CH_4} and low $CR_{C_2H_2}$ for PJ6. Indeed, we need to increase the quantity of CH_4 and lower the quantity of C_2H_2 in both cases to find a good fit.

Similarly to the previous case, we observe that when fixing the CH_4 or C_2H_2 adjustment factors at 1.0, the resulting adjustment factors for the other two hydrocarbons are very similar to those obtained when all three factors are free parameters. Consequently, the fit is similar to the case with all adjustment factors modified. However, it is less accurate specifically in the absorption range of the constituent whose adjustment factor is fixed to 1.0 as can be observed in figures 5.26 and 5.27.

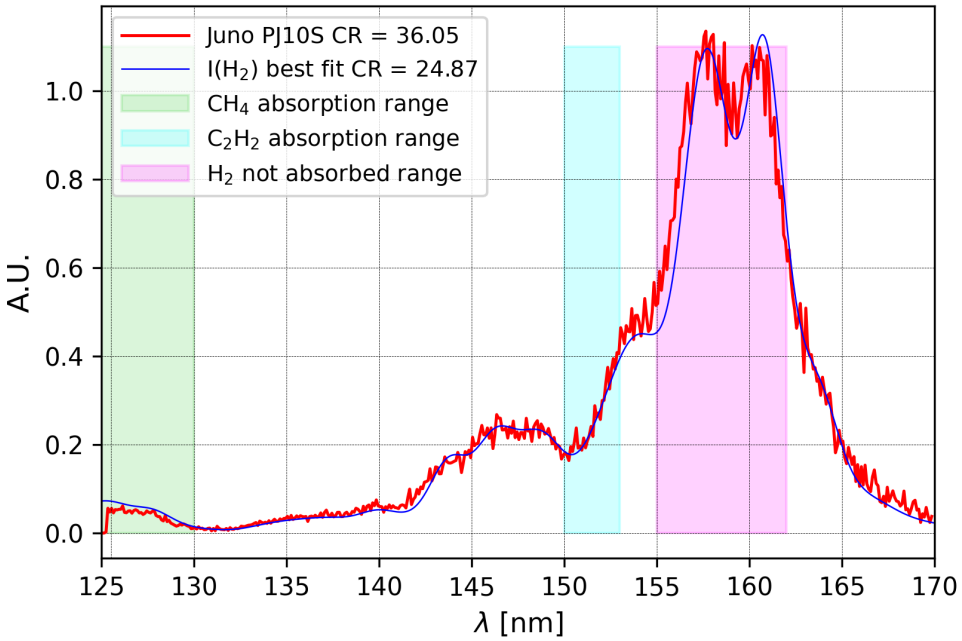

FIGURE 5.26: Comparison of the spectrum modeled with TransPlanet (blue solid line) with $\langle E \rangle = 542.3$ keV, $F_{CH_4} = 1.0$, $F_{C_2H_2} = 0.3$, $F_{C_2H_6} = 0.4$ and the observed spectrum (noisy red line) for a region with low $CR_{C_2H_2}$ and high CR_{CH_4} in PJ10 (see region selected in fig 5.3).

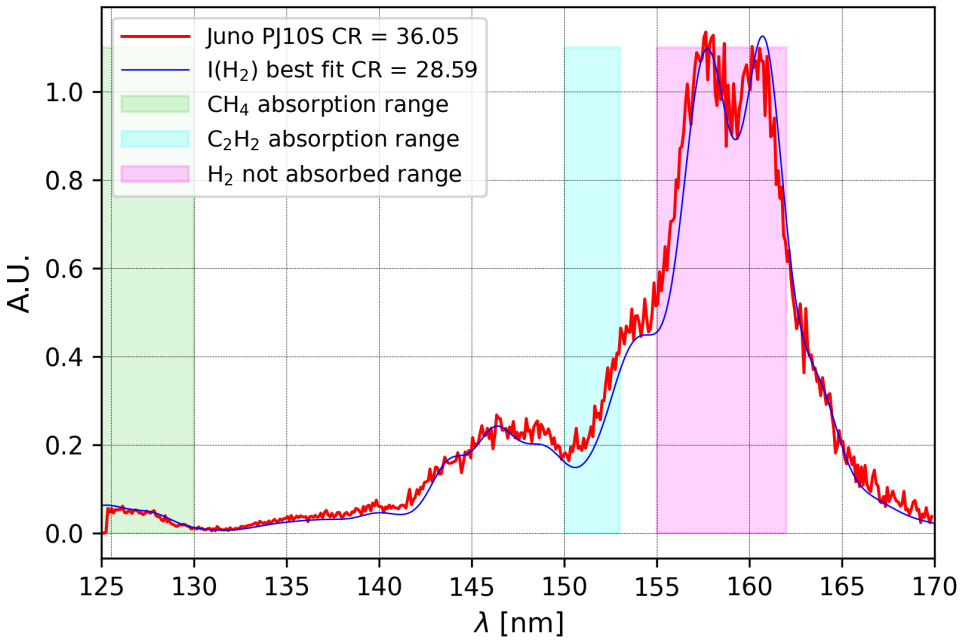

FIGURE 5.27: Comparison of the spectrum modeled with TransPlanet (blue solid line) with $\langle E \rangle = 542.3$ keV, $F_{CH_4} = 1.8$, $F_{C_2H_2} = 1.0$, $F_{C_2H_6} = 0.3$ and the observed spectrum (noisy red line) for a region with low $CR_{C_2H_2}$ and high CR_{CH_4} in PJ10 (see region selected in fig 5.3).

5.3 Discussion

In this section, we briefly retrace the steps that were taken to better understand some of the characteristics of Jupiter's southern color ratio maps and discuss our results.

We note that some zones in the color ratio maps from annex A present anomalies. We were intrigued by the fact that some zones presented a high C_2H_2 color ratio compared to the rest of the map while their CH_4 color ratio was low compared to the rest of the map. Since we know that the C_2H_2 homopause is lower than the CH_4 homopause in Jupiter's atmosphere, we expect to see: 1) regions with both CH_4 and C_2H_2 absorption, 2) regions with only CH_4 absorption, and 3) regions with no absorption of either hydrocarbon. The zones that appear suspicious to us might also have a lower CH_4 color ratio than the rest of the map because it is particularly high in the rest of the map due to a higher density of CH_4.

We then studied some spectral characteristics of spatial regions of interest, limited by polygons in the auroral maps, and attempted to model the observed spectra extracted from these regions. For these modelings, we used TransPlanet to simulate the precipitation of electrons in an atmosphere and the subsequent H_2 emission spectrum.

Firstly, the polygons that presented what we considered anomalies do not actually challenge our models. Indeed, the observed spectra of the two polygons studied in section 5.2.1 are quite easy to fit with our model. Adding a C_2H_6 vertical density profile to our atmospheric model and lowering the energy predicted by the CR(E_0, θ) relation gave us reasonable fits for both PJ6 and PJ10. One explanation would be that, by not taking into account the presence of C_2H_6 in Jupiter's atmosphere, the relation overestimates the energy. This would mean that our models, with some adjustments, predict correctly the observed spectrum. For PJ6, in the polygon with high $CR_{C_2H_2}$ and low CR_{CH_4}, the mean energy predicted by the CR(E_0, θ) relation was 184.1 keV. The addition of the C_2H_6 vertical profile as well as the lowering of this mean energy to 150 keV provided a satisfactory fit. The same kind of result was achieved for PJ10 by lowering the mean energy from 203.0 keV to 150 keV.

Another possibility is that the composition of the atmosphere has changed. If this is the case, our simulations indicate that these regions should be depleted in CH_4 and contain a larger amount of C_2H_2 than what is predicted by our atmospheric model. The difference between the initial modeling and the observed spectrum could also be explained by a combination of these two scenarios or another phenomenon not yet uncovered. Further research and modeling are required to draw conclusions and discriminate between these hypotheses.

The auroral regions we tested and for which we assumed our models would work since we didn't observe anything intriguing when we looked at the color ratio maps turned out to be the ones that challenged our models the most. Even by adjusting the energy and adding a C_2H_6 vertical density profile like we had done for the previous cases, it was not possible to obtain a satisfactory fit. Modifying the values of the three adjustment factors eventually gave the best fits for the two cases studied, and involved increasing the amount of CH_4 and decreasing the amount of C_2H_2 (while also adjusting the C_2H_6 adjustment factor). This could mean that there is a change in the atmospheric composition of these regions with a high CH_4 color ratio but could also be the result of a combination of factors, including a poor estimate of the mean

energy of the electrons.

It is very difficult to draw conclusions from these models because of the number of free parameters to be set. The mean energy of the population of precipitating electrons and the adjustment factors of all three hydrocarbons can be adjusted and modify the intensity of various parts of the spectrum. We must also consider that some other atmospheric constituents might be absorbing in the 125 to 170 nm range and modify the CR(E_0, θ) relation as well as the atmospheric composition. Discriminating between these scenarios is a task beyond the scope of a Master's thesis, and involves adding features to TransPlanet to take account of possible changes in the atmospheric composition of Jupiter's atmosphere due to the precipitation of energetic electrons.

5.4 Conclusion

In this section, we aim to better understand the characteristics of Jupiter's southern color ratio maps by investigating anomalies and their implications. We observe that certain regions exhibit unusual C_2H_2 and CH_4 color ratios. Given the atmospheric homopauses of these hydrocarbons, we expect to see three types of regions: those with both CH_4 and C_2H_2 absorption, those with only CH_4 absorption, and those with neither. The anomalies might result from spatially localized variations in CH_4 density.

We then analyze the spectral characteristics of these anomalous regions using TransPlanet to simulate electron precipitation. The spectra from the suspected anomalous regions fit well with our models after adjusting for C_2H_6 density and lowering the predicted energy. This suggests that our models are robust, with the possibility that the presence of C_2H_6 causes an overestimation of energy by the CR(E_0, θ) relation. Alternatively, these regions may have altered atmospheric compositions with increased C_2H_2 and decreased CH_4 levels.

Interestingly, the regions that initially appeared normal pose more challenges for our models. Satisfactory fits are only achieved by significantly altering the amounts of CH_4 and C_2H_2, suggesting potential atmospheric composition changes or inaccuracies in the mean energy estimates of the precipitating electrons.

In conclusion, the complexity of the interactions and the number of adjustable parameters in the models make it difficult to draw definitive conclusions. Further research and improvements to the TransPlanet code are necessary to fully understand the atmospheric composition changes and the implications of energetic electron precipitation in Jupiter's aurora.

6

Conclusion

This master's thesis provides a comprehensive analysis of electron precipitation in Jupiter's auroral regions, focusing on their mean energy, correlation with H_2 brightness, and the spectral characteristics of anomalous regions in the southern aurora color ratio maps.

The analysis of the mean energy of electrons precipitating in the auroral regions reveals several important trends. In the outer auroral regions, electrons consistently exhibit the lowest median mean energy compared to other sub-regions. In the northern hemisphere, electrons in the polar auroral region have a higher median mean energy than those in the main emission region, a trend which is reversing in the southern hemisphere. Additionally, the electrons in the southern outer auroral region generally have a higher energy than those in the northern outer emission region, a trend also observed, though less clearly, in the main emission region. Furthermore, there is no strong correlation in the mean median energy of precipitating electrons between each sub-region and their magnetic counterparts in the other hemisphere over time.

The study of the correlation between H_2 brightness and the energy of the precipitating electrons reveals no correlation in the northern auroral region and only a slight correlation in the southern auroral region. Detailed analysis by auroral sub-regions, however, demonstrates that the initial apparent correlation in the southern auroral regions is misleading, highlighting the risk of false correlations when considering the entire auroral region rather than distinct sub-regions. These findings align with previous research, indicating that zones of highest electron energy do not necessarily coincide with areas of large electron precipitation flux.

The investigation into the southern aurora color ratio maps aimed to understand anomalies in certain zones. Some zones exhibit unusual C_2H_2 and CH_4 color ratios, possibly due to variations in CH_4 density. Spectral analysis using TransPlanet shows that observed spectra from these zones fit well with models after adjustments for C_2H_6 density and recalibration of energy, suggesting robust models but also potential atmospheric composition changes. Interestingly, zones that initially appeared normal posed greater challenges for the models, requiring significant adjustments and indicating possible atmospheric composition changes or inaccuracies in the mean energy estimates of the precipitating electrons.

This master's thesis opens many scientific questions that would need further research in order to be thoroughly investigated. The evolution of the mean median energy of electrons precipitating in each auroral sub-region is directly linked to the complex acceleration processes that occur in the jovian magnetosphere. These processes,

especially in the polar auroral regions, are not yet fully understood. A deeper comprehension of them would surely explain the difference in energy of the precipitating electrons between the sub-regions and between the northern and southern auroral regions.

We have established that the auroral H_2 brightness and the energy of the precipitating electrons are not correlated. However, we have also observed that their relation varies for different auroral sub-regions. Future studies combining the statistical robustness of this work with the detailed analysis conducted by Gérard et al. (2016) would be valuable, as the mechanisms behind the varying correlation coefficients in different sub-regions remain unclear.

The last part of this work leaves many questions hanging. The fits that we have produced for the observed spectra raise doubts about the consistency of the auroral atmospheric model of Jupiter over the whole auroral region. Indeed, for several zones, the atmospheric model has to be modified in order to fit the observed spectrum. Finding the best fit of the observed spectra by modifying the adjustment factor of CH_4, C_2H_2 and C_2H_6 is a complex and degenerate problem. Moreover, other constituents that we did not considere in this study might also cause discrepancies between model and observation. A thorough investigation of the constituents that absorb in the 125-170 nm band would be needed for a more exhaustive study and an electron transport model with atmospheric feedback would clarify the actual change in atmospheric composition rather than infering it through spectral modeling. Additionally, the CR(E_0, θ) needs modification as it appears to overestimate the energy in some cases.

Bibliography

Armstrong, R. A. (2019). Should Pearson's correlation coefficient be avoided? *Ophthalmic and Physiological Optics*, 39(5), 316–327. _eprint: https://onlinelibrary.wiley.com/doi/pdf/10.1111/opo.12636.

Atreya, S., Mahaffy, P., Niemann, H., Wong, M., & Owen, T. (2003). Composition and origin of the atmosphere of jupiter—an update, and implications for the extrasolar giant planets. *Planetary and Space Science*, 51(2), 105–112. Recent Advances on the Atmosphere of Outer Planets and Titan.

Bagenal, F., Adriani, A., Allegrini, F., Bolton, S. J., Bonfond, B., Bunce, E. J., Connerney, J. E. P., Cowley, S. W. H., Ebert, R. W., Gladstone, G. R., Hansen, C. J., Kurth, W. S., Levin, S. M., Mauk, B. H., McComas, D. J., Paranicas, C. P., Santos-Costa, D., Thorne, R. M., Valek, P., Waite, J. H., & Zarka, P. (2017). Magnetospheric Science Objectives of the Juno Mission. *Space Science Reviews*, 213(1), 219–287.

Bagenal, F., Dowling, T. E., McKinnon, W. B., & McKinnon, W. (2006). *Jupiter: The Planet, Satellites and Magnetosphere*. Cambridge University Press. Google-Books-ID: aMERHqj9ivcC.

Benmahi, B. (2022). *Étude de la dynamique et de la composition des atmosphères des planètes géantes : préparation de la mission JUICE.* phdthesis, Université de Bordeaux.

Benmahi, B., Bonfond, B., Benne, B., Grodent, D., Hue, V., Gladstone, G. R., Gronoff, G., Lilensten, J., Sicorello, G., Head, L. A., Barthélemy, M., Simon Wedlund, C., Giles, R. S., & Greathouse, T. K. (2024). Energy mapping of Jupiter's auroral electrons from Juno/UVS data using a new H2 UV emission model. *A&A*, 685, A26.

Bolton, S. J., Bagenal, F., Blanc, M., Cassidy, T., Chané, E., Jackman, C., Jia, X., Kotova, A., Krupp, N., Milillo, A., Plainaki, C., Smith, H. T., & Waite, H. (2015). Jupiter's Magnetosphere: Plasma Sources and Transport. *Space Science Reviews*, 192(1), 209–236.

Bolton, S. J., Lunine, J., Stevenson, D., Connerney, J. E. P., Levin, S., Owen, T. C., Bagenal, F., Gautier, D., Ingersoll, A. P., Orton, G. S., Guillot, T., Hubbard, W., Bloxham, J., Coradini, A., Stephens, S. K., Mokashi, P., Thorne, R., & Thorpe, R. (2017). The Juno Mission. *Space Science Reviews*, 213(1), 5–37.

Bonfond, B., Grodent, D., Gérard, J.-C., Radioti, A., Saur, J., & Jacobsen, S. (2008). UV Io footprint leading spot: A key feature for understanding the UV Io footprint multiplicity? *Geophysical Research Letters*, 35(5). _eprint: https://onlinelibrary.wiley.com/doi/pdf/10.1029/2007GL032418.

Bonfond, B., Yao, Z., & Grodent, D. (2020). Six Pieces of Evidence Against the Corotation Enforcement Theory to Explain the Main Aurora at Jupiter. *Journal of Geophysical Research: Space Physics*, 125(11), e2020JA028152. _eprint: https://onlinelibrary.wiley.com/doi/pdf/10.1029/2020JA028152.

Broadfoot, A. L., Belton, M. J. S., Takacs, P. Z., Sandel, B. R., Shemansky, D. E., Holberg, J. B., Ajello, J. M., Atreya, S. K., Donahue, T. M., Moos, H. W., Bertaux, J. L., Blamont, J. E., Strobel, D. F., McConnell, J. C., Dalgarno, A., Goody, R., & McElroy, M. B. (1979). Extreme ultraviolet observations from voyager 1 encounter with jupiter. *Science*, 204(4396), 979–982.

Bunce, E., Nichols, J., & Cowley, S. (2005). Solar wind-magnetosphere–ionosphere coupling at jupiter. *Advances in Space Research*, 36(11), 2090–2099. Planetary Atmospheres, Ionospheres, and Magnetospheres.

Burke, B. F. & Franklin, K. L. (1955). Observations of a variable radio source associated with the planet Jupiter. *Journal of Geophysical Research (1896-1977)*, 60(2), 213–217. _eprint: https://onlinelibrary.wiley.com/doi/pdf/10.1029/JZ060i002p00213.

Cowley, S. W. H. & Bunce, E. J. (2001). Origin of the main auroral oval in Jupiter's coupled magnetosphere–ionosphere system. *Planetary and Space Science*, 49(10), 1067–1088.

Delamere, P. A. & Bagenal, F. (2010). Solar wind interaction with Jupiter's magnetosphere. *Journal of Geophysical Research: Space Physics*, 115(A10). _eprint: https://onlinelibrary.wiley.com/doi/pdf/10.1029/2010JA015347.

Dumont, M., Grodent, D., Radioti, A., Bonfond, B., Roussos, E., & Paranicas, C. (2018). Evolution of the Auroral Signatures of Jupiter's Magnetospheric Injections. *Journal of Geophysical Research: Space Physics*, 123(10), 8489–8501. _eprint: https://onlinelibrary.wiley.com/doi/pdf/10.1029/2018JA025708.

Encrenaz, T. (1999). The planet Jupiter. *The Astronomy and Astrophysics Review*, 9(3), 171–219.

Eviatar, A., Williams, D. J., Paranicas, C., McEntire, R. W., Mauk, B. H., & Kivelson, M. G. (2000). Trapped Energetic Electrons in the Magnetosphere of Ganymede. *Journal of Geophysical Research: Space Physics*, 105(A3), 5547–5553. _eprint: https://onlinelibrary.wiley.com/doi/pdf/10.1029/1999JA900450.

Gladstone, G. R., Persyn, S. C., Eterno, J. S., Walther, B. C., Slater, D. C., Davis, M. W., Versteeg, M. H., Persson, K. B., Young, M. K., Dirks, G. J., Sawka, A. O., Tumlinson, J., Sykes, H., Beshears, J., Rhoad, C. L., Cravens, J. P., Winters, G. S., Klar, R. A., Lockhart, W., Piepgrass, B. M., Greathouse, T. K., Trantham, B. J., Wilcox, P. M., Jackson, M. W., Siegmund, O. H. W., Vallerga, J. V., Raffanti, R., Martin, A., Gérard, J.-C., Grodent, D. C., Bonfond, B., Marquet, B., & Denis, F. (2017). The Ultraviolet Spectrograph on NASA's Juno Mission. *Space Science Reviews*, 213(1), 447–473.

Grammier, R. S. (2009). A look inside the juno mission to jupiter. (pp. 1–10).

Greathouse, T., Gladstone, R., Versteeg, M., Hue, V., Kammer, J., Giles, R., Davis, M., Bolton, S., Levin, S., Connerney, J., Gérard, J.-C., Grodent,

D., Bonfond, B., Bunce, E., & Vogt, M. F. (2021). Local Time Dependence of Jupiter's Polar Auroral Emissions Observed by Juno UVS. *Journal of Geophysical Research: Planets*, 126(12), e2021JE006954. _eprint: https://onlinelibrary.wiley.com/doi/pdf/10.1029/2021JE006954.

Greathouse, T. K., Gladstone, G. R., Davis, M. W., Slater, D. C., Versteeg, M. H., Persson, K. B., Walther, B. C., Winters, G. S., Persyn, S. C., & Eterno, J. S. (2013). Performance results from in-flight commissioning of the Juno Ultraviolet Spectrograph (Juno-UVS). In *UV, X-Ray, and Gamma-Ray Space Instrumentation for Astronomy XVIII*, volume 8859 (pp. 216–226).: SPIE.

Grodent, D. (2015). A Brief Review of Ultraviolet Auroral Emissions on Giant Planets. *Space Science Reviews*, 187(1), 23–50.

Grodent, D., Waite Jr., J. H., & Gérard, J.-C. (2001). A self-consistent model of the Jovian auroral thermal structure. *Journal of Geophysical Research: Space Physics*, 106(A7), 12933–12952. _eprint: https://onlinelibrary.wiley.com/doi/pdf/10.1029/2000JA900129.

Groulard, A., Bonfond, B., Grodent, D., Gérard, J.-C., Greathouse, T., Hue, V., Gladstone, G., & Versteeg, M. (2024). Dawn-dusk asymmetry in the main auroral emissions at jupiter observed with juno-uvs. *Icarus*, 413, 116005.

Gurnett, D. A., Persoon, A. M., Kurth, W. S., Roux, A., & Bolton, S. J. (2000). Plasma densities in the vicinity of Callisto from Galileo plasma wave observations. *Geophysical Research Letters*, 27(13), 1867–1870. _eprint: https://onlinelibrary.wiley.com/doi/pdf/10.1029/2000GL003751.

Gérard, J. C., Bonfond, B., Grodent, D., & Radioti, A. (2016). The color ratio-intensity relation in the Jovian aurora: Hubble observations of auroral components. *Planetary and Space Science*, 131, 14–23.

Gérard, J.-C., Bonfond, B., Grodent, D., Radioti, A., Clarke, J. T., Gladstone, G. R., Waite, J. H., Bisikalo, D., & Shematovich, V. I. (2014). Mapping the electron energy in Jupiter's aurora: Hubble spectral observations. *Journal of Geophysical Research: Space Physics*, 119(11), 9072–9088. _eprint: https://onlinelibrary.wiley.com/doi/pdf/10.1002/2014JA020514.

Gérard, J. C., Grodent, D., Radioti, A., Bonfond, B., & Clarke, J. T. (2013). Hubble observations of Jupiter's north–south conjugate ultraviolet aurora. *Icarus*, 226(2), 1559–1567.

Haewsantati, K., Bonfond, B., Wannawichian, S., Gladstone, G. R., Hue, V., Versteeg, M. H., Greathouse, T. K., Grodent, D., Yao, Z., Dunn, W., Gérard, J.-C., Giles, R., Kammer, J., Guo, R., & Vogt, M. F. (2021). Morphology of Jupiter's Polar Auroral Bright Spot Emissions via Juno-UVS Observations. *Journal of Geophysical Research: Space Physics*, 126(2), e2020JA028586. _eprint: https://onlinelibrary.wiley.com/doi/pdf/10.1029/2020JA028586.

Hansen, C. J., Bolton, S. J., Matson, D. L., Spilker, L. J., & Lebreton, J.-P. (2004). The cassini–huygens flyby of jupiter. *Icarus*, 172(1), 1–8. Special Issue: Cassini-Huygens at Jupiter.

Head, L., Grodent, D., Bonfond, B., Moirano, A., Benmahi, B., Sicorello, G., Gérard, J., Vogt, M., Hue, V., Greathouse, T., et al. (2024). Effect of magnetospheric

conditions on the morphology of jupiter's uv main auroral emission, as observed by juno-uvs. *arXiv preprint arXiv:2404.04030*.

Hue, V., Gladstone, G. R., Greathouse, T. K., Kammer, J. A., Davis, M. W., Bonfond, B., Versteeg, M. H., Grodent, D. C., Gérard, J.-C., Bolton, S. J., Levin, S. M., & Byron, B. D. (2019). In-flight Characterization and Calibration of the Juno-ultraviolet Spectrograph (Juno-UVS). *The Astronomical Journal*, 157(2), 90. Publisher: The American Astronomical Society.

Khurana, K. K., Kivelson, M. G., Vasyliunas, V. M., Krupp, N., Woch, J., Lagg, A., Mauk, B. H., & Kurth, W. S. (2004). The configuration of jupiter's magnetosphere. *Jupiter. The planet, satellites and magnetosphere*, 1, 593–616.

Knight, S. (1973). Parallel electric fields. *Planetary and Space Science*, 21(5), 741–750.

Krupp, N. (2007). New surprises in the largest magnetosphere of our solar system. *Science*, 318(5848), 216–217.

Lilensten, J. (1989). *Resolution de l'equation de transport et applications dans le plasma ionospherique*. phdthesis, Institut National Polytechnique de Grenoble - INPG.

Liou, K. N. (2002). *An Introduction to Atmospheric Radiation*. Elsevier. Google-Books-ID: mQ1DiDpX34UC.

Liu, X., Ahmed, S. M., Multari, R. A., James, G. K., & Ajello, J. M. (1995). High-Resolution Electron-Impact Study of the Far-Ultraviolet Emission Spectrum of Molecular Hydrogen. *The Astrophysical Journal Supplement Series*, 101, 375. Publisher: IOP ADS Bibcode: 1995ApJS..101..375L.

Lopes, R. M. C. & Williams, D. A. (2015). Chapter 43 - Volcanism on Io. In H. Sigurdsson (Ed.), *The Encyclopedia of Volcanoes (Second Edition)* (pp. 747–762). Amsterdam: Academic Press.

Masters, A., Dunn, W. R., Stallard, T. S., Manners, H., & Stawarz, J. (2021). Magnetic Reconnection Near the Planet as a Possible Driver of Jupiter's Mysterious Polar Auroras. *Journal of Geophysical Research: Space Physics*, 126(8), e2021JA029544. _eprint: https://onlinelibrary.wiley.com/doi/pdf/10.1029/2021JA029544.

Mauk, B., Haggerty, D., Paranicas, C., Clark, G., Kollmann, P., Rymer, A., Mitchell, D., Bolton, S., Levin, S., Adriani, A., et al. (2017). Juno observations of energetic charged particles over jupiter's polar regions: Analysis of monodirectional and bidirectional electron beams. *Geophysical Research Letters*, 44(10), 4410–4418.

Mauk, B. H., Clarke, J. T., Grodent, D., Waite, J. H., Paranicas, C. P., & Williams, D. J. (2002). Transient aurora on Jupiter from injections of magnetospheric electrons. *Nature*, 415(6875), 1003–1005. Publisher: Nature Publishing Group.

Mauk, B. H., Haggerty, D. K., Paranicas, C., Clark, G., Kollmann, P., Rymer, A. M., Peachey, J. M., Bolton, S. J., Levin, S. M., Adriani, A., Allegrini, F., Bagenal, F., Bonfond, B., Connerney, J. E. P., Ebert, R. W., Gladstone, G. R., Kurth, W. S., McComas, D. J., Ranquist, D., & Valek, P. (2018). Diverse electron and ion acceleration characteristics observed over jupiter's main aurora. *Geophysical Research Letters*, 45(3), 1277–1285.

Moses, J. I., Fouchet, T., Bézard, B., Gladstone, G. R., Lellouch, E., & Feuchtgruber, H. (2005). Photochemistry and diffusion in jupiter's stratosphere: Constraints from iso observations and comparisons with other giant planets. *Journal of Geophysical Research: Planets*, 110(E8).

Parkinson, C., Koskinen, T., & Esposito, L. (2019). Monitoring saturn's upper atmosphere density variations and he mixing ratio using cassini helium 584 å airglow observations. 2019, EPSC–DPS2019.

Russell, C. T. (1993). Planetary magnetospheres. *Reports on Progress in Physics*, 56(6), 687.

Rutherfurd, L. M. (1863). Astronomical observations with spectroscope. *American journal of science*, 2(103), 71–77.

Salveter, A., Saur, J., Clark, G., & Mauk, B. H. (2022). Jovian Auroral Electron Precipitation Budget—A Statistical Analysis of Diffuse, Mono-Energetic, and Broadband Auroral Electron Distributions. *Journal of Geophysical Research: Space Physics*, 127(8), e2021JA030224. _eprint: https://onlinelibrary.wiley.com/doi/pdf/10.1029/2021JA030224.

Saur, J., Janser, S., Schreiner, A., Clark, G., Mauk, B. H., Kollmann, P., Ebert, R. W., Allegrini, F., Szalay, J. R., & Kotsiaros, S. (2018). Wave-Particle Interaction of Alfvén Waves in Jupiter's Magnetosphere: Auroral and Magnetospheric Particle Acceleration. *Journal of Geophysical Research: Space Physics*, 123(11), 9560–9573. _eprint: https://onlinelibrary.wiley.com/doi/pdf/10.1029/2018JA025948.

Saur, J., Pouquet, A., & Matthaeus, W. H. (2003). An acceleration mechanism for the generation of the main auroral oval on jupiter. *Geophysical Research Letters*, 30(5).

Schreier, R., Eviatar, A., Vasyliūnas, V. M., & Richardson, J. D. (1993). Modeling the Europa plasma torus. *Journal of Geophysical Research: Space Physics*, 98(A12), 21231–21243. _eprint: https://onlinelibrary.wiley.com/doi/pdf/10.1029/93JA02585.

Sinclair, J. A., Greathouse, T. K., Giles, R. S., Antuñano, A., Moses, J. I., Fouchet, T., Bézard, B., Tao, C., Martín-Torres, J., Clark, G. B., Grodent, D., Orton, G. S., Hue, V., Fletcher, L. N., & Irwin, P. G. J. (2020). Spatial Variations in the Altitude of the CH4 Homopause at Jupiter's Mid-to-high Latitudes, as Constrained from IRTF-TEXES Spectra. *The Planetary Science Journal*, 1(3), 85. Publisher: IOP Publishing.

Uno, T., Kasaba, Y., Tao, C., Sakanoi, T., Kagitani, M., Fujisawa, S., Kita, H., & Badman, S. V. (2014). Vertical emissivity profiles of jupiter's northern h3+ and h2 infrared auroras observed by subaru/ircs. *Journal of Geophysical Research: Space Physics*, 119(12), 10,219–10,241.

Vasavada, A. R., Bouchez, A. H., Ingersoll, A. P., Little, B., & Anger, C. D. (1999). Jupiter's visible aurora and io footprint. *Journal of Geophysical Research: Planets*, 104(E11), 27133–27142.

Yung, Y. L., Gladstone, G. R., Chang, K. M., Ajello, J. M., & Srivastava, S. (1982). H2 fluorescence spectrum from 1200 to 1700 a by electron impact-laboratory study and application to jovian aurora. *Astrophysical Journal, Part 2-Letters to the Editor, vol. 254, Mar. 15, 1982, p. L65-L69.*, 254, L65–L69.

Zarka, P. (1998). Auroral radio emissions at the outer planets: Observations and theories. *Journal of Geophysical Research: Planets*, 103(E9), 20159–20194.

Zhang, B., Delamere, P. A., Yao, Z., Bonfond, B., Lin, D., Sorathia, K. A., Brambles, O. J., Lotko, W., Garretson, J. S., Merkin, V. G., Grodent, D., Dunn, W. R., & Lyon, J. G. (2021). How Jupiter's unusual magnetospheric topology structures its aurora. *Science Advances*, 7(15), eabd1204. Publisher: American Association for the Advancement of Science.

A

Maps

In this annex, we display all the maps of H_2 brightness, CH_4 and C_2H_2 color ratio and electron energy computed in section 2 for the northern and southern auroral regions.

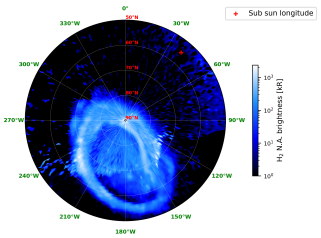

PJ1 North brightness map

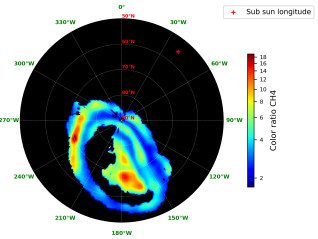

PJ1 North CR map for CH_4

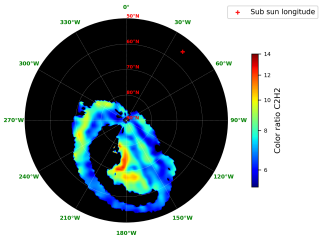

PJ1 North CR map for C_2H_2

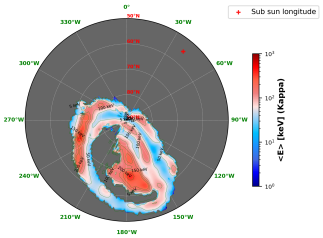

PJ1 North Mean energy map for electrons with a kappa distribution

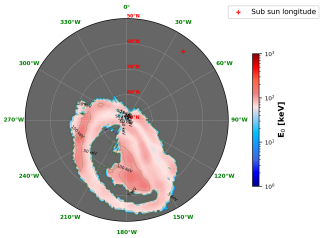

PJ1 North Characteristic energy map for electrons with a monoenergetic distribution

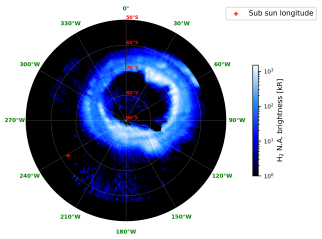

PJ1 South brightness map

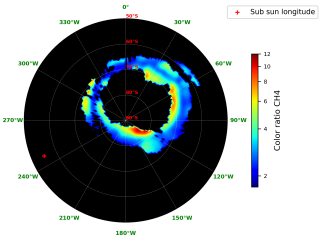

PJ1 South CR map for CH_4

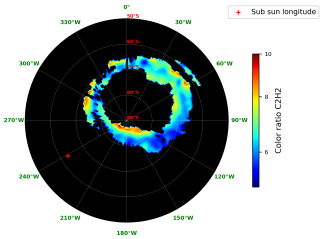

PJ1 South CR map for C_2H_2

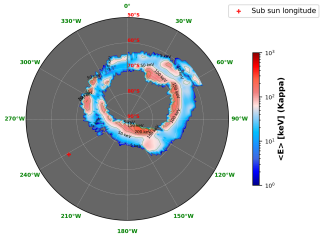

PJ1 South Mean energy map for electrons with a kappa distribution

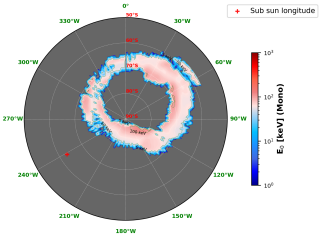

PJ1 South Characteristic energy map for electrons with a monoenergetic distribution

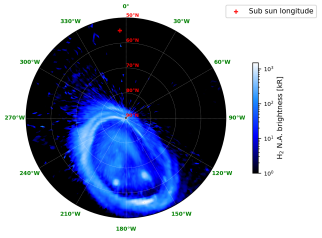

PJ3 North brightness map

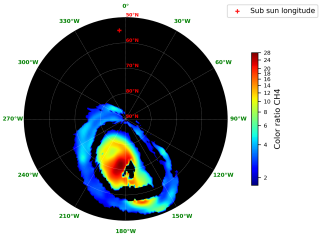

PJ3 North CR map for CH_4

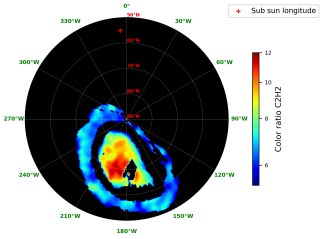

PJ3 North CR map for C_2H_2

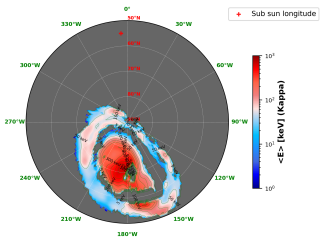

PJ3 North Mean energy map for electrons with a kappa distribution

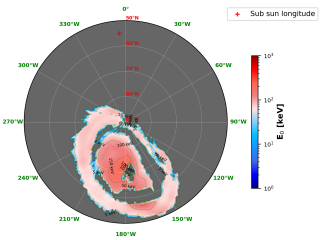

PJ3 North Characteristic energy map for electrons with a monoenergetic

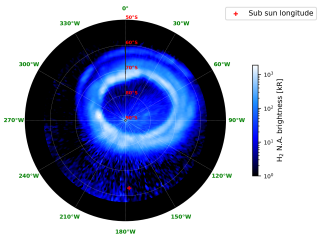

PJ3 South brightness map

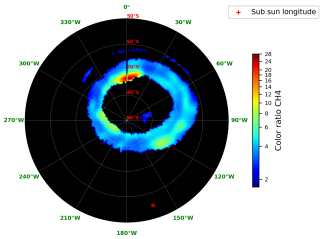

PJ3 South CR map for CH_4

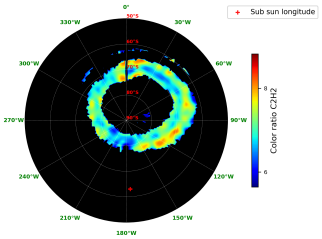

PJ3 South CR map for C_2H_2

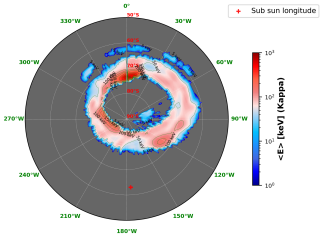

PJ3 South Mean energy map for electrons with a kappa distribution

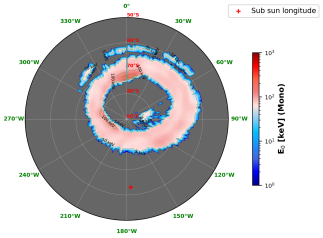

PJ3 South Characteristic energy map for electrons with a monoenergetic distribution

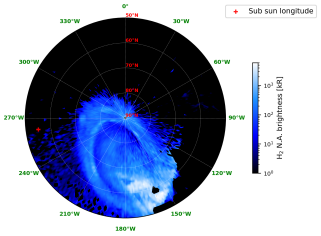

PJ4 North brightness map

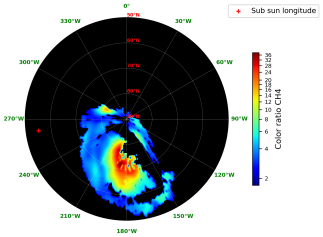

PJ4 North CR map for CH_4

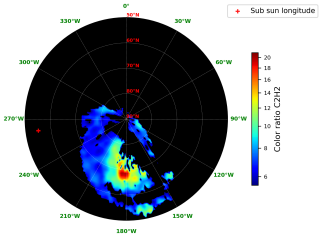

PJ4 North CR map for C_2H_2

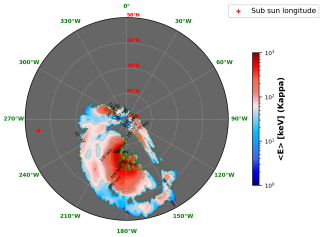

PJ4 North Mean energy map for electrons with a kappa distribution

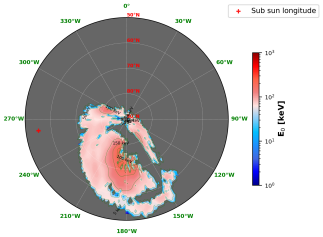

PJ4 North Characteristic energy map for electrons with a monoenergetic distribution

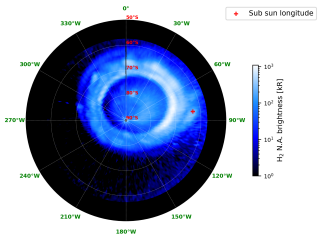

PJ4 South brightness map

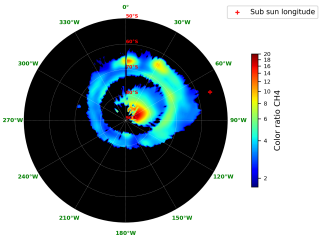

PJ4 South CR map for CH_4

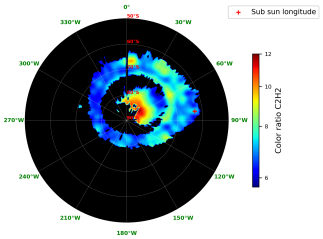

PJ4 South CR map for C_2H_2

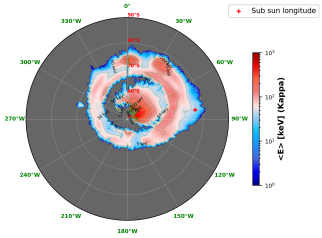

PJ4 South Mean energy map for electrons with a kappa distribution

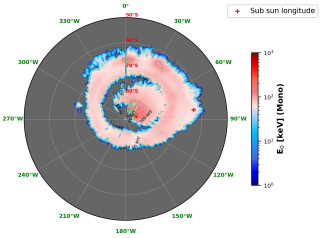

PJ4 South Characteristic energy map for electrons with a monoenergetic distribution

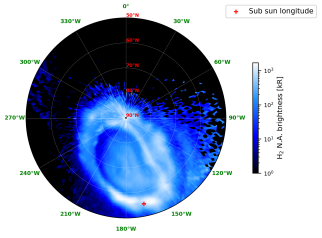

PJ5 North brightness map

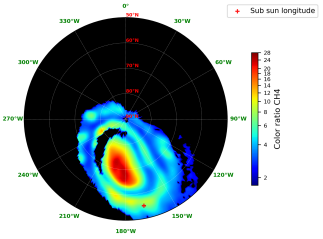

PJ5 North CR map for CH_4

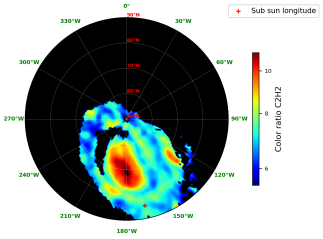

PJ5 North CR map for C_2H_2

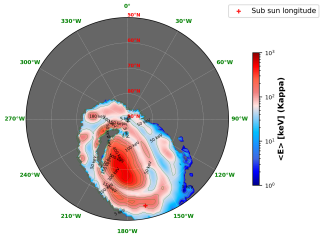

PJ5 North Mean energy map for electrons with a kappa distribution

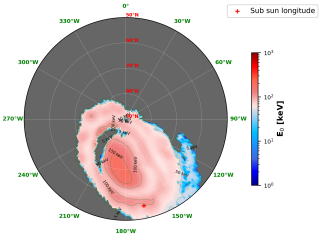

PJ5 North Characteristic energy map for electrons with a monoenergetic

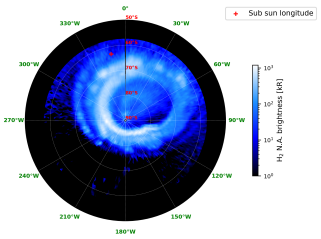

PJ5 South brightness map

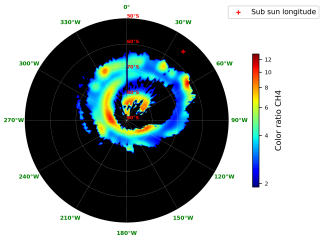

PJ5 South CR map for CH_4

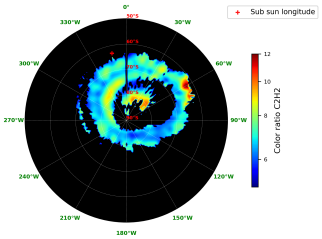

PJ5 South CR map for C_2H_2

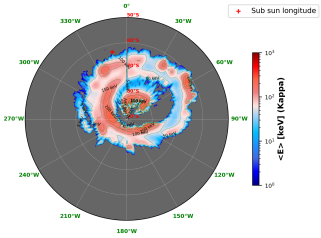

PJ5 South Mean energy map for electrons with a kappa distribution

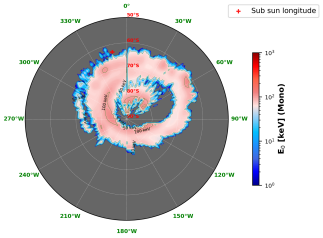

PJ5 South Characteristic energy map for electrons with a monoenergetic distribution

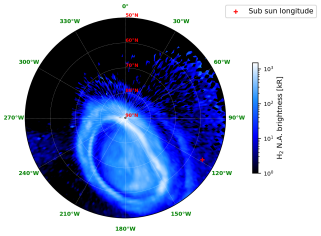

PJ6 North brightness map

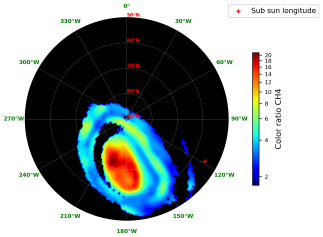

PJ6 North CR map for CH_4

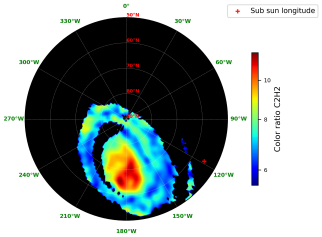

PJ6 North CR map for C_2H_2

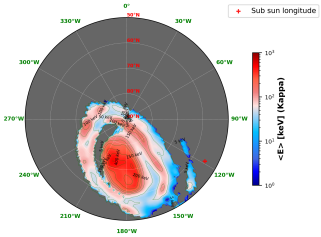

PJ6 North Mean energy map for electrons with a kappa distribution

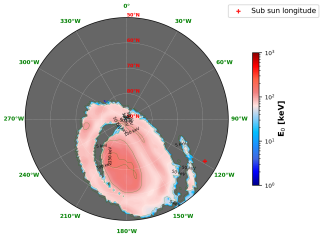

PJ6 North Characteristic energy map for electrons with a monoenergetic distribution

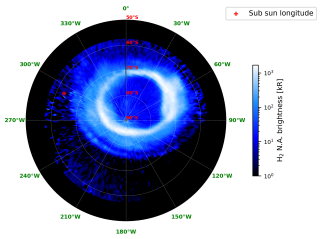

PJ6 South brightness map

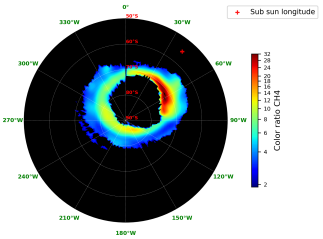

PJ6 South CR map for CH_4

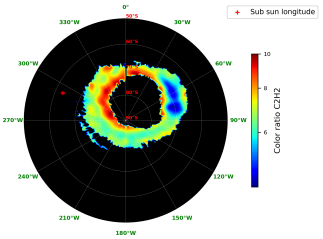

PJ6 South CR map for C_2H_2

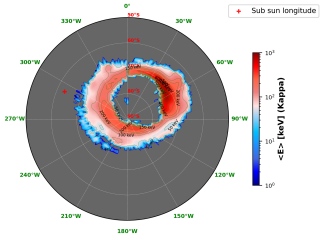

PJ6 South Mean energy map for electrons with a kappa distribution

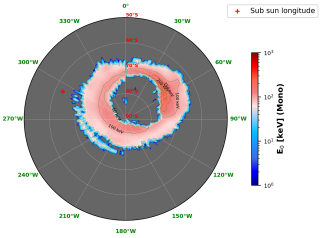

PJ6 South Characteristic energy map for electrons with a monoenergetic distribution

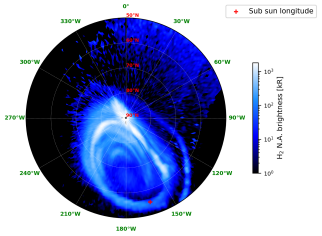

PJ7 North brightness map

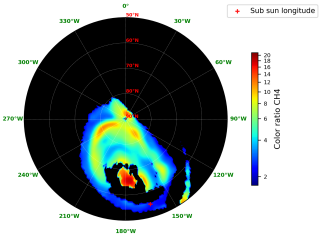

PJ7 North CR map for CH_4

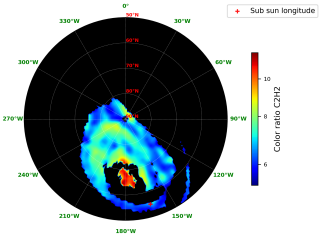

PJ7 North CR map for C_2H_2

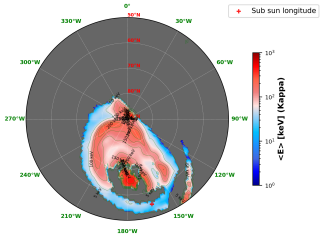

PJ7 North Mean energy map for electrons with a kappa distribution

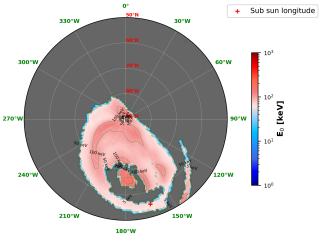

PJ7 North Characteristic energy map for electrons with a monoenergetic

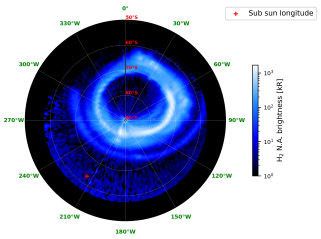

PJ7 South brightness map

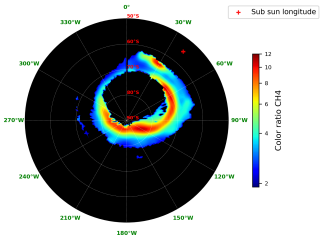

PJ7 South CR map for CH_4

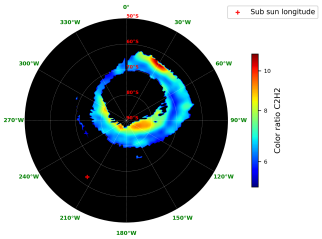

PJ7 South CR map for C_2H_2

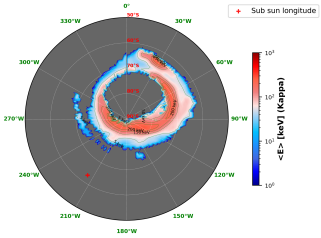

PJ7 South Mean energy map for electrons with a kappa distribution

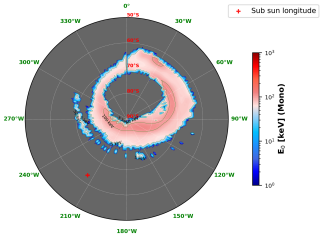

PJ7 South Characteristic energy map for electrons with a monoenergetic distribution

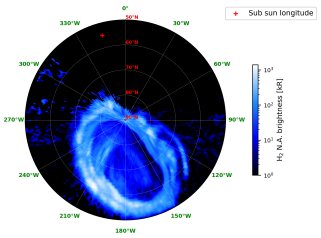

PJ8 North brightness map

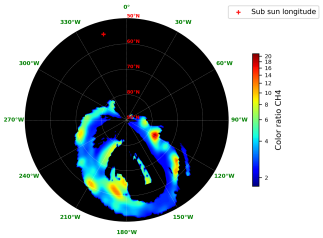

PJ8 North CR map for CH_4

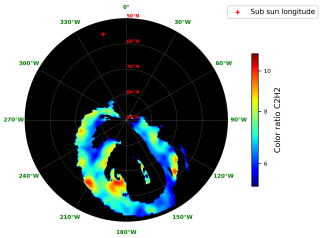

PJ8 North CR map for C_2H_2

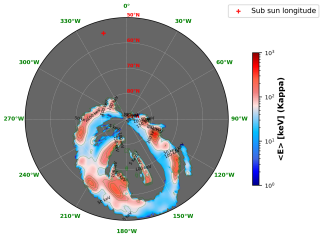

PJ8 North Mean energy map for electrons with a kappa distribution

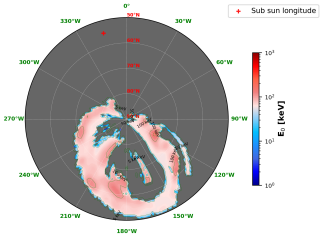

PJ8 North Characteristic energy map for electrons with a monoenergetic distribution

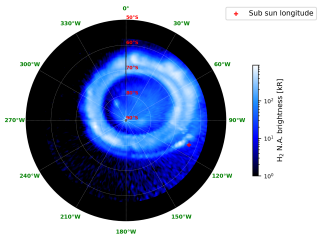

PJ8 South brightness map

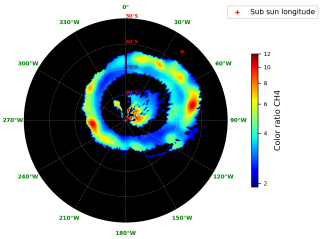

PJ8 South CR map for CH_4

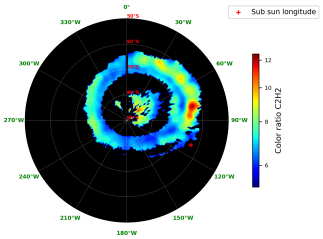

PJ8 South CR map for C_2H_2

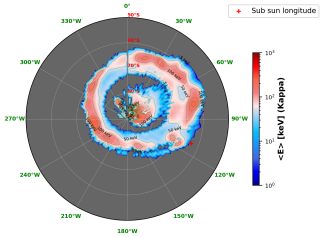

PJ8 South Mean energy map for electrons with a kappa distribution

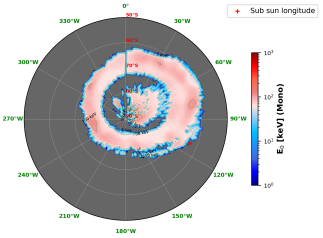

PJ8 South Characteristic energy map for electrons with a monoenergetic distribution

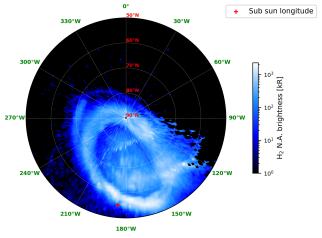

PJ9 North brightness map

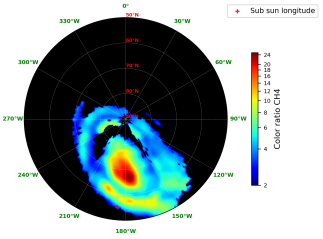

PJ9 North CR map for CH_4

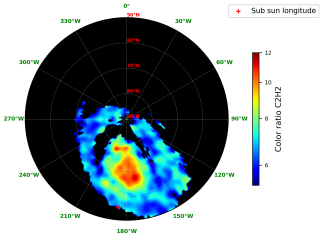

PJ9 North CR map for C_2H_2

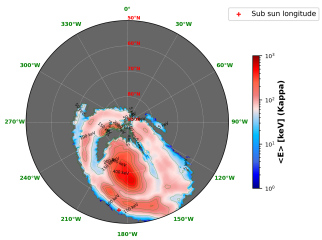

PJ9 North Mean energy map for electrons with a kappa distribution

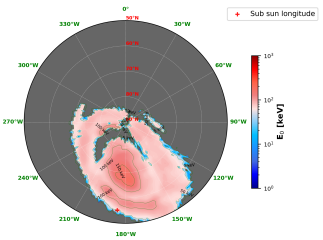

PJ9 North Characteristic energy map for electrons with a monoenergetic

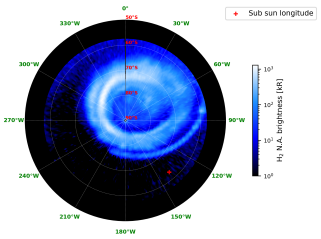

PJ9 South brightness map

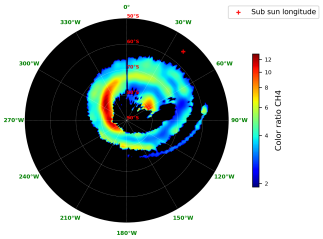

PJ9 South CR map for CH_4

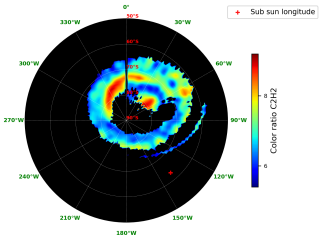

PJ9 South CR map for C_2H_2

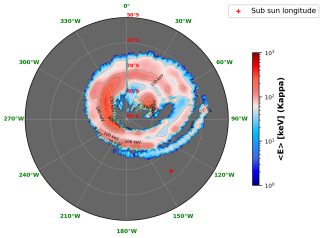

PJ9 South Mean energy map for electrons with a kappa distribution

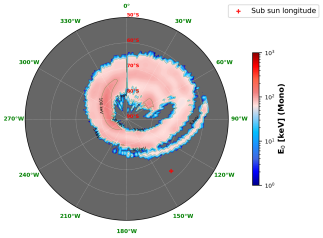

PJ9 South Characteristic energy map for electrons with a monoenergetic distribution

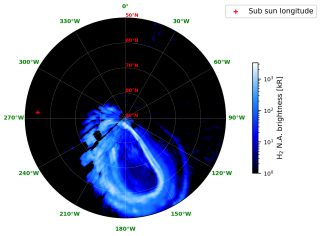

PJ10 North brightness map

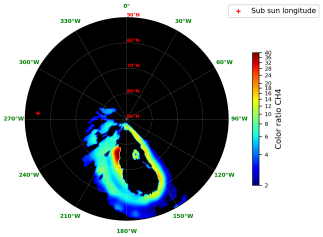

PJ10 North CR map for CH_4

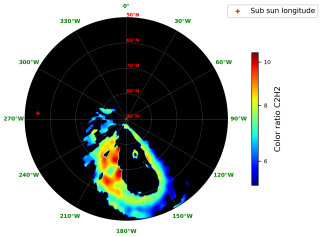

PJ10 North CR map for C_2H_2

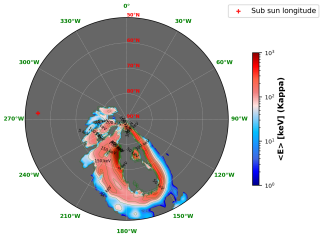

PJ10 North Mean energy map for electrons with a kappa distribution

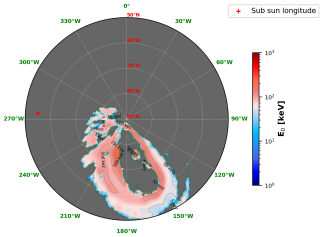

PJ10 North Characteristic energy map for electrons with a monoenergetic distribution

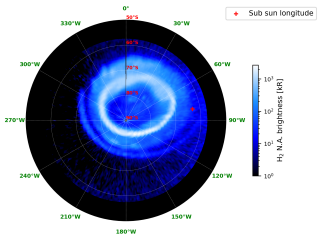

PJ10 South brightness map

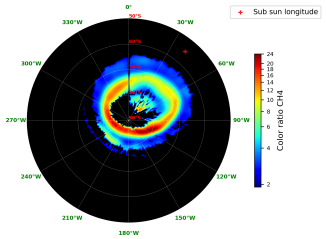

PJ10 South CR map for CH_4

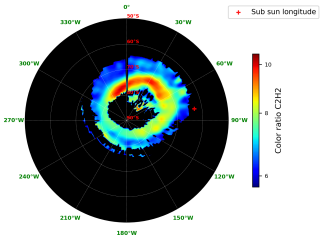

PJ10 South CR map for C_2H_2

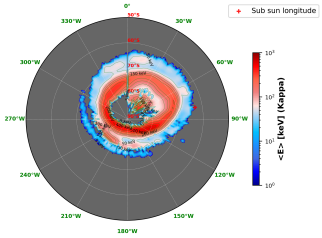

PJ10 South Mean energy map for electrons with a kappa distribution

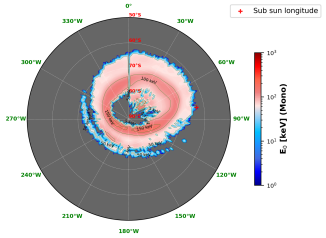

PJ10 South Characteristic energy map for electrons with a monoenergetic distribution

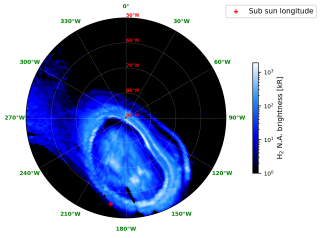

PJ11 North brightness map

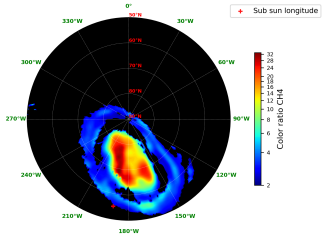

PJ11 North CR map for CH_4

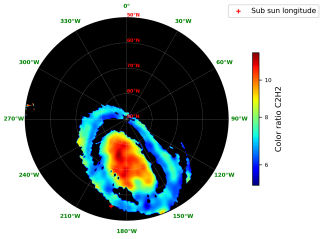

PJ11 North CR map for C_2H_2

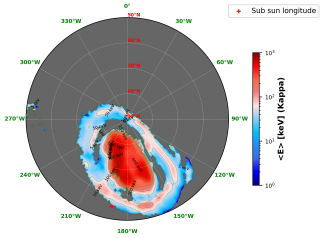

PJ11 North Mean energy map for electrons with a kappa distribution

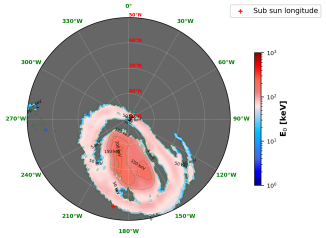

PJ11 North Characteristic energy map for electrons with a monoenergetic distribution

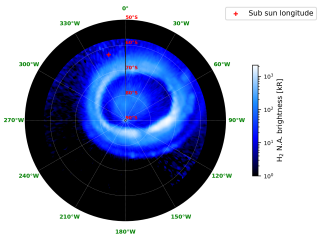

PJ11 South brightness map

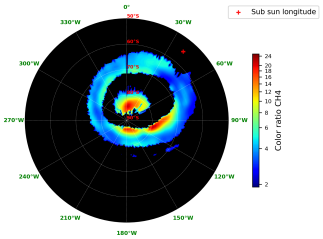

PJ11 South CR map for CH_4

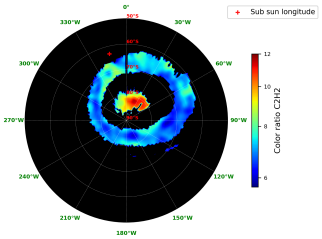

PJ11 South CR map for C_2H_2

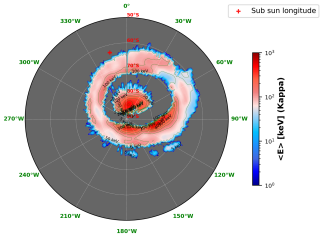

PJ11 South Mean energy map for electrons with a kappa distribution

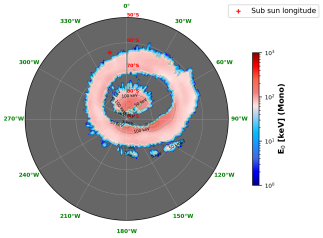

PJ11 South Characteristic energy map for electrons with a monoenergetic distribution

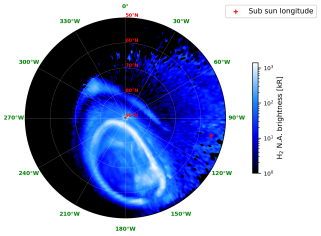

PJ12 North brightness map

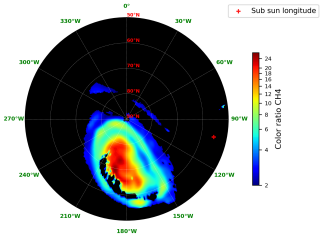

PJ12 North CR map for CH_4

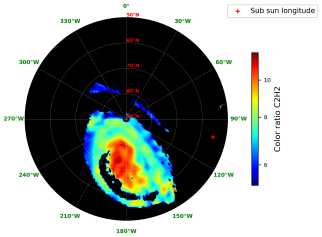

PJ12 North CR map for C_2H_2

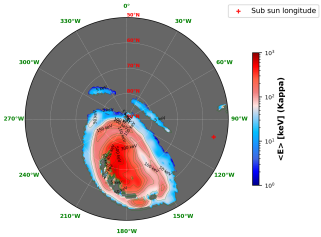

PJ12 North Mean energy map for electrons with a kappa distribution

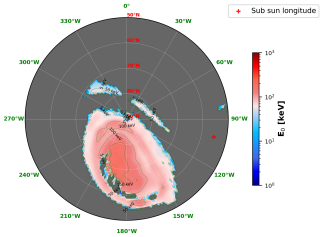

PJ12 North Characteristic energy map for electrons with a monoenergetic distribution

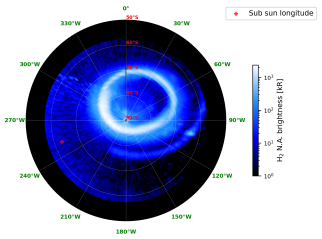

PJ12 South brightness map

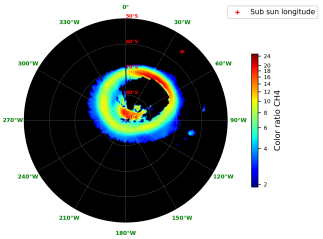

PJ12 South CR map for CH_4

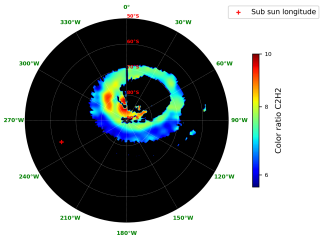

PJ12 South CR map for C_2H_2

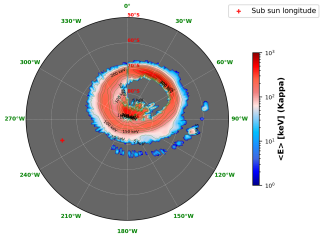

PJ12 South Mean energy map for electrons with a kappa distribution

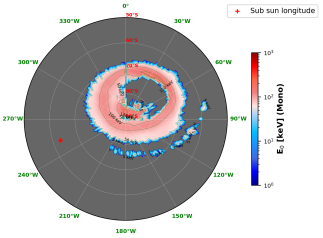

PJ12 South Characteristic energy map for electrons with a monoenergetic distribution

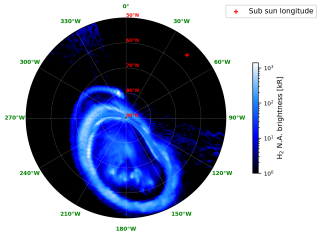

PJ13 North brightness map

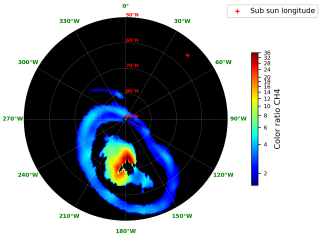

PJ13 North CR map for CH_4

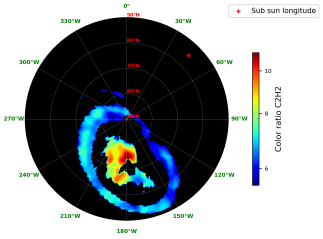

PJ13 North CR map for C_2H_2

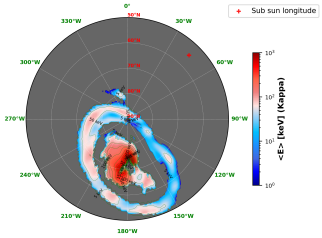

PJ13 North Mean energy map for electrons with a kappa distribution

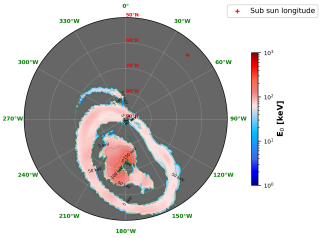

PJ13 North Characteristic energy map for electrons with a monoenergetic distribution

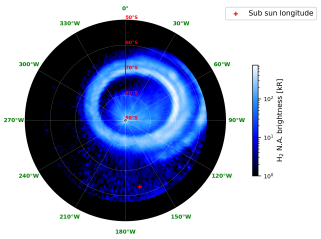

PJ13 South brightness map

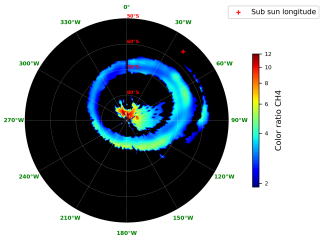

PJ13 South CR map for CH_4

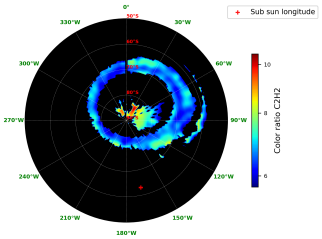

PJ13 South CR map for C_2H_2

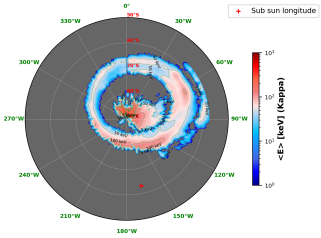

PJ13 South Mean energy map for electrons with a kappa distribution

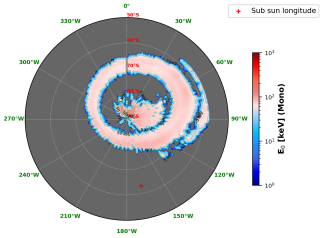

PJ13 South Characteristic energy map for electrons with a monoenergetic distribution

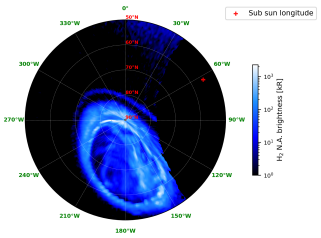

PJ14 North brightness map

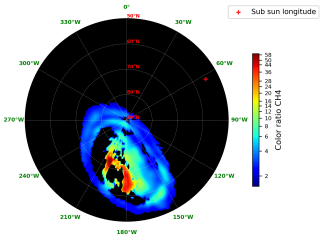

PJ14 North CR map for CH_4

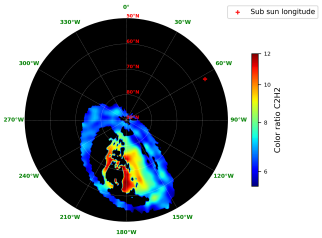

PJ14 North CR map for C_2H_2

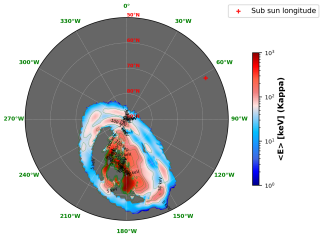

PJ14 North Mean energy map for electrons with a kappa distribution

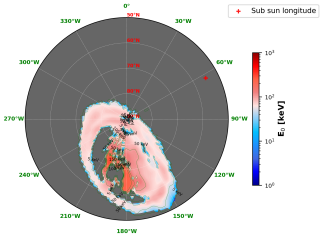

PJ14 North Characteristic energy map for electrons with a monoenergetic distribution

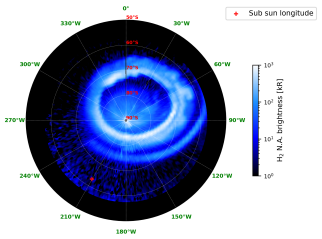

PJ14 South brightness map

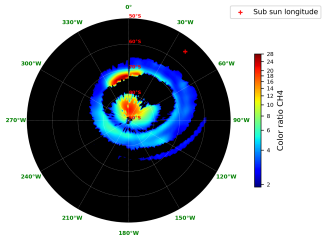

PJ14 South CR map for CH_4

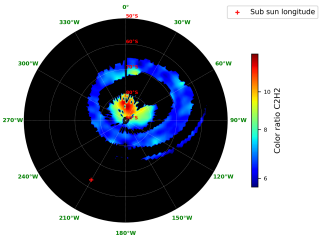

PJ14 South CR map for C_2H_2

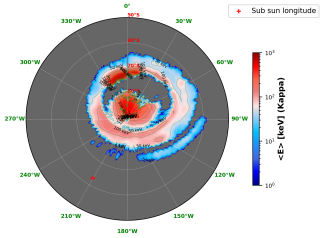

PJ14 South Mean energy map for electrons with a kappa distribution

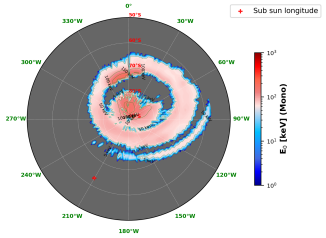

PJ14 South Characteristic energy map for electrons with a monoenergetic distribution

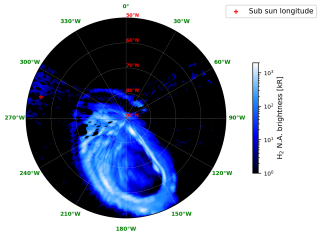

PJ15 North brightness map

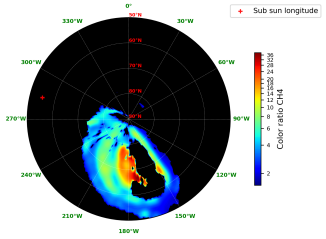

PJ15 North CR map for CH_4

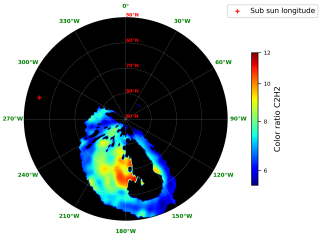

PJ15 North CR map for C_2H_2

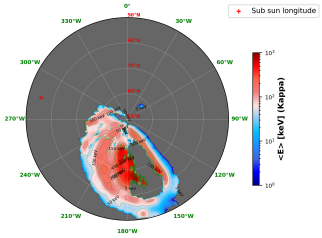

PJ15 North Mean energy map for electrons with a kappa distribution

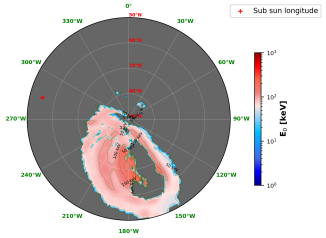

PJ15 North Characteristic energy map for electrons with a monoenergetic distribution

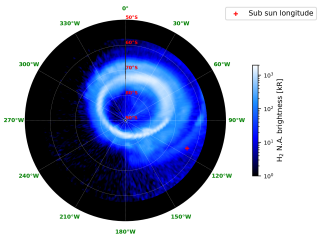

PJ15 South brightness map

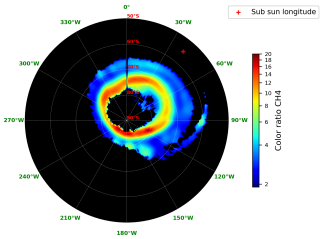

PJ15 South CR map for CH_4

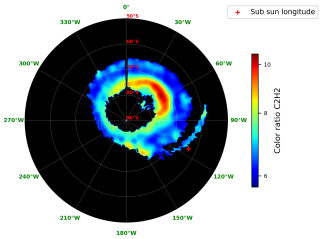

PJ15 South CR map for C_2H_2

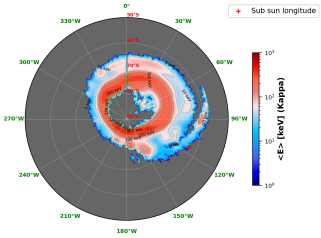

PJ15 South Mean energy map for electrons with a kappa distribution

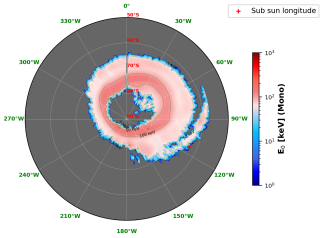

PJ15 South Characteristic energy map for electrons with a monoenergetic distribution

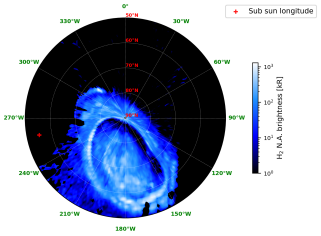

PJ16 North brightness map

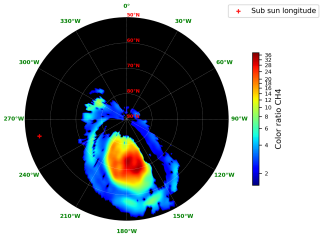

PJ16 North CR map for CH_4

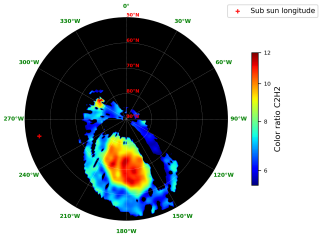

PJ16 North CR map for C_2H_2

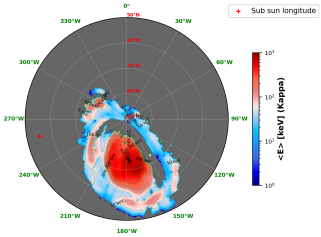

PJ16 North Mean energy map for electrons with a kappa distribution

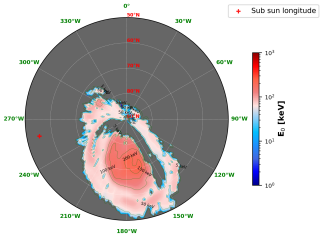

PJ16 North Characteristic energy map for electrons with a monoenergetic distribution

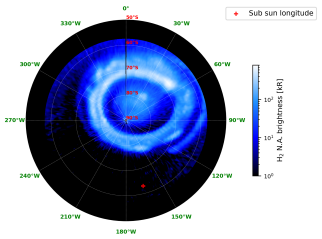

PJ16 South brightness map

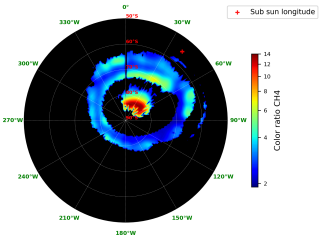

PJ16 South CR map for CH_4

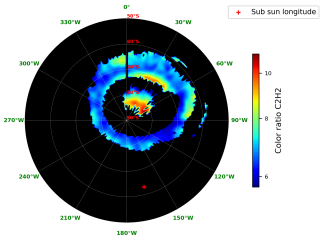

PJ16 South CR map for C_2H_2

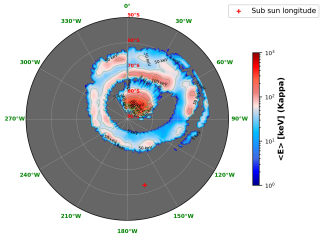

PJ16 South Mean energy map for electrons with a kappa distribution

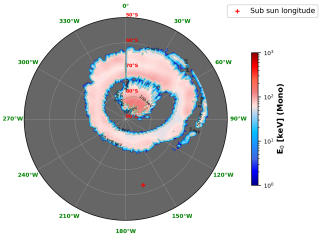

PJ16 South Characteristic energy map for electrons with a monoenergetic distribution

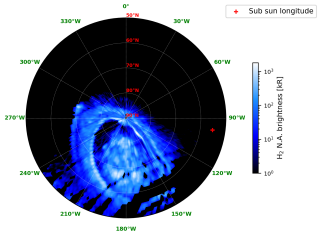

PJ17 North brightness map

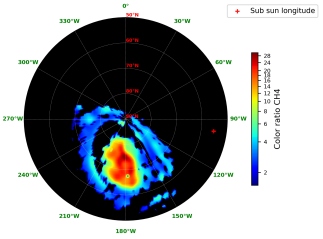

PJ17 North CR map for CH_4

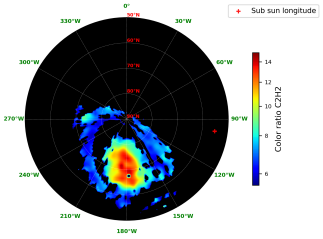

PJ17 North CR map for C_2H_2

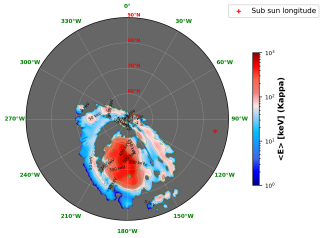

PJ17 North Mean energy map for electrons with a kappa distribution

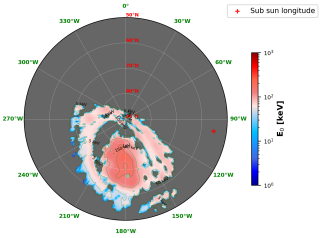

PJ17 North Characteristic energy map for electrons with a monoenergetic distribution

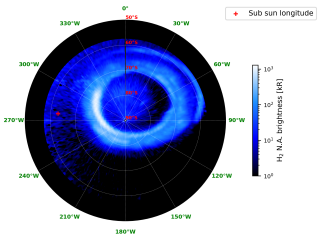

PJ17 South brightness map

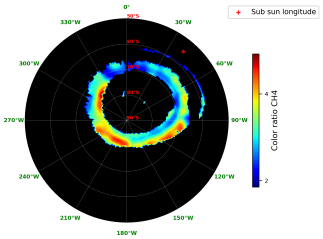

PJ17 South CR map for CH_4

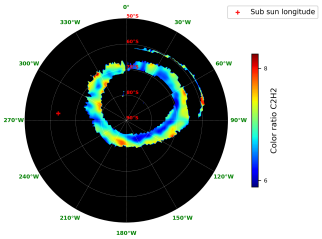

PJ17 South CR map for C_2H_2

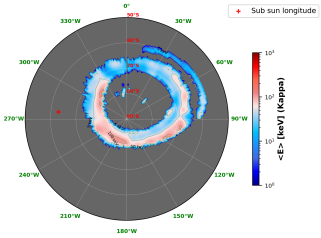

PJ17 South Mean energy map for electrons with a kappa distribution

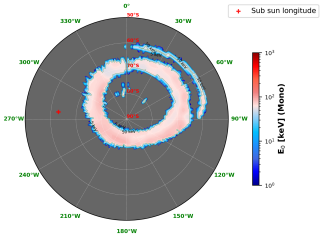

PJ17 South Characteristic energy map for electrons with a monoenergetic distribution

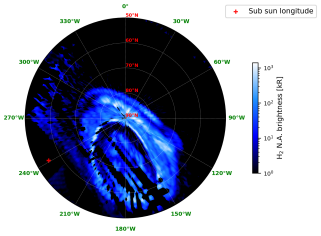

PJ18 North brightness map

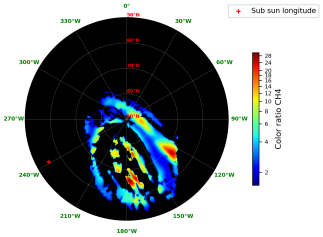

PJ18 North CR map for CH_4

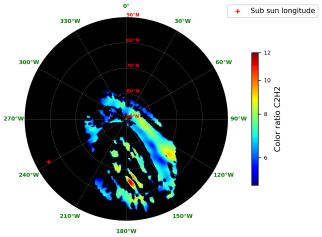

PJ18 North CR map for C_2H_2

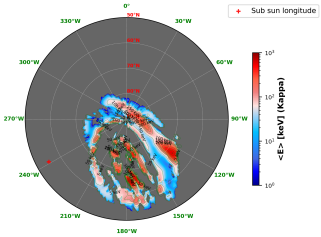

PJ18 North Mean energy map for electrons with a kappa distribution

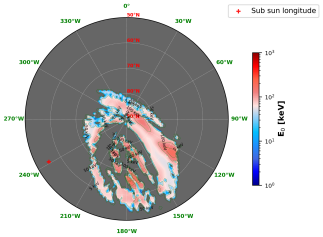

PJ18 North Characteristic energy map for electrons with a monoenergetic distribution

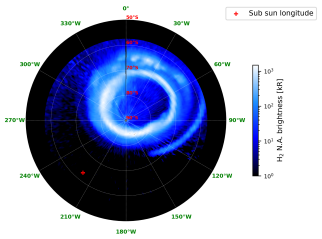

PJ18 South brightness map

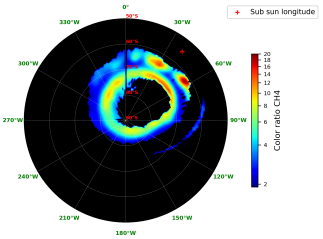

PJ18 South CR map for CH_4

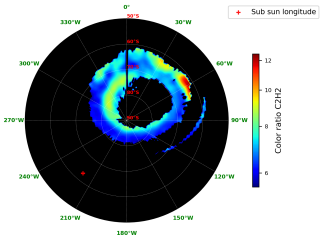

PJ18 South CR map for C_2H_2

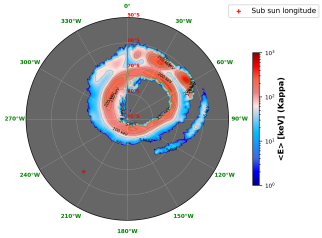

PJ18 South Mean energy map for electrons with a kappa distribution

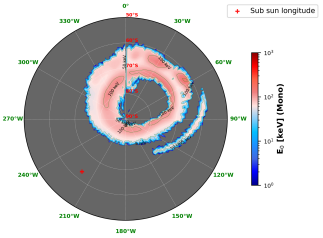

PJ18 South Characteristic energy map for electrons with a monoenergetic distribution

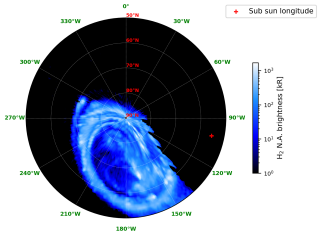

PJ19 North brightness map

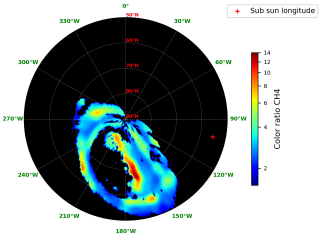

PJ19 North CR map for CH_4

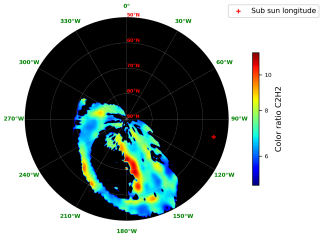

PJ19 North CR map for C_2H_2

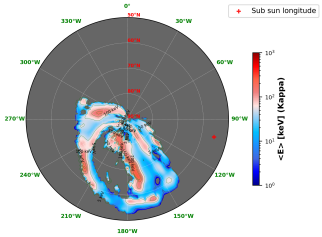

PJ19 North Mean energy map for electrons with a kappa distribution

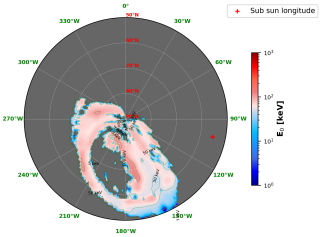

PJ19 North Characteristic energy map for electrons with a monoenergetic distribution

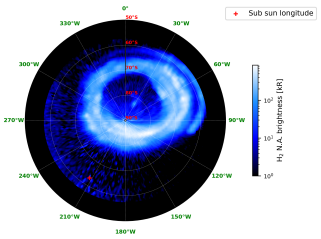

PJ19 South brightness map

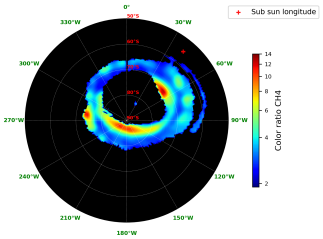

PJ19 South CR map for CH_4

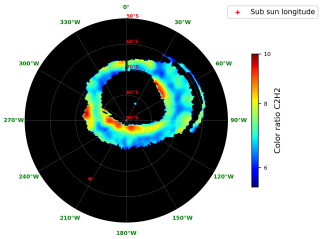

PJ19 South CR map for C_2H_2

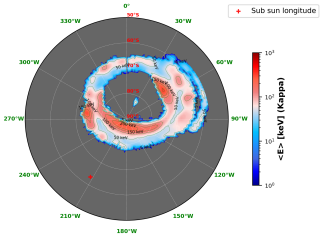

PJ19 South Mean energy map for electrons with a kappa distribution

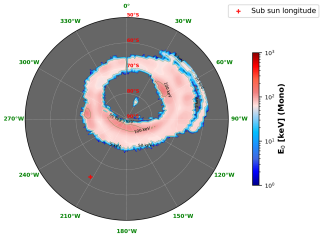

PJ19 South Characteristic energy map for electrons with a monoenergetic distribution

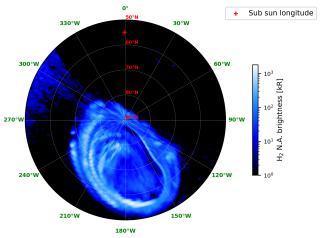

PJ20 North brightness map

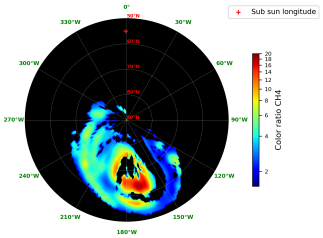

PJ20 North CR map for CH_4

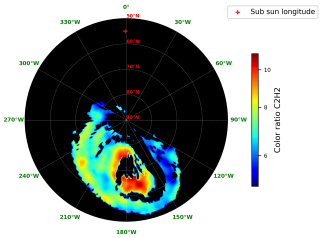

PJ20 North CR map for C_2H_2

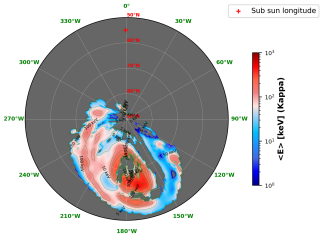

PJ20 North Mean energy map for electrons with a kappa distribution

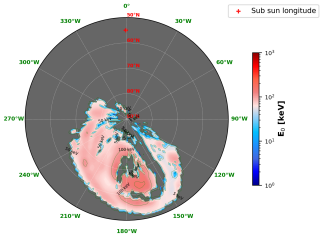

PJ20 North Characteristic energy map for electrons with a monoenergetic distribution

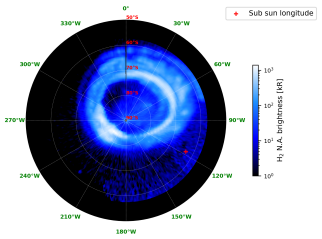

PJ20 South brightness map

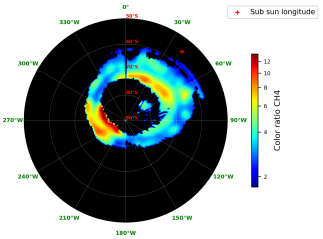

PJ20 South CR map for CH_4

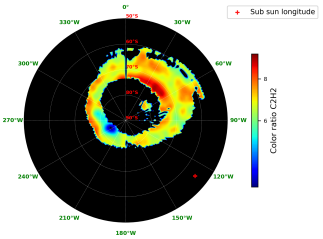

PJ20 South CR map for C_2H_2

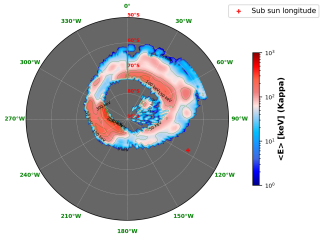

PJ20 South Mean energy map for electrons with a kappa distribution

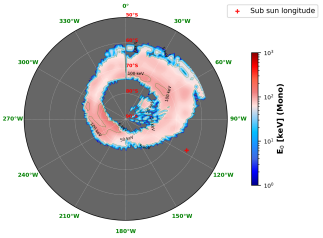

PJ20 South Characteristic energy map for electrons with a monoenergetic distribution

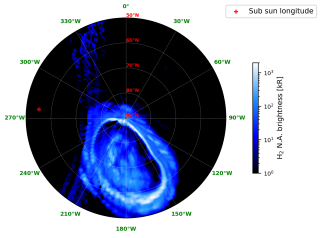

PJ21 North brightness map

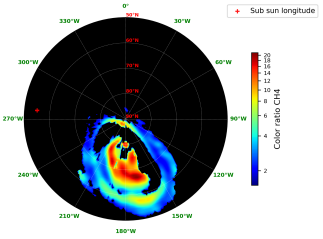

PJ21 North CR map for CH_4

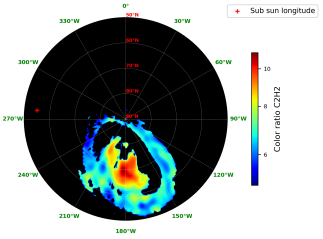

PJ21 North CR map for C_2H_2

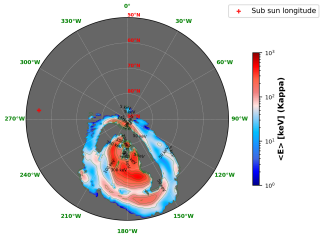

PJ21 North Mean energy map for electrons with a kappa distribution

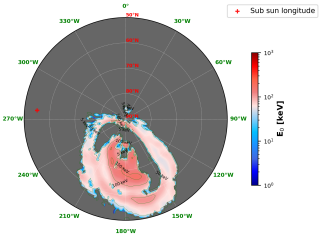

PJ21 North Characteristic energy map for electrons with a monoenergetic distribution

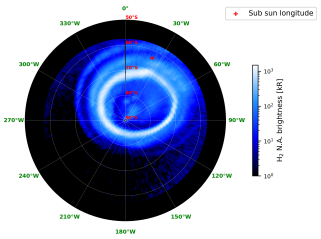

PJ21 South brightness map

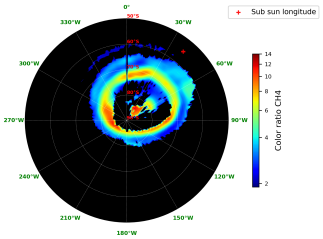

PJ21 South CR map for CH_4

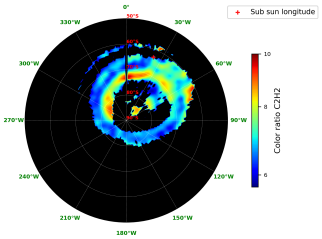

PJ21 South CR map for C_2H_2

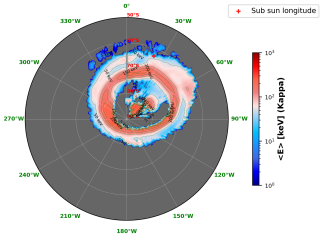

PJ21 South Mean energy map for electrons with a kappa distribution

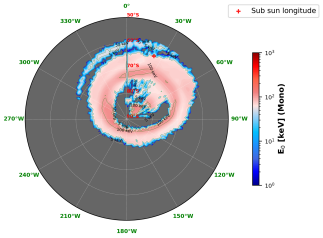

PJ21 South Characteristic energy map for electrons with a monoenergetic distribution

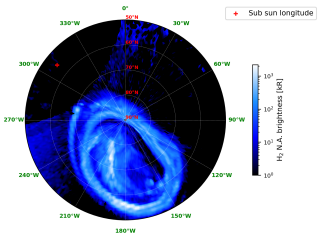

PJ22 North brightness map

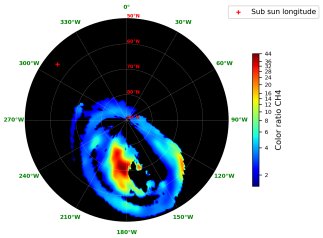

PJ22 North CR map for CH_4

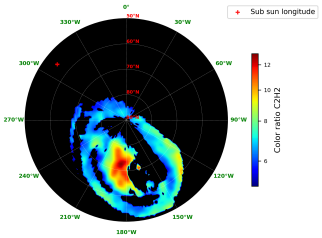

PJ22 North CR map for C_2H_2

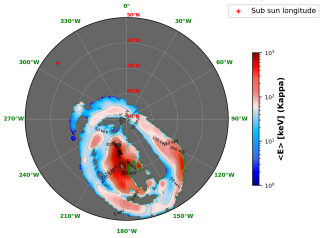

PJ22 North Mean energy map for electrons with a kappa distribution

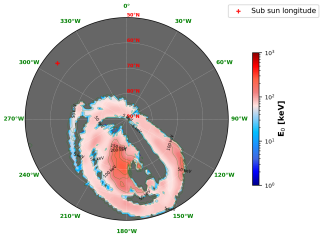

PJ22 North Characteristic energy map for electrons with a monoenergetic distribution

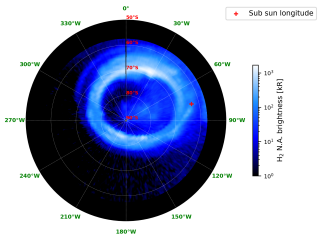

PJ22 South brightness map

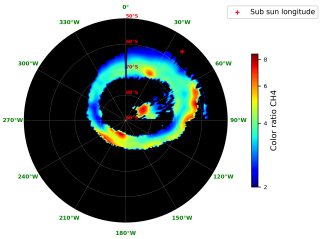

PJ22 South CR map for CH_4

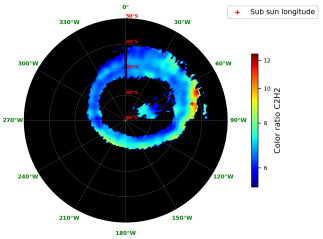

PJ22 South CR map for C_2H_2

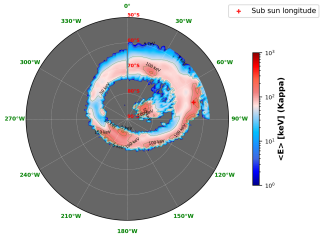

PJ22 South Mean energy map for electrons with a kappa distribution

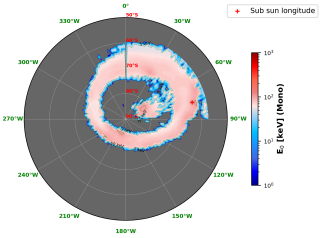

PJ22 South Characteristic energy map for electrons with a monoenergetic distribution

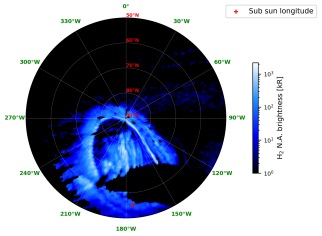

PJ23 North brightness map

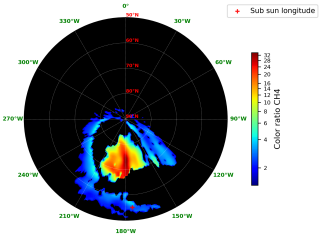

PJ23 North CR map for CH_4

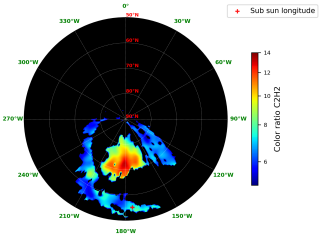

PJ23 North CR map for C_2H_2

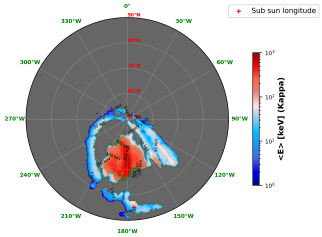

PJ23 North Mean energy map for electrons with a kappa distribution

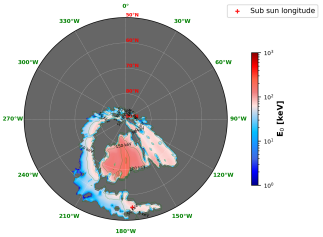

PJ23 North Characteristic energy map for electrons with a monoenergetic distribution

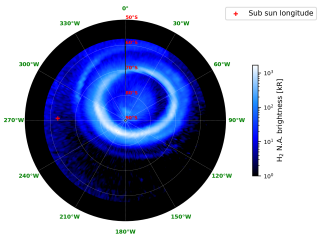

PJ23 South brightness map

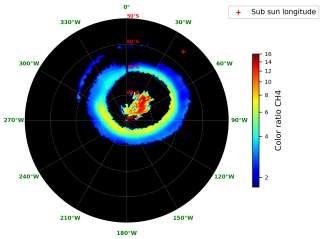

PJ23 South CR map for CH_4

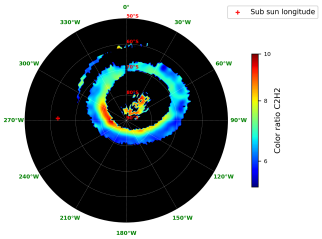

PJ23 South CR map for C_2H_2

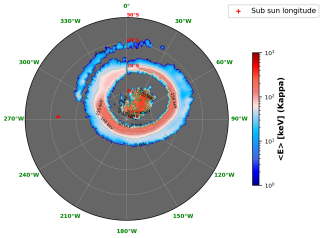

PJ23 South Mean energy map for electrons with a kappa distribution

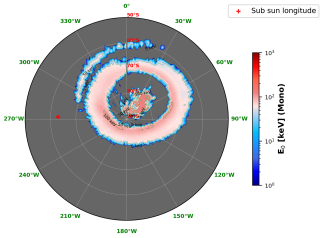

PJ23 South Characteristic energy map for electrons with a monoenergetic distribution

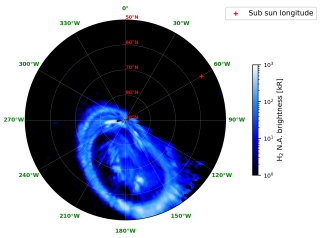

PJ24 North brightness map

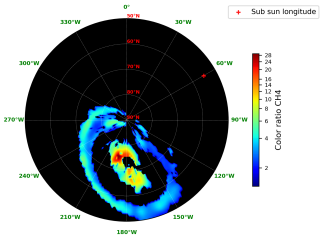

PJ24 North CR map for CH_4

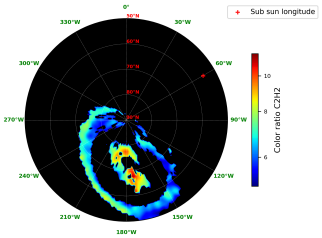

PJ24 North CR map for C_2H_2

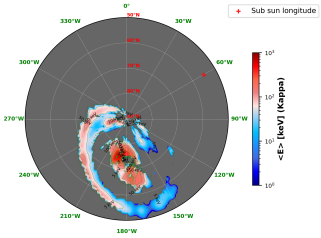

PJ24 North Mean energy map for electrons with a kappa distribution

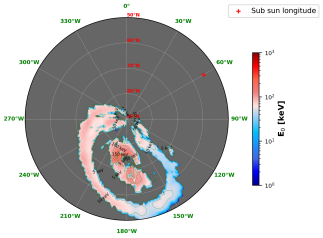

PJ24 North Characteristic energy map for electrons with a monoenergetic distribution

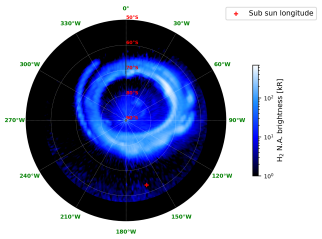

PJ24 South brightness map

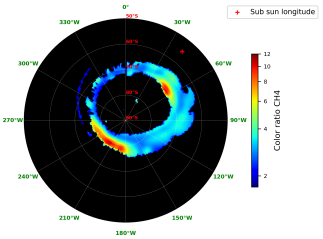

PJ24 South CR map for CH_4

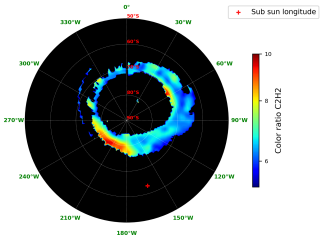

PJ24 South CR map for C_2H_2

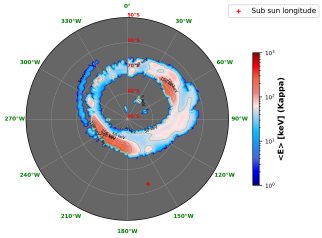

PJ24 South Mean energy map for electrons with a kappa distribution

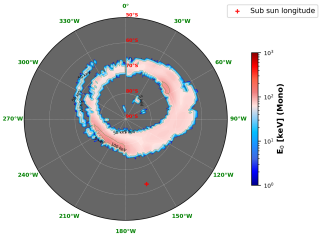

PJ24 South Characteristic energy map for electrons with a monoenergetic distribution

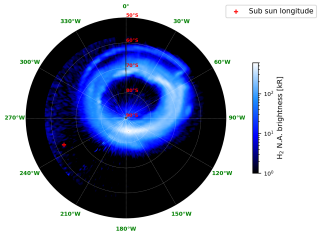

PJ25 South brightness map

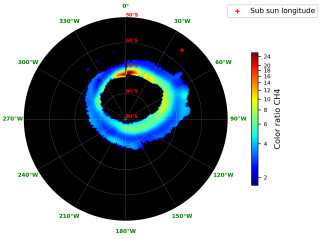

PJ25 South CR map for CH_4

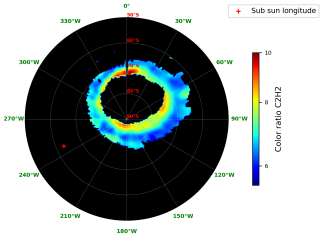

PJ25 South CR map for C_2H_2

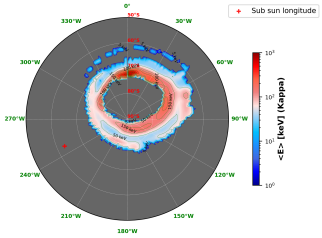

PJ25 South Mean energy map for electrons with a kappa distribution

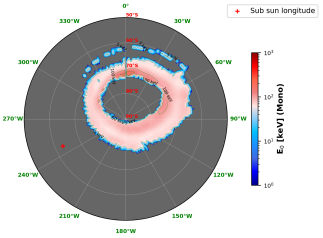

PJ25 South Characteristic energy map for electrons with a monoenergetic distribution

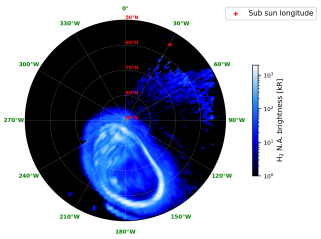

PJ26 North brightness map

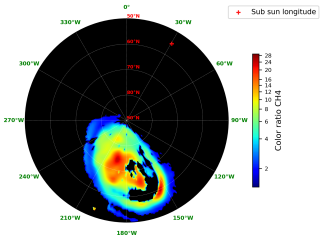

PJ26 North CR map for CH_4

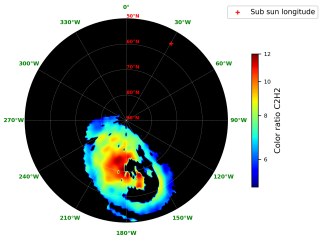

PJ26 North CR map for C_2H_2

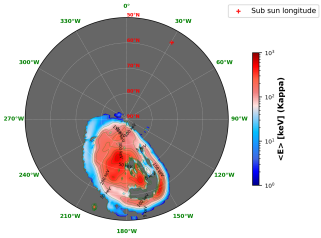

PJ26 North Mean energy map for electrons with a kappa distribution

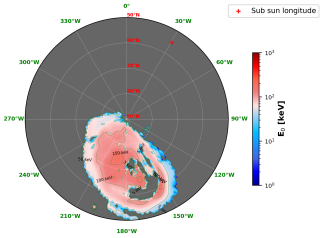

PJ26 North Characteristic energy map for electrons with a monoenergetic distribution

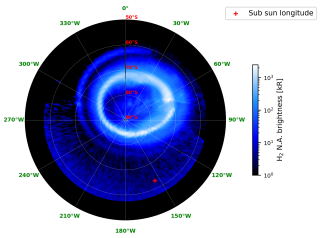

PJ26 South brightness map

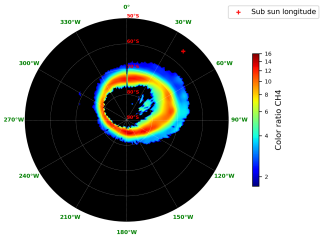

PJ26 South CR map for CH_4

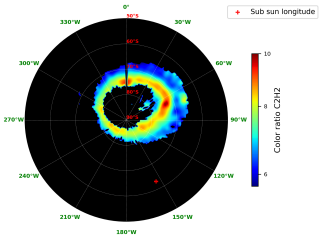

PJ26 South CR map for C_2H_2

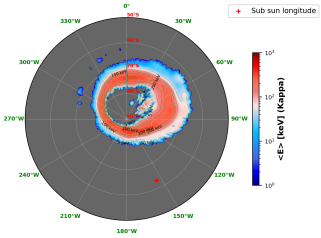

PJ26 South Mean energy map for electrons with a kappa distribution

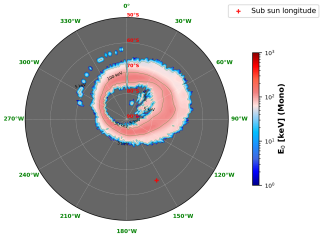

PJ26 South Characteristic energy map for electrons with a monoenergetic distribution

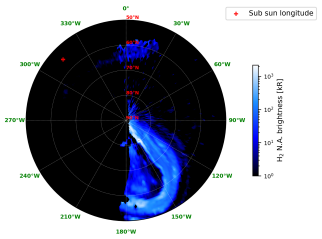

PJ27 North brightness map

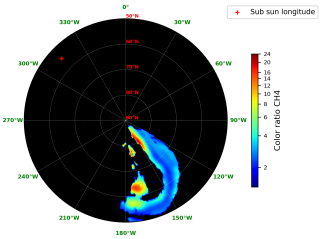

PJ27 North CR map for CH_4

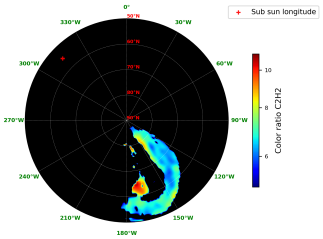

PJ27 North CR map for C_2H_2

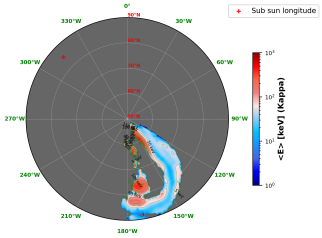

PJ27 North Mean energy map for electrons with a kappa distribution

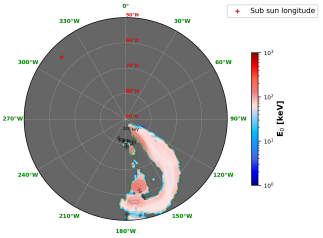

PJ27 North Characteristic energy map for electrons with a monoenergetic distribution

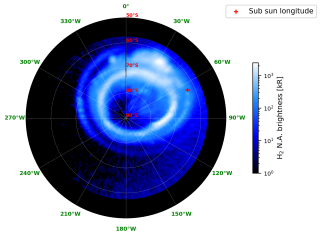

PJ27 South brightness map

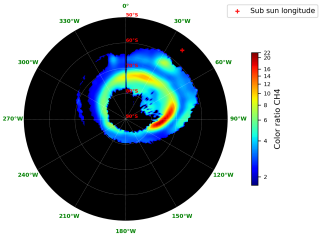

PJ27 South CR map for CH_4

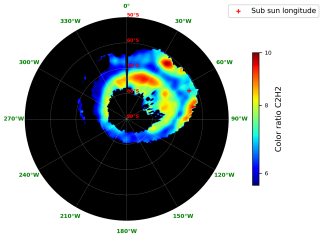

PJ27 South CR map for C_2H_2

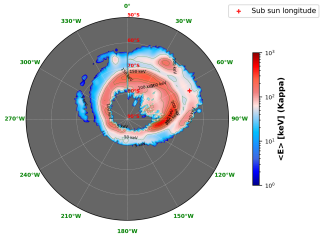

PJ27 South Mean energy map for electrons with a kappa distribution

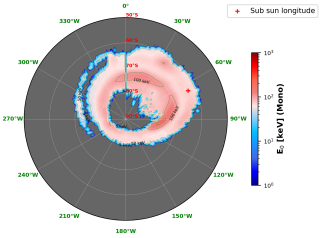

PJ27 South Characteristic energy map for electrons with a monoenergetic distribution

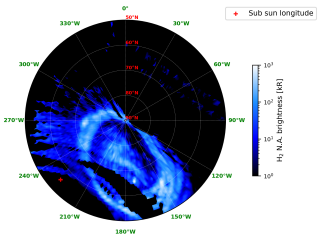

PJ28 North brightness map

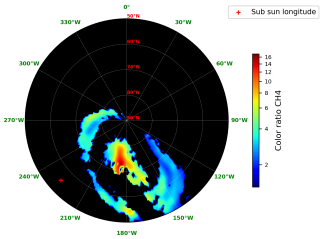

PJ28 North CR map for CH_4

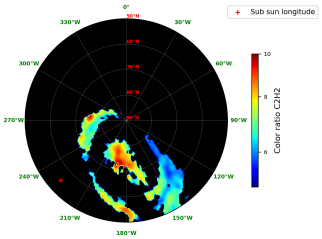

PJ28 North CR map for C_2H_2

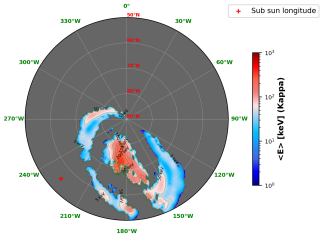

PJ28 North Mean energy map for electrons with a kappa distribution

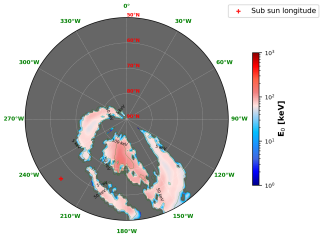

PJ28 North Characteristic energy map for electrons with a monoenergetic distribution

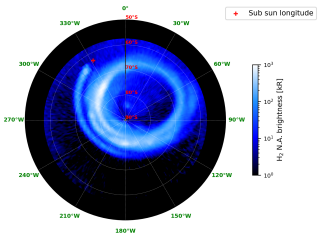

PJ28 South brightness map

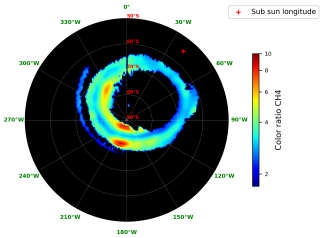

PJ28 South CR map for CH_4

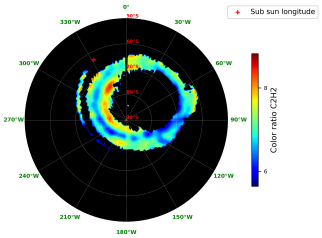

PJ28 South CR map for C_2H_2

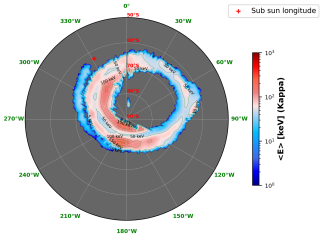

PJ28 South Mean energy map for electrons with a kappa distribution

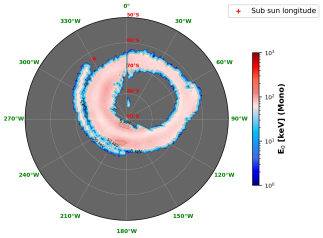

PJ28 South Characteristic energy map for electrons with a monoenergetic distribution

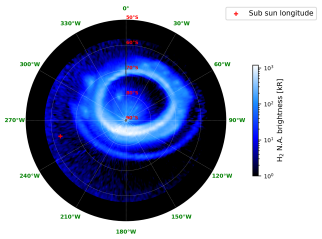

PJ29 South brightness map

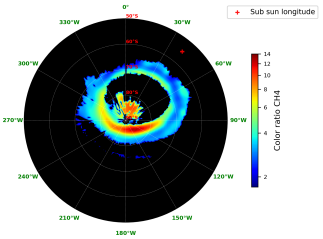

PJ29 South CR map for CH_4

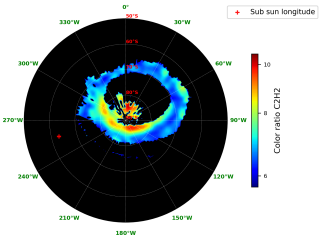

PJ29 South CR map for C_2H_2

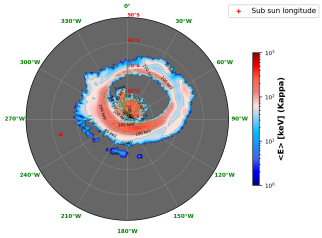

PJ29 South Mean energy map for electrons with a kappa distribution

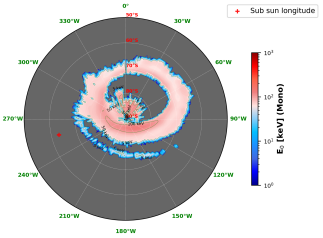

PJ29 South Characteristic energy map for electrons with a monoenergetic distribution

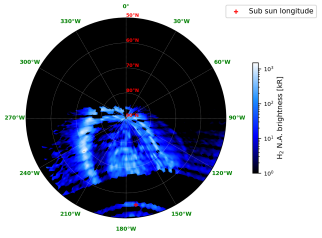

PJ30 North brightness map

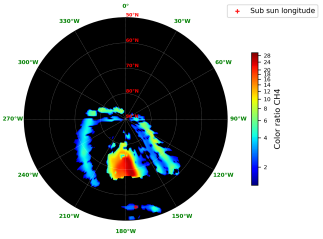

PJ30 North CR map for CH_4

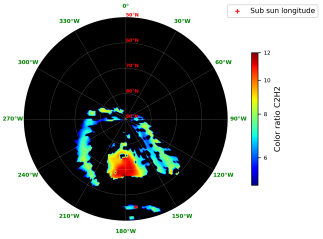

PJ30 North CR map for C_2H_2

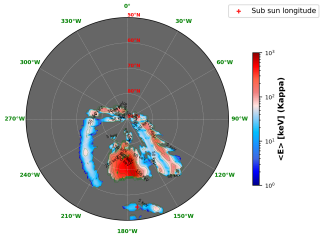

PJ30 North Mean energy map for electrons with a kappa distribution

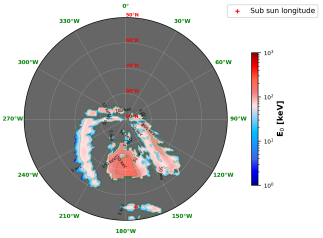

PJ30 North Characteristic energy map for electrons with a monoenergetic distribution

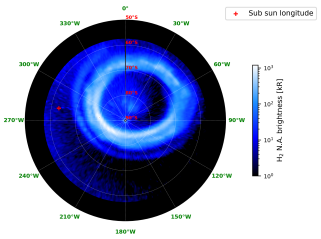

PJ30 South brightness map

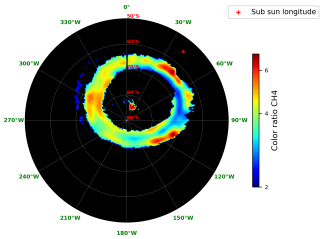

PJ30 South CR map for CH_4

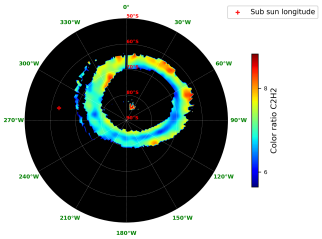

PJ30 South CR map for C_2H_2

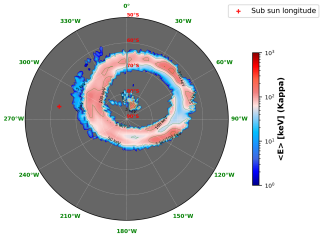

PJ30 South Mean energy map for electrons with a kappa distribution

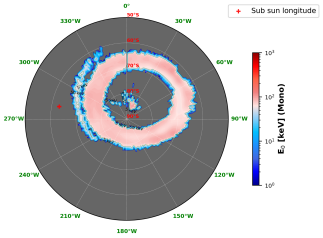

PJ30 South Characteristic energy map for electrons with a monoenergetic distribution

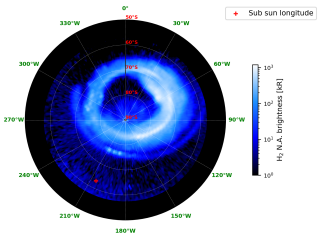

PJ31 South brightness map

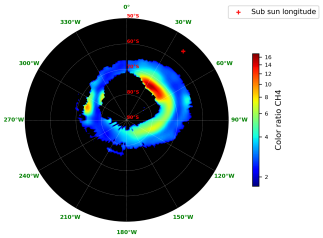

PJ31 South CR map for CH_4

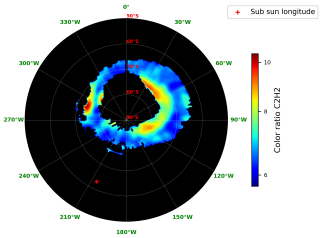

PJ31 South CR map for C_2H_2

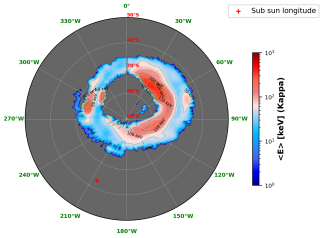

PJ31 South Mean energy map for electrons with a kappa distribution

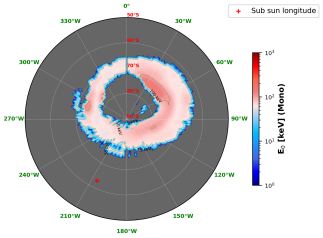

PJ31 South Characteristic energy map for electrons with a monoenergetic distribution

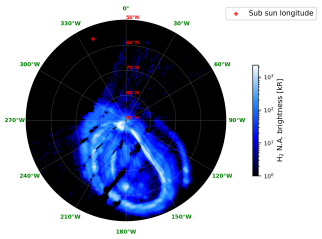

PJ32 North brightness map

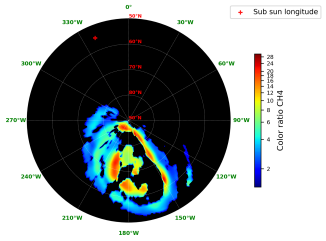

PJ32 North CR map for CH_4

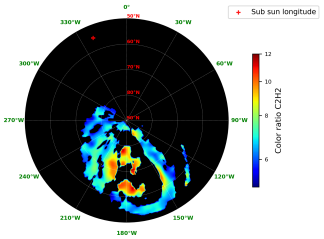

PJ32 North CR map for C_2H_2

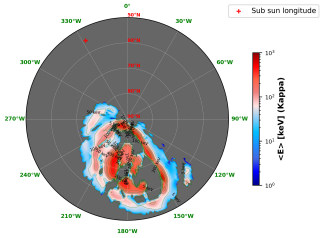

PJ32 North Mean energy map for electrons with a kappa distribution

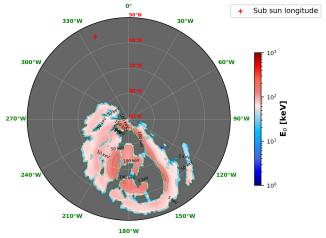

PJ32 North Characteristic energy map for electrons with a monoenergetic distribution

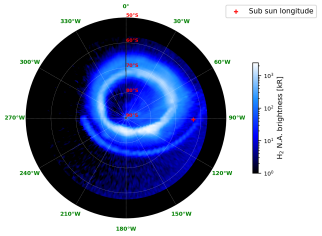

PJ32 South brightness map

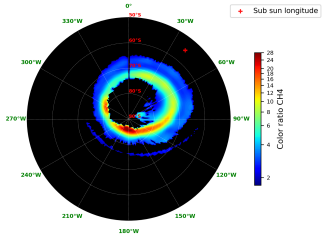

PJ32 South CR map for CH_4

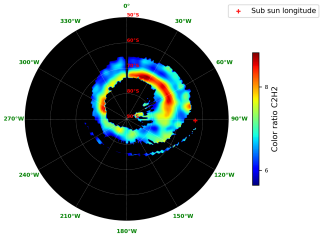

PJ32 South CR map for C_2H_2

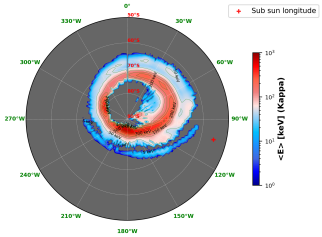

PJ32 South Mean energy map for electrons with a kappa distribution

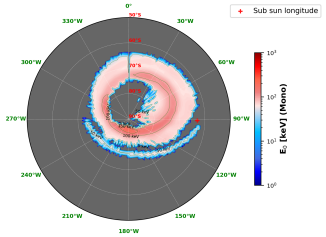

PJ32 South Characteristic energy map for electrons with a monoenergetic distribution

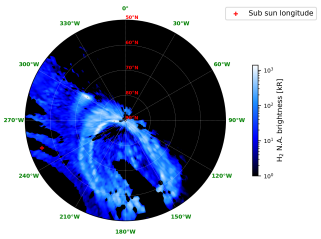

PJ33 North brightness map

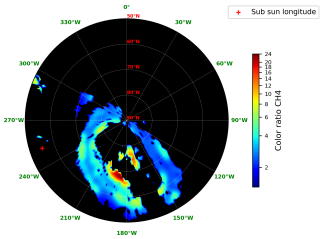

PJ33 North CR map for CH_4

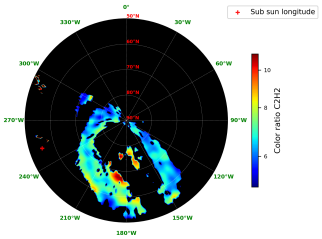

PJ33 North CR map for C_2H_2

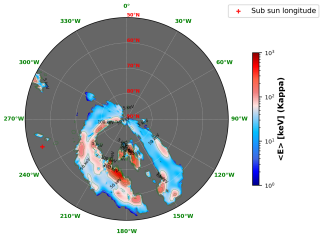

PJ33 North Mean energy map for electrons with a kappa distribution

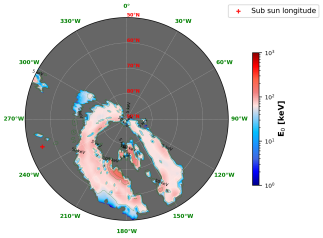

PJ33 North Characteristic energy map for electrons with a monoenergetic distribution

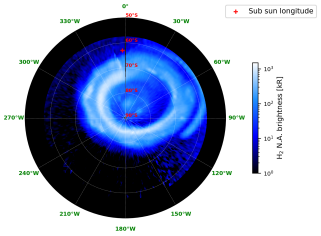

PJ33 South brightness map

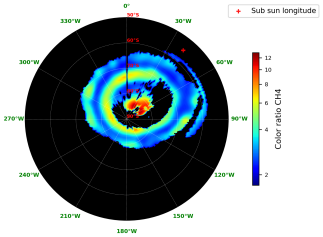

PJ33 South CR map for CH_4

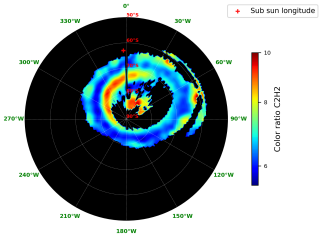

PJ33 South CR map for C_2H_2

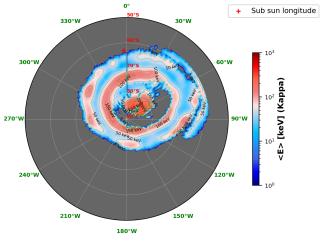

PJ33 South Mean energy map for electrons with a kappa distribution

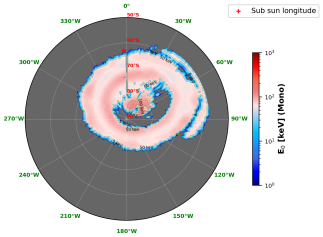

PJ33 South Characteristic energy map for electrons with a monoenergetic distribution

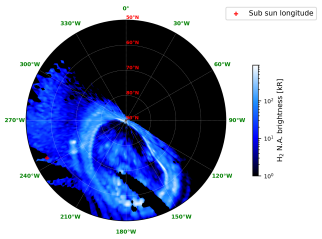

PJ34 North brightness map

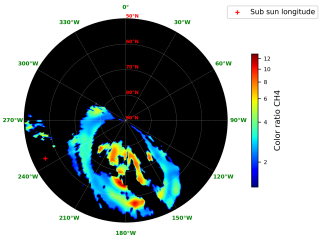

PJ34 North CR map for CH_4

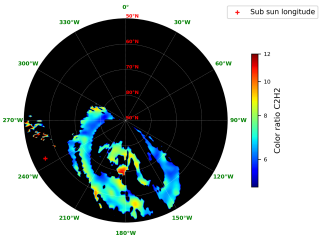

PJ34 North CR map for C_2H_2

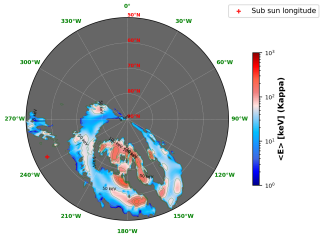

PJ34 North Mean energy map for electrons with a kappa distribution

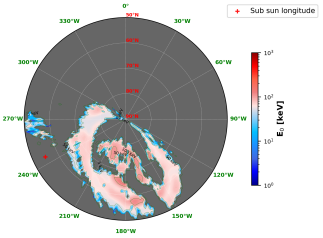

PJ34 North Characteristic energy map for electrons with a monoenergetic distribution

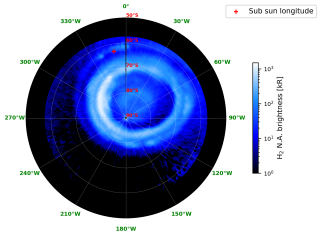

PJ34 South brightness map

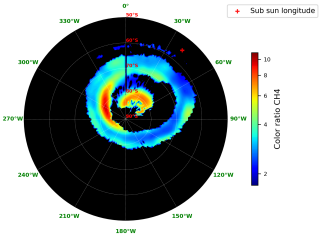

PJ34 South CR map for CH_4

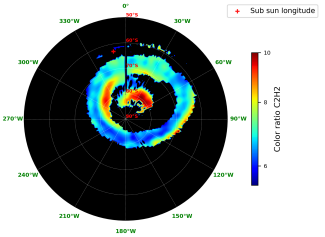

PJ34 South CR map for C_2H_2

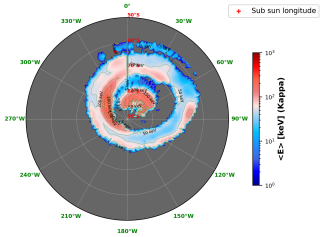

PJ34 South Mean energy map for electrons with a kappa distribution

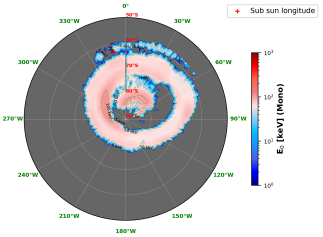

PJ34 South Characteristic energy map for electrons with a monoenergetic distribution

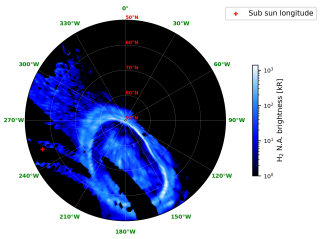

PJ35 North brightness map

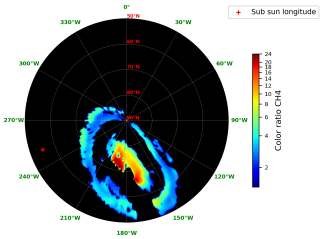

PJ35 North CR map for CH_4

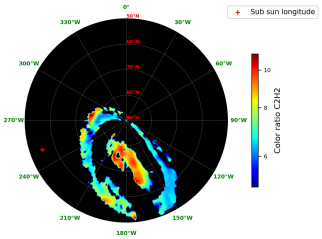

PJ35 North CR map for C_2H_2

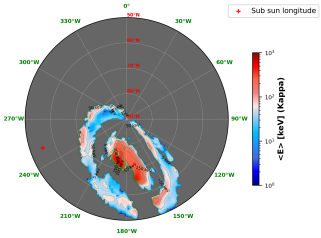

PJ35 North Mean energy map for electrons with a kappa distribution

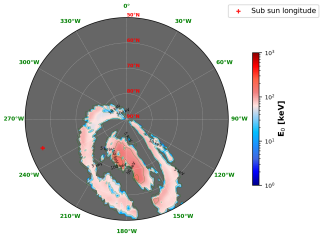

PJ35 North Characteristic energy map for electrons with a monoenergetic distribution

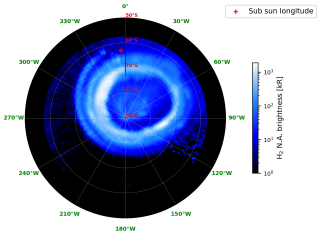

PJ35 South brightness map

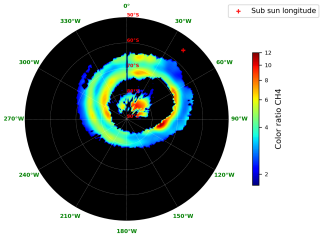

PJ35 South CR map for CH_4

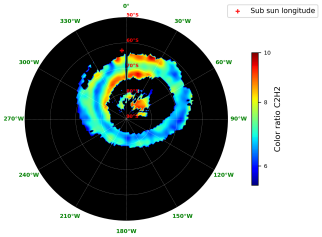

PJ35 South CR map for C_2H_2

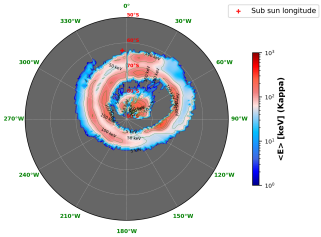

PJ35 South Mean energy map for electrons with a kappa distribution

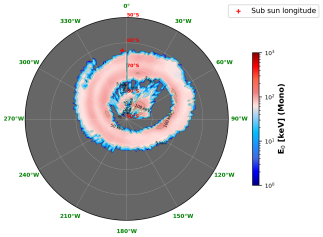

PJ35 South Characteristic energy map for electrons with a monoenergetic distribution

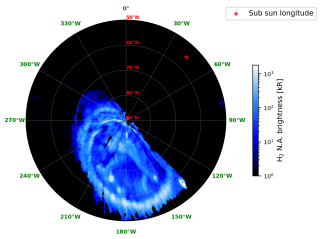

PJ36 North brightness map

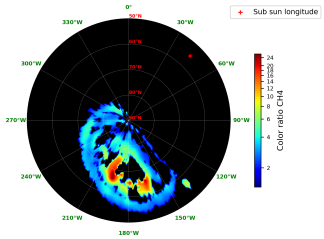

PJ36 North CR map for CH_4

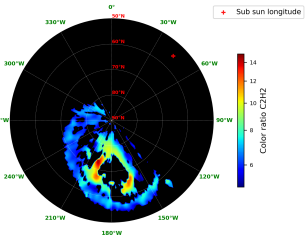

PJ36 North CR map for C_2H_2

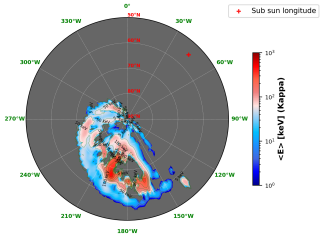

PJ36 North Mean energy map for electrons with a kappa distribution

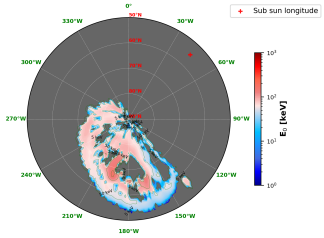

PJ36 North Characteristic energy map for electrons with a monoenergetic distribution

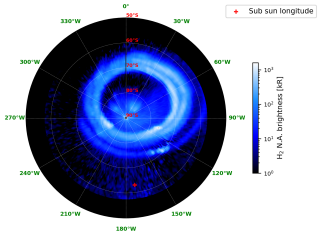

PJ36 South brightness map

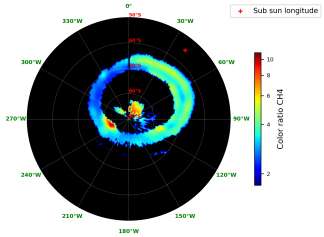

PJ36 South CR map for CH_4

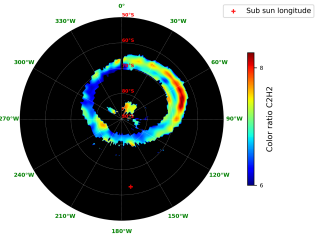

PJ36 South CR map for C_2H_2

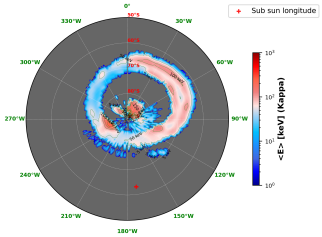

PJ36 South Mean energy map for electrons with a kappa distribution

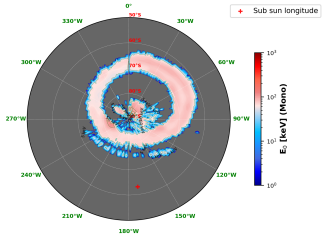

PJ36 South Characteristic energy map for electrons with a monoenergetic distribution

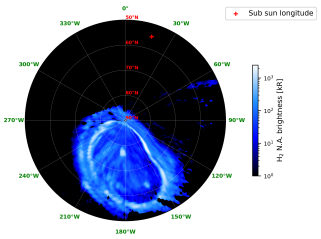

PJ38 North brightness map

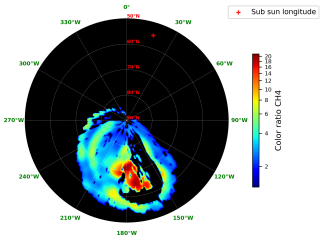

PJ38 North CR map for CH_4

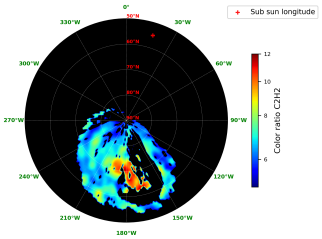

PJ38 North CR map for C_2H_2

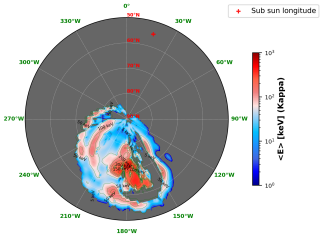

PJ38 North Mean energy map for electrons with a kappa distribution

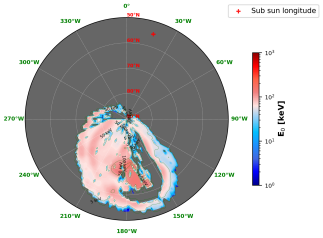

PJ38 North Characteristic energy map for electrons with a monoenergetic distribution

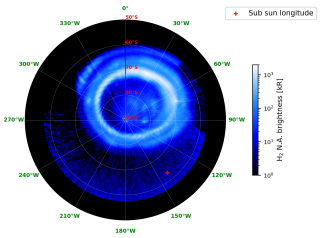

PJ38 South brightness map

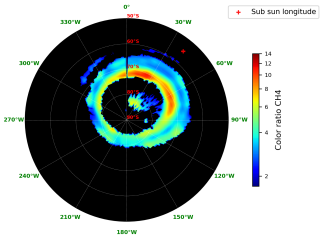

PJ38 South CR map for CH_4

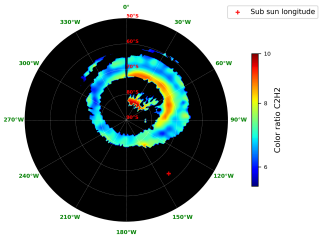

PJ38 South CR map for C_2H_2

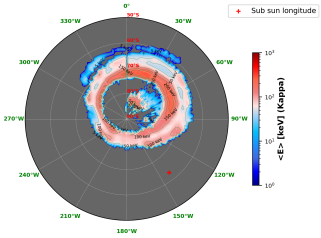

PJ38 South Mean energy map for electrons with a kappa distribution

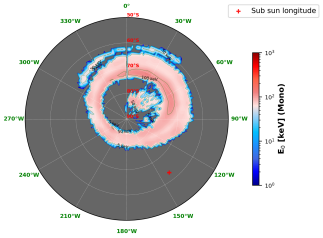

PJ38 South Characteristic energy map for electrons with a monoenergetic distribution

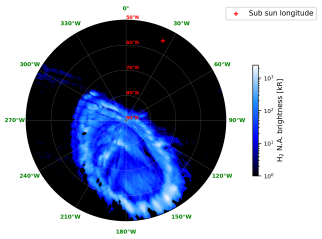

PJ39 North brightness map

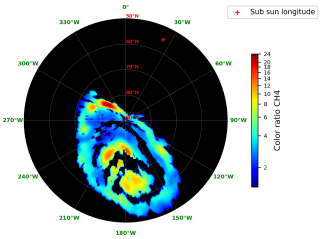

PJ39 North CR map for CH_4

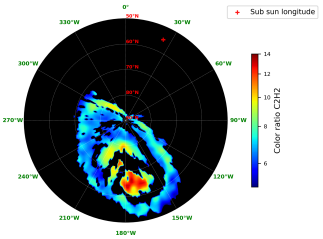

PJ39 North CR map for C_2H_2

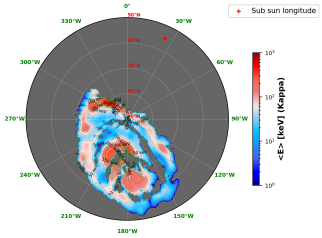

PJ39 North Mean energy map for electrons with a kappa distribution

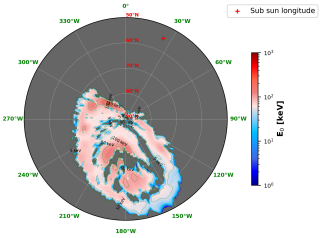

PJ39 North Characteristic energy map for electrons with a monoenergetic distribution

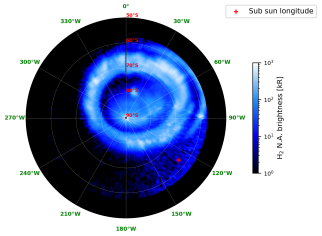

PJ39 South brightness map

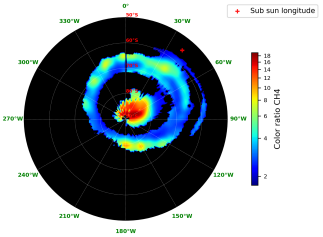

PJ39 South CR map for CH_4

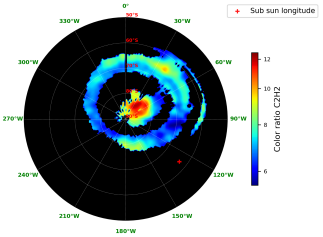

PJ39 South CR map for C_2H_2

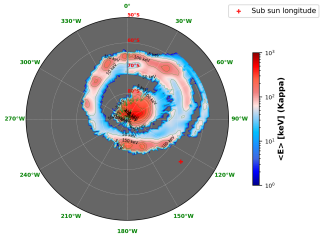

PJ39 South Mean energy map for electrons with a kappa distribution

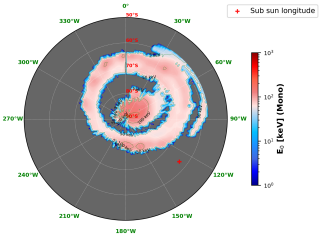

PJ39 South Characteristic energy map for electrons with a monoenergetic distribution

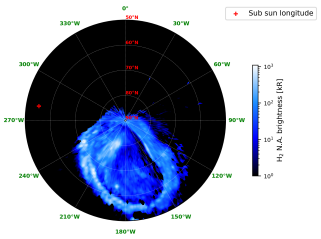

PJ41 North brightness map

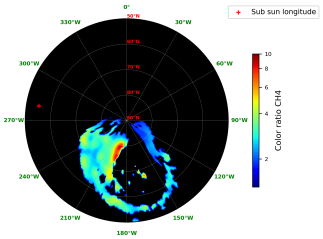

PJ41 North CR map for CH_4

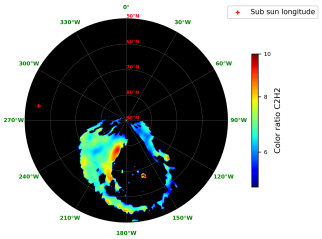

PJ41 North CR map for C_2H_2

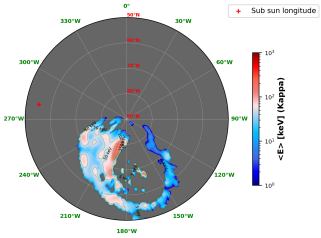

PJ41 North Mean energy map for electrons with a kappa distribution

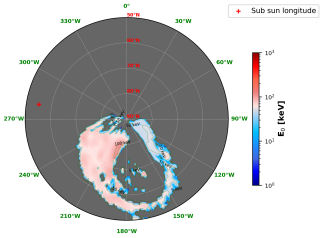

PJ41 North Characteristic energy map for electrons with a monoenergetic distribution

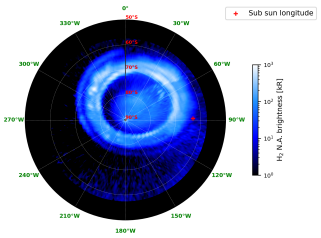

PJ41 South brightness map

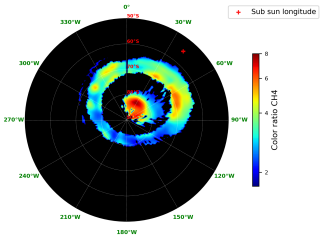

PJ41 South CR map for CH_4

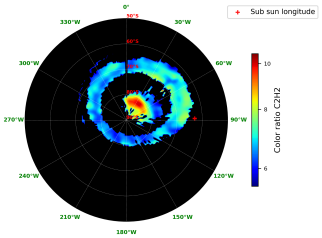

PJ41 South CR map for C_2H_2

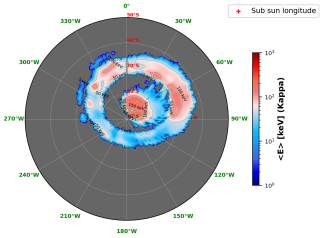

PJ41 South Mean energy map for electrons with a kappa distribution

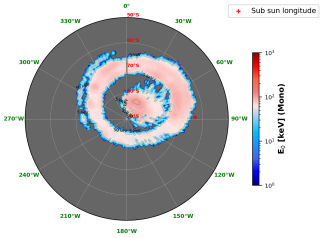

PJ41 South Characteristic energy map for electrons with a monoenergetic distribution

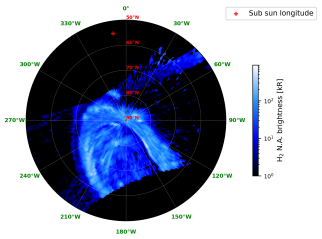

PJ42 North brightness map

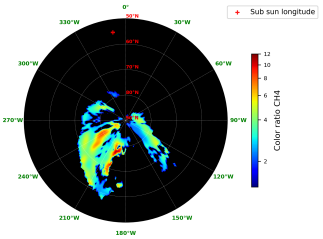

PJ42 North CR map for CH_4

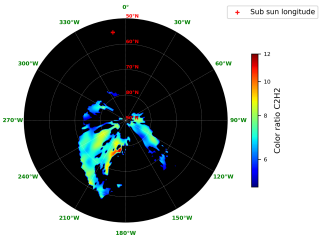

PJ42 North CR map for C_2H_2

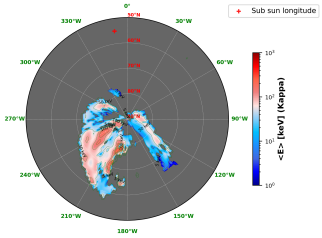

PJ42 North Mean energy map for electrons with a kappa distribution

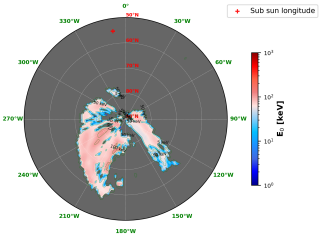

PJ42 North Characteristic energy map for electrons with a monoenergetic distribution

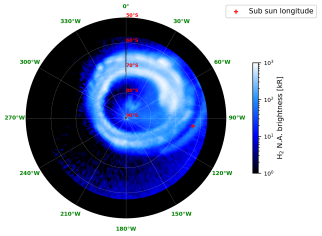

PJ42 South brightness map

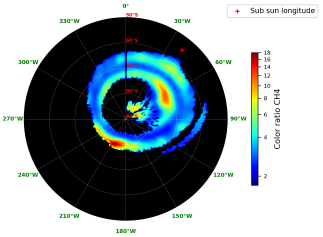

PJ42 South CR map for CH_4

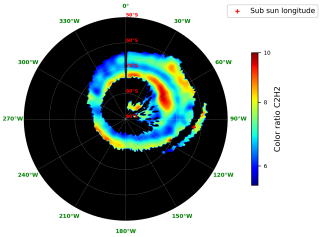

PJ42 South CR map for C_2H_2

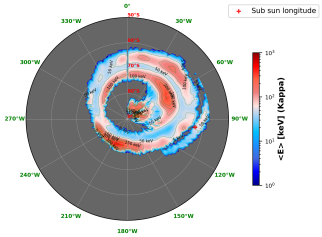

PJ42 South Mean energy map for electrons with a kappa distribution

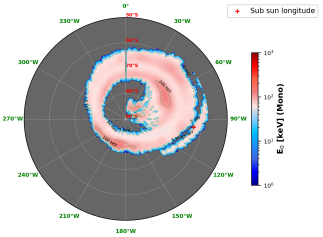

PJ42 South Characteristic energy map for electrons with a monoenergetic distribution

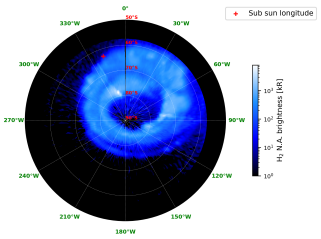

PJ43 South brightness map

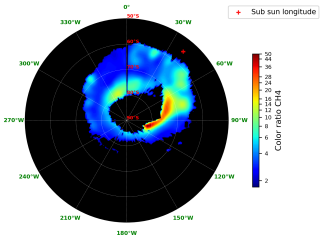

PJ43 South CR map for CH_4

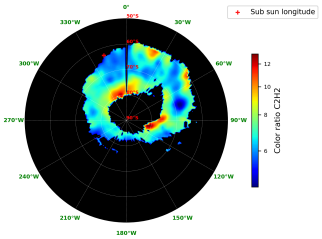

PJ43 South CR map for C_2H_2

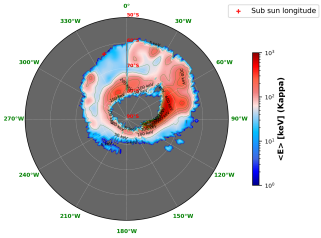

PJ43 South Mean energy map for electrons with a kappa distribution

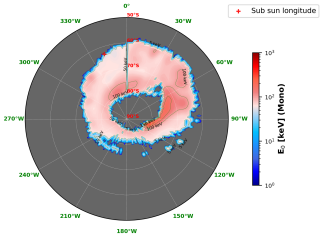

PJ43 South Characteristic energy map for electrons with a monoenergetic distribution

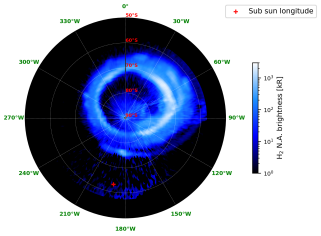

PJ44 South brightness map

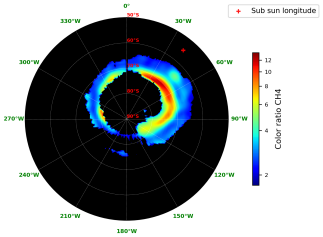

PJ44 South CR map for CH_4

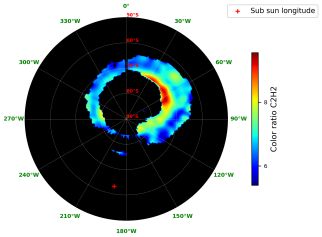

PJ44 South CR map for C_2H_2

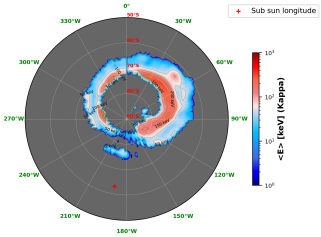

PJ44 South Mean energy map for electrons with a kappa distribution

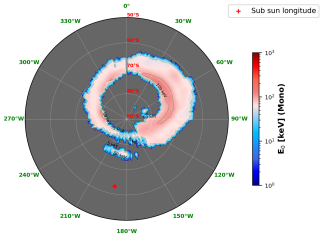

PJ44 South Characteristic energy map for electrons with a monoenergetic distribution

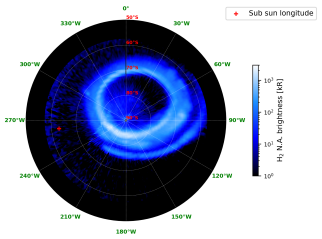

PJ45 South brightness map

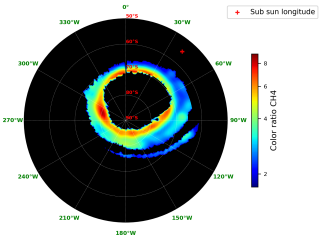

PJ45 South CR map for CH_4

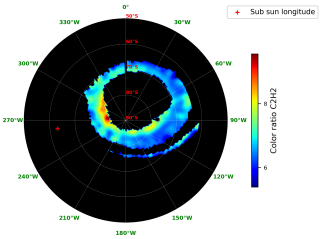

PJ45 South CR map for C_2H_2

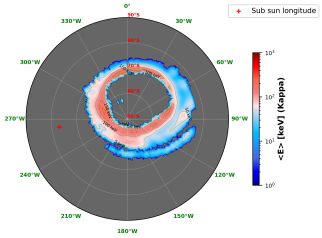

PJ45 South Mean energy map for electrons with a kappa distribution

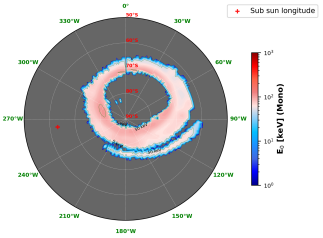

PJ45 South Characteristic energy map for electrons with a monoenergetic distribution

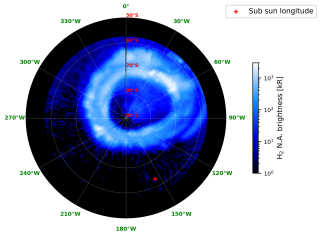

PJ46 South brightness map

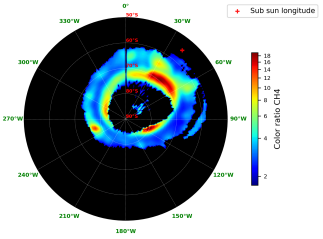

PJ46 South CR map for CH_4

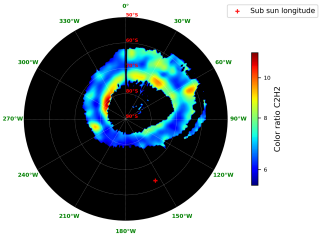

PJ46 South CR map for C_2H_2

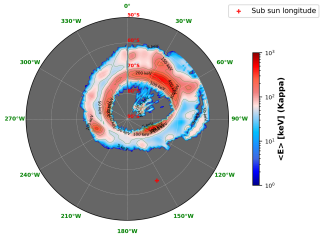

PJ46 South Mean energy map for electrons with a kappa distribution

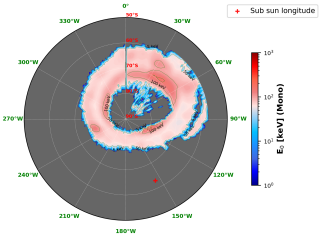

PJ46 South Characteristic energy map for electrons with a monoenergetic distribution

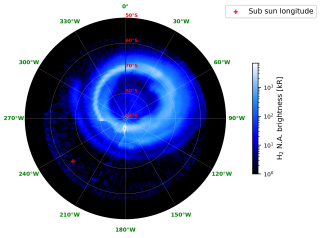

PJ48 South brightness map

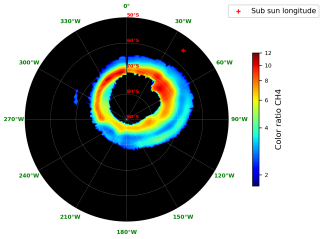

PJ48 South CR map for CH_4

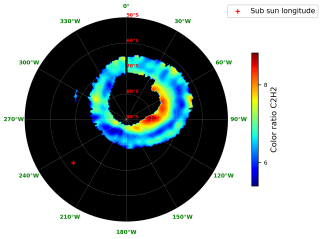

PJ48 South CR map for C_2H_2

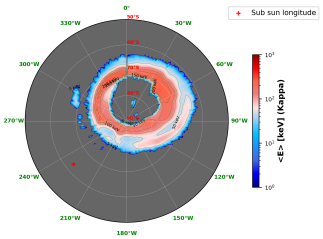

PJ48 South Mean energy map for electrons with a kappa distribution

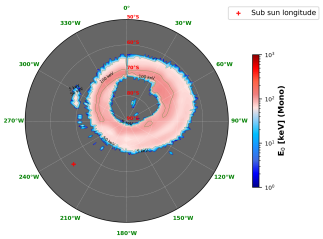

PJ48 South Characteristic energy map for electrons with a monoenergetic distribution

B

Masks

In this annex, we display the masks used to discriminate the auroral sub-regions (outer, main and polar emission regions) for the northern and southern auroral regions based on the work of Groulard et al. (2024). The outer emission region is represented in red, the main emission region in orange and the polar emission region in green.

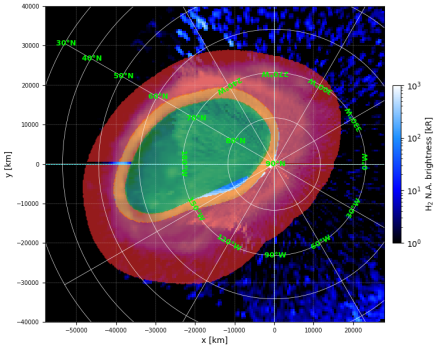

PJ1 North

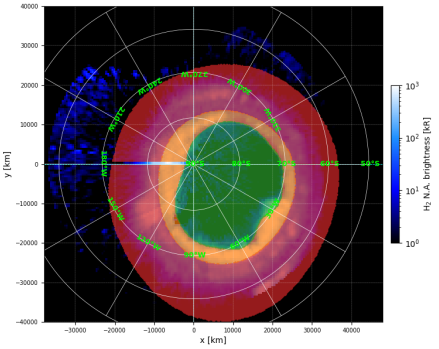

PJ1 South

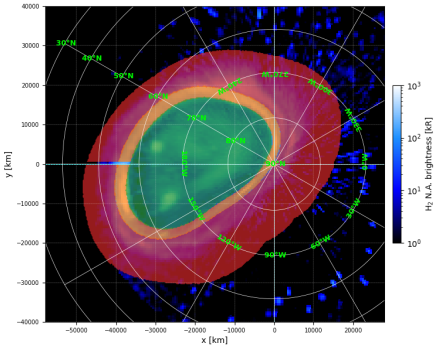

PJ3 North

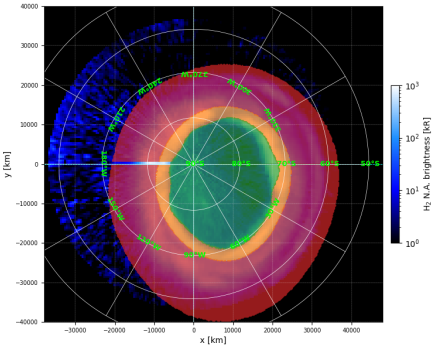

PJ3 South

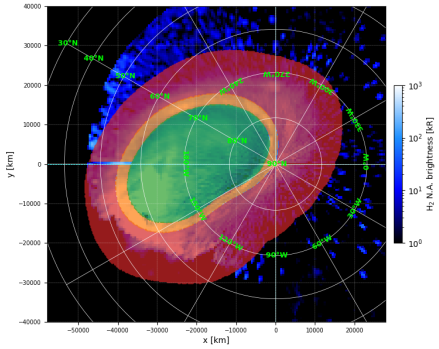

PJ4 North

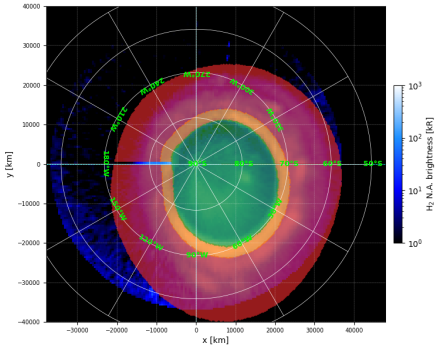

PJ4 South

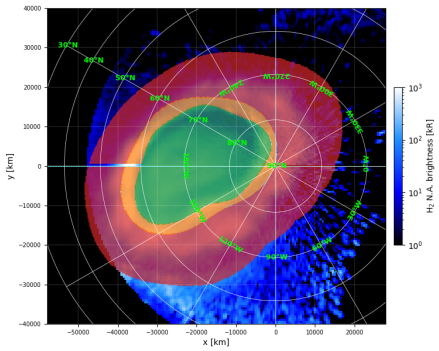

PJ5 North

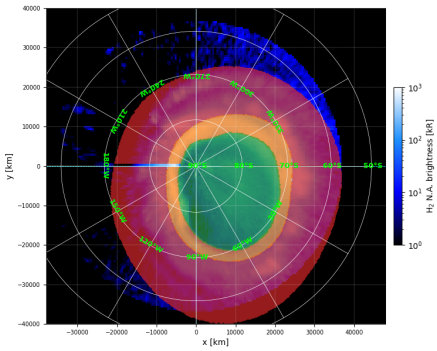

PJ5 South

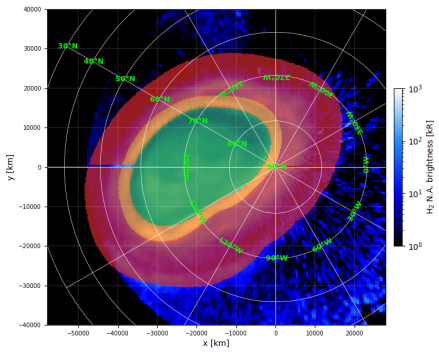

PJ6 North

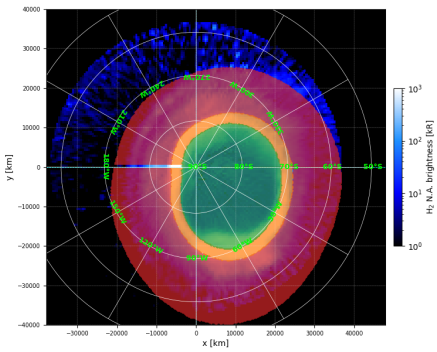

PJ6 South

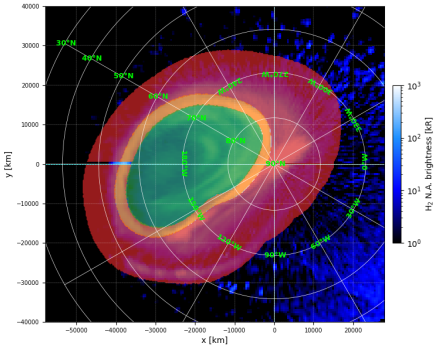

PJ7 North

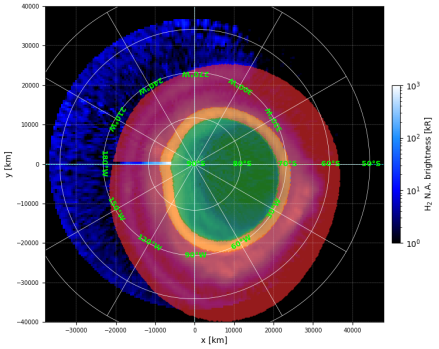

PJ7 South

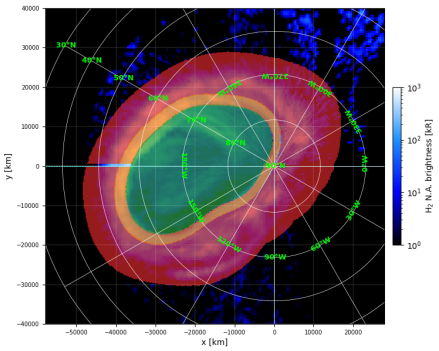

PJ8 North

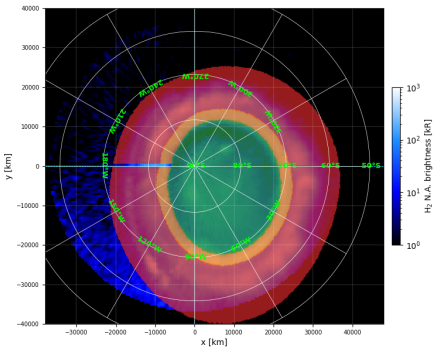

PJ8 South

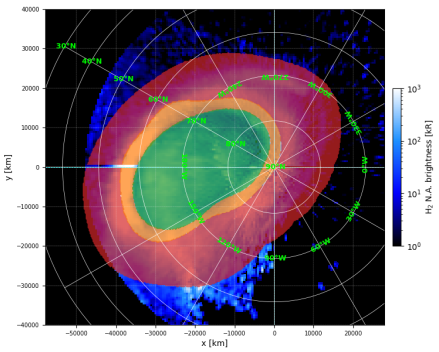

PJ9 North

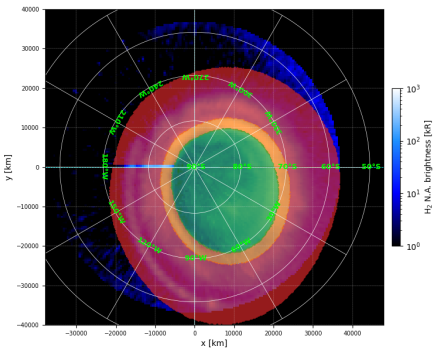

PJ9 South

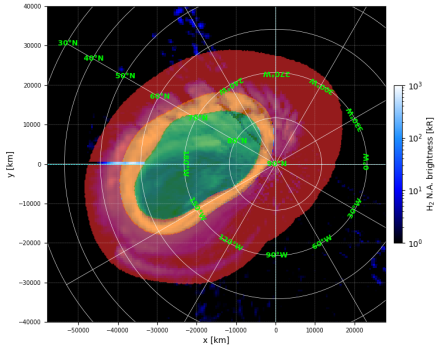

PJ10 North

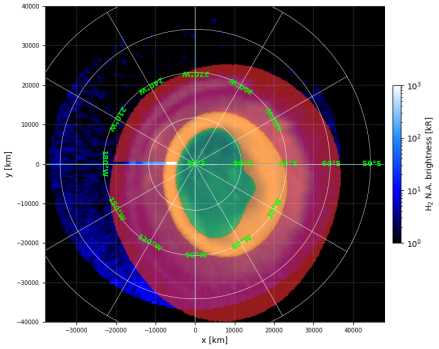

PJ10 South

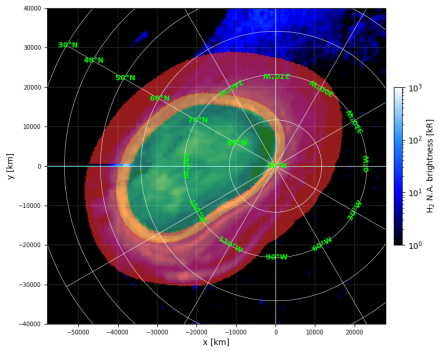

PJ11 North

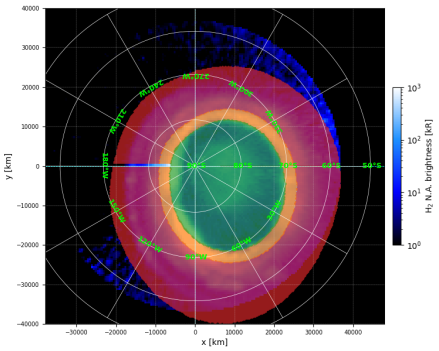

PJ11 South

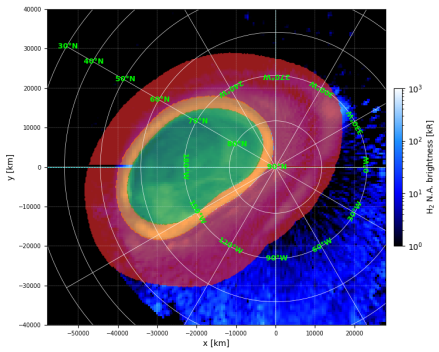

PJ12 North

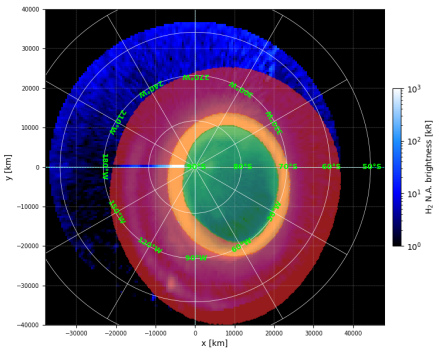

PJ12 South

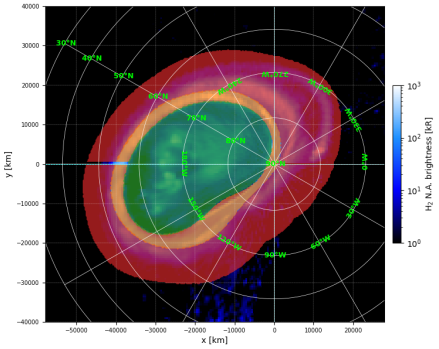

PJ13 North

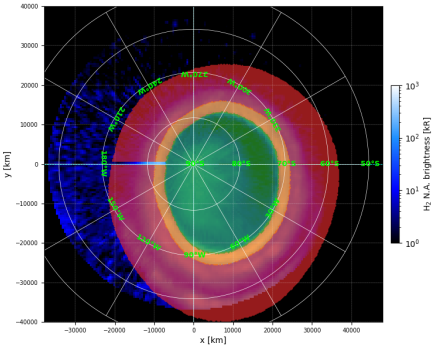

PJ13 South

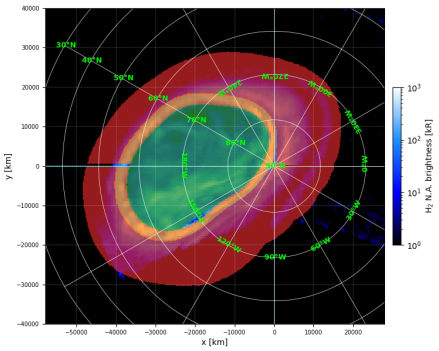

PJ14 North

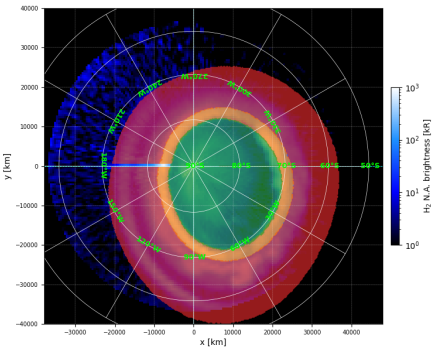

PJ14 South

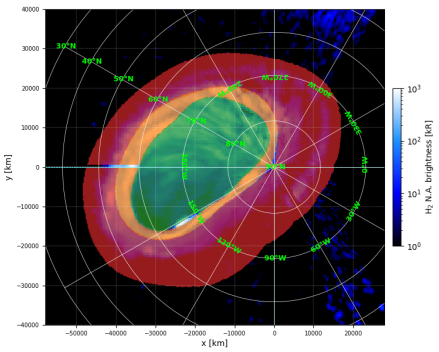

PJ15 North

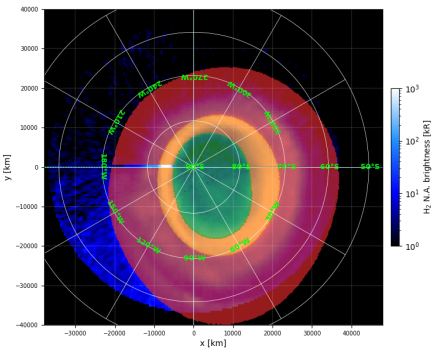

PJ15 South

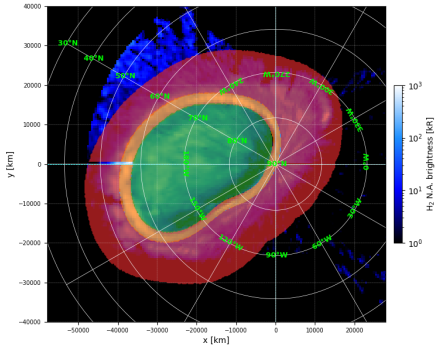

PJ16 North

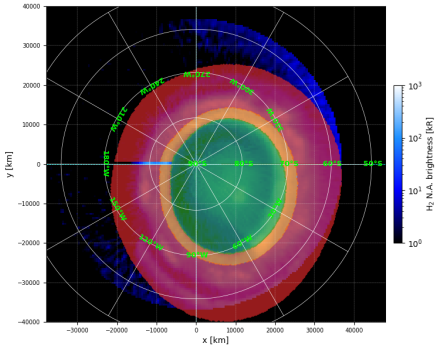

PJ16 South

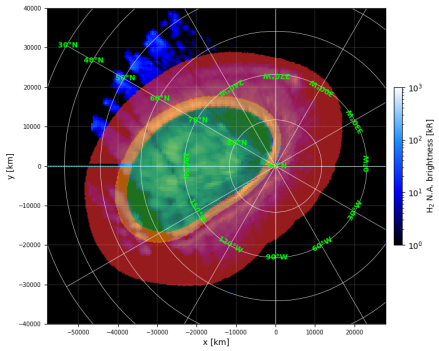

PJ17 North

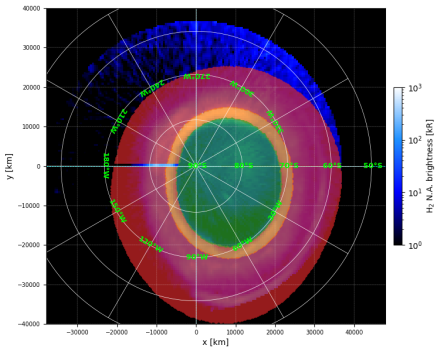

PJ17 South

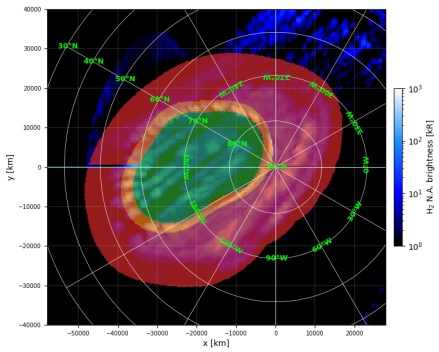

PJ18 North

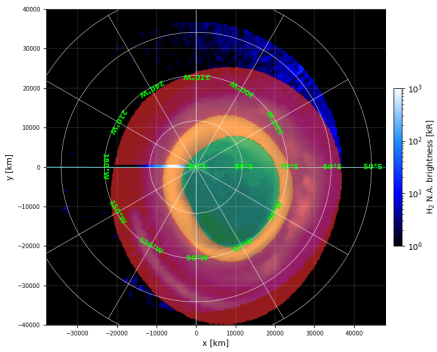

PJ18 South

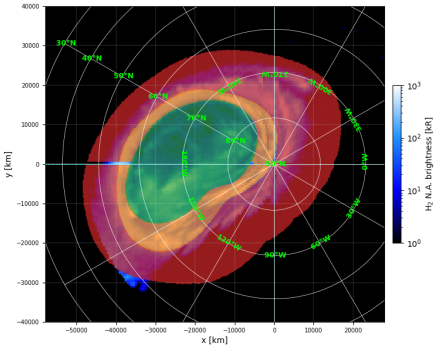

PJ19 North

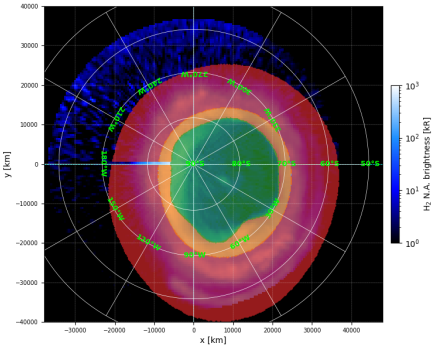

PJ19 South

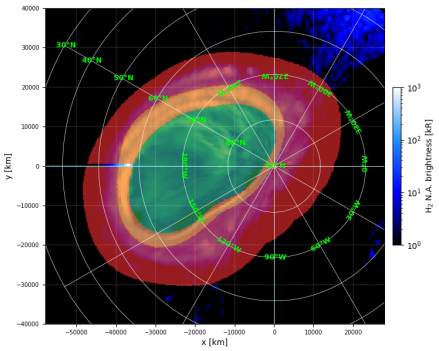

PJ20 North

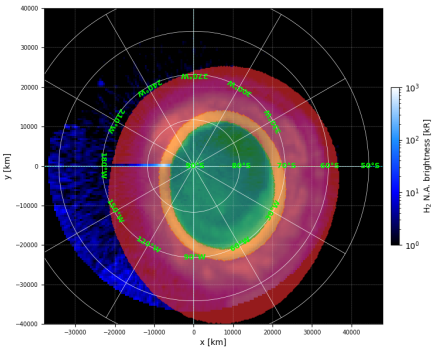

PJ20 South

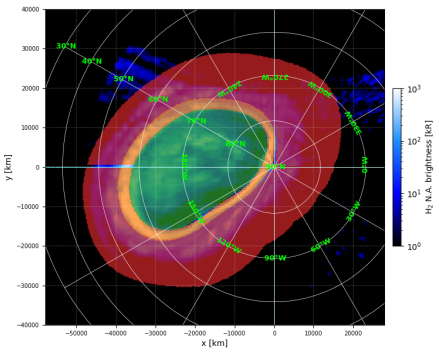

PJ21 North

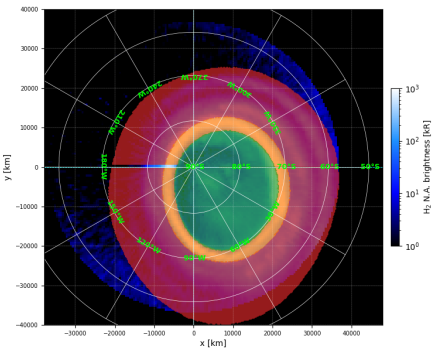

PJ21 South

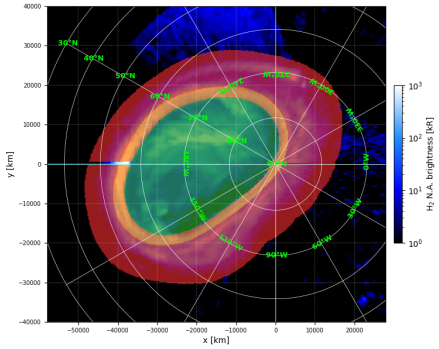

PJ22 North

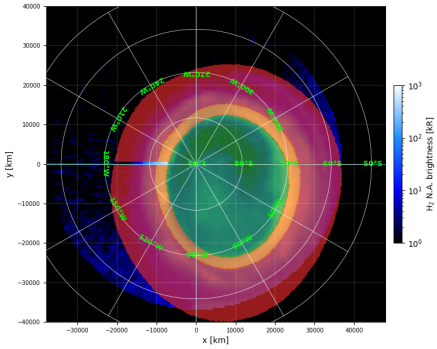

PJ22 South

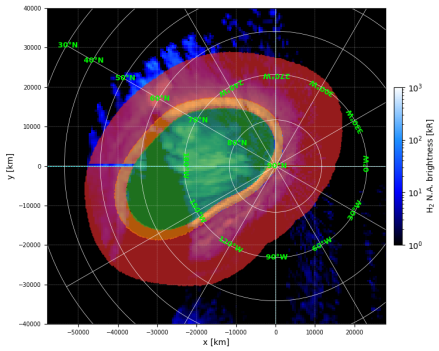

PJ23 North

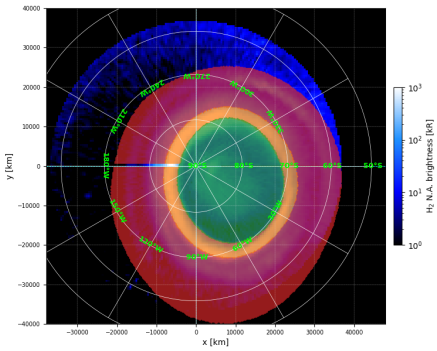

PJ23 South

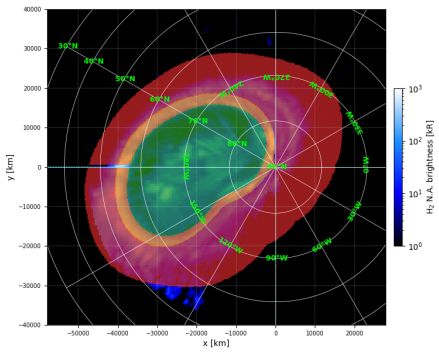

PJ24 North

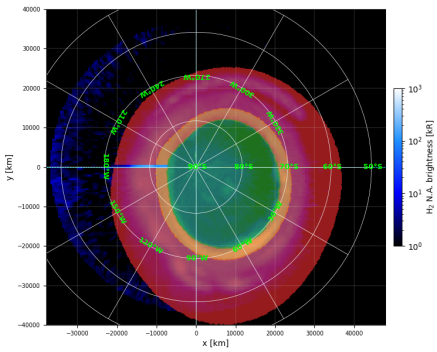

PJ24 South

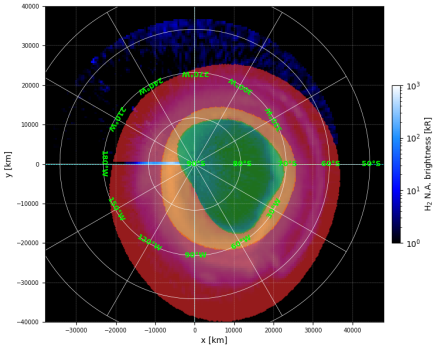

PJ25 South

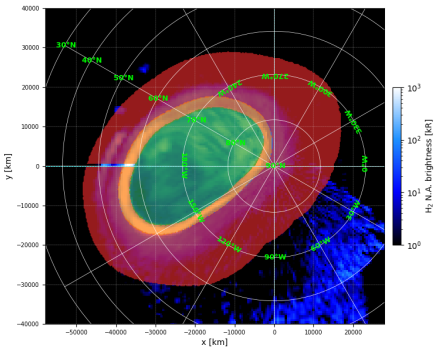

PJ26 North

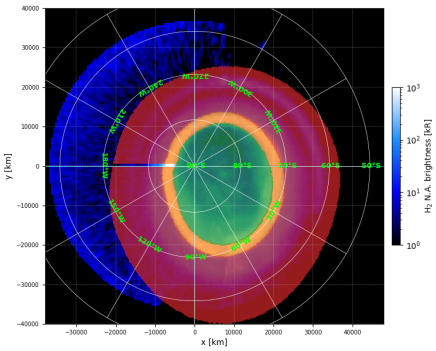

PJ26 South

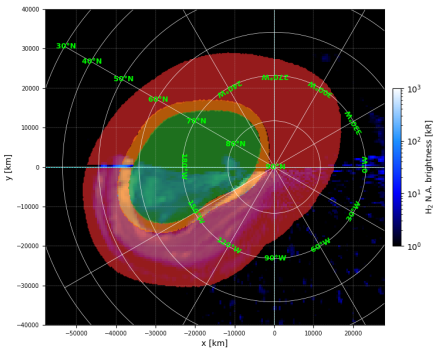

PJ27 North

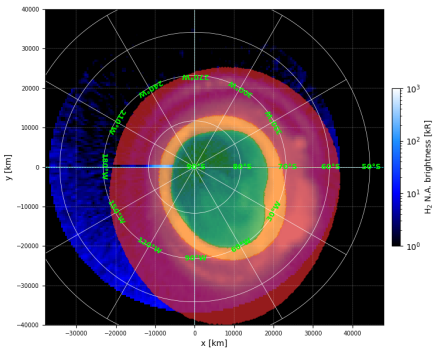

PJ27 South

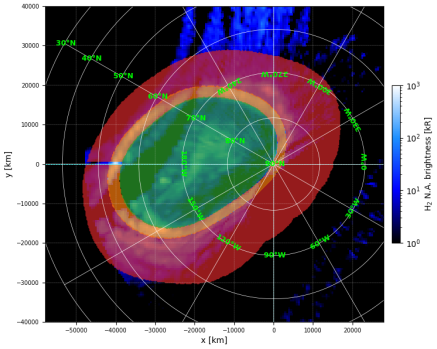

PJ28 North

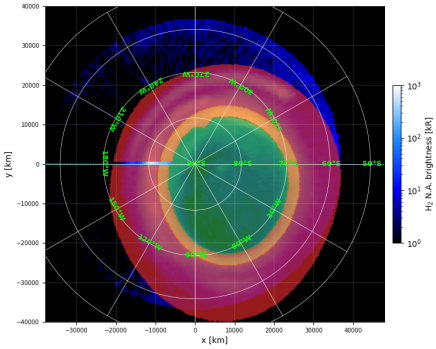

PJ28 South

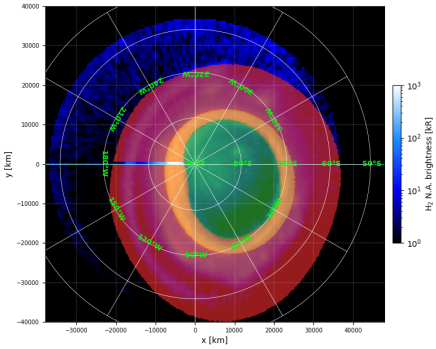

PJ29 South

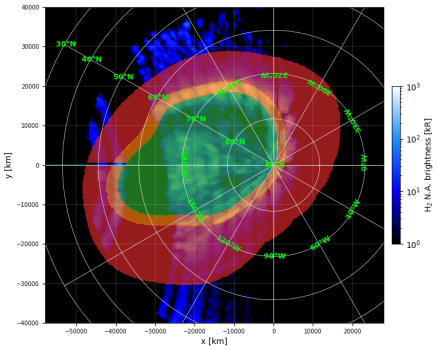

PJ30 North

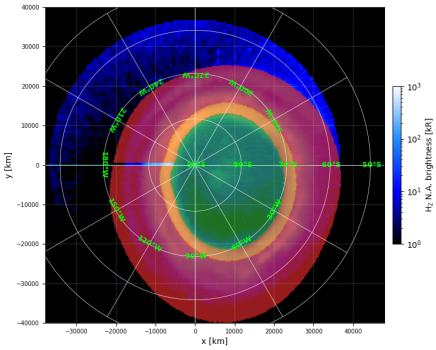

PJ30 South

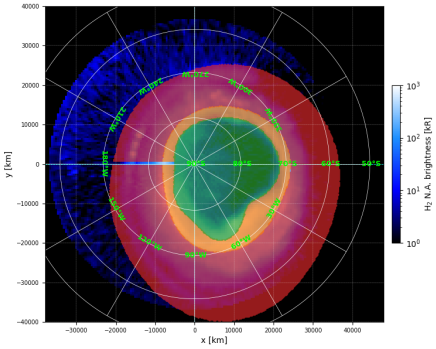

PJ31 South

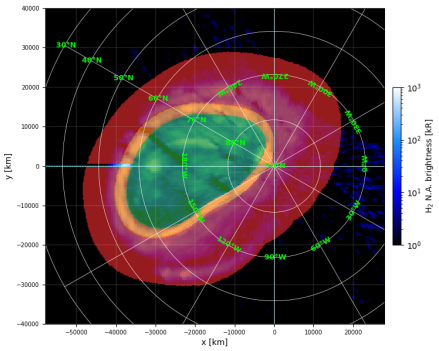

PJ32 North

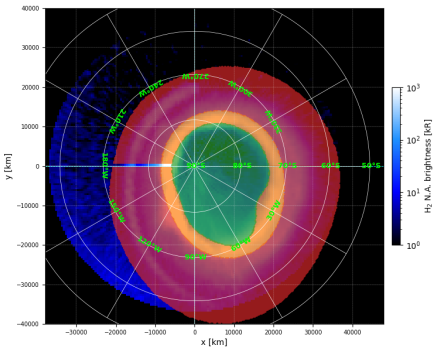

PJ32 South

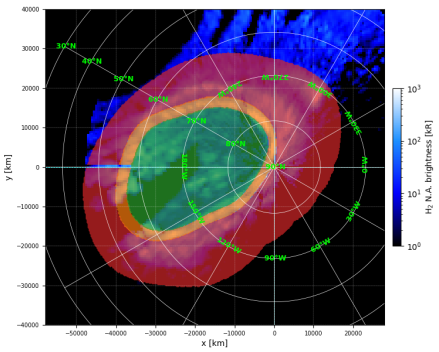

PJ33 North

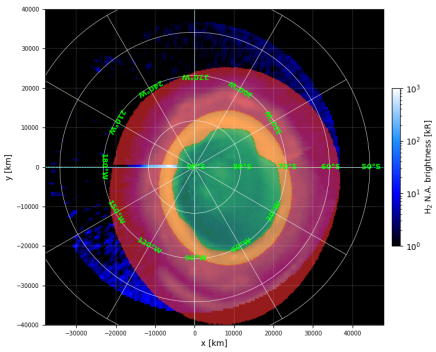

PJ33 South

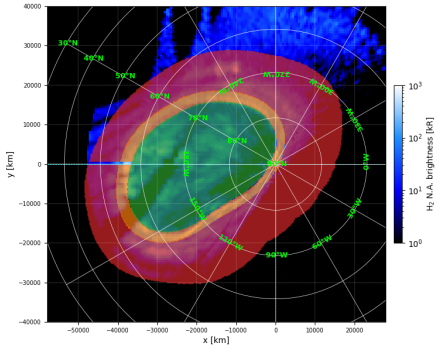

PJ34 North

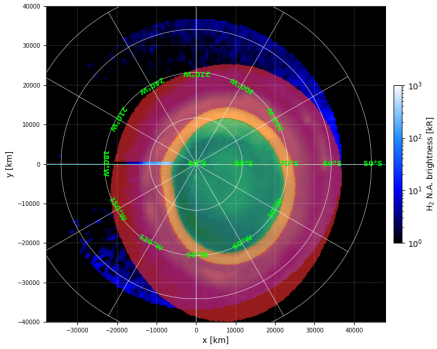

PJ34 South

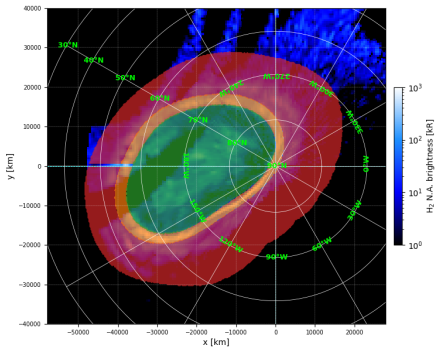

PJ35 North

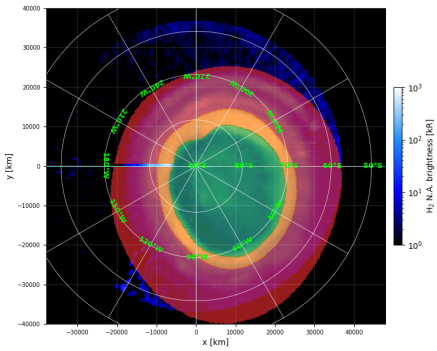

PJ35 South

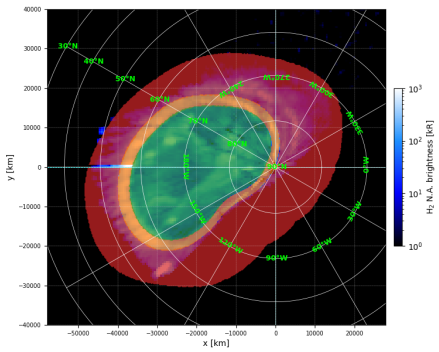

PJ36 North

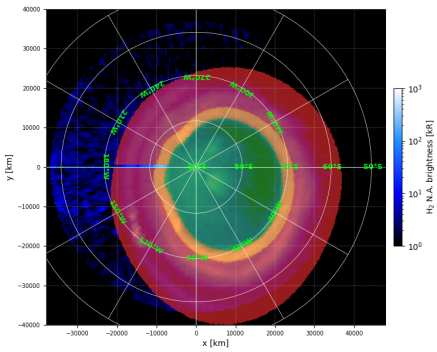

PJ36 South

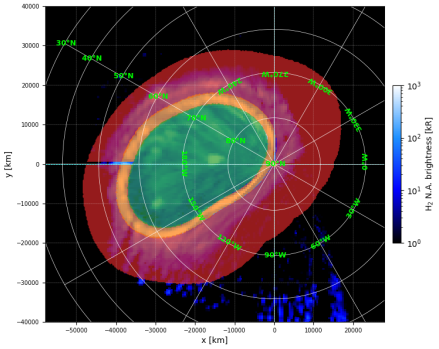

PJ38 North

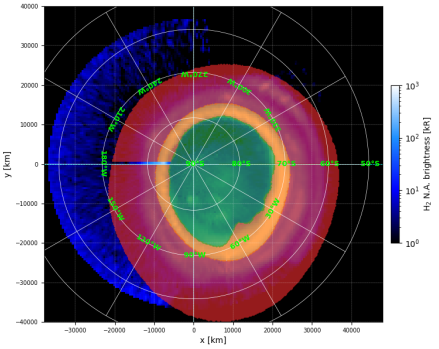

PJ38 South

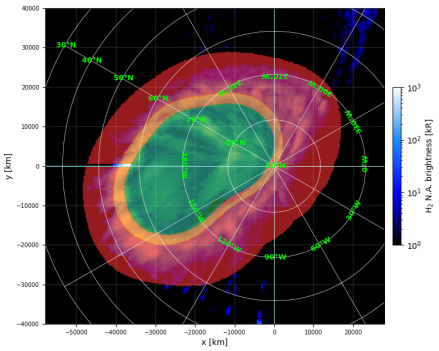

PJ39 North

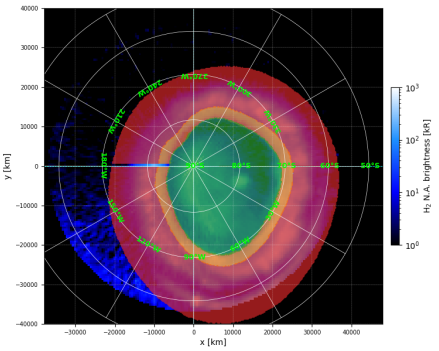

PJ39 South

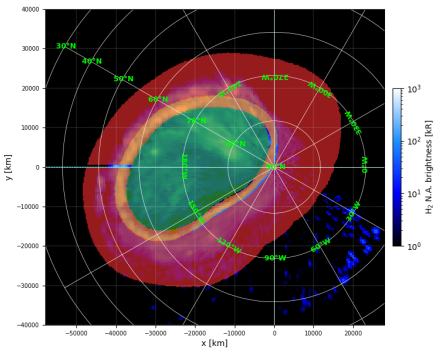

PJ41 North

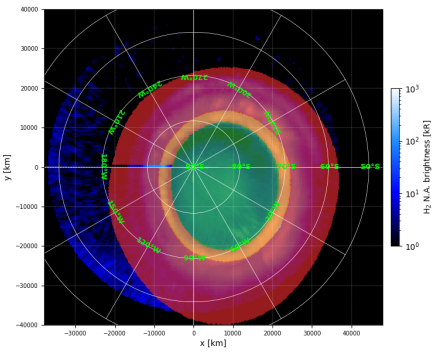

PJ41 South

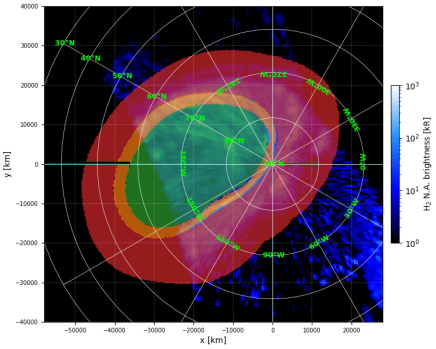

PJ42 North

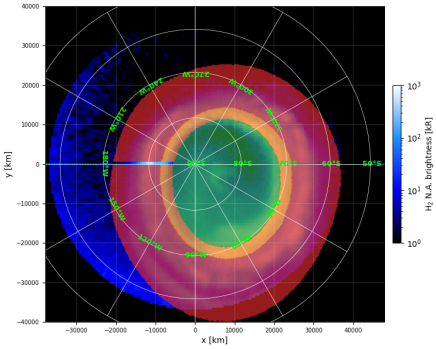

PJ42 South

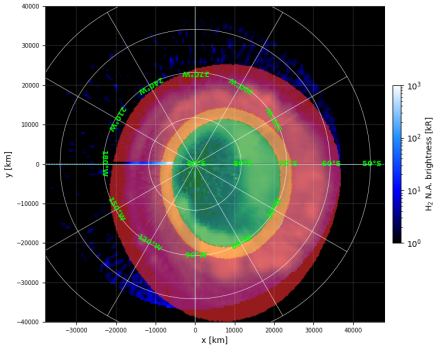

PJ43 South

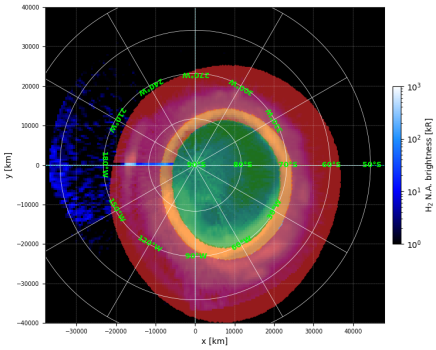

PJ44 South

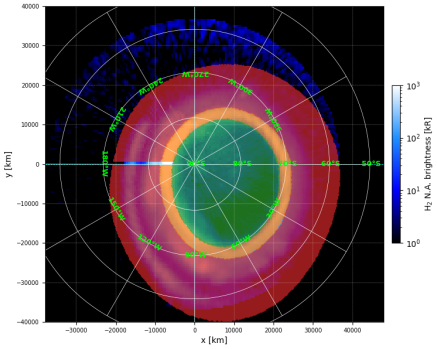

PJ45 South

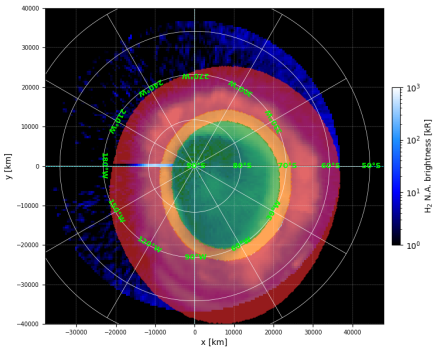

PJ46 South

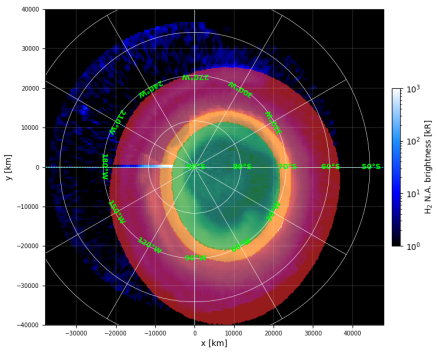

PJ48 South

C

Energy tables

In this section, we display the tables of the mean, median and standard deviation of the energy of the precipitating electrons for each auroral subregion for each perijove for a kappa or monoenergetic electron flux.

TABLE C.1: Mean, median and standard deviation of the energy of the precipitating electrons for the northern outer emission region for a kappa energy flux of electrons.

N Kappa	Outer emission region				
	Mean energy (eV)	Median energy (eV)	Standard deviation	16^{th} percentile	84^{th} percentile
PJ1	61493.81107	43898.88609	61227.95176	10436.66287	108633.652
PJ3	35309.63139	32626.22028	29419.27587	3115.779966	64589.56619
PJ4	42170.0799	33301.97609	46640.84712	3712.259688	69389.34377
PJ5	39085.80072	38402.01148	31955.38805	2867.301525	71665.19994
PJ6	36160.26912	30752.89773	32520.9906	2320.72258	67460.85632
PJ7	48438.80196	34635.41355	51260.38847	3559.537586	95150.6472
PJ8	54158.10333	38726.15024	58544.90382	3371.706539	98045.42571
PJ9	48609.76757	50579.13347	35179.79069	4757.339547	84321.53184
PJ10	15401.87402	6379.585521	20024.97449	84.47594441	35221.639
PJ11	28226.90878	27511.3949	22858.92074	1481.077616	52553.25847
PJ12	17992.79718	13349.85182	17739.08196	462.9549509	37338.03334
PJ13	25691.11511	18742.73908	25256.11661	151.2392996	56584.3409
PJ14	23434.14678	19493.92117	21248.07216	585.0935856	47973.78291
PJ15	26540.26223	16435.16217	30760.78145	622.2368826	50173.77115
PJ16	27601.30154	21696.63273	29041.20031	1771.429558	48733.92674
PJ17	25637.21258	14820.52932	27144.61749	93.74907519	60487.69549
PJ18	50188.50886	18452.46169	84933.14418	1240.523951	88853.11109
PJ19	30777.75914	19458.89903	36061.8509	92.54221393	65786.51764
PJ20	31211.52831	20630.41423	31666.44079	2182.320046	63916.66271
PJ21	19670.70962	15331.08615	18959.3562	459.0566946	39515.50179
PJ22	48790.25698	31898.69606	63001.25262	1132.559209	81360.57683
PJ23	9866.405392	1470.552142	15327.71653	56.88662072	23285.35494
PJ24	26525.37512	9825.535086	32447.36446	91.66358814	68250.96359
PJ26	12225.6213	3360.125457	21622.64845	46.84564082	28630.42974
PJ27	27421.42134	25842.97569	19908.54191	4584.240546	45285.30305
PJ28	21213.92223	16929.54931	20687.04788	101.8375721	41255.44811
PJ30	34573.0631	10844.5192	46107.597	70.8939503	86096.8798
PJ32	24738.09061	21678.19687	22400.61967	1199.314381	46668.85868
PJ33	22424.21416	17834.21157	24549.30874	100.00000	44065.24255
PJ34	21113.76576	14816.04478	19779.03283	1280.789591	44417.66876
PJ35	27297.00016	22759.62945	24753.81051	1829.919542	50979.33871
PJ36	25399.1408	14130.2887	27707.2906	42.0669518	54934.5045
PJ38	20748.5738	11011.51766	25737.27283	100.00000	42801.94375
PJ39	46339.78144	25729.19434	69634.54596	100.00000	81528.87319
PJ41	14992.70969	5344.980661	20101.37772	108.4807362	36392.6272
PJ42	30451.53074	22133.0932	28425.61141	2429.289696	61406.05841
Mean	30608.92	21412.07	33184.31		
Std	12515.31	11398.42	16494.73		

TABLE C.2: Mean, median and standard deviation of the energy of the precipitating electrons for the northern main emission region for a kappa energy flux of electrons.

N Kappa	Main emission region				
	Mean energy (eV)	Median energy (eV)	Standard deviation	16^{th} percentile	84^{th} percentile
PJ1	61533.3811	57166.59031	28214.0616	34524.28511	90011.33609
PJ3	59569.39589	46159.72477	52196.582	26360.9437	78406.63963
PJ4	50452.79596	50635.35604	32238.05105	17245.44005	76901.45171
PJ5	96422.36537	81552.36735	51929.93774	47743.10466	157653.6748
PJ6	75020.00127	67642.60338	32411.82683	46587.46207	109182.7703
PJ7	96484.48509	79418.78649	68442.58296	28498.3596	177431.0614
PJ8	45577.73017	34656.51703	31897.02687	21092.89647	76071.04987
PJ9	96995.39063	80059.28591	53042.91937	52511.56084	163480.1517
PJ10	124197.3744	107710.69	86697.84827	44508.77424	209622.3499
PJ11	51852.63658	48259.19784	25866.90861	24746.04277	78972.57
PJ12	92223.09915	89882.50093	47476.14689	41016.31523	138327.4792
PJ13	38188.25472	35454.59058	23837.33146	13488.08074	65100.72257
PJ14	51641.23783	46756.58752	31652.66124	19334.04564	84180.33986
PJ15	84653.79666	72465.0497	47596.62008	46208.7368	126206.9255
PJ16	49973.80644	44116.98719	33931.83555	17071.11083	89043.64767
PJ17	33538.87565	32023.14619	25241.02981	5168.425999	56631.58711
PJ18	61130.9316	53613.00378	46332.60769	15081.72744	99603.07312
PJ19	34066.24702	30271.37995	25585.52488	7641.237092	62158.28873
PJ20	70501.81439	72649.7706	48113.69346	18989.83852	111798.5642
PJ21	69792.30576	59512.59013	46462.64802	26747.51479	105349.4112
PJ22	49893.9174	46047.64329	23349.43089	31261.81696	64327.03852
PJ23	30476.45763	27817.45934	22435.81932	8052.643814	49689.39527
PJ24	32366.12023	26409.14548	27683.54775	4126.144098	57946.8979
PJ26	93554.03316	79446.31637	74790.06835	29148.89244	143983.4619
PJ27	90737.08372	66898.66134	83249.27859	16432.66876	161259.5107
PJ28	32493.91883	30174.27333	21581.67634	11985.85265	50450.85567
PJ30	34809.01853	28743.87101	32290.33158	5922.828231	54446.34924
PJ32	119623.6074	83208.58654	97144.77403	48939.83337	217275.9258
PJ33	44672.27211	37183.27511	31138.31964	16550.70899	73358.85586
PJ34	35951.73436	30999.52493	28103.91151	11360.04824	53709.083
PJ35	47205.97028	43966.92329	27401.17781	21435.25698	69106.85592
PJ36	19394.41342	13058.31714	20477.61463	100.00000	40986.04349
PJ38	62161.64035	57703.69743	35586.47975	26391.25328	100500.5376
PJ39	31950.77302	27023.3419	21143.56435	9623.160357	57279.50037
PJ41	26057.14165	27539.57497	19724.43182	1508.355238	46326.19921
PJ42	37507.59764	29824.86487	29815.49132	4486.45297	74478.92775
Mean	59240.88	51279.23	39863.44		
Std	27475.96	22629.35	20113.41		

TABLE C.3: Mean, median and standard deviation of the energy of the precipitating electrons for the northern polar emission region for a kappa energy flux of electrons.

N Kappa	Polar emission region				
	Mean energy (eV)	Median energy (eV)	Standard deviation	16^{th} percentile	84^{th} percentile
PJ1	96447.28187	75400.24547	81012.3192	10585.78706	180247.454
PJ3	163860.1167	116373.7471	161141.2585	9137.656282	322582.6828
PJ4	163171.0977	88764.33916	165411.5083	25170.30567	333887.2383
PJ5	173421.3962	111824.0759	144387.7734	57034.97112	335745.5599
PJ6	169878.7787	123462.5772	129685.3592	43979.72576	329530.2822
PJ7	111879.1011	95403.63862	81034.41782	48489.70635	169380.8916
PJ8	60555.68453	38288.43119	63400.22293	3061.190676	128618.0263
PJ9	146406.87	107324.6064	119891.6416	49516.84223	270283.4155
PJ10	139629.0952	120433.8328	143958.9141	23927.42675	195141.7274
PJ11	220860.1158	150053.9786	207247.8957	20081.41386	462601.7307
PJ12	215086.2607	160486.9979	148636.848	78235.22281	398975.6044
PJ13	123159.91	58035.96433	156437.0226	4059.147155	261080.1226
PJ14	170813.293	89541.5718	229582.4539	21222.65199	269190.6388
PJ15	174065.5085	122883.9082	156410.9784	52041.38981	351413.7491
PJ16	231718.5782	144255.7711	214569.6541	37185.89889	473120.4997
PJ17	150912.3271	82256.06908	156766.6803	10182.36964	353084.7036
PJ18	99849.77715	52590.63693	117300.8419	6040.048933	215264.7713
PJ19	46651.74908	25244.92179	53430.9432	3530.808708	93653.61721
PJ20	97644.78739	65689.13936	97304.06246	13834.83396	193969.0438
PJ21	144262.1523	103382.121	123897.5225	23666.08838	294739.5408
PJ22	147535.1338	58981.50142	208081.9509	10800.14837	306910.0131
PJ23	177308.046	133675.3847	169875.4905	7637.117435	352258.1025
PJ24	77786.26477	35718.48812	101896.797	1390.506214	162513.4749
PJ26	175591.0344	161899.3028	116897.5955	53362.72069	309559.8093
PJ27	92317.24132	58451.57799	98622.92934	5218.111517	193937.7851
PJ28	66990.11042	41663.48247	73831.33261	2537.267074	136356.5267
PJ30	117921.7498	34043.54612	163335.4896	3881.583795	282117.2874
PJ32	122895.798	86525.77682	113223.1469	16404.57043	239695.9873
PJ33	71718.82771	43833.05314	88391.97285	6256.892215	133110.8918
PJ34	62301.19168	43206.00659	57864.56882	5861.660164	128274.8893
PJ35	96004.76887	40047.63192	117941.9381	3250.662607	225638.1016
PJ36	59278.81015	29743.33772	78770.12268	1948.076097	106446.167
PJ38	80369.62238	44617.96926	91906.86801	12175.49333	149262.7815
PJ39	56659.767	30300.76618	63839.51603	4275.447633	130828.0897
PJ41	37328.43819	30955.36775	36462.60597	2968.860291	64066.59013
PJ42	58777.7151	48435.49381	50300.17335	8390.888288	113020.456
Mean	122251.62	79272.09	121743.08		
Std	52865.34	41775.77	49841.96		

TABLE C.4: Mean, median and standard deviation of the energy of the precipitating electrons for the southern outer emission region for a kappa energy flux of electrons.

S Kappa	Outer emission region				
	Mean energy (eV)	Median energy (eV)	Standard deviation	16^{th} percentile	84^{th} percentile
PJ1	29162.38361	23792.77489	28225.09938	2447.690372	53242.95564
PJ3	43671.2546	44117.00868	35794.57051	2872.299881	80641.51291
PJ4	47412.74112	46928.53331	40554.49031	2100.347229	79720.87977
PJ5	50157.16717	46212.32905	42415.11812	3701.996985	88981.57232
PJ6	54964.05366	54020.81082	43548.84163	4967.62027	96983.45942
PJ7	40241.76772	34715.32704	37736.08345	2702.140262	71888.18552
PJ8	65374.48387	61116.37523	48681.18452	9474.420128	115373.8583
PJ9	52868.00939	53467.94402	37037.00141	7361.891347	88729.60192
PJ10	36456.68941	34793.50332	32505.23592	3685.874325	59411.35339
PJ11	51840.1281	57268.64236	33858.82402	6080.852694	86291.33868
PJ12	36577.41639	29441.33819	34571.06236	1784.223706	70659.98721
PJ13	40684.61633	39402.15408	31829.54541	3630.806422	74440.18156
PJ14	33691.41639	29848.01725	28992.81572	1716.462203	64006.97992
PJ15	41513.93177	40046.09079	30266.83005	7060.920098	71387.57409
PJ16	35962.29143	36061.59001	25327.79028	5726.73228	60390.75744
PJ17	34440.85953	30884.1262	28353.16162	3561.059991	66051.73847
PJ18	48468.97972	30267.47579	63684.03059	3415.672434	77714.36904
PJ19	46642.76141	45358.3865	35226.0627	9787.767319	72396.12887
PJ20	52768.86355	45816.94521	46589.78667	6770.788451	86189.74571
PJ21	35488.88921	38644.25235	28615.47372	1007.61442	65074.14379
PJ22	52751.00716	49271.40384	41029.03163	6912.658831	96471.29478
PJ23	21558.96399	18576.03646	18268.68107	1280.472265	42777.99833
PJ24	46852.93556	40940.2403	47250.64969	4682.479932	68014.07581
PJ25	36125.38973	37594.38883	26556.73087	3737.442526	64114.8105
PJ26	35309.27041	28335.62549	32829.45578	1602.672254	66525.67201
PJ27	37436.61584	34069.40246	32703.57721	2054.184606	64270.78884
PJ28	42086.44638	42991.91391	34405.9603	4794.836517	71282.49254
PJ29	33169.53071	36253.21991	26416.00233	1279.951856	61469.45171
PJ30	53275.21579	55656.49757	41160.46296	3243.347048	96319.28221
PJ31	34190.61075	31213.01835	30614.56024	4002.31127	55513.08297
PJ32	29964.99203	28645.31417	27156.4329	1909.817566	53263.1862
PJ33	37283.08018	34265.16379	25345.38961	10419.51956	59824.60207
PJ34	34754.80471	36300.94312	24590.56461	4173.642086	59538.83156
PJ35	46661.14926	42359.45393	36711.71256	5812.283586	90216.03879
PJ36	39743.2497	37788.99039	31974.86541	2387.480994	76156.32182
PJ38	42043.05865	46279.3383	31392.29285	3858.884833	73788.04746
PJ39	59982.58777	50963.04812	45873.806	12257.18456	106383.6471
PJ41	35708.83518	30763.56451	30365.55992	2764.390171	70820.1499
PJ42	56978.66562	45557.56631	54056.6979	12074.15772	91602.28307
PJ43	55100.10438	42915.21668	52332.22068	5891.217985	95526.78503
PJ44	26264.34143	26691.57202	19703.86687	2679.132768	45713.12107
PJ45	28765.2901	24024.02197	24628.83432	2286.413525	56047.67108
PJ46	55614.71461	48573.03813	43531.89271	16657.99597	86542.38388
PJ48	40770.29794	39737.84835	33377.86445	3708.364974	69256.36938
Mean	42290.45	39362.96	35138.41		
Std	9855.73	9695.91	9403.85		

TABLE C.5: Mean, median and standard deviation of the energy of the precipitating electrons for the southern main emission region for a kappa energy flux of electrons.

S Kappa	Main emission region				
	Mean energy (eV)	Median energy (eV)	Standard deviation	16^{th} percentile	84^{th} percentile
PJ1	75898.63902	67399.06298	50811.52243	27034.89321	121965.6193
PJ3	93548.46907	81942.39515	43592.3516	59223.55415	130307.4665
PJ4	75457.13167	74592.71184	29556.1173	45378.43479	107428.5809
PJ5	89510.85056	73541.89855	54633.55066	37713.98846	152950.1807
PJ6	203120.9558	187880.2296	85888.20556	120327.4275	285458.0089
PJ7	114329.8338	106801.6204	61868.04979	50764.23813	188388.3245
PJ8	48420.79245	48203.48173	16786.4845	32542.66461	65598.4274
PJ9	109828.3161	86210.40464	71617.06132	53316.5106	189607.065
PJ10	225140.9597	207429.5352	113234.2614	113276.2491	336359.3096
PJ11	106553.0399	97770.67243	49234.23007	64851.26266	140014.4109
PJ12	213668.1524	203646.9001	86636.92737	138487.0465	268785.6213
PJ13	45577.28197	46134.77678	16597.8791	27781.00593	64096.76888
PJ14	103962.7755	92810.27096	67132.69902	55415.12603	127711.4685
PJ15	215020.3904	214206.4547	82771.26938	125723.6072	305026.743
PJ16	37968.91606	37650.62881	20342.53309	14237.3183	57714.35433
PJ17	37982.2041	31996.16121	25000.6169	13398.69193	68173.67108
PJ18	140845.6384	133991.6904	58389.89459	80002.00363	200495.1616
PJ19	79690.24663	68730.24096	53074.90194	32074.62658	125160.683
PJ20	103584.4659	87397.78704	63698.81763	49136.38495	163986.5301
PJ21	146007.4819	145498.9832	46113.52468	97138.43246	193889.8087
PJ22	68368.1019	69821.3386	29123.30347	36941.38518	89079.45881
PJ23	98826.03827	88420.76762	40990.30756	61169.94678	149502.3005
PJ24	50479.83281	45269.76809	37642.08449	17631.04159	70830.47696
PJ25	106965.4653	105026.8068	53750.90971	48008.3194	157942.2881
PJ26	198776.2952	201425.3457	64567.46628	128202.3578	267571.9114
PJ27	145344.1555	124022.227	87578.00618	67202.98346	224085.5789
PJ28	50142.05048	49971.85945	21329.23078	28477.31814	69123.82716
PJ29	113255.0383	98418.38919	67007.27364	49995.7528	181248.5471
PJ30	65220.30608	67091.9773	30252.25041	31082.93187	97908.32098
PJ31	109887.4589	92430.90435	84649.15748	30689.42281	170726.2506
PJ32	172656.1461	152599.2275	93724.44032	81697.5537	260013.6325
PJ33	71881.76397	63998.55434	35745.57535	36097.07066	112233.0457
PJ34	63335.77568	57973.70703	29208.95558	36526.63868	88436.09081
PJ35	90417.94501	81709.14411	36826.71912	56721.36412	128249.1041
PJ36	60657.3325	58997.52542	37502.40477	24600.82499	87771.4211
PJ38	124871.3553	115706.7762	51462.32729	76927.55061	181410.0141
PJ39	40050.92925	38272.81983	21008.89216	20324.70523	61312.65399
PJ41	58419.55138	51267.1519	34057.87824	24862.58437	97970.51046
PJ42	58129.58219	52199.38209	28130.34078	32990.89286	86840.93712
PJ43	93355.16976	69119.95473	68722.77003	42574.1559	145305.4663
PJ44	84624.78167	76869.2821	49549.52618	37981.82758	136942.4327
PJ45	97701.26247	96465.53078	39001.08408	54115.17701	137939.2685
PJ46	133066.4612	88062.66248	107833.1214	49564.13832	245063.5704
PJ48	137974.5367	140022.1321	60839.99455	63499.65684	203051.9045
Mean	103648.27	94977.25	52442.84		
Std	50563.02	48658.26	24696.03		

TABLE C.6: Mean, median and standard deviation of the energy of the precipitating electrons for the southern polar emission region for a kappa energy flux of electrons.

S Kappa	Polar emission region				
	Mean energy (eV)	Median energy (eV)	Standard deviation	16^{th} percentile	84^{th} percentile
PJ1	49569.56884	21717.28448	55585.72162	1528.772623	118533.7707
PJ3	70626.65962	23390.23377	115183.9137	1786.489792	124744.3604
PJ4	85053.2088	64206.14589	80907.68521	12214.66245	137057.9361
PJ5	63336.61949	45680.25474	58997.81864	7981.782954	131508.0994
PJ6	210972.9004	172827.9318	196301.428	18601.92161	420810.5127
PJ7	115123.9123	112965.0284	79437.56805	15461.05801	207324.6512
PJ8	43053.86283	29184.32086	45679.28635	4277.601934	79537.49865
PJ9	84504.44978	71649.34074	66252.72922	17587.08283	140866.8542
PJ10	113353.8758	82249.37116	100179.3775	25152.12504	205562.3943
PJ11	131873.3034	92203.21198	129392.8927	8454.707101	279253.6333
PJ12	144231.0826	132316.4312	102162.0578	36244.3273	238237.6289
PJ13	47769.71743	31861.80449	52428.65829	3045.035063	90655.83244
PJ14	131715.808	81121.54592	138629.486	13431.91253	266992.3297
PJ15	89630.07911	62956.89885	83775.77139	11449.21974	180446.9502
PJ16	75307.84715	54872.0316	81119.47198	4605.427948	135988.554
PJ17	18342.49723	5958.682517	26119.68639	404.1949609	43948.71681
PJ18	82531.92368	70701.79547	68249.25268	8006.974964	163824.4354
PJ19	86896.79133	66752.58702	79436.89926	2368.799979	179778.2037
PJ20	76754.91123	54485.36851	74502.68824	5322.728577	162534.6253
PJ21	72268.24056	51322.1912	66027.27458	8792.924157	144479.4254
PJ22	44581.30282	33792.39441	42573.094	4020.190527	82746.74219
PJ23	90762.42571	65793.7289	88826.01131	6699.843799	179115.6604
PJ24	36023.28204	21289.88013	46533.12082	1537.804818	63201.7399
PJ25	121362.1002	83042.67522	129202.2856	12187.41574	237110.3559
PJ26	125123.2664	119827.1515	87651.41182	19853.61279	229399.5818
PJ27	91381.86159	87785.94137	64914.57626	16816.56654	150812.2767
PJ28	66457.31926	66340.40654	51122.19139	5902.052311	118695.7961
PJ29	86541.38834	76104.48102	67715.03618	12240.0346	165548.5113
PJ30	43673.90958	25292.46555	43115.50831	2064.734954	97707.27195
PJ31	76391.10057	64906.32437	69813.20318	6132.776588	142055.397
PJ32	104555.8569	70561.8642	121222.9943	12615.18522	184419.5649
PJ33	77775.56034	60154.91955	65889.75971	14573.72623	138437.7322
PJ34	73382.12322	57976.24778	64555.32956	6530.433225	153823.9431
PJ35	65743.25099	48653.3186	62511.28982	2662.862861	136460.5887
PJ36	35730.34981	18086.35828	44291.14821	2130.681357	73612.13734
PJ38	55100.40401	32140.75011	56099.32184	3454.299082	123115.5592
PJ39	103427.5495	48354.88939	120983.5453	6199.87625	248944.3487
PJ41	47183.20733	28656.09114	48439.52027	4113.674494	102908.1599
PJ42	84563.76098	70729.62338	68246.45245	16958.6649	155615.0651
PJ43	166326.2242	109742.0076	171398.867	30187.67558	297071.9947
PJ44	112982.9234	111688.0873	85229.69759	12065.56056	206607.1599
PJ45	71559.75451	63041.6038	57646.77137	6029.59076	138275.0646
PJ46	88939.91588	54703.90122	94742.31162	4091.988018	186698.9862
PJ48	119096.6576	130555.6456	68391.3258	26314.49523	180853.621
Mean	85945.06	65400.98	80033.74		
Std	37122.85	34904.53	34801.04		

TABLE C.7: Mean, median and standard deviation of the energy of the precipitating electrons for the northern outer emission region for a monoenergetic flux of electrons.

N Mono	Outer emission region				
	Mean energy (eV)	Median energy (eV)	Standard deviation	16^{th} percentile	84^{th} percentile
PJ1	61364.16055	67536.24887	31912.35231	17177.48837	88516.99177
PJ3	48131.17253	59745.59324	28909.49338	7573.168564	75741.70673
PJ4	46777.67257	54525.31392	31471.4448	6205.797494	76390.93502
PJ5	55457.59899	64207.83963	24846.75392	25179.33284	77304.45723
PJ6	49439.46722	58640.40102	28850.35843	8966.616927	76787.00737
PJ7	53472.26096	63520.4155	32090.3595	8418.361445	83998.68138
PJ8	55217.12411	64050.7019	33322.68845	9136.340025	85344.13724
PJ9	54734.39162	67908.62485	29877.39206	10895.5064	81579.29433
PJ10	35859.22332	41238.0981	24661.19074	4058.134407	61474.69847
PJ11	45772.86915	57522.03053	26800.40491	7599.494849	70935.07249
PJ12	39684.08871	46834.09246	25400.48251	5284.580554	65862.69812
PJ13	43702.93647	51363.44377	27711.05289	6211.895889	73242.42822
PJ14	45148.51696	54668.92494	25530.38437	9145.629762	70233.68335
PJ15	42707.31791	50687.50269	28140.85898	5414.137758	69795.34817
PJ16	41666.20802	48279.54149	27642.98326	5579.438833	68916.66842
PJ17	39017.46919	40028.51039	28587.68145	4286.947979	73443.95934
PJ18	49353.07149	52137.46874	36591.70785	7095.561312	80746.17282
PJ19	42840.98518	44229.85885	30015.35232	5733.940061	75344.41253
PJ20	44720.03106	52115.5732	28388.04144	7228.570422	74788.09238
PJ21	40845.98611	51189.98806	26088.19664	4258.761436	66585.05593
PJ22	52699.15758	60334.70752	33139.7726	9232.033924	80918.83255
PJ23	30282.22654	29117.71931	23108.11994	3039.269122	56948.59739
PJ24	39483.14829	40546.59192	28655.75451	3551.822677	75227.28904
PJ26	32772.86144	33292.0099	24143.81819	3305.081649	60925.89033
PJ27	49936.20795	60508.98656	23945.26687	14773.75055	68906.57306
PJ28	41076.90494	48548.84858	25865.00519	5878.800613	66596.94369
PJ30	36498.79318	27872.19004	32652.07644	2103.615697	76386.1415
PJ32	41784.7514	49328.00409	27192.63096	5255.335638	69247.75172
PJ33	40155.8934	46117.9575	27362.19699	4292.884976	67597.78344
PJ34	39835.64242	47703.7644	26050.98896	5119.162764	67405.02249
PJ35	40501.97551	46543.10149	27676.8014	5129.901205	69224.93261
PJ36	35806.63524	30441.57754	29762.39152	1734.306031	71000.4067
PJ38	39301.17459	43200.47508	25898.89078	5662.548905	65702.20829
PJ39	48166.08532	50282.8888	34511.39865	5797.648227	80138.25277
PJ41	33813.21122	33656.07371	25033.31552	4136.968114	62740.36755
PJ42	41751.5425	43972.57691	28303.43342	6434.979127	73541.17022
Mean	43882.74	49497.16	28337.25		
Std	7079.77	10668.53	3220.96		

TABLE C.8: Mean, median and standard deviation of the energy of the precipitating electrons for the northern main emission region for a monoenergetic flux of electrons.

N Mono	Main emission region				
	Mean energy (eV)	Median energy (eV)	Standard deviation	16^{th} percentile	84^{th} percentile
PJ1	71413.73164	73263.08395	15509.35628	63029.22211	84114.32731
PJ3	68298.14754	69061.57119	22222.79962	56844.87418	80462.39628
PJ4	60870.6891	69175.1408	23807.79656	35767.73394	79563.03227
PJ5	83730.3672	80958.27969	15081.76909	70097.64348	101505.6588
PJ6	78197.68868	76650.75766	10611.81059	69199.47763	89541.20192
PJ7	81167.01659	81077.07465	23817.90674	61096.03161	106554.5776
PJ8	65393.76834	65301.71412	17461.53177	58825.82482	79974.39629
PJ9	82325.81457	80455.09635	18174.89092	70888.21129	102205.109
PJ10	83147.55573	87769.34001	31406.63234	59304.8839	109366.0896
PJ11	68017.44996	69549.22994	14232.46968	59616.50276	80176.7301
PJ12	80255.59623	83493.98119	19925.69238	65648.90036	96899.44476
PJ13	62410.73646	64918.91286	15720.39343	52045.9713	76158.79631
PJ14	67310.81385	68546.96629	15347.88904	56606.57661	81066.79277
PJ15	79080.25853	78315.34028	18218.03048	68630.44618	94092.37029
PJ16	63880.22379	67079.44136	20072.44497	50429.5621	81928.5941
PJ17	51943.04316	60501.84511	22290.56838	25213.86831	69790.92474
PJ18	56654.43138	65512.88262	29383.37639	17184.69748	83284.75956
PJ19	58244.53586	60486.94254	16644.91532	43193.00484	74359.16091
PJ20	71731.68491	78481.89976	23585.24773	54584.53825	90319.48449
PJ21	72729.87714	73496.12567	19043.46728	59135.45188	87925.51854
PJ22	67715.77721	69240.17562	13837.40702	60821.00628	76261.25474
PJ23	49148.78221	57144.41158	22349.86783	20091.79147	67575.10579
PJ24	54182.47401	57097.80159	21051.23147	33908.0897	73259.73888
PJ26	79561.60601	80135.39002	22418.76978	61748.56025	96608.40407
PJ27	66546.0522	73266.67471	37676.61344	16826.40378	102414.0276
PJ28	54035.8477	60926.33968	21003.12229	30718.99067	69840.26193
PJ30	49227.64775	56633.52545	25069.80991	15818.07601	69523.97928
PJ32	84382.69146	81037.51031	28213.16885	66620.27165	111209.4315
PJ33	61435.34582	63836.68567	19552.33866	45111.93436	77741.33267
PJ34	58044.95743	63046.76204	20029.54476	42967.14018	71763.56268
PJ35	62564.78624	67615.42049	19111.3905	47718.85468	76422.60343
PJ36	45214.63639	47060.10481	20395.81451	22045.60383	65101.42167
PJ38	67615.20716	70949.82661	19954.69472	50528.03285	85527.19923
PJ39	56599.42777	58791.84333	16768.97169	44014.95839	73042.07848
PJ41	49527.33387	57729.57741	22270.25529	20544.14652	69379.75983
PJ42	52493.57771	61527.61219	27502.40283	13788.17103	79403.93874
Mean	65697.21	68892.65	20826.79		
Std	11437.14	9366.78	5362.91		

TABLE C.9: Mean, median and standard deviation of the energy of the precipitating electrons for the northern polar emission region for a monoenergetic flux of electrons.

N Mono	Polar emission region				
	Mean energy (eV)	Median energy (eV)	Standard deviation	16^{th} percentile	84^{th} percentile
PJ1	68942.36213	77203.00776	39642.56596	11686.97964	107080.7308
PJ3	81088.5493	84373.49066	53922.45461	12509.26161	134819.8534
PJ4	83805.37129	79295.9259	48566.5885	26731.13227	134523.9812
PJ5	97409.87186	89671.2764	38977.55319	71396.36869	139247.4243
PJ6	96193.43997	92637.80663	38101.11244	66791.1168	138031.1761
PJ7	78438.82788	84841.62727	34267.55797	41175.13219	103112.6868
PJ8	49978.00545	51799.02708	37706.23642	4752.476881	92510.01898
PJ9	89331.65503	88463.57277	37703.67767	65785.73132	125806.0349
PJ10	75666.01815	90051.13542	48074.75922	14722.76495	106526.328
PJ11	99905.81109	97805.37676	57708.36984	35579.2794	163200.2162
PJ12	104982.3665	100814.3877	41730.70865	74211.22582	150824.153
PJ13	66689.12704	67260.60208	52793.46092	6258.232091	122490.1613
PJ14	82566.5509	76868.98269	55600.24355	24731.68202	118030.7569
PJ15	90906.74666	91154.87637	44444.94038	45687.76619	136586.6886
PJ16	105413.756	97339.05155	55002.95634	57957.76926	165241.4042
PJ17	81081.54438	77774.34261	50436.27908	19531.36131	141184.42
PJ18	51849.03596	41313.04802	45561.35272	4819.894351	104190.2896
PJ19	51597.52339	55893.35561	31109.0236	9995.543682	81669.87987
PJ20	67819.96965	73208.09358	39609.02391	15425.4809	107042.3852
PJ21	81949.71928	83515.00103	44823.65698	21994.76171	130511.5018
PJ22	77181.06771	70562.47874	56599.19952	15788.80715	131619.3378
PJ23	81647.95681	88113.96168	57119.89675	9191.6082	139846.0385
PJ24	50532.97376	44342.70345	43644.23334	3507.184353	99089.00801
PJ26	93104.04216	101387.7699	41517.84288	44947.94799	133378.7891
PJ27	52944.32961	43687.03955	44961.37644	4551.580142	103544.9678
PJ28	52060.95058	52122.47413	39499.62344	5294.079189	95250.49461
PJ30	65184.59465	57232.09175	53343.3699	7926.488343	126916.7316
PJ32	69884.84346	74492.41941	45171.49533	12289.72207	116292.0423
PJ33	52704.04586	57031.33253	38324.05822	7206.838195	87913.26161
PJ34	52480.07749	57594.46128	35283.77632	8239.050245	92261.64186
PJ35	58342.21012	55161.68078	47122.43154	5216.954913	114782.1798
PJ36	50466.09228	50331.08069	34730.33686	9091.965609	83362.63723
PJ38	62008.6573	65578.24406	36125.21819	16514.88353	93673.99875
PJ39	51796.19509	56323.81779	34399.99293	8347.893523	90844.00548
PJ41	45314.46698	57157.58739	31578.81535	4221.049933	74642.69166
PJ42	53616.54798	63422.74055	33463.10844	9831.583181	87827.74479
Mean	71524.59	72106.27	43574.09		
Std	18201.65	17838.76	7944.35		

TABLE C.10: Mean, median and standard deviation of the energy of the precipitating electrons for the southern outer emission region for a monoenergetic flux of electrons.

S Mono	Outer emission region				
	Mean energy (eV)	Median energy (eV)	Standard deviation	16^{th} percentile	84^{th} percentile
PJ1	43825.02723	53911.80385	25518.43062	8513.703294	66929.85369
PJ3	49490.73139	63334.65263	29117.72801	8357.383711	76687.17167
PJ4	53166.24609	65450.67493	28252.77413	12364.38049	76448.2856
PJ5	51134.65582	64234.25731	30220.34991	8545.129269	78506.90949
PJ6	52645.89469	66991.28091	30999.07457	9252.199912	81369.84256
PJ7	47301.00408	60456.74164	29446.4351	6101.584439	74103.17714
PJ8	59806.75214	69527.01352	29200.8338	18450.90301	85767.31205
PJ9	53292.87329	67205.4688	29335.13356	9875.190754	78871.03544
PJ10	47195.90244	60513.16133	27156.56706	8648.790423	70133.54904
PJ11	52871.62384	68770.23486	29409.86413	8731.385162	78239.62758
PJ12	42691.74001	48084.11329	29985.71203	4654.165692	73915.00694
PJ13	48923.91633	60760.06943	27590.402	9253.963355	74518.86255
PJ14	45376.36181	57531.95691	27611.39132	6634.978075	71827.17327
PJ15	52415.51607	63357.32323	25839.44458	14121.68269	74028.97241
PJ16	48149.37527	60904.18749	26058.93942	9800.964613	70600.37493
PJ17	46607.38808	57777.94115	26811.2407	8101.476062	71972.74978
PJ18	51248.06729	58865.72674	30600.0514	10043.6106	75077.72727
PJ19	53852.64865	65219.08278	26213.95789	16352.32464	74272.34435
PJ20	56259.42109	65381.37594	27691.09688	18494.40666	78077.22269
PJ21	47832.17596	61401.25568	26818.44543	9952.841124	72409.93369
PJ22	55989.53985	64666.15862	26884.51696	19588.72353	80242.57263
PJ23	40030.72211	49402.61102	25174.15639	5657.593913	65424.9736
PJ24	50487.21305	62743.44752	29243.14366	10264.72567	72717.94976
PJ25	46937.57028	61985.51611	27227.41396	8281.644775	71929.76743
PJ26	46674.18426	58306.35479	27961.89054	7023.555838	72680.50444
PJ27	50227.10358	60856.30822	26456.4376	11469.74596	71835.37237
PJ28	49855.35079	61414.70709	27399.05392	11233.74934	73969.64675
PJ29	44488.13705	56044.36236	27535.76664	6237.202158	71207.68865
PJ30	53453.91914	66210.05529	29776.35363	10915.76816	81147.77865
PJ31	48666.72571	60611.13619	25712.14726	11556.67361	69146.76656
PJ32	45321.38215	56294.61981	26336.18019	7756.082073	68742.92
PJ33	51581.6284	61143.97158	23738.86888	17464.11993	69998.45406
PJ34	47859.19703	60830.57575	25947.70803	9710.878267	70172.41774
PJ35	53311.96776	63588.9772	27402.67997	13497.03055	79374.01522
PJ36	47509.08011	61299.96077	29036.1681	6856.282187	75718.74893
PJ38	49660.39598	63623.13495	27737.32437	10143.02586	74622.76672
PJ39	58530.17198	66247.35968	27683.75255	22117.10436	83271.81846
PJ41	48059.37768	58513.28138	26894.24766	9689.384632	74189.42506
PJ42	57386.93706	65706.67342	28290.1263	18324.38392	79386.70546
PJ43	55486.50522	64114.50099	30034.07252	12877.01894	81027.80854
PJ44	44892.51412	58632.87924	24855.8114	8001.435573	66063.29516
PJ45	45113.50381	56359.80318	25539.9929	8170.300405	69248.29702
PJ46	58782.47581	66418.12902	26195.89038	24942.50192	78255.84614
PJ48	50364.79053	63955.09735	27948.77861	8250.158233	73736.66556
Mean	50108.13	61560.18	27611.14		
Std	4519.68	4561.35	1687.23		

TABLE C.11: Mean, median and standard deviation of the energy of the precipitating electrons for the southern main emission region for a monoenergetic flux of electrons.

S Mono	Main emission region				
	Mean energy (eV)	Median energy (eV)	Standard deviation	16^{th} percentile	84^{th} percentile
PJ1	67940.45705	71504.09501	23090.8035	49485.22272	87189.37271
PJ3	78239.11593	76898.66414	13052.39436	69844.39598	88731.87775
PJ4	72237.74385	74597.6367	14363.19038	63922.4948	84294.81467
PJ5	76027.12317	74780.09315	18740.57452	63487.68528	95227.83534
PJ6	104965.7955	102988.436	17992.57227	87082.13925	121924.8733
PJ7	80143.99908	83221.90845	24341.56676	65046.58773	102999.9973
PJ8	65080.148	67001.77498	10452.59927	61329.39732	72539.3197
PJ9	80764.34386	78253.88016	21945.32556	67047.86148	103552.2191
PJ10	108700.3679	106988.0953	23858.70041	85392.08613	132289.2062
PJ11	82328.62461	81458.89921	13387.62133	71600.27802	92245.13843
PJ12	106237.3151	106167.5084	19453.89748	90582.57871	118682.9741
PJ13	63920.71571	66337.02418	10545.84845	58379.39445	72199.50403
PJ14	80596.87396	80110.79635	17514.99288	68398.43043	89301.13365
PJ15	106138.4256	107693.3046	20298.72786	87064.23764	126354.6637
PJ16	60817.23546	63581.68789	12323.72592	54162.92969	70080.50673
PJ17	56229.43437	60860.00007	19259.81774	36838.49467	73243.46718
PJ18	89991.51147	90102.52692	16139.60217	75728.88043	105382.1416
PJ19	72835.06943	73305.50401	19132.75943	61153.092	88128.53606
PJ20	78959.27832	78666.21492	21179.76618	66746.46736	97541.79401
PJ21	92216.89525	92900.67231	11617.76837	80715.76897	103695.5535
PJ22	71184.92618	73882.69376	13060.1089	62276.81683	79247.77239
PJ23	78886.28154	78272.34498	14722.80603	69105.07109	94239.30973
PJ24	60442.91608	65443.61357	21558.3895	40766.24649	73937.96906
PJ25	81088.70996	82415.61343	17279.89585	66063.73725	96172.83362
PJ26	104211.83	105520.9747	14307.81013	88644.55066	119027.7273
PJ27	91285.52347	87886.55026	20025.35674	72682.50987	110664.9554
PJ28	64652.45108	67753.91362	13846.58157	59518.61653	73622.2421
PJ29	81618.54866	80874.442	20600.28002	65689.22427	101566.604
PJ30	68228.00159	72556.04157	17536.68687	60434.1332	81804.13757
PJ31	81245.23561	80009.55558	22229.12231	60860.10814	98917.24828
PJ32	97653.06315	95150.38453	20624.37175	76631.75441	117169.0379
PJ33	73464.47901	71683.06961	10312.22887	62982.5556	85146.4454
PJ34	70116.74078	70133.27594	10986.91024	62242.32495	79219.90185
PJ35	78646.21813	77169.69025	10508.88276	69402.48307	88986.45536
PJ36	67084.90948	69847.17159	15947.55096	57417.73157	78743.2799
PJ38	85437.08842	85374.30047	16921.36718	74383.89817	101622.8386
PJ39	57456.83677	63656.10743	18844.64259	39924.95274	70864.2132
PJ41	64305.64202	67542.6381	19269.87217	50849.9904	81212.67944
PJ42	66536.00481	68064.7913	15658.66612	60692.3804	78764.76623
PJ43	78459.96969	73418.18747	16992.23546	65030.37174	93288.46637
PJ44	71310.94447	74703.50197	22771.60212	54575.0827	90889.71622
PJ45	78125.38999	79948.58975	14900.18161	65997.59133	91428.3889
PJ46	85654.09526	78229.29525	26998.5168	66738.53739	114689.0516
PJ48	90477.73796	91754.35886	14840.92297	71974.05235	106249.085
Mean	78907.82	79516.13	17259.94		
Std	13704.84	12435.75	4253.58		

TABLE C.12: Mean, median and standard deviation of the energy of the precipitating electrons for the southern polar emission region for a monoenergetic flux of electrons.

S Mono	Polar emission region				
	Mean energy (eV)	Median energy (eV)	Standard deviation	16^{th} percentile	84^{th} percentile
PJ1	32056.19057	17229.37015	32861.74737	1820.587668	80441.35675
PJ3	41369.34289	27688.4624	42180.63671	2573.152645	81199.18988
PJ4	60762.40875	68646.69073	35173.57729	13997.08246	89812.67734
PJ5	51347.52051	55253.02971	32441.7772	9239.792001	86576.67932
PJ6	85281.91819	94946.8869	57289.39089	11860.04842	143618.9943
PJ7	69172.19954	82067.75255	38545.93746	12978.71426	106763.8492
PJ8	41017.792	39998.91721	29591.04493	5859.059163	72910.12923
PJ9	63303.54079	71704.14746	33129.25103	16186.19334	91292.64016
PJ10	64278.65227	71525.53948	38268.68543	15815.044	98461.06368
PJ11	64817.03573	64603.84724	47765.98279	7895.499131	119603.0624
PJ12	75215.70371	86460.48074	39667.33655	19791.03412	110054.0599
PJ13	41348.08203	36773.48977	32080.4809	4797.362832	76675.60993
PJ14	68602.47207	70990.0376	45123.87548	13912.26232	113696.5423
PJ15	57616.04387	64861.6165	38365.39788	9426.279931	99331.48512
PJ16	53479.52535	58693.76148	37244.24025	7464.551348	88303.08372
PJ17	19027.90078	8803.270777	22636.75104	844.2950755	45381.57663
PJ18	54955.88523	63903.11082	37170.43237	7640.19516	96117.21259
PJ19	56018.44186	64664.31379	41023.64024	3981.800772	101227.4709
PJ20	51053.73603	49394.44151	38303.77492	6113.177248	96598.0542
PJ21	55147.10058	61328.66289	33381.34148	11652.6564	89224.8537
PJ22	42598.41827	41845.74002	30374.81579	6561.661755	76562.18042
PJ23	51154.98631	48226.49505	39412.39336	5439.49551	95515.0468
PJ24	30956.74516	20817.83284	29830.23217	1639.770895	66618.17164
PJ25	61187.16077	67476.6607	44316.81172	8502.466057	105008.1838
PJ26	72092.22376	84529.13794	39463.52751	16479.96634	111716.0282
PJ27	64739.96568	77646.17974	34090.95835	15700.35791	94444.02597
PJ28	54579.19723	68064.49511	33350.52455	8650.468212	86918.73326
PJ29	54159.82826	56021.9687	36237.58672	9390.044108	94920.69408
PJ30	35843.80989	23836.39194	32361.37676	2345.922459	80322.03806
PJ31	53710.84028	61237.08446	36679.44287	7674.677218	91147.72995
PJ32	64406.11074	68432.20061	39920.16173	16564.94037	98311.42359
PJ33	59139.28385	64639.99359	32528.57062	14919.65373	90053.49819
PJ34	57203.39505	62644.05496	33780.02257	13104.86291	95058.20237
PJ35	48460.68632	46436.76746	35086.58807	6611.530698	89587.18936
PJ36	31986.15266	22910.2306	28668.50108	3361.282595	65759.24635
PJ38	43183.9862	40322.00198	33814.16718	4259.454731	85706.43197
PJ39	60455.4852	59148.03053	43730.49959	8531.001321	112777.9288
PJ41	45953.65982	48447.21415	30757.39233	7903.58213	80582.76461
PJ42	62700.03744	68639.62757	32821.52648	19013.24614	94372.7841
PJ43	82350.69007	82939.31556	47194.33971	25719.52814	122547.3936
PJ44	66706.14357	82138.14334	40753.354	10291.54683	106380.1668
PJ45	49802.39317	48705.14495	36743.37239	5063.253433	91783.84259
PJ46	55242.48583	51762.98941	41642.55504	6313.743907	102067.7507
PJ48	74037.00899	88974.47094	35144.28509	20488.37825	101536.2705
Mean	55193.69	57849.55	36839.73		
Std	13835.52	20456.28	6055.11		

D

Brightness - energy correlation

In this annex, we display the correlation plots between the H_2 brightness and the energy of the electrons for each auroral subregion for the 20 first perijoves.

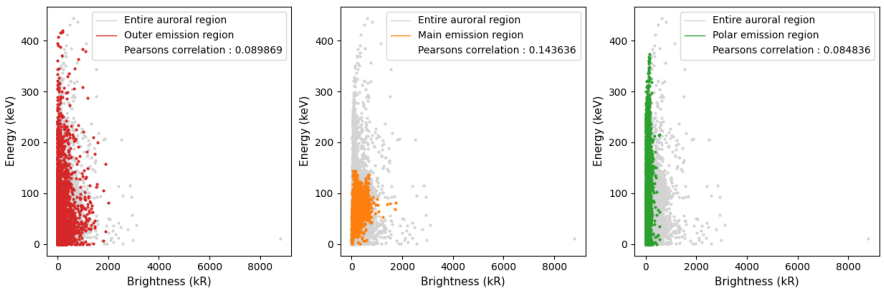

Relation between the brightness of the northern aurora (x-axis) and the mean energy of the population of electrons following a kappa distribution precipitating in the jovian atmosphere (y-axis) during PJ1. The grey dots represent the relation for the whole northern aurora, on top of which we have plotted in red the relation for the outer zone, in orange for the main emission zones and in green for the polar emission zone.

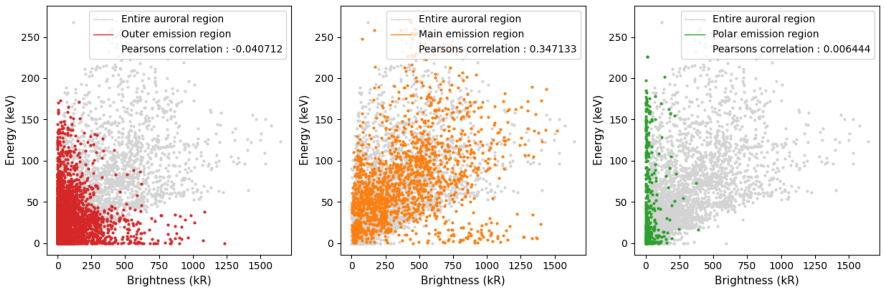

Relation between the brightness of the southern aurora (x-axis) and the mean energy of the population of electrons following a kappa distribution precipitating in the jovian atmosphere (y-axis) during PJ1. The grey dots represent the relation for the whole northern aurora, on top of which we have plotted in red the relation for the outer zone, in orange for the main emission zones and in green for the polar emission zone.

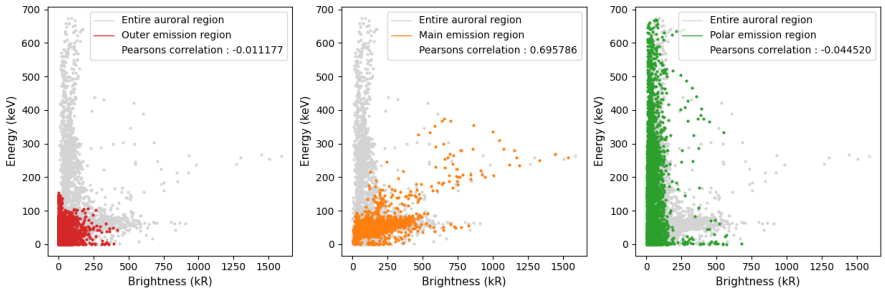

Relation between the brightness of the northern aurora (x-axis) and the mean energy of the population of electrons following a kappa distribution precipitating in the jovian atmosphere (y-axis) during PJ3. The grey dots represent the relation for the whole northern aurora, on top of which we have plotted in red the relation for the outer zone, in orange for the main emission zones and in green for the polar emission zone.

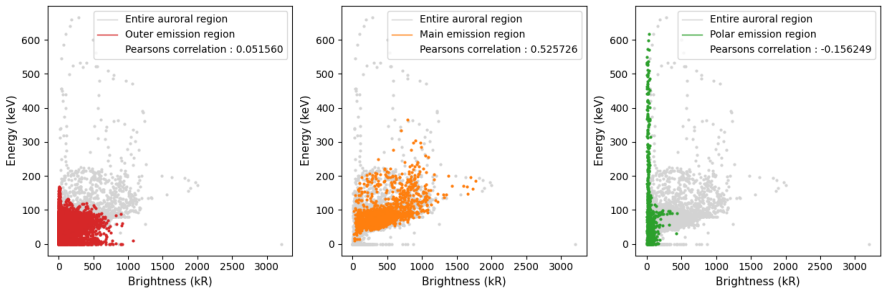

Relation between the brightness of the southern aurora (x-axis) and the mean energy of the population of electrons following a kappa distribution precipitating in the jovian atmosphere (y-axis) during PJ3. The grey dots represent the relation for the whole northern aurora, on top of which we have plotted in red the relation for the outer zone, in orange for the main emission zones and in green for the polar emission zone.

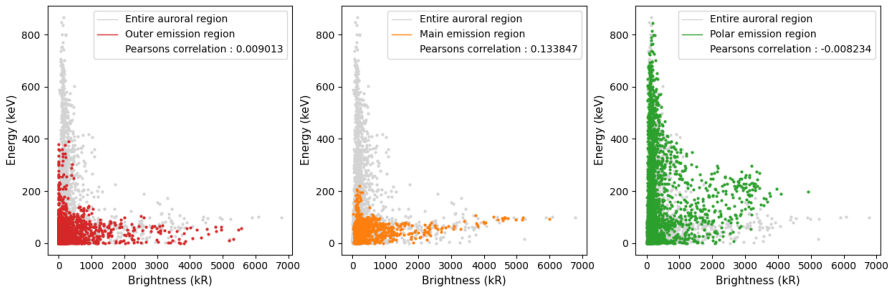

Relation between the brightness of the northern aurora (x-axis) and the mean energy of the population of electrons following a kappa distribution precipitating in the jovian atmosphere (y-axis) during PJ4. The grey dots represent the relation for the whole northern aurora, on top of which we have plotted in red the relation for the outer zone, in orange for the main emission zones and in green for the polar emission zone.

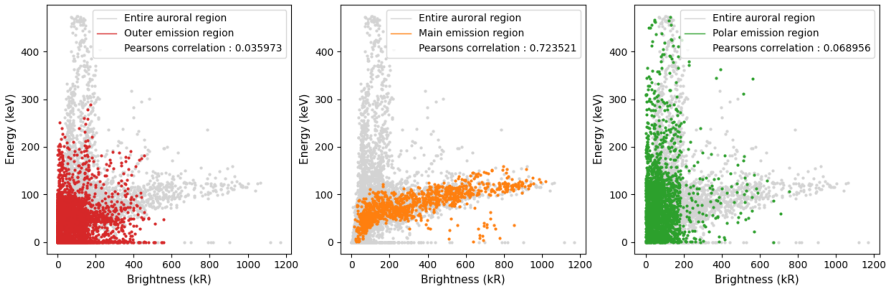

Relation between the brightness of the southern aurora (x-axis) and the mean energy of the population of electrons following a kappa distribution precipitating in the jovian atmosphere (y-axis) during PJ4. The grey dots represent the relation for the whole northern aurora, on top of which we have plotted in red the relation for the outer zone, in orange for the main emission zones and in green for the polar emission zone.

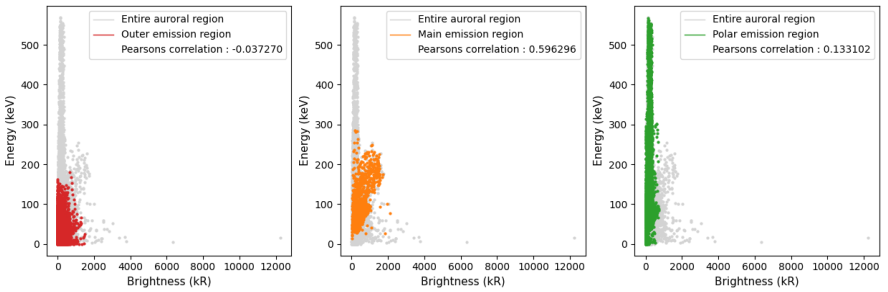

Relation between the brightness of the northern aurora (x-axis) and the mean energy of the population of electrons following a kappa distribution precipitating in the jovian atmosphere (y-axis) during PJ5. The grey dots represent the relation for the whole northern aurora, on top of which we have plotted in red the relation for the outer zone, in orange for the main emission zones and in green for the polar emission zone.

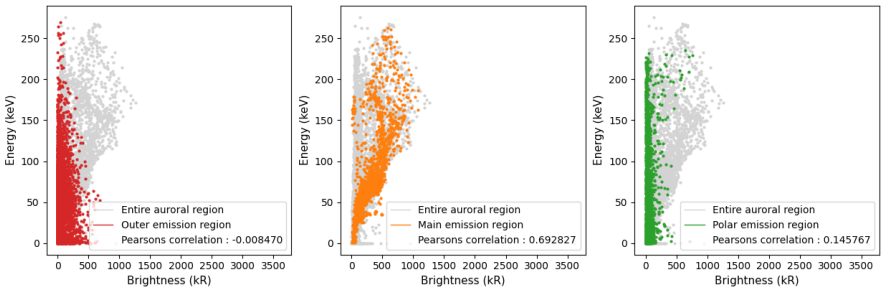

Relation between the brightness of the southern aurora (x-axis) and the mean energy of the population of electrons following a kappa distribution precipitating in the jovian atmosphere (y-axis) during PJ5. The grey dots represent the relation for the whole northern aurora, on top of which we have plotted in red the relation for the outer zone, in orange for the main emission zones and in green for the polar emission zone.

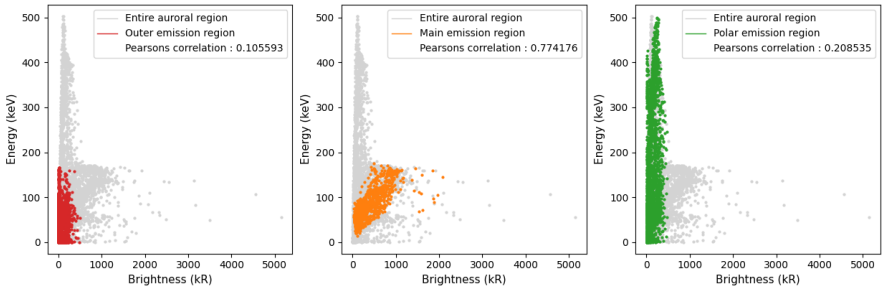

Relation between the brightness of the northern aurora (x-axis) and the mean energy of the population of electrons following a kappa distribution precipitating in the jovian atmosphere (y-axis) during PJ6. The grey dots represent the relation for the whole northern aurora, on top of which we have plotted in red the relation for the outer zone, in orange for the main emission zones and in green for the polar emission zone.

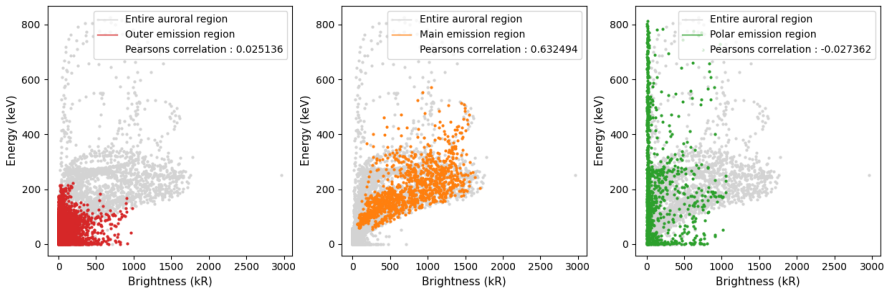

Relation between the brightness of the southern aurora (x-axis) and the mean energy of the population of electrons following a kappa distribution precipitating in the jovian atmosphere (y-axis) during PJ6. The grey dots represent the relation for the whole northern aurora, on top of which we have plotted in red the relation for the outer zone, in orange for the main emission zones and in green for the polar emission zone.

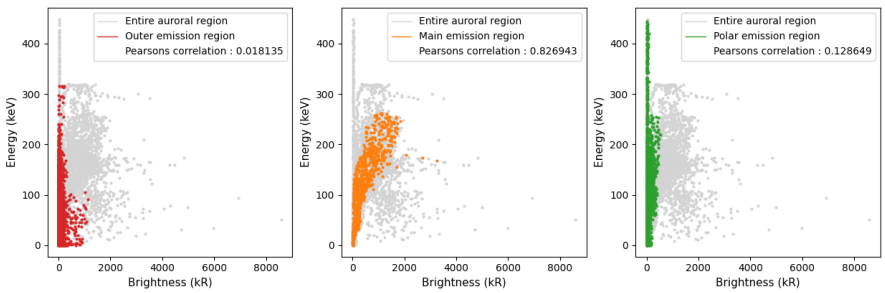

Relation between the brightness of the northern aurora (x-axis) and the mean energy of the population of electrons following a kappa distribution precipitating in the jovian atmosphere (y-axis) during PJ7. The grey dots represent the relation for the whole northern aurora, on top of which we have plotted in red the relation for the outer zone, in orange for the main emission zones and in green for the polar emission zone.

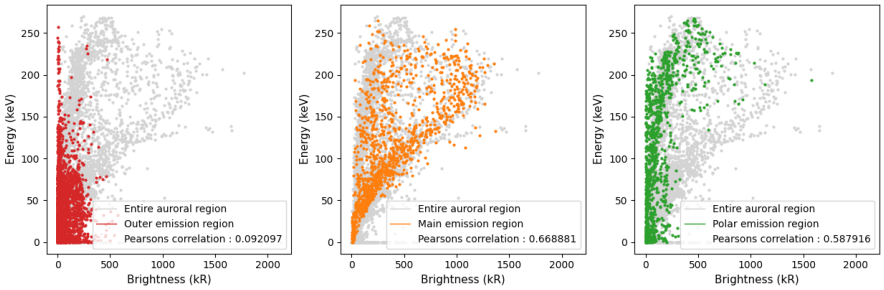

Relation between the brightness of the southern aurora (x-axis) and the mean energy of the population of electrons following a kappa distribution precipitating in the jovian atmosphere (y-axis) during PJ7. The grey dots represent the relation for the whole northern aurora, on top of which we have plotted in red the relation for the outer zone, in orange for the main emission zones and in green for the polar emission zone.

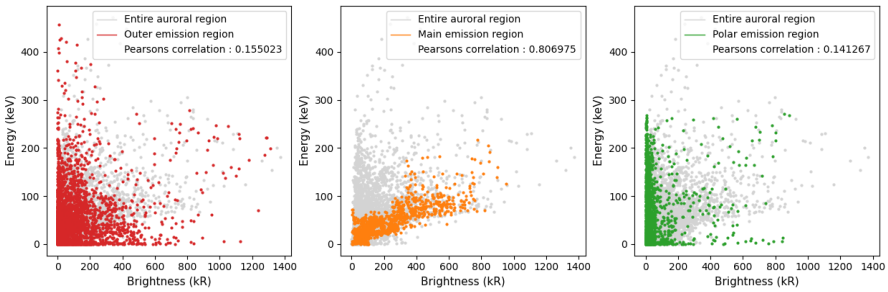

Relation between the brightness of the northern aurora (x-axis) and the mean energy of the population of electrons following a kappa distribution precipitating in the jovian atmosphere (y-axis) during PJ8. The grey dots represent the relation for the whole northern aurora, on top of which we have plotted in red the relation for the outer zone, in orange for the main emission zones and in green for the polar emission zone.

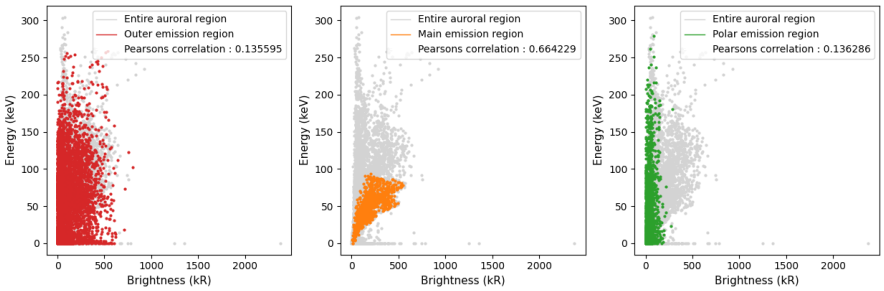

Relation between the brightness of the southern aurora (x-axis) and the mean energy of the population of electrons following a kappa distribution precipitating in the jovian atmosphere (y-axis) during PJ8. The grey dots represent the relation for the whole northern aurora, on top of which we have plotted in red the relation for the outer zone, in orange for the main emission zones and in green for the polar emission zone.

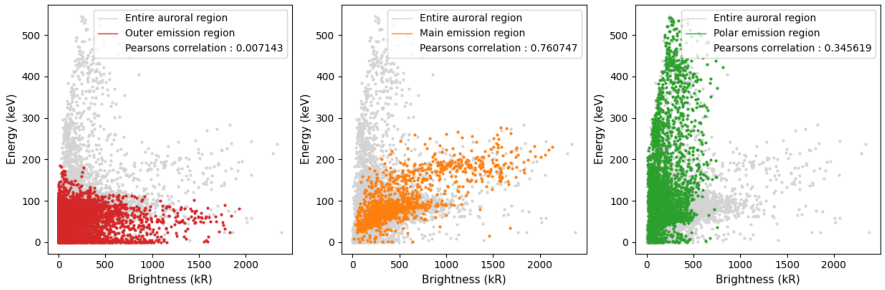

Relation between the brightness of the northern aurora (x-axis) and the mean energy of the population of electrons following a kappa distribution precipitating in the jovian atmosphere (y-axis) during PJ9. The grey dots represent the relation for the whole northern aurora, on top of which we have plotted in red the relation for the outer zone, in orange for the main emission zones and in green for the polar emission zone.

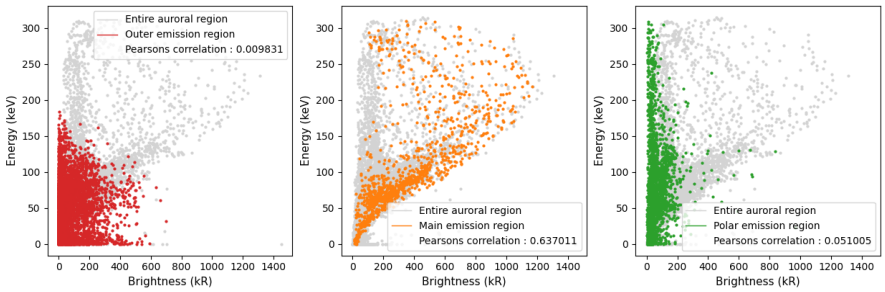

Relation between the brightness of the southern aurora (x-axis) and the mean energy of the population of electrons following a kappa distribution precipitating in the jovian atmosphere (y-axis) during PJ9. The grey dots represent the relation for the whole northern aurora, on top of which we have plotted in red the relation for the outer zone, in orange for the main emission zones and in green for the polar emission zone.

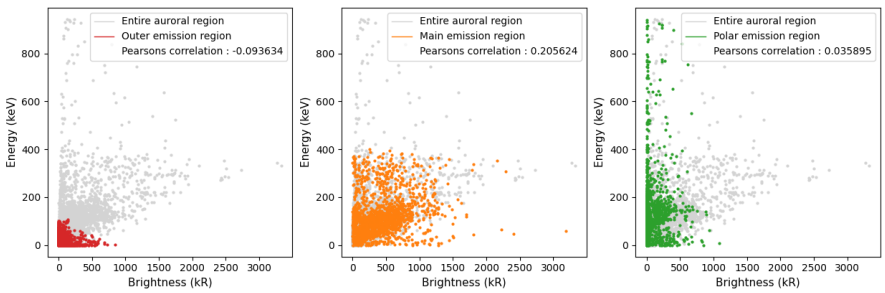

Relation between the brightness of the northern aurora (x-axis) and the mean energy of the population of electrons following a kappa distribution precipitating in the jovian atmosphere (y-axis) during PJ10. The grey dots represent the relation for the whole northern aurora, on top of which we have plotted in red the relation for the outer zone, in orange for the main emission zones and in green for the polar emission zone.

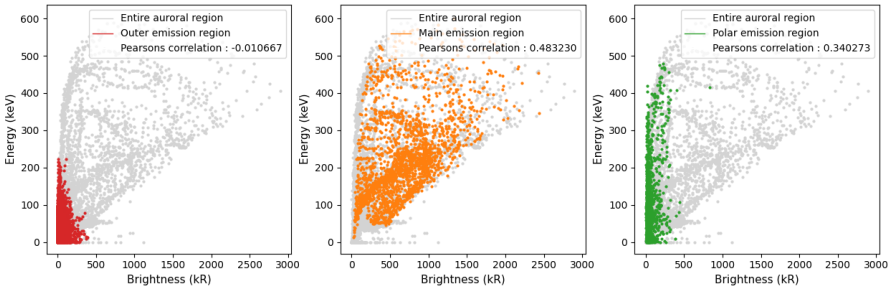

Relation between the brightness of the southern aurora (x-axis) and the mean energy of the population of electrons following a kappa distribution precipitating in the jovian atmosphere (y-axis) during PJ10. The grey dots represent the relation for the whole northern aurora, on top of which we have plotted in red the relation for the outer zone, in orange for the main emission zones and in green for the polar emission zone.

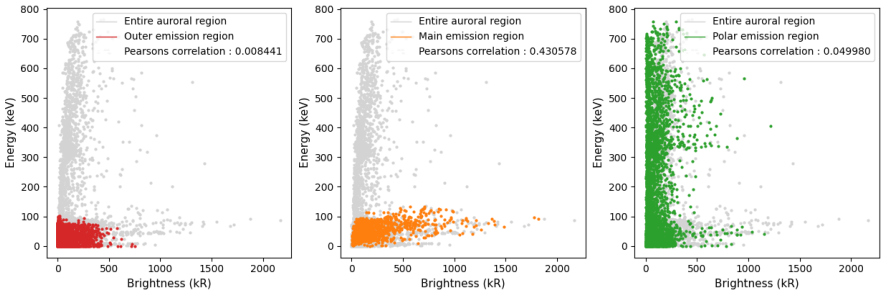

Relation between the brightness of the northern aurora (x-axis) and the mean energy of the population of electrons following a kappa distribution precipitating in the jovian atmosphere (y-axis) during PJ11. The grey dots represent the relation for the whole northern aurora, on top of which we have plotted in red the relation for the outer zone, in orange for the main emission zones and in green for the polar emission zone.

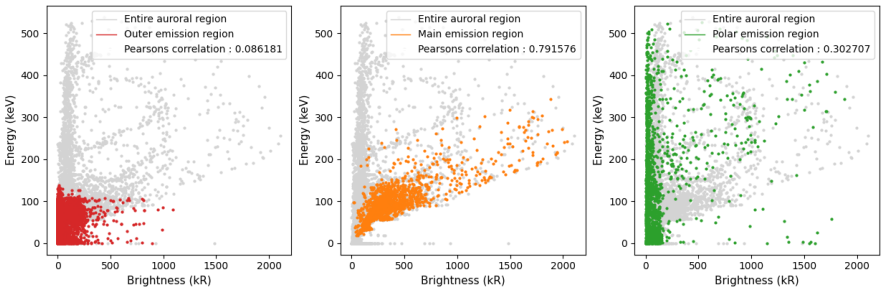

Relation between the brightness of the southern aurora (x-axis) and the mean energy of the population of electrons following a kappa distribution precipitating in the jovian atmosphere (y-axis) during PJ11. The grey dots represent the relation for the whole northern aurora, on top of which we have plotted in red the relation for the outer zone, in orange for the main emission zones and in green for the polar emission zone.

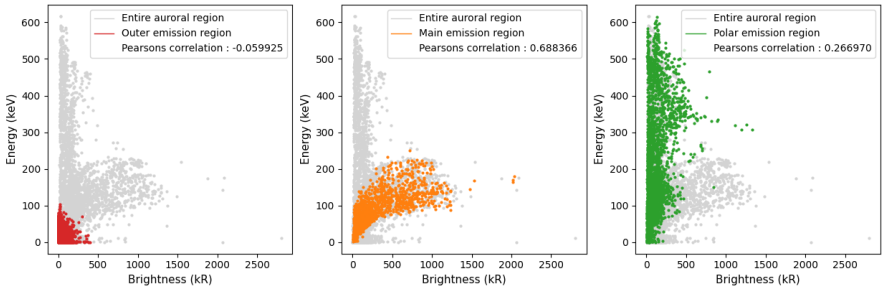

Relation between the brightness of the northern aurora (x-axis) and the mean energy of the population of electrons following a kappa distribution precipitating in the jovian atmosphere (y-axis) during PJ12. The grey dots represent the relation for the whole northern aurora, on top of which we have plotted in red the relation for the outer zone, in orange for the main emission zones and in green for the polar emission zone.

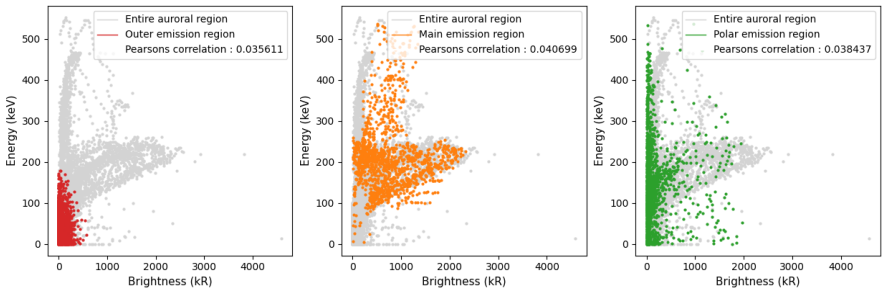

Relation between the brightness of the southern aurora (x-axis) and the mean energy of the population of electrons following a kappa distribution precipitating in the jovian atmosphere (y-axis) during PJ12. The grey dots represent the relation for the whole northern aurora, on top of which we have plotted in red the relation for the outer zone, in orange for the main emission zones and in green for the polar emission zone.

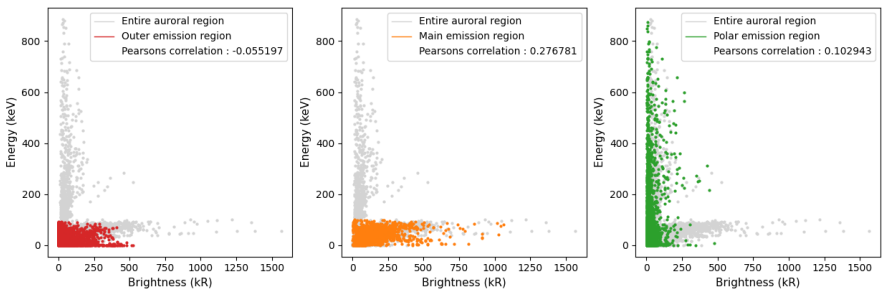

Relation between the brightness of the northern aurora (x-axis) and the mean energy of the population of electrons following a kappa distribution precipitating in the jovian atmosphere (y-axis) during PJ13. The grey dots represent the relation for the whole northern aurora, on top of which we have plotted in red the relation for the outer zone, in orange for the main emission zones and in green for the polar emission zone.

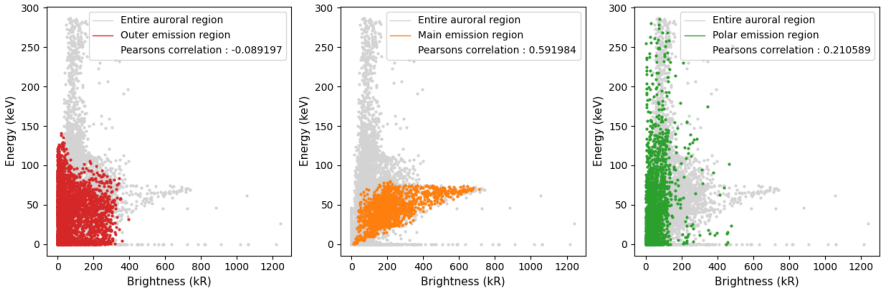

Relation between the brightness of the southern aurora (x-axis) and the mean energy of the population of electrons following a kappa distribution precipitating in the jovian atmosphere (y-axis) during PJ13. The grey dots represent the relation for the whole northern aurora, on top of which we have plotted in red the relation for the outer zone, in orange for the main emission zones and in green for the polar emission zone.

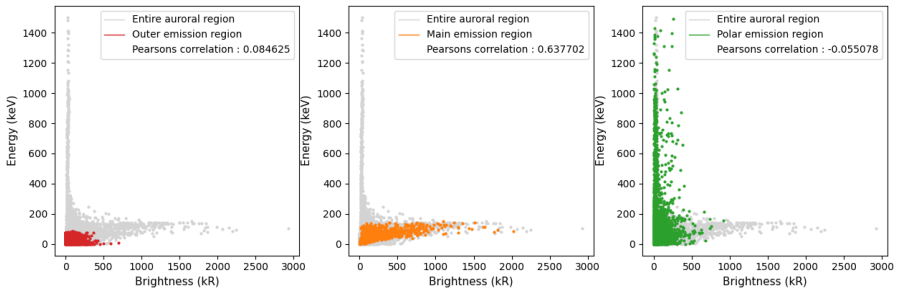

Relation between the brightness of the northern aurora (x-axis) and the mean energy of the population of electrons following a kappa distribution precipitating in the jovian atmosphere (y-axis) during PJ14. The grey dots represent the relation for the whole northern aurora, on top of which we have plotted in red the relation for the outer zone, in orange for the main emission zones and in green for the polar emission zone.

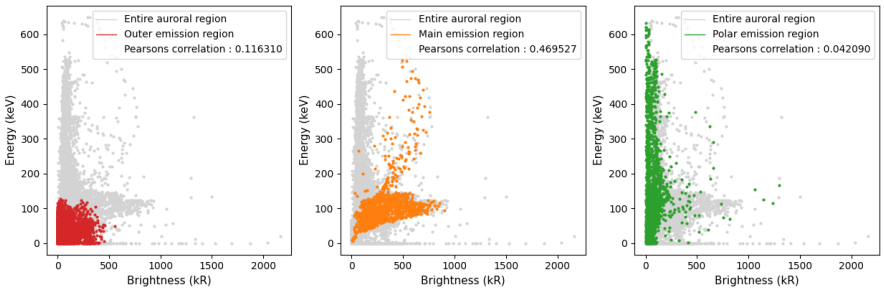

Relation between the brightness of the southern aurora (x-axis) and the mean energy of the population of electrons following a kappa distribution precipitating in the jovian atmosphere (y-axis) during PJ14. The grey dots represent the relation for the whole northern aurora, on top of which we have plotted in red the relation for the outer zone, in orange for the main emission zones and in green for the polar emission zone.

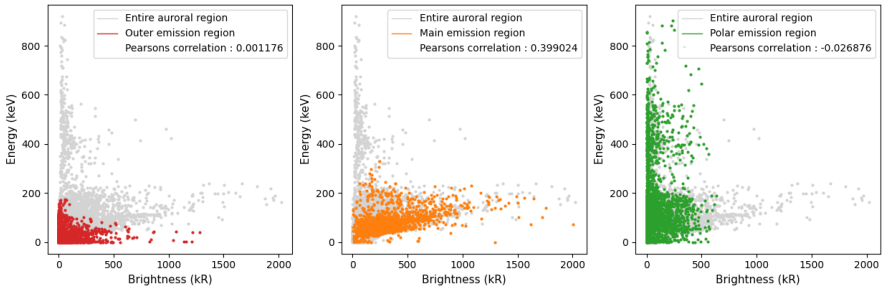

Relation between the brightness of the northern aurora (x-axis) and the mean energy of the population of electrons following a kappa distribution precipitating in the jovian atmosphere (y-axis) during PJ15. The grey dots represent the relation for the whole northern aurora, on top of which we have plotted in red the relation for the outer zone, in orange for the main emission zones and in green for the polar emission zone.

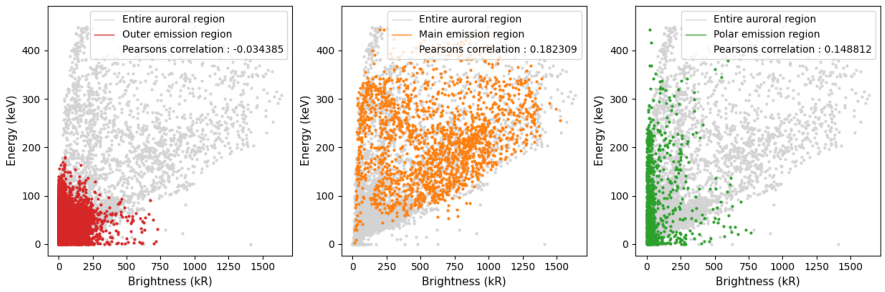

Relation between the brightness of the southern aurora (x-axis) and the mean energy of the population of electrons following a kappa distribution precipitating in the jovian atmosphere (y-axis) during PJ15. The grey dots represent the relation for the whole northern aurora, on top of which we have plotted in red the relation for the outer zone, in orange for the main emission zones and in green for the polar emission zone.

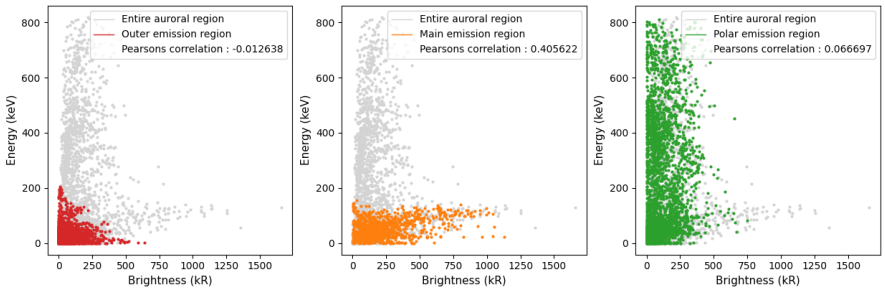

Relation between the brightness of the northern aurora (x-axis) and the mean energy of the population of electrons following a kappa distribution precipitating in the jovian atmosphere (y-axis) during PJ16. The grey dots represent the relation for the whole northern aurora, on top of which we have plotted in red the relation for the outer zone, in orange for the main emission zones and in green for the polar emission zone.

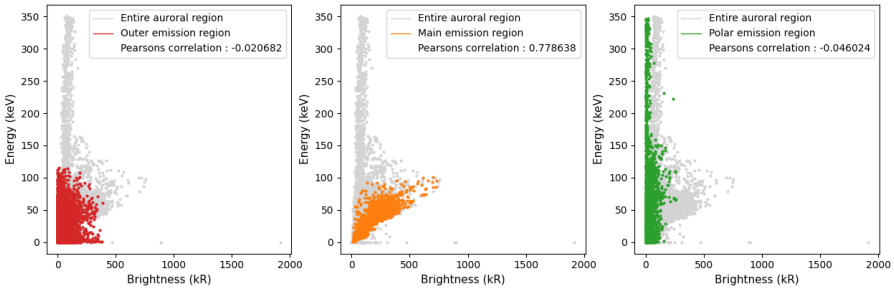

Relation between the brightness of the southern aurora (x-axis) and the mean energy of the population of electrons following a kappa distribution precipitating in the jovian atmosphere (y-axis) during PJ16. The grey dots represent the relation for the whole northern aurora, on top of which we have plotted in red the relation for the outer zone, in orange for the main emission zones and in green for the polar emission zone.

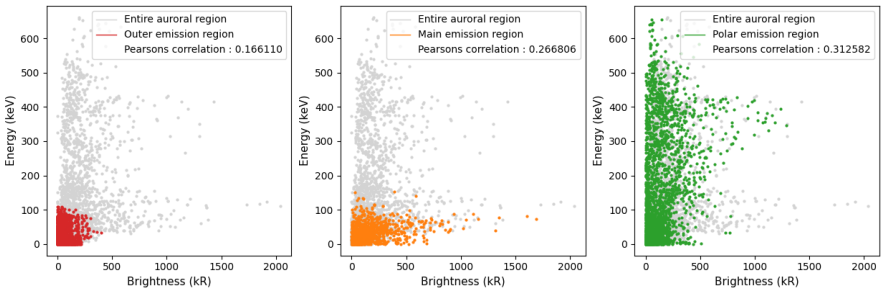

Relation between the brightness of the northern aurora (x-axis) and the mean energy of the population of electrons following a kappa distribution precipitating in the jovian atmosphere (y-axis) during PJ17. The grey dots represent the relation for the whole northern aurora, on top of which we have plotted in red the relation for the outer zone, in orange for the main emission zones and in green for the polar emission zone.

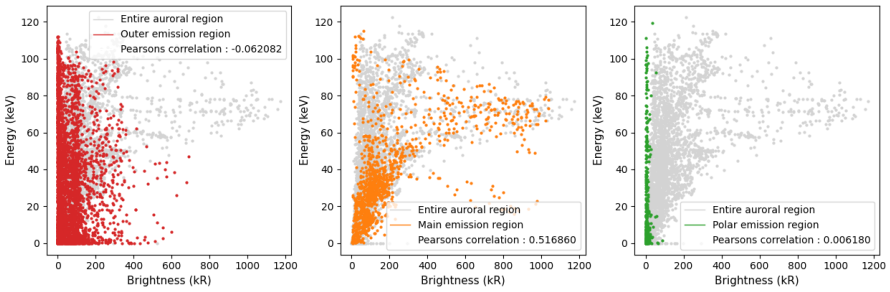

Relation between the brightness of the southern aurora (x-axis) and the mean energy of the population of electrons following a kappa distribution precipitating in the jovian atmosphere (y-axis) during PJ17. The grey dots represent the relation for the whole northern aurora, on top of which we have plotted in red the relation for the outer zone, in orange for the main emission zones and in green for the polar emission zone.

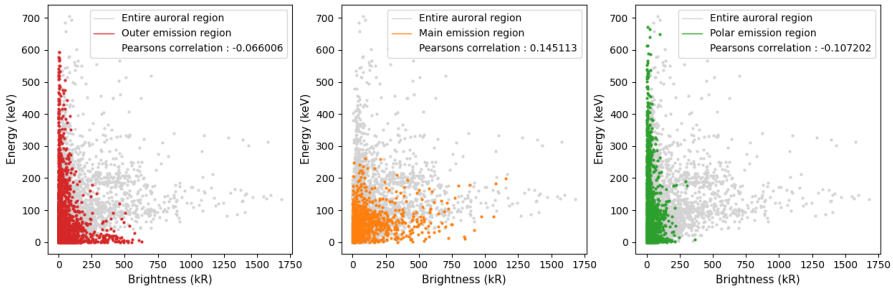

Relation between the brightness of the northern aurora (x-axis) and the mean energy of the population of electrons following a kappa distribution precipitating in the jovian atmosphere (y-axis) during PJ18. The grey dots represent the relation for the whole northern aurora, on top of which we have plotted in red the relation for the outer zone, in orange for the main emission zones and in green for the polar emission zone.

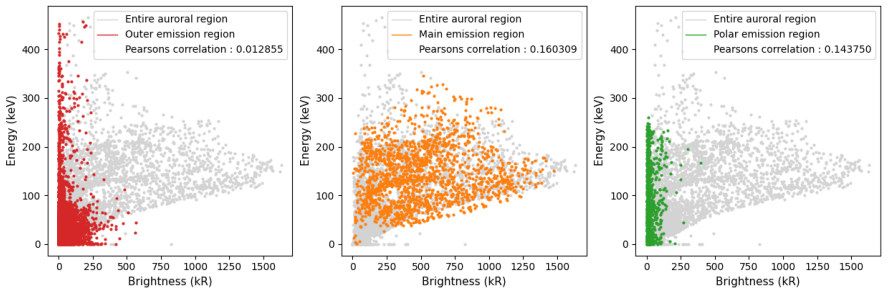

Relation between the brightness of the southern aurora (x-axis) and the mean energy of the population of electrons following a kappa distribution precipitating in the jovian atmosphere (y-axis) during PJ18. The grey dots represent the relation for the whole northern aurora, on top of which we have plotted in red the relation for the outer zone, in orange for the main emission zones and in green for the polar emission zone.

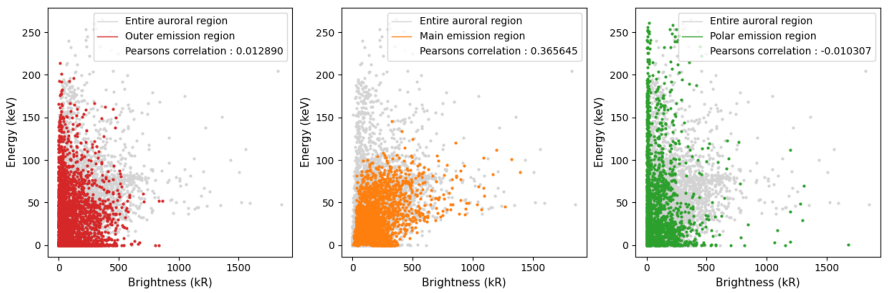

Relation between the brightness of the northern aurora (x-axis) and the mean energy of the population of electrons following a kappa distribution precipitating in the jovian atmosphere (y-axis) during PJ19. The grey dots represent the relation for the whole northern aurora, on top of which we have plotted in red the relation for the outer zone, in orange for the main emission zones and in green for the polar emission zone.

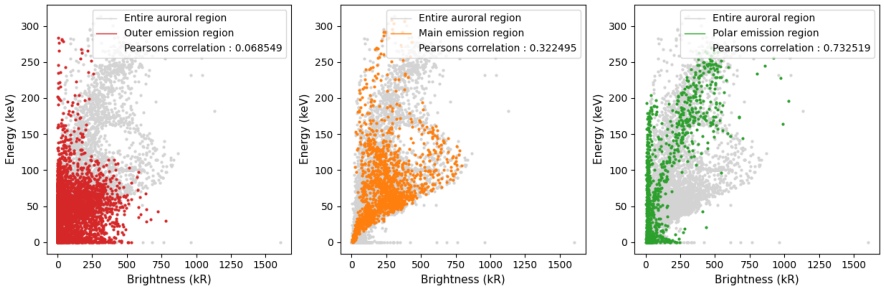

Relation between the brightness of the southern aurora (x-axis) and the mean energy of the population of electrons following a kappa distribution precipitating in the jovian atmosphere (y-axis) during PJ19. The grey dots represent the relation for the whole northern aurora, on top of which we have plotted in red the relation for the outer zone, in orange for the main emission zones and in green for the polar emission zone.

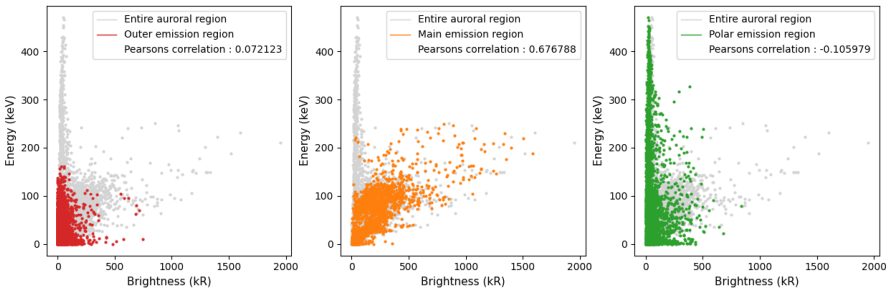

Relation between the brightness of the northern aurora (x-axis) and the mean energy of the population of electrons following a kappa distribution precipitating in the jovian atmosphere (y-axis) during PJ20. The grey dots represent the relation for the whole northern aurora, on top of which we have plotted in red the relation for the outer zone, in orange for the main emission zones and in green for the polar emission zone.

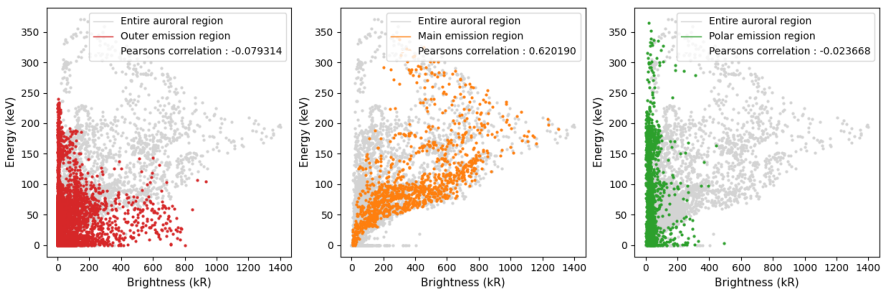

Relation between the brightness of the southern aurora (x-axis) and the mean energy of the population of electrons following a kappa distribution precipitating in the jovian atmosphere (y-axis) during PJ20. The grey dots represent the relation for the whole northern aurora, on top of which we have plotted in red the relation for the outer zone, in orange for the main emission zones and in green for the polar emission zone.